Multi-wavelength Studies of Non-magnetic Cataclysmic Variables

Rachel Joanna Dickinson

Thesis submitted for the Degree of Doctor of Philosophy

UNIVERSITY

COLLEGE LONDON

November 1997

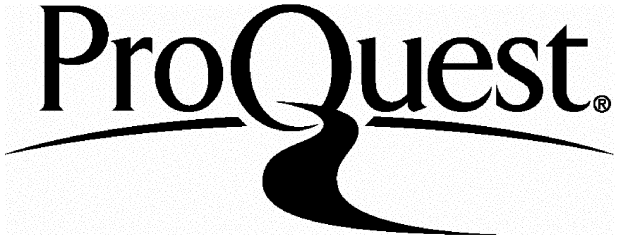

for

Eric and Rena Gummery

and

Lillian and Leonard Dickinson

Abstract

This thesis comprises spectroscopic case studies of three non-magnetic nova-like and dwarf nova type cataclysmic variables (CVs). The principal goals were to investigate the accretion disk and optical spectral line properties of a sample of CVs which are known (usually from ultraviolet studies) to drive a fast outflow or wind. New optical, time-series data sets, secured from La Palma and Canada, are used to establish the (often complex) time- and phase-dependent behaviour of the emission and absorption line sources. The optical analyses have also been compared and contrasted with constraints from *Hubble Space Telescope* (*HST*) and archive *International Ultraviolet Explorer* (*IUE*) data.

High resolution optical spectroscopy of V795 Herculis is presented. Separate low and high velocity fluctuations phased on the 2.6 hr orbital period are observed in the Balmer lines. This thesis argues against models which invoke channelled accretion columns flowing onto a synchronously rotating white dwarf, instead presenting disk-overflow model simulations which quantitatively account for several of the observed dynamical properties of V795 Her. The discrepancies of this model are addressed. A comparison of these optical spectra to quasi-simultaneous HST observations (which provide an unprecedented multi-wavelength data set) is made. A strong correlation between the overall UV and optical line strength changes implies that the UV changes cannot be principally due to the fast outflow.

A time-resolved orbital study of the dwarf nova SS Cygni is also presented. These observations were taken at the maximum of a long, asymmetric type outburst, and confirm the presence of stationary, low velocity emission previously reported during a long, symmetric outburst. Possible sources for this emission, including a wind origin, are investigated.

The peculiar nova-like BZ Camelopardalis, associated with a bow-shock nebula, has previously shown unambiguous evidence for a wind in its optical spectrum. New optical data reveal wind-formed features in the Balmer lines. Model fits constrain the inclination angle and archive *IUE* spectra are used to estimate the wind mass loss.

Acknowledgements

Firstly I wish to thank my supervisor, Raman Prinja, for his unfailing support throughout my time at UCL. It is also a pleasure to thank the following people for their useful advice, informative discussions and their support: Simon Rosen, Paul Crowther, Matthew Dalton, Richard Townsend, Keith Smith and Danny Steeghs. I would like to thank Keith Horne for the use of his tomography code, Janet Drew for the use of her CV wind modelling code and Coel Hellier for providing Figure 2.31. In this research, I have used, and acknowledge with thanks, data from the AAVSO International Database, based on observations submitted to the AAVSO by variable star observers worldwide.

Financially, I am indebted to the Leigh Trust, the Edwards Kenilworth School Charity and my parents without whose assistance this work would not have been possible. I acknowledge the receipt from UCL of the Thomas Momber Scholarship and a Department of Physics and Astronomy Bursary.

Finally my thanks go to Sarah, Graham and Darian for keeping me sane and to Ian for all his help, encouragement and support.

Contents

List of Tables

List of Figures

Chapter 1

Introduction

The research presented in this thesis is principally concerned with optical spectroscopic studies of the 3 non-magnetic cataclysmic variables (CVs) V795 Herculis, SS Cygni and BZ Camelopardalis. Investigations of each system are extended by additional analyses based on new *HST* and archive *IUE* ultraviolet (UV) spectroscopy. The fundamental aim of the research is to establish the detailed optical spectral line characteristics of CVs which are known (from the properties of the UV resonance lines) to drive fast winds. The studies concentrate on the optical emission (and absorption) line sources and investigate the (often complex) time- and phase-dependent line profile behaviour. The optical line contributions likely arise from the accretion disk and from stream overflow regions and, in the exceptional case of BZ Cam, from an outflowing wind.

This chapter aims to place these studies within the broader context of CV observational studies and physical models for the formation of accretion disks, line formation properties and the incidence of fast disk-driven outflows. Section 1.1 provides a basic introduction to CV systems and begins with a description of the various classes of CVs. Section 1.1.1 introduces the physics of CVs and accretion disks and Section 1.1.2 goes on to discuss the observed 'period gap' and the secular evolution of CVs. Current theories on dwarf nova outburst mechanisms, described in Section 1.1.3, lead on to the unification model of outbursts in Section 1.1.4. The final part of this basic introduction deals with the topic of line formation (Section 1.1.5).

The CVs studied in this thesis are linked because they are all known (usually from UV studies) to drive outflows. Section 1.2 discusses CV winds. The formation of the P Cygni-type line profiles seen in the UV is discussed in Section 1.2.1. Section 1.2.2 presents some observational evidence

for CV winds and for wind variability. Finally the current status of wind modelling is examined in Section 1.2.3.

Having placed this thesis within a broader context, I go on to describe an important analytical tool in Section 1.3: the technique of Doppler imaging, used throughout this thesis to constrain the line formation regions. Finally, in Section 1.4, I outline the broader aims of the thesis and present an overview of the structure of the remaining chapters.

1.1 Cataclysmic Variables

CVs are semi-detached binary systems which consist of an accreting white dwarf (WD) and a cool, low mass star whose surface is in contact with its Roche lobe (Section 1.1.1). Their properties are dominated by the mass transfer which occurs from the secondary star to the WD via the inner Lagrangian point. An accretion disk forms around the WD unless the accretion is channelled by a strongly magnetic primary.

CVs may be viewed as 'laboratories' in which accretion theory can be tested. The binary nature of the systems often allows important system parameters, such as the orbital period, the binary separation, the inclination angle and the masses of the primary and secondary stars, to be measured. The accretion disk can frequently be examined separately from the binary components thus aiding our understanding of the physical processes that occur in it. These processes are likely to be analogous to processes occurring in less well-studied systems with accretion disks, namely protostars and active galactic nuclei. Accretion processes are also important in X-ray binaries. The unpredictable nature of CVs and their apparent brightness during outburst has also made them popular targets with amateur observers. The resultant light curves span many decades and provide a valuable observational constraint.

It is thought that CVs form from long period close binaries via a common envelope phase. This evolution scenario, outlined by Webbink & Politano (1993), is shown in Figure 1.1. The primary star in the primordial long period binary evolves until it reaches the giant branch (or even the asymptotic giant branch) before mass transfer is initiated. Supercritical mass transfer *onto* the secondary occurs until the entire system becomes immersed in a common envelope. The envelope removes orbital energy and angular momentum from both the primary (now a degenerate core) and the secondary (still a relatively dense unevolved star), the angular momentum being shed in

an equatorial belt. The dissipation of a sufficient amount of orbital energy unbinds the envelope and exposes the embedded core: a pre-cataclysmic white dwarf-red dwarf binary. Further angular momentum losses, or the evolution of the secondary star, occur until the system interacts again, this time as a CV.

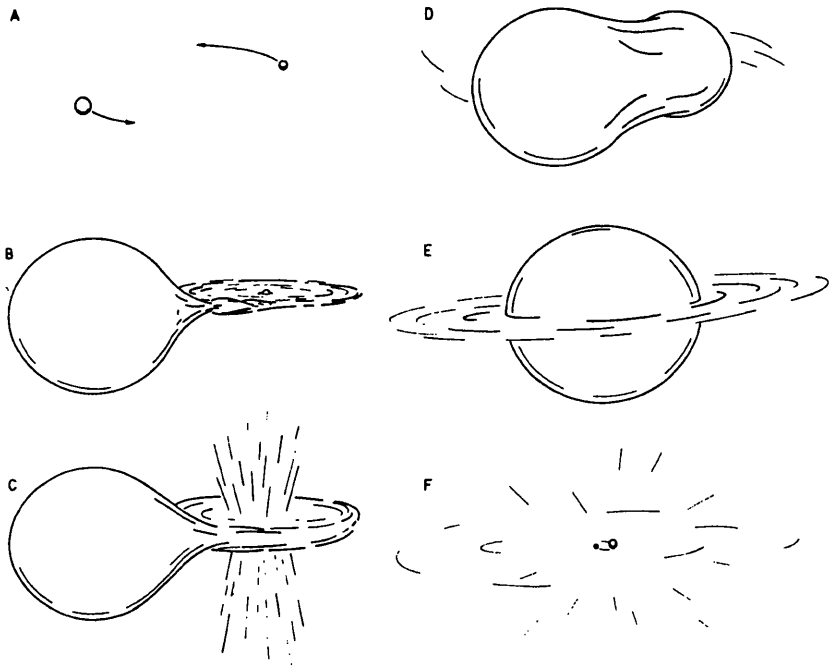

Figure 1.1: Evolution of a long period primordial binary (A) to a pre-CV (F). B shows the onset of mass transfer, supercritical mass transfer develops in C, D shows the immersion into a common envelope and in E angular momentum is being shed in an equatorial belt. From Webbink & Politano (1993).

Traditionally CVs are classified according to the frequency and magnitude of their outbursts and the magnetic properties of the WD. Initially the light curve morphology was used as a classification tool but later this was refined by also considering the spectroscopic properties. There are four main classes of CVs: (i) the classical novae (one nova outburst in historical times), (ii) the recurrent novae (more than one outburst; shortest recurrence time $\sim$ few decades), (iii) the dwarf novae (more frequent but less spectacular outbursts) and (iv) the nova-likes (do not undergo prominent outburst; photometric and spectroscopic properties similar to the maximum light properties of the other classes) (Robinson 1976). These classes may be further sub-divided (see later; Warner 1995).

The single eruption of the classical novae, during which the system brightens by between about 6 and 19 magnitudes, is caused by a build-up of the hydrogen-rich material that is accreting onto

the WD primary. The pressure and density of the material increases to the point where nuclear reactions are ignited and a thermonuclear runaway occurs. The same physical process is also behind the eruptions of the recurrent novae, all of which were previously recognised as classical novae until they suffered repeated eruptions. In a dwarf nova, however, the outburst is caused by the release of gravitational energy following a large, temporary increase in the rate of mass transfer through the disk. The two rival mechanisms which may cause this increase are discussed in Section 1.1.3. Dwarf novae have outburst cycles which repeat over intervals of ten days to tens of years, with outbursts that last for 2 – 20 days and which cause the system to brighten by between 2 and 5 magnitudes. This class is split into three sub-classes: (i) Z Cam stars, which show protracted standstills, (ii) SU UMa stars, which show occasional superoutbursts and (iii) U Gem stars, which include all the remaining dwarf novae. The fourth class of CVs, the nova-likes, are often described as 'non-eruptive' CVs but it is more appropriate to describe them as undergoing 'permanent eruption'. This class is also sub-divided, this time into (i) UX UMa stars, (ii) VY Scl stars (which show an occasional reduction in brightness) and (iii) magnetic systems. A magnetic WD can disrupt the formation of an accretion disk around the primary, either totally (giving the class of the polars, or AM Her stars) or partially (the intermediate polars, or DQ Her stars).

CVs may also be classified according to their accretion structure, as reviewed by Giovannelli & Martínez-Pais (1991). CV accretion structure is influenced by the mass transfer rate, the magnetic field of the WD and by some parameters of the binary system. This classification is shown in Table 1.1.

Type	Magnetic Field	Disk	Boundary layer	Accretion Columns
Non-magnetic	Weak	Yes	Yes	No
Intermediate Polar	Moderate	Yes	No	Yes
Polar	Strong	No	No	Yes

Table 1.1: Classification of CVs following the accretion structure (from Giovannelli and Martínez-Pais 1991).

The CVs studied in this thesis are classified as nova-likes or dwarf novae, *i.e.* supposedly they are all non-magnetic CVs. V795 Her[1] and BZ Cam are nova-like variables and SS Cyg is a U Gem

[1]The CV V795 Her (Chapters 2 and 3) is currently classed as a nova-like variable, although some authors have proposed intermediate polar scenarios for this object.

type dwarf nova. The following section summarises the physics of non-magnetic systems.

1.1.1 The Roche potential and accretion disk formation

CVs belong to the group of 'interacting' binary stars, which means that the binary separation is small enough to allow the two stars to interact both gravitationally and tidally. While the small radius of the WD leaves it unaffected by the tidal influence of the secondary, the secondary star is greatly distorted by the gravitational field of the primary. A tidal interaction causes the secondary to rotate synchronously with the orbital motion of the system, and tends to eliminate any initial eccentricity in the orbit. The two stars therefore describe circular Keplerian orbits about one another in a plane and Kepler's third law allows the binary separation a to be written in terms of the orbital period P_{orb}:

$$4\pi a^3 = G(M_1 + M_2)P_{orb}^2 \tag{1.1}$$

The standard theoretical treatment of CVs (Frank, King & Raine 1985; Warner 1995) begins with a calculation to find the total potential at any point in the system. This is carried out in a frame of reference that corotates with the binary system and has its origin at the WD primary. The x-axis runs along the line of centres and the y-axis is perpendicular to it, in the orbital plane. The coordinate system therefore rotates with the binary. The total potential at any point in the system is the sum of the gravitational potential of the two stars and the effective potential of the fictitious centrifugal force. The highly distorted secondary star in most CVs appears to be very similar to a single main sequence star or to a giant, both of which have masses which are quite centrally condensed. Thus the 'Roche approximation' may be used and the gravitational field of the secondary is approximated by that of an undistorted star. The gravitational potentials of both the WD and the secondary are therefore equivalent to the potentials due to point masses. The Roche potential ϕ_R is given by

$$\phi_R = -\frac{GM_1}{(x^2+y^2+z^2)^{1/2}} - \frac{GM_2}{[(x-a)^2+y^2+z^2]^{1/2}} - \frac{1}{2}\Omega_{orb}^2[(x-\mu a)^2+y^2] \tag{1.2}$$

where $\mu = \frac{M_2}{(M_1+M_2)}$ and $\Omega_{orb} = \frac{2\pi}{P_{orb}}$. Using this formulation the shapes of the Roche equipotentials (*i.e.* where ϕ_R = constant) may be calculated (Figure 1.2).

The shapes of the Roche equipotentials are determined only by the mass ratio q (= M_2/M_1), with the binary separation a operating essentially as a scale factor. From Figure 1.2 one sees that to

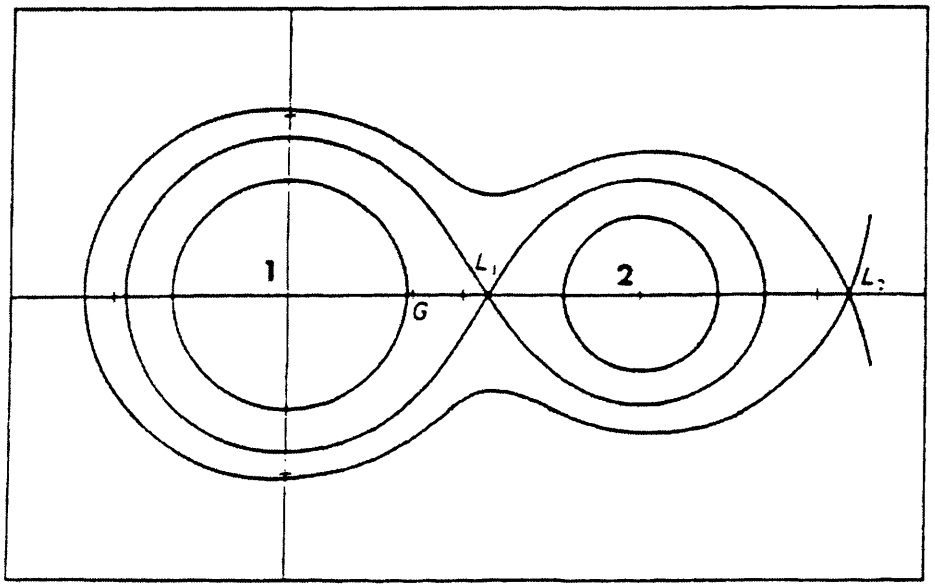

Figure 1.2: The Roche equipotentials. The numbers 1 and 2 mark the centres of the WD and the secondary respectively, and G marks the centre of mass of the binary. L_1 marks the inner Lagrangian point, through which mass transfer occurs. (L_2 is one of two outer Lagrangian points). From Warner (1995).

matter at large distances ($r \ggg a$) the Roche equipotentials appear to be due to a point mass viewed in a rotating frame, and to matter which is close to either of the stars, the equipotentials are circular and the gravitational attraction of the nearest star dominates. The heavy line in Figure 1.2 shows the critical surface, or Roche lobe, surrounding each star, which is the largest *closed* equipotential. As the secondary star expands beyond its Roche lobe, mass will be transferred into the Roche lobe of the primary via L_1, the inner Lagrangian point.

In a CV the binary system is semi-detached: the secondary fills its Roche lobe while the primary lies well within its lobe. A gas particle at L_1 is equally attracted to both stars, and gas can escape from the atmosphere of the secondary into the Roche lobe of the primary. Gas particles are ejected through L_1 at thermal velocities ($\approx 10\,\mathrm{km\,s^{-1}}$). This results in a gas stream whose trajectory may be calculated by integrating the equations of motion for a particle in the rotating binary frame. This trajectory lies both in the orbital plane and within the Roche lobe of the primary. It flows past the (non-magnetic) primary and collides with itself at supersonic speeds thus radiating away the kinetic energy of the impact as the gas is shocked to high temperatures. Figure 1.3 shows schematically how the initial gas stream forms into a ring, a circular orbit being the configuration with the least energy for a given angular momentum. The ring is of finite extent and rotates differentially. This results in a shearing flow which leads to energy losses as heat is generated by viscous processes in the gas.

To compensate for this energy loss, some material must move deeper into the primary's gravitational field. To conserve angular momentum other particles must then move outwards and thus the ring spreads and a disk is formed. (If the magnetic field of the WD is strong enough, it is the magnetic forces which control the flow of the accretion stream and the formation of a disk is prevented).

The gas stream now impacts a fully established accretion disk at its outer rim. This creates a bright spot on the disk as the supersonic collision shock-heats the impact area, generating turbulence which causes the bright spot to vary rapidly in both structure and position. This turbulence is a possible origin of the short timescale ($\sim$ few minutes) flickering that is characteristic of all CVs. Modelling of the stream-disk impact (Livio, Soker & Dgani 1986; Rozyczka & Shwarzenberg-Czerny 1987; Rozyczka 1988; Dgani, Livio & Soker 1989; Hirose, Osaki & Mineshige 1991; Lanzafame, Belvedere & Molteni 1992, 1993) has shown that the gas stream may interact with the accretion disk in several important ways. The dense stream core locally heats the rim as it penetrates

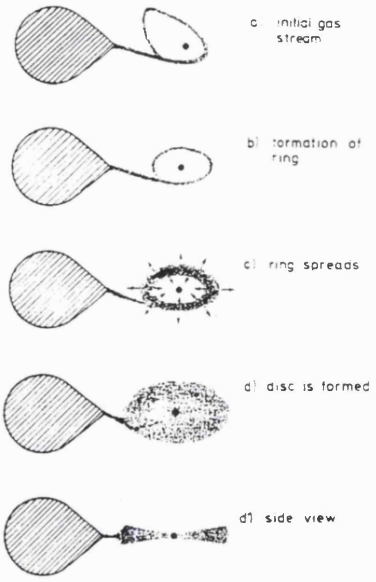

Figure 1.3: The formation of an accretion ring and its evolution into a disk. From Verbunt (1982).

the disk edge, resulting in a bulge that runs around the disk edge for roughly half the perimeter. A further important interaction occurs when the gas stream overflows the disk rim and continues to follow its single particle trajectory. A second bright spot is formed at the re-impact site. This form of interaction is discussed as an explanation for the line profile variations seen in the nova-like variable V795 Her in Chapter 2 (see Section 2.7.2).

Disk material spirals inwards towards the WD. A 'boundary layer' region exists between the accretion disk and the WD. In this region the disk material decelerates from Keplerian velocities until it reaches the surface velocity of the WD, resulting in a release of energy. By conservation of energy and angular momentum, Kley (1991) showed that the energy released is

$$L_{BL} = L_{disk}\left[1 - \frac{\Omega_{WD}}{\Omega_{Kep}(R_{WD})}\right]^2 \tag{1.3}$$

where $\Omega_{Kep}(R_{WD})$ is the Keplerian velocity evaluated at R_{WD}, the radius of the WD and Ω_{WD} is the surface velocity of the WD. The boundary layer can therefore have a luminosity which is comparable to that of the accretion disk when the WD rotates well below its break-up velocity. An optically thick boundary layer emits mainly in the soft X-ray and extreme ultraviolet (EUV) spectral regions, and an optically thin boundary layer radiates hard X-rays.

The accretion disk is normally the dominant light source in non-magnetic CVs at optical and

UV wavelengths. Further contributions arise from the bright spot, the irradiated secondary star, the gas stream, and regions of gas stream-accretion disk interaction; their relative strengths and importance depend upon the physical properties of the system in question. Section 1.1.5 discusses line formation in CVs but before that topic is reached, Section 1.1.2 examines the observed CV 'period gap' and Sections 1.1.3 and 1.1.4 look at the current models of outburst mechanisms. It is clear from these sections that the rate of mass transfer from the secondary star is critical in determining the observational properties of a CV.

1.1.2 The period gap and secular evolution

Observational studies show that the orbital periods of most CVs lie in the range 80 min – 20 hr, with a 'period gap' between 2 – 3 hr which contains relatively few systems (see Figure 1.4). As CVs are thought to continuously lose angular momentum and evolve to shorter orbital periods, the existence of a period gap is somewhat of a puzzle. Generally it is thought that this is unlikely to be an observational selection effect, which leaves three possibilities: (i) CVs above the period gap reverse the direction of their evolution once they reach ~ 3 hr (Eggleton 1976; Taam & McDermott 1989); (ii) CVs evolve quickly across the period gap; (iii) mass transfer is switched off at ~ 3 hr (Spruit & Ritter 1983).

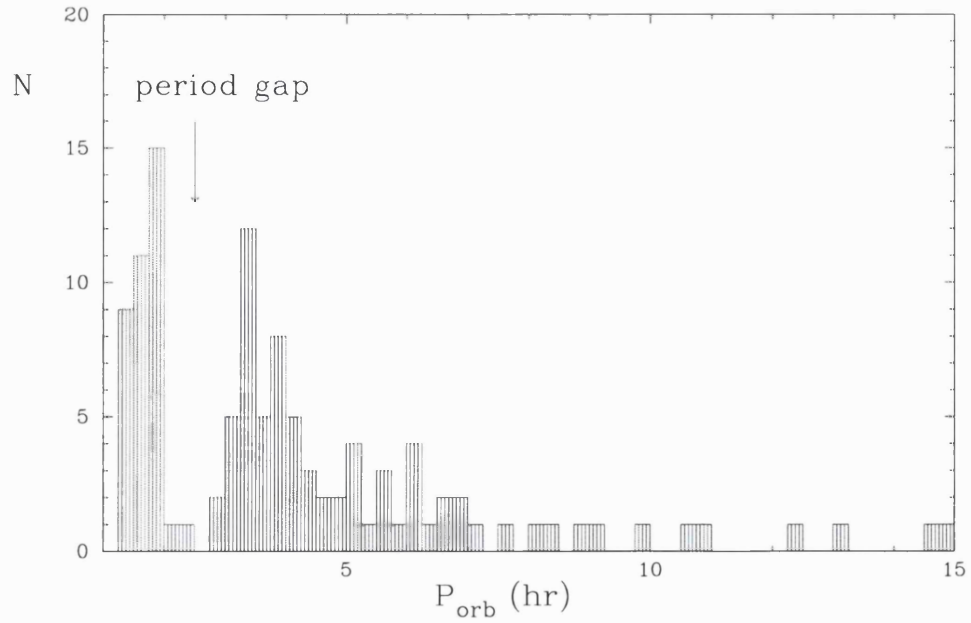

Figure 1.4: The observed CV 'period gap'.

The third explanation is currently the most favoured. CVs are believed to undergo angular momentum losses due to magnetic braking by the stellar wind of the secondary star. The stellar wind of the secondary is forced by the magnetic field to corotate with it, which exerts a magnetic torque and removes spin angular momentum from the star. In turn, this removes orbital angular momentum from the system because the secondary is held in synchronous rotation. The system spins down. When the mass of the secondary reaches $\sim 0.3\,M_{\odot}$(corresponding to P $\sim$ 3hr) it will become fully convective (Robinson *et al.* 1981), which could switch off the magnetic braking (it has been speculated that a radiative core is required to produce a dynamo field). The secondary now decreases its radius on a thermal timescale and becomes detached from its Roche lobe. The transfer of mass ceases and the system will no longer be recognised as a CV. Angular momentum losses will still be occurring, but now gravitational radiation is the dominant loss mechanism. This causes the Roche lobe to shrink on a gravitational timescale, eventually making contact with the secondary star again. The lower limit of the period gap has been reached and mass transfer resumes (Rappaport, Verbunt & Joss 1983; Paczynski & Sienkiewicz 1981).

A very recent study by Verbunt (1997) has suggested that the existence of the period gap may be a selection effect. By reclassifying the VY Scl stars (currently classified as nova-likes which exhibit occasional reductions in brightness) as a sub-class of the dwarf novae, the statistical significance of a period gap for nova-likes decreases dramatically. The observed gap remains statistically significant for the dwarf novae (including the VY Scl systems) and for the magnetic systems combined (the polars and the intermediate polars). The existence of these observed period gaps could perhaps be explained by phenomena that increase the detection probability of certain CV classes in a particular period range.

The nova-like variable V795 Her, examined in Chapters 2 and 3, is claimed to have an orbital period of 2.6 hr and therefore appears to lie in the period gap. Its evolutionary status may have significant effects on its observable properties.

1.1.3 Dwarf nova outburst theory

The changes in luminosity of a dwarf nova over its outburst cycle are due to a brightening of the accretion disk. Unlike the physical process responsible for classical novae and recurrent novae, thermonuclear runaway cannot explain the dwarf novae outburst cycles as the recurrence time of the outbursts is too short. Dwarf novae outbursts decline after just a few days whereas in models

of thermonuclear runaways for such systems, the amount of energy injected would take roughly 15 years to radiate away (Starrfield, Sparks & Truran 1974). The observations of the dwarf nova SS Cyg presented in Chapter 4 were recorded near the maximum of an outburst.

Two theories exist to explain the cause of the disk brightening: the mass transfer instability model and the disk instability model. The outbursts are triggered either by an instability in the actual rate of mass transfer from the secondary or by an instability mechanism that is inherent to the disk. These two theories are discussed below.

Mass transfer instability

In the mass transfer instability model the source of the instability lies on the secondary star. The instability causes an increase in the rate of mass transfer from the secondary and results in enhanced mass accretion through the disk. In one of the first instability mechanisms proposed (Bath 1974; also see Papaloizou & Bath 1975), the secondary star taps into the recombination energy available in the ionization zones which lie below the convective surface layers. The secondary stars in CVs are low mass main sequence stars, whose outer layers may be dynamically unstable. Instabilities may develop on the dynamical timescale of the secondary, and the quiescence timescale would be determined by the thermal timescale of the envelope layers. Problems with this model arise for CVs with lower mass secondaries ($M_2 < 0.5\,M_\odot$) whose convective envelopes are so deep it would be difficult to tap into the ionization zones. Such low mass systems are still observed to exhibit dwarf nova outbursts.

A second instability mechanism could be controlled by the magnetic activity of the secondary star. A dynamo field may be generated by the secondary as it has a convective envelope and it is in forced corotation. Current observations of magnetic cycles indicate, however, that changes in magnetic activity tend to occur on a longer timescale than that observed for dwarf novae outbursts (Bianichimi 1990; Warner 1988).

Disk instability

In the second set of models describing dwarf nova outbursts the source of the instability lies on the accretion disk (first suggested by Osaki 1974). The mass transfer rate from the secondary star is believed to be constant, with outbursts occurring due to changes in the mass accretion rate onto the

WD. Hoshi (1979) first proposed a mechanism whereby an instability could arise. In solving the equations describing the outer parts of an accretion disk he discovered *two* solutions. The disk can exist in either a low viscosity, optically thin state with the hydrogen neutral, or in a high viscosity, hot state with the hydrogen ionized. Meyer & Meyer-Hofmeister (1981) developed this idea further and calculated the thermal equilibrium curve. The equations describing the accretion disk are set up by considering the conservation of mass and angular momentum. By including the condition of thermal equilibrium (*i.e.* that the local viscous heat generation is equal to the radiative cooling from the disk surface), a plot of the effective temperature vs. the surface density may be obtained (Figure 1.5). The thermal equilibrium curve shows bistable behaviour, and a thermal limit cycle arises. For a constant viscosity parameter, this instability is localized. To create full outburst-quiescence behaviour, different values of the viscosity parameter must be chosen for the hot and cold branches to allow the cooling front to propagate through a large enough radial extent of the disk.

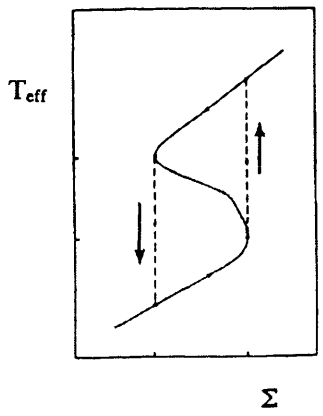

Figure 1.5: The thermal equilibrium 's-curve': a plot of the effective temperature (T_{eff}) versus the surface density (Σ). The thermal equilibrium curve shows bistable behaviour, and a thermal limit cycle arises. From Warner (1995).

The thermal instability limit cycle produces outbursts as follows: during quiescence the dwarf nova stores mass in the disk in a low viscosity state until a critical mass has been accumulated ($\dot{M}_{disk} < \dot{M}_2$). At the critical surface density, the thermal instability sets in, the disk jumps to the high viscosity state and the system goes into outburst as matter is dumped onto the WD. Once the mass in the disk has been sufficiently depleted the disk returns to the low viscosity cold state and the outburst ends. Full treatment of the disk to include realistic opacities and a smooth interpolation of the viscosity parameter between the hot and cold branches results in a thermal equilibrium curve which has a stable, intermediate branch. This additional stable state could explain the 'UV delay'

seen in some dwarf novae outbursts (*e.g.* in VW Hyi, Pringle, Verbunt & Wade 1986) in which the rise to outburst is delayed in the UV relative to the optical (Mineshige 1988).

The outbursts caused by the thermal disk instability may occur in two distinct ways, depending on the disk region in which ignition to the hot state first happens (Smak 1984). If the mass transfer rate is high, there is a lot of matter accumulating at the outer edge of the disk and this will be the region that reaches the critical density first. The outburst then proceeds 'outside-in' as the warm front moves from the outer disk regions to the inner disk. When the mass transfer rate is low, the disk has time to transport material to the inner disk regions via viscous diffusion. The inner disk is then first to reach the critical density, the warm front moves outwards and an 'inside-out' type outburst occurs.

Whitehurst (1988) proposed a second instability mechanism intrinsic to accretion disks: the tidal instability. The secondary star exerts periodic tidal stresses on the disk, which result in a precessing, eccentric accretion disk (Osaki 1989). The eccentric precession produces large-amplitude modulations in the light curve, known as superhumps, which occur at an anomalous period that exceeds the orbital period by a few percent. This phenomenon is a well known feature of dwarf novae in superoutburst (Warner 1985) and has now been observed in many non-eruptive stars (Patterson *et al.* 1993; Skillman & Patterson 1993). The tidal instability only acts in binaries with low mass ratios ($q < 0.25$), and superhumps are only observed for systems below the period gap (Osaki 1996).

1.1.4 The unification model of outbursts

Osaki (1996) discusses a unified model of dwarf nova outbursts. By appropriate combination of the thermal instability and the tidal instability mechanisms, he describes the different outburst behaviour of all non-magnetic CVs. Two parameters are used to characterize these systems: the orbital period (which fixes the disk radius) and the mass transfer rate from the secondary ($\dot{M}_2$). The mass transfer rate determines the thermal stability of a system and the mass ratio (dependent on the orbital period) determines the system's tidal stability. Figure 1.6 shows the four resultant kinds of outburst behaviour. In the upper right are the nova-likes, thought to be steady accretors with hot disks and therefore both thermally and tidally stable. The permanent superhumpers lie in the upper left of the diagram. These are nova-likes which exhibit permanent superhump behaviour; they are thermally stable but tidally unstable. In the lower right are the tidally stable but thermally unstable

CVs: the ordinary, U Gem type dwarf novae. Finally, in the lower left are the CVs which are both thermally and tidally unstable. These are the SU UMa stars which are the class of dwarf novae that exhibit superhumps and superoutbursts. Lying on the borders between these four regions are various other sub-classes of CV, such as the Z Cam stars. They, for example, are on the borderline of thermal stability and thus show occasional standstill behaviour.

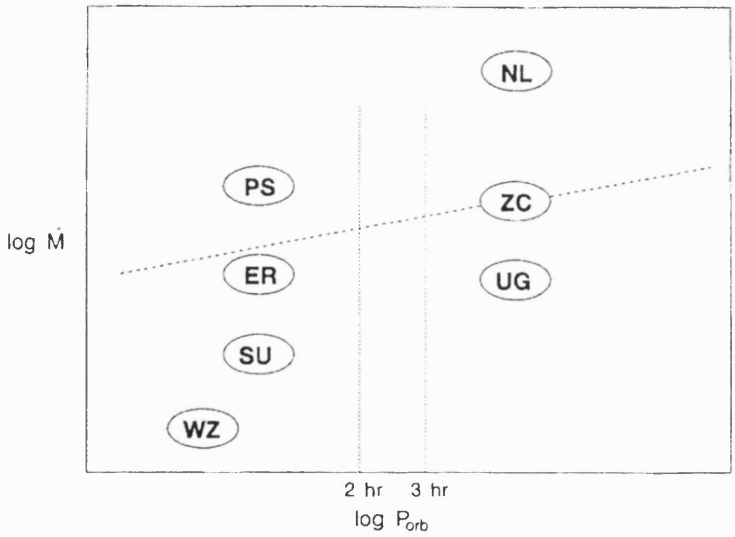

Figure 1.6: A plot of the mass transfer rate $\dot{M}$ against orbital period P_{orb} showing the different outburst behaviours of non-magnetic CVs according to the unification model of Osaki (1996). The vertical dotted lines show the period gap region (2 – 3hr) and the diagonal dashed line shows the borderline between thermally stable and unstable disks (see text). NL: nova-likes, ZC: Z Cam stars, UG: U Gem stars, PS: permanent superhumpers, ER: 'ER UMa stars' (extreme SU UMa stars with very short supercycle recurrence times), SU: SU UMa stars, WZ: WZ Sge stars (extreme SU UMa stars with rare, very large outbursts). From Osaki (1996).

1.1.5 Emission line formation in disks

The mechanisms of line formation in any given CV are not yet well understood. Line formation is certainly complicated, as evidenced by the wide range of ionization states observed (indicating line formation in more than one site) and the uncorrelated behaviour of the different lines during, for example, a dwarf nova outburst cycle.

The dominant light source in non-magnetic CVs, the accretion disk, produces characteristic

double-peaked emission line profiles. The formation of such profiles is discussed by Horne & Marsh (1986). The orbital motion of the disk material about the WD causes the accretion disk emission lines to be Doppler broadened. The Keplerian velocity of material in a physically thin disk moving in a circular orbit at radius r from the WD is

$$v_{Kep} = \left(\frac{GM_{WD}}{r}\right)^{1/2} \tag{1.4}$$

resulting in a Doppler shift along the line of sight to the observer of

$$v_{Dop} = v_{Kep}\sin(i)\sin(\theta) \tag{1.5}$$

where i is the inclination angle and θ is azimuth angle relative to the line of sight. Panel (a) of Figure 1.7 shows the loci of constant radial velocity on the face of a Keplerian disk. Panel (b) shows the resultant emission line profile. Emission in each shaded velocity bin arises from the correspondingly shaded region of the disk.

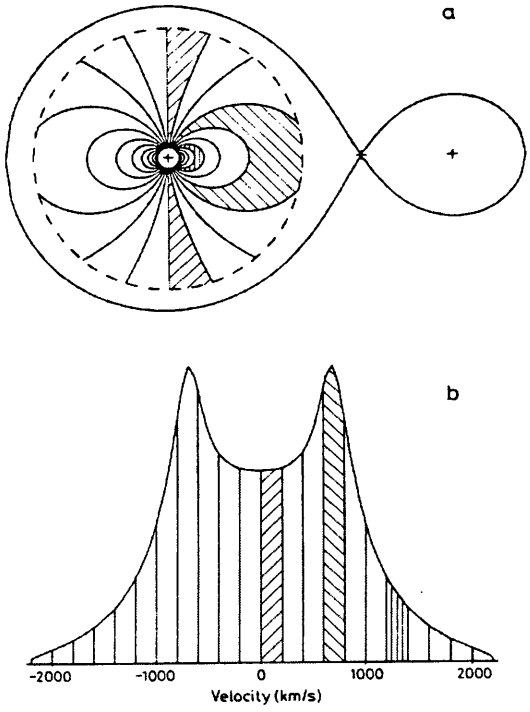

Figure 1.7: A Keplerian accretion disk (panel a) and the resultant double-peaked emission line profile (panel b). Loci of constant radial velocity are marked on the accretion disk. The shaded disk regions produce the correspondingly shaded emission in the line profile. From Horne & Marsh (1986).

Although the basic double-peaked shape of the emission line profiles is readily reproduced by models, the details of line formation are not so well understood. The three main sites of line formation suggested are (i) optically thin emission, (ii) chromospheric emission and (iii) emission from an outflow (Warner 1995). Mechanisms (i) and (ii) are dealt with below, and wind emission is discussed in Section 1.2.

An emission spectrum will be produced in any part of an accretion disk where the continuum is optically thin but the lines have significant optical thickness. Modelling such regions (*e.g.* Williams & Shipman 1988) has had limited success: the computed spectra have strong emission lines but they are generally weaker than the observed lines (Williams 1983; Patterson 1984). Observations of high inclination systems also do not agree with the predictions that models of this particular mechanism make. The disks of high inclination systems are expected to be optically thick in the continuum which would result in weak emission lines, contrary to the strong emission observed in quiescent dwarf novae with low accretion rates through their disks.

Chromospheric emission arises in the heated, optically thin upper layers of the disk atmosphere. The most likely mechanism to heat the upper layers is irradiation by the central regions (the primary, the boundary layer or the hot inner regions of the disk). The optically thin upper layers are heated and the gas is photoionized and excited, resulting in a recombination spectrum. The recombination spectrum plus an optically thick disk continuum can account for the Balmer emission continuum observed in dwarf novae in quiescence. A study of accretion disk atmospheres by Mineshige & Wood (1990) suggests that the emission lines observed in quiescent dwarf novae could be generated in disk chromospheres and coronae. A third site of line formation, emission from CV winds, is discussed in Section 1.2.

1.2 Winds from CVs

The 3 CVs studied in this thesis are all known to drive outflows. The principal evidence for this results from UV observations of wind-formed P Cygni-type line profiles. Section 1.2.1 describes the formation of P Cygni-type profiles, first for the case of a single, early-type star and then in CVs. The observational evidence for CV winds is described in Section 1.2.2, which goes on to examine the evidence for variability in the winds. Section 1.2.3 discusses the current status of CV wind models.

1.2.1 The formation of P Cygni-type line profiles

The actual driving mechanism of CV winds is not currently known, although radiation pressure, the mechanism known to drive the winds of early-type stars (Castor, Abbott & Klein 1975), is likely to play a role. The existence of a CV wind is observationally correlated with high disk luminosities, implying that radiative pressure in the lines may play a role in accelerating the wind (Cordova & Mason 1982). Gravitational accretion energy is liberated in the hot inner disk, causing the production of high energy X-ray and EUV emission. Therefore the inner accretion disk is a source of ionizing photons. When this radiation is absorbed and then re-emitted isotropically, the absorbing material will experience a net force because radiation carries momentum. P Cygni-type line profiles are indicative of wind outflow. Initially I discuss the formation of such profiles in early-type stars, before considering the effects due to the physical differences between single, early-type stars and CVs.

P Cygni-type line profiles are formed by scattering in the wind. The wind material lying between the observer and the continuum source scatters photons out of the line of sight and produces an absorption feature. This absorption is blueshifted with respect to the rest frequency of the resonance line being considered because the wind material is moving towards the observer. The observer will also receive photons which have been scattered into the line of sight by all the other wind regions (with the exception of those regions hidden behind the continuum source). The range of positive and negative velocities of this wind material results in the formation of an emission component which is symmetrical about the rest frequency. The observer therefore sees a combination of the blueshifted absorption trough and a central emission component which together produce the P Cygni-type line profile that is indicative of mass loss.

CVs differ, of course, from single, early-type stars in a number of significant ways, all of which will affect the observed profiles. Perhaps the most notable of these is the inclination angle of the system. Assuming that the central region of the accretion disk is driving a spherical wind (possible wind geometries are discussed below), then in the extreme case of an edge-on system there will be no part of the wind lying between the observer and the accretion disk. There is therefore no absorption and the P Cygni-type profile will consist purely of emission. At the other extreme, a face-on system will hide a large part of the wind behind the accretion disk (part of the red-shifted portion of the wind) and part of the blue-shifted portion of the wind will be seen in projection against the disk. The profile will consist of strong absorption with little or no emission. Between these two

extremes the fraction of the wind seen in projection against the disk will vary; as it increases the contribution to the absorption increases. Meanwhile, the disk hides an increasing volume of the wind and the amount of emission decreases accordingly. The shape of the P Cygni-type profile is strongly dependent on the inclination angle of the observed system.

Another significant factor is the wind geometry. The winds of early-type stars are generally considered to be spherical whereas, if the accretion disk does play a significant role in driving the wind (*e.g.* in providing the continuum source), it is likely that CV winds are bipolar in nature. In order to obtain physically reasonable values of $\dot{M}_{wind}$ (the mass loss rate from the wind) when fitting model profiles to observed wind-formed features, enhanced outflow over the WD poles, *i.e.* bipolarity, is required (Drew 1990 and references therein). A further difference between the winds of early type stars and the winds of CVs is the source function of the scattered continuum source. This can depend, for example, on the temperature distribution of the accretion disk, the accretion rate, the mass and radius of the WD, and the emissivity of the Planck function.

Other factors that will affect the observed profiles are $\xi(r)$, the ionization law of the wind, $V(r)$, the velocity law of the wind, and $\dot{M}_{wind}$, the mass loss rate of the wind. The fraction of photons scattered in the expanding wind is, in the Sobolev approximation to the radiation transfer (see *e.g.* Mauche & Raymond 1995):

$$f = 1 - e^{-\tau(r)} \tag{1.6}$$

The optical depth $\tau(r)$ is given by the expression

$$\tau(r) \propto \frac{\dot{M}_{wind}\xi(r)r^{-2}}{V(r)[\frac{dV(r)}{dr}]} \tag{1.7}$$

Equations 1.6 and 1.7 show that the fraction of scattering, and hence the line profile shape, depends upon the ionization and velocity laws of the wind and the mass loss rate.

Observational studies of the UV line profiles of early-type stars may be used in conjunction with theoretical models to constrain the mass loss rate, velocity law and ionization structure that characterize their winds. Although the same information can be obtained from observations of CV winds, the uncertainties in the wind geometry do not permit the same level of understanding to be reached. A further uncertainty is the unknown contribution to the UV line profiles by emission from the accretion disk.

1.2.2 Observational evidence for CV winds and wind variability

CV winds were first observed at UV wavelengths using the *IUE* satellite (*e.g.* see the review by Cordova & Howarth 1986) and are seen only in dwarf novae during outburst and in nova-like variables. The presence of a wind is indicated by P Cygni-type profiles and broad, blueshifted absorption troughs in the higher ionization resonance line doublets, *e.g.* C IV $\lambda\lambda$1550, Si IV $\lambda\lambda$1400 and N V $\lambda\lambda$1240. An example of a typical *IUE* spectrum showing wind-formed features is shown in Figure 1.8. This spectrum of the nova-like variable V3885 Sgr clearly shows a P Cygni-type profile in the C IV $\lambda\lambda$1550 UV resonance line.

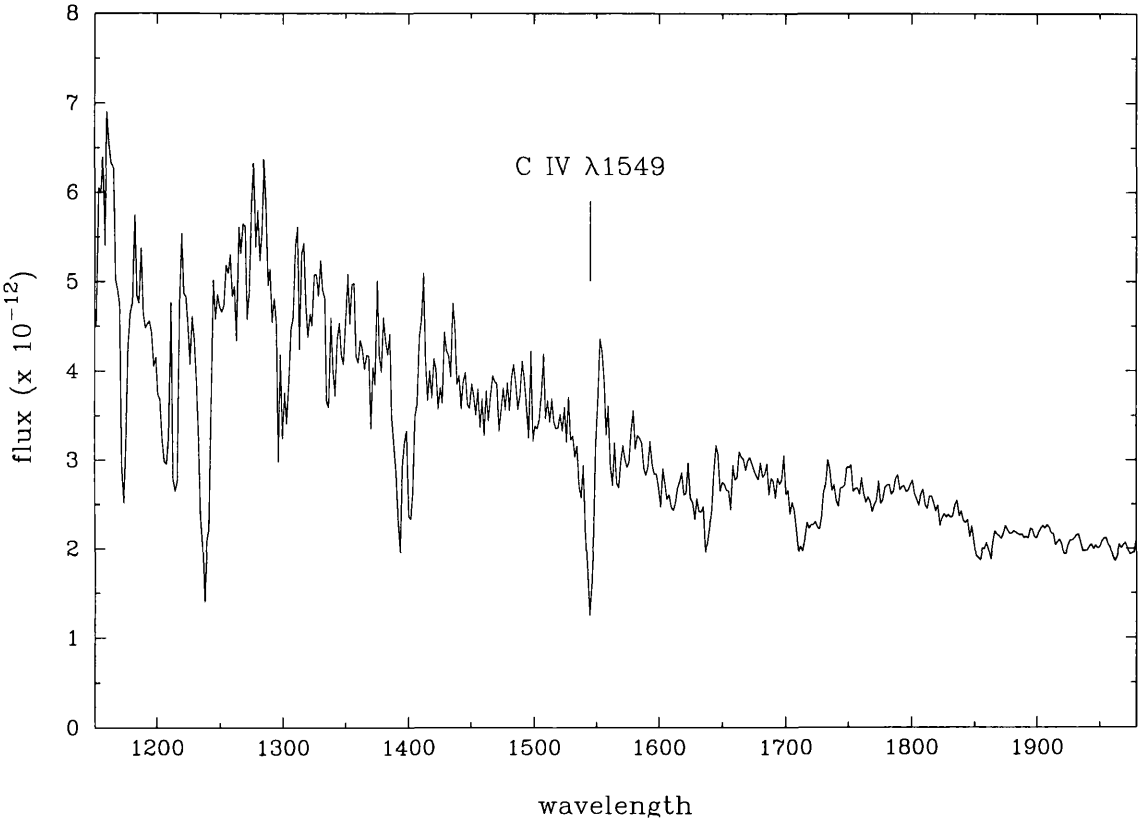

Figure 1.8: An *IUE* spectrum of V3885 Sgr (image number SWP 38512), showing a wind-formed P Cygni-type line profile in the C IV $\lambda\lambda$1550 UV resonance line.

As discussed above (Section 1.2.1), the shape of the line profiles in a wind-driving CV is highly dependent on the inclination angle of the system. The C IV $\lambda\lambda$1550 line profiles are shown in velocity space for 3 CVs in Figure 1.9. The nova-like variable RW Sex has an inclination angle of 43° and the dwarf novae WW Cet and Z Cha have inclination angles of 54° and 82° respectively. As the inclination angle increases, the amount of wind that is being seen projected against the disk

decreases, and so the profiles change from mainly absorption (RW Sex) to pure emission (Z Cha).

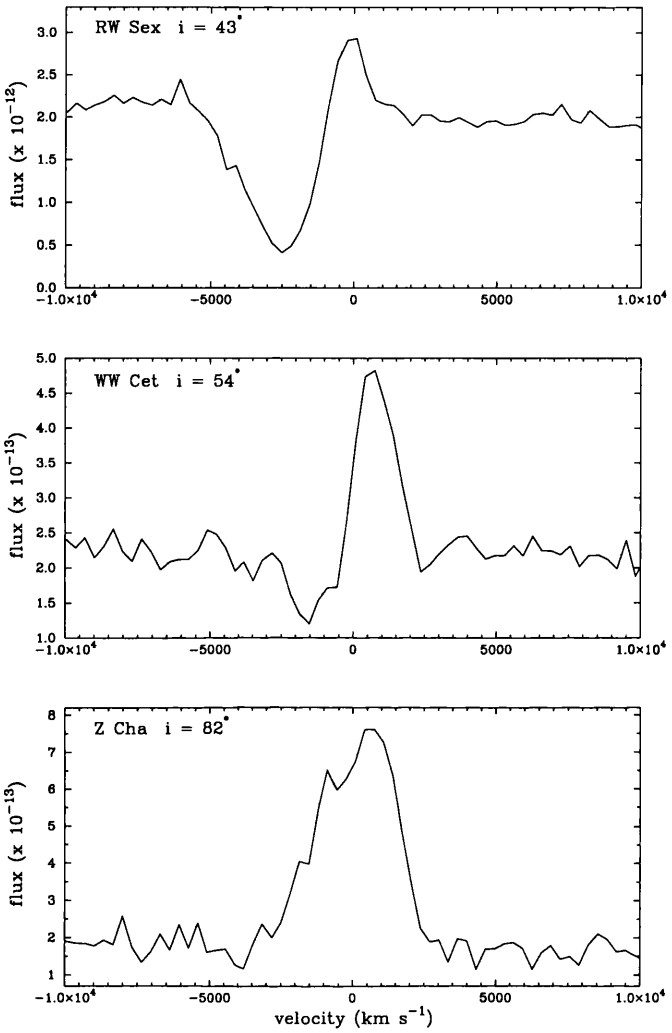

Figure 1.9: The dependence of the C IV $\lambda\lambda$1550 line profile shape on the inclination angle of the system. From top to bottom: RW Sex ($i = 43°$, image number SWP 7500), WW Cet ($i = 54°$, image number SWP 10664) and Z Cha ($i = 82°$, image number SWP 30707).

Studies of CV winds can provide a handle on some of the physical properties of the observed system. By measuring the position of the blueward edge of the absorption component, the terminal velocity of the wind is estimated. The terminal velocities generally lie in the range 3000 – 5000 km s^{-1}, which is comparable to the WD escape velocity. This fact is widely interpreted as implying that the wind originates from the inner accretion disk or the boundary layer (Cordova & Mason 1982). The behaviour of eclipsing CV winds may also be used to provide constraints on the line-forming regions: the UV emission lines are not eclipsed to the same degree as the UV contin-

uum, even when the continuum suffers a very deep eclipse. This behaviour is demonstrated by RW Tri in Figure 1.10, where the out-of-eclipse (top panel) and eclipse (middle panel) C IV $\lambda\lambda$1550 line profiles are shown. The bottom panel contains the difference between these two profiles; the lack of a strong emission feature in the difference spectrum indicates that the line-forming region has not been strongly eclipsed. If the wind-formed emission feature is not being eclipsed, the implication is that the line-forming region must be of about the same size as the secondary star (*i.e.* it is must be much larger than the continuum source).

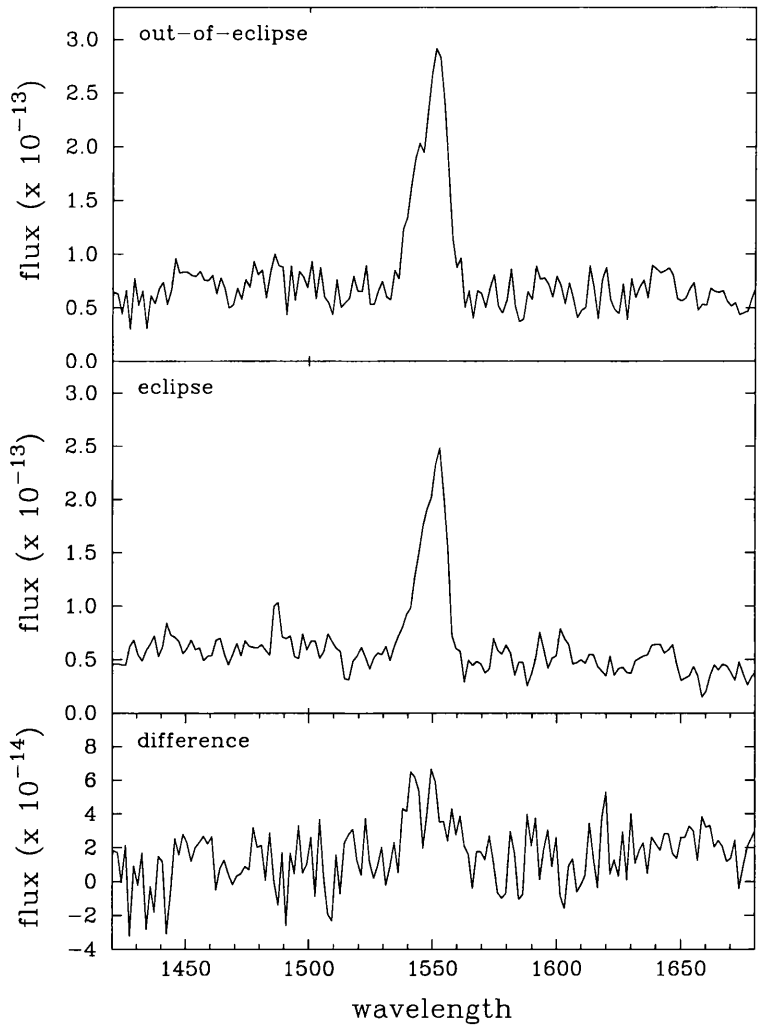

Figure 1.10: Out-of eclipse (top panel; *IUE* image number SWP 16063) and eclipse (middle panel; *IUE* image number SWP 16037) UV spectra of the nova-like variable RW Tri. The bottom panel shows the difference between the two spectra, the lack of an emission feature revealing the shallow eclipse of the line.

Two cases of UV line profile variability in CVs have been identified: (i) variations that occur

over the outburst cycle and (ii) variations that occur over the orbital cycle. Dwarf novae only drive winds when they are in outburst, so one expects to see changes in the profile shapes over the course of the outburst cycle. The absorption is strongest at the maximum of the outburst then, as the total system luminosity declines, the absorption strength decreases (*e.g.* see the study of SU UMa by Woods *et al.* 1990). Observations of CV winds are observationally correlated with high disk luminosities. This is interpreted as implying that the higher radiation pressure that would be associated with such higher disk luminosities is driving the wind (Cordova & Mason 1982). As the outburst begins, the accretion rate through the disk increases causing the disk luminosity to increase to the point where it begins to drive a wind. At outburst maximum the strongest absorption, and therefore the strongest wind, is observed.

While all dwarf novae show variations in their wind profiles over the outburst cycle, by no means do all wind-driving CVs show evidence for *orbital* variability in their wind-formed features. Orbital phase dependence has been noted in the nova-likes V3885 Sgr (Woods *et al.* 1992) and IX Vel (Mauche 1991) and in the dwarf novae Z Cam (Szkody & Mateo 1986), YZ Cnc and IR Gem (Drew & Verbunt 1988; Woods *et al.* 1992) and SU UMa (Drew 1990). The orbital phase dependence of the line profiles suggests an azimuthal asymmetry which may be seated in either the accretion disk or in the wind. Possible asymmetries may exist in the brightness of the accretion disk, the geometry of the wind, the velocity field of the wind and the ionization structure of the wind.

Currently there is limited observational evidence of CV winds at optical wavelengths. Patterson *et al.* (1996) report P Cygni events in optical spectroscopy of the nova-like BZ Cam (which also shows strong evidence for an outflow at UV wavelengths; Griffith, Fabian & Sion 1995). The clearest events occurred in the He I λ5876 line, where a strong P Cygni absorption trough, extending 2000 km s^{-1} blueward of the line centre, is observed to decrease in strength gradually over a period of about 40 min. A similar event occurs several hours later, although the phenomenon does not repeat on the orbital period. Chapter 5 presents new optical spectroscopy of BZ Cam recorded in 1997 January and re-examines the UV *IUE* archive spectra. A wind origin has also been suggested for the extended He II emission region seen in SW Sex (Honeycutt, Schlegel & Kaitchuck 1986). A stationary component was reported in Hα observations of Z Cam (Robinson 1973) which Szkody & Wade (1981) reanalysed to calculate a mass loss rate of 7×10^{-10} M$_{\odot}$yr^{-1}. Stationary components have also been observed in IP Peg (Marsh & Horne 1990; Piché & Szkody 1989) and in SS Cyg (Steeghs *et al.* 1996). The stationary component in SS Cyg is examined in Chapter 4.

1.2.3 Wind modelling

Initial attempts to model the winds of CVs took as their starting point the modelling of the winds of early-type stars. In addition to the differences arising from the inclination angle of the CV system and the possibly bipolar wind geometry, CV wind models must also allow for the different source function of the scattered continuum. To summarise, the construction of theoretical CV wind profiles requires the specification of (i) the mass loss rate $\dot{M}_{wind}$, (ii) the velocity law of the wind $v(r)$, (iii) the ionization law of the wind $\xi(r)$, (iv) the source function and geometry of the wind, and (v) the source function of the scattered continuum.

The first calculations of theoretical profiles (Drew 1987; Mauche & Raymond 1987) therefore used simple geometries. The wind was assumed to be spherical and to originate in the boundary layer or the inner accretion disk. The only departure from spherical symmetry in Drew's code is to allow the scattering-ion mass loss rate to vary as a function of the polar angle. The ionization state of the wind was assumed to be constant with radius and the velocity law was assumed to be either a power law (Drew 1987) or a linear function of radius (Mauche & Raymond 1987). The studies resulted in several interesting conclusions. If the wind origin is assumed to be near the WD then, in comparison to the winds of early-type stars, the wind acceleration needs to be very slow. Some form of bipolarity is also required in order that the calculated profiles for high inclination systems are pure emission. This bipolarity could be introduced in the wind density profile or in the radiation field of the continuum source (*e.g.* limb darkening of the accretion disk).

One of the critical components of a CV wind model is the ionization state of the wind. The wind mass loss rate ($\dot{M}_{wind}$) is determined by the absolute concentration of the ions, the relative strengths of the line profiles are determined by the relative ion concentration, and the actual shapes of the line profiles are governed by the ion concentration versus radius (in conjunction with the velocity law of the wind). Simple models (*e.g.* Pringle 1977; Patterson & Raymond 1985) predict ionization beyond the stages that are observed. A relatively slow velocity law (Drew & Verbunt 1985) alleviates this to a certain extent but not to the point that theory agrees with observation. Kallman & Jensen (1985) increased the wind density to allow photoelectric absorption of the boundary layer's EUV and soft X-ray flux but the wind mass loss rate required becomes greater than the accretion rate, thereby breaking the conservation of energy. The inclusion of shock compressions in the wind (Mauche & Raymond 1987) allows more sensible mass loss rates but the model wind then produces UV line fluxes that are too large. All these difficulties have called into question the

treatment of the boundary layer radiation.

More successful models (Hoare & Drew 1993) have since considered cool, luminous boundary layers and systems without a boundary layer. They are able to model satisfactorily the C IV and N V line profile strengths but not the Si IV blueshifted absorption. Using a model with a cool, or even a non-existent, boundary layer also presents difficulties when interpreting the observed soft X-ray flux. Shocks in the wind could provide an alternative to the boundary layer as the origin of the X-ray flux but this seems unlikely as the flux from some systems (*e.g.* VW Hyi; van der Woerd *et al.* 1987) exhibits quasi-periodic oscillations (QPOs).

In their work on wind modelling, Shlosman & Vitello (1993) and Vitello & Shlosman (1993) have considered an alternative wind origin: the accretion disk. The wind is assumed to arise from an annulus of the accretion disk and to rotate, initially at its local Keplerian velocity. There are several advantages of such models over models with a wind origin at the WD. Less energy is required to drive a wind of a given mass loss rate to the escape velocity because the accretion disk surface is at a lower gravitational potential than the WD. Also, the larger spatial extent of the accretion disk implies that the photon scattering volume is greater than with a WD origin, accounting for the shallow eclipses observed in wind-formed profiles. The models of Vitello & Shlosman have successfully fitted the line profiles of RW Sex and RW Tri, but the number of free parameters in their model (*e.g.* temperature of the boundary layer, mass accretion rate, mass loss rate) means that these fits are not unique.

The complexity required of the models and the large number of parameters involved combine to make CV wind modelling a difficult problem. It is hoped that multi-wavelength studies of CVs, such as those presented in this thesis, may be used to constrain the construction of wind models. A simultaneous multi-wavelength study (such as the study of V795 Her in Chapters 2 and 3) may be used to examine the contaminating influence of accretion disk emission and absorption to the 'wind-formed' UV line profiles. *Ab initio* radiation pressure driven wind models that use both boundary layer (if present) and inner disk radiation are still under development. This area of study can also benefit from new observations such as the *HST* data of V795 Her presented in Chapter 3.

1.3 Doppler imaging

Doppler tomography is a very powerful, indirect imaging tool that is being increasingly utilised in the study of CVs. It was first developed by Marsh and Horne (1988). To employ this technique, time-resolved spectra of reasonable signal-to-noise are required, ideally covering the full orbital cycle of the object. Doppler imaging produces a Doppler map, or tomogram, which is an image of the system in velocity space.

Consider the potential emission sites in a CV: *e.g.* the accretion disk, the secondary star, the accretion stream and the bright spot. As the orbital phase changes, the observed radial velocity of each emission site changes with respect to the observer and its contribution to an emission line profile is accordingly Doppler shifted. This results in the production of an s-wave of emission in the trailed spectrogram (a two-dimensional representation of the flux variations versus orbital phase) by, for example, the bright spot. When emission from more than one site is present, the resulting line profiles may be very complex and the trailed spectrograms difficult to interpret. Doppler tomography uses the observed line profiles, transformed into velocity space, to reconstruct the distribution of the emitting material. A Doppler map is thus the image of a CV in velocity coordinates.

The first step is to set up a coordinate system (X, Y) which has its origin at the centre of mass of the binary, with the x-axis along the line of centres and the y-axis perpendicular to it, in the orbital plane. The coordinate system therefore rotates with the binary. In a steady state, the velocity at each point (V_X, V_Y) is constant. A spot of emission sited at (X, Y) traces out a sinusoidal radial velocity curve, where the velocity at orbital phase ϕ is given by

$$V(X, Y, \phi) = \gamma - [V_X \sin(2\pi\phi) + V_Y \cos(2\pi\phi)] \sin(i) + V_Z \cos(i) \tag{1.8}$$

where γ is the systematic radial velocity of the binary system, i is the inclination angle and V_Z is the velocity component perpendicular to the orbital plane. When Doppler imaging techniques are employed it is generally assume that the material moves in the orbital plane and has no velocity component in the z direction, which simplifies Equation 1.8 to

$$V(X, Y, \phi) = \gamma - V_X \sin(2\pi\phi) - V_Y \cos(2\pi\phi) \tag{1.9}$$

where V_X and V_Y now include the factor $\sin(i)$ and are therefore the velocities projected along the line of sight.

An emission line profile at a particular orbital phase ϕ is a one-dimensional projection of the two-dimensional Doppler image. Consider a point on the Doppler image at V_X, V_Y. Equation 1.8

can be used to calculate the sinusoid traced out by that point and thereby create a trailed spectrogram from the Doppler map. However, it is the *inverse* process that is of more interest: this would enable the construction of a Doppler map in velocity space from the observed line profiles from different orbital phases (*i.e.* from an *observed* trailed spectrogram). The algorithm employed to carry out this transformation is called 'back projection' (Horne 1991; Russ 1992). Every possible s-wave through the trailed spectrogram is traced, thereby calculating the average flux from that s-wave. This gives the intensity of each point on the Doppler map.

This simple back projection does not allow for the problem of neighbouring s-waves crossing one another's paths. Consider an observed data set with one strong s-wave that is created by emission at the spot with velocity V_{X_1}, V_{Y_1}. When the back projection algorithm is applied every possible s-wave through the observed trailed spectrogram is traced and the average flux in each s-wave is calculated. It is inevitable that some of these possible s-waves will cross the observed s-wave and therefore will have non-zero average flux. S-waves that follow the observed s-wave quite closely will have reasonably high average fluxes (although obviously, the traced s-wave with the greatest average flux will be the one that corresponds exactly to the observed s-wave). The result of this in the Doppler image is that the point at V_{X_1}, V_{Y_1} will be smeared out. The exact formulation of this effect is called the 'point spread function of the back projection algorithm', and has been examined by Horne (1991) and Marsh and Horne (1988).

The effect of the point spread function can be minimised by altering the back projection algorithm to include a Fourier filter (Horne 1991; also see Kaitchuck *et al.* 1994). In this 'Fourier filtered back projection' algorithm the observed data is Fourier filtered before it is back-projected. A strong s-wave in the *filtered* observed data now has negative values either side of the s-wave. When an s-wave crosses the observed s-wave during the back projection algorithm, its average flux will now total zero, as the filter is designed to add negative values that cancel the positive s-wave values. This is the algorithm applied in the Doppler tomography code used in this thesis.

An alternative way of reconstructing the Doppler maps from the observed trailed spectrograms is to use the maximum entropy method (Marsh and Horne 1988). The predicted data is compared to the observed data by a χ^2 statistic. The reduction of the χ^2 statistic is carried out only to a predetermined point of reasonable consistency, and then the best of these images is chosen by selecting the image of maximum entropy (the smoothest image). This method is, however, both non-linear and computationally intensive. It is generally applied only in situations where it will produce better

results than the back-projection methods described above, namely for poorly sampled data sets. The tomography code used in this thesis employs the Fourier filtered back-projection algorithm.

Doppler imaging is a very useful tool with which to interpret complex trailed spectrograms. However, it does have its limitations. The major limitation arises from the assumption that the line emission from any part of the binary system is equally visible at all phases of the orbital cycle. The most obvious violation of this assumption occurs in eclipsing systems, although it is easily surmounted by excluding the eclipse data. (A reliable Doppler map can always be produced provided there is at least half a binary orbit's worth of continuous data). The assumption that the emitting material lies in the orbital plane (see Equation 1.9) results in a further limitation. If any of the line emission arises from a wind, the interpretation of the Doppler map will potentially be less straightforward. This limitation is of particular concern in this thesis as all the CVs studied here are known to drive outflows.

A further point to bear in mind when using Doppler tomography is that the resultant image is in velocity space. The Doppler image of a disk, for example, is 'inside-out'. The high-velocity gas of the inner disk is mapped to the outer portions of the ring on the Doppler image. The fact the image is in velocity space means that potentially there are emission sites with precisely the same velocity coordinates but with different spatial locations. The Doppler map cannot be transformed to spatial coordinates because the velocity field is unknown. Appendix A gives the reader a short 'tutorial' on the interpretation of Doppler maps.

The limitations discussed above should be borne in mind when using the technique of Doppler imaging. Two of the systems studied in this thesis have been mapped using Doppler tomography (V795 Her in Section 2.4 and SS Cyg in Section 4.4), thus providing useful constraints on their emission line regions.

1.4 Aims

This research is primarily concerned with optical spectroscopic studies of the 3 CVs V795 Her, SS Cyg and BZ Cam, chosen because they are known from UV studies to drive fast winds . The fundamental aim is to establish detailed optical spectral line characteristics of these systems. These characteristics should expose any optical signatures of the winds observed at UV wavelengths. By extending the analyses to include new *HST* and archive *IUE* UV spectroscopy, any correlated be-

haviour could be confirmed.

New high quality time-resolved optical spectra of the nova-like variable V795 Her are presented in Chapter 2. The precise nature and classification of this system are currently the subject of some controversy and this thesis looks in detail at the optical emission and absorption line properties. This work examines recently proposed magnetic scenarios that invoke channelled accretion columns flowing onto a synchronously rotating WD. It also suggests a new disk-overflow interpretation for this system in which the accreting gas stream overflows the outer rim of the disk and re-impacts in the inner disk regions.

Chapter 3 makes a comparison between the optical spectra and quasi-simultaneous UV *HST* observations of V795 Her, obtained during the same week in a related program (Rosen *et al.* 1997). These unique data sets provide an unprecedented opportunity to carry out a multi-wavelength study of this object where it is possible to be confident that the system was in the same state when both sets of observations were made. The *HST* data reveal for the first time UV variability on the orbital timescale of V795 Her. This study compares and contrasts these variations to the orbital variations observed in the optical line profiles. An attempt is made to apply the same disk-overflow model to the UV line profile behaviour.

A key issue yet to be determined is the cause of the orbital variability observed in the UV resonance line profiles of some CVs. Are these changes due entirely to wind changes, or do additional non-wind emission sources (*e.g.* with an accretion disk origin) also vary and thus contribute to the UV resonance line profile changes? Asymmetries in the wind may be seated in its geometry, in its velocity field or in its ionization structure. Orbital phase dependence may also arise in the wind if the continuum source which drives it (*e.g.* from the accretion disk) possesses an azimuthal asymmetry. If emission from the accretion disk itself makes a significant contribution to the 'wind-formed' profiles, then the source of the orbital variability may lie in non-axisymmetric disk emission. The uniquely simultaneous optical INT and UV *HST* data sets of V795 Her, presented in Chapters 2 and 3 are used to address these issues in detail.

The multi-wavelength study of V795 Her may also be used to constrain the construction of wind models. Currently, wind modelling ignores the potential contribution of disk emission, and absorption, to the UV line profiles. Simultaneous optical and UV observations are able to examine such contributions and determine if the disk contribution is significant.

The dwarf nova SS Cyg is studied in Chapter 4. New time-resolved optical spectroscopy re-

corded at the maximum of an outburst is presented along with archive *IUE* spectra recorded during the same outburst (but one week after the optical observations). The optical spectroscopy, taken during a long, asymmetric-type outburst, confirms the presence of stationary low velocity emission, reported previously during a long, symmetric-type outburst. Possible sources of this emission are investigated, including emission from a wind, and a slingshot prominence model that involved magnetic activity on the secondary star. The contemporaneous archive *IUE* spectra allow the UV wind properties to be examined and the potential wind origin of the low velocity optical emission to be considered.

New optical spectroscopy and archive *IUE* spectra of the nova-like BZ Cam are presented in Chapter 5. This is the only CV which has shown *unambiguous* evidence of a wind at optical wavelengths. The data presented here display P Cygni-type Hβ and Hγ line profiles; optical P Cygni profiles were reported previously in the Hα and He I λ5876 lines. Model profile fits to the Hβ line are used to constrain the inclination angle. BZ Cam is also of interest because it is associated with a 'bow-shock' nebula. The origin of this nebula may have important implications in the theory of CV evolution. The archive *IUE* spectra are used to place constraints on the wind mass loss rate. This value has implications for dynamical studies that investigate if the nebula was created by an interstellar bubble formed by the CV wind interacting with the interstellar medium.

Finally, Chapter 6 brings this thesis to a conclusion by summarising the main findings. Suggestions are also made for future investigations which follow on from these studies.

Chapter 2

V795 Herculis: the optical line behaviour

2.1 Introduction

The precise nature and classification of V795 Herculis (PG 1711+336), a 13th magnitude nova-like CV, remain unresolved issues. Its optical spectrum shows weak hydrogen and helium lines, and a C/N blend ($\lambda\lambda 4640-4650$ Å), superimposed on a blue continuum. Several spectroscopic periods, and one photometric period have been observed in this system (Table 2.1). The most prominent of these is the 2.6 hr spectroscopic period which, when interpreted as the binary orbital period, places V795 Her inside the CV 'period gap' (see Section 1.1.2).

The presence of the 2.8 hr photometric period, first observed by Mironov, Moshkalev & Sugarov (1983), was confirmed by later studies (see Table 2.1), whereas no subsequent detection of the 14.8 hr spectroscopic period reported by Thorstensen (1986) has been made. The study of Shafter *et al.* (1990) then confirmed the presence of *two distinct* periodicities: the 2.8 hr photometric period recorded on numerous occasions previously and a new 2.6 hr spectroscopic period.

Two models, discussed by Zhang *et al.* (1991) and Patterson and Skillman (1994), have been advanced to explain the 2.8 hr photometric period. In the first model, suggested by Shafter *et al.* (1990; supported by Zhang *et al.* 1991), an intermediate polar (IP) scenario for V795 Her is proposed, in which the spectroscopic period is identified with the binary orbital period and the (longer) photometric period with a beat period between the orbital period and the (undetected) rotation pe-

Period (hr)	Type	Reference
2.8	photometric	Mironov, Moshkalev & Sugarov (1983)
		Rosen *et al.* (1989), Shafter *et al.* (1990)
		Zhang *et al.* (1991)
14.6	spectroscopic (Hα)	Thorstensen (1986)
2.6	spectroscopic	Shafter *et al.* (1990), Haswell *et al.* (1994),
	(Hα, Hβ, He II λ4686)	Casares *et al.* (1995), this study
4.9	UV emission lines	Prinja, Drew and Rosen (1992),
		Prinja & Rosen (1993)

Table 2.1: Reported periods of V795 Her.

riod of a magnetic WD. (As the rotation period of a WD is expected always to be less than the orbital period of the binary system, the 2.8 hr photometric period cannot be immediately identified with the WD rotation period. In this model the beating is caused by the reprocessing of beamed X-ray radiation from the WD by the pole, or poles, of the secondary component). From the beat relation the two possible values of the WD rotation period can be predicted (P_{WD} = 1.35 hr or 1.77 hr); however there is no evidence for either of these periods in the data of Shafter *et al.* (1990). The later photometric study of Zhang *et al.* (1991), with a baseline of 7 years, concludes that the 2.8 hr period is very stable ($\dot{P}_{2.8} < 1.7 \times 10^{-9}$). As there are few other physical mechanisms that can produce such high stability, they too conclude that V795 Her is an IP.

A study by Patterson & Skillman (1994), using photometry obtained between 1990 and 1994, aimed to examine further the stability of the 2.8 hr periodicity. Their data reveal that the 2.8 hr period essentially disappeared during this epoch, its amplitude reduced by a factor > 10. This disappearance is coincident with a brightening of the system of ~ 0.3 mag. Patterson & Skillman regard the reliability of the long-term cycle count used by Zhang *et al.* as very poor due to the scarcity of the timings of minima and their unfavourable distribution. The only certainty is that the 2.8 hr signal is stable on timescales < 20 d. They regard a 'superhump' model (first considered, and rejected, by Zhang *et al.* 1991) as the most likely interpretation of the 2.8 hr photometric signal. In this second model large-amplitude modulations in the light curve, occurring at an anomalous period that exceeds the orbital period by a few percent, are thought to be caused by the precession of an eccentric accretion disk. The variation may be produced by tidal stresses in the disk (Osaki

1989; see Section 1.1.3). This phenomenon is a well known feature of dwarf novae in superoutburst (Warner 1985) and has now been observed in many non-eruptive stars (Patterson *et al.* 1993; Skillman and Patterson 1993). Patterson & Skillman (1994) also detected a photometric signal in their data set at 2.59 hr with a semi-amplitude of ~ 0.018 mag that is low enough to have gone unnoticed in previous studies.

Further details of the optical emission line behaviour of V795 Her have been presented by Haswell *et al.* (1994) and Casares *et al.* (1996), both groups highlighting low and high velocity amplitude s-waves in the Balmer lines. The authors claim that these line characteristics support models of magnetically channelled accretion columns. Casares *et al.* (1996) suggest that V795 Her may be an SW Sex star, invoking an IP scenario with a synchronously rotating WD to qualitatively explain its complex behaviour. In their interpretation SW Sex stars are IPs seen at intermediate to high inclination angles.

As discussed above, the stability of the 2.8 hr period remains a mystery and cannot be used to discriminate conclusively between the precessing disk and IP hypotheses. There are several important obstacles which stand in the way of an IP scenario for V795 Her. Most significantly, there is an apparent absence of the substantial hard X-ray emission which is expected if the photometric period is due to the reprocessing of a rotational signal. The system was not detected in the *EXOSAT* observations of Rosen *et al.* (1989; 0.1 – 10 keV), although a weak *ROSAT* PSPC detection has been made, indicating a modest column density of $\sim 5 \times 10^{20}$ cm^{-2} and a lower bound bremsstrahlung temperature of 0.5 keV (Rosen *et al.* 1995). In addition, Prinja, Drew & Rosen (1992) have argued that the overall absorption dominated morphology of the UV spectrum of V795 Her is discordant with an IP classification. They report instead a 4.86 hr variation in low resolution *IUE* spectra of the UV resonance lines, which are thought to be at least partly formed in a fast outflowing wind. The recent UV *HST* spectroscopy of Rosen *et al.* (1997; see also Chapter 3) has, however, revealed only a 2.60 ± 0.03 hr modulation, which may be associated with a localised emission source on the accretion disk. A further characteristic normally seen in IPs is polarization, of which V795 Her shows no evidence. Furthermore, the predicted WD rotation period has not been detected in any data set, and the spectrum of V795 Her looks more like that of a nova-like: if it is an IP, then it is one with unusually weak He II lines (Shafter *et al.* 1990, and references therein). As an aside, perhaps, it is also noted that V795 Her has one of the lowest quoted upper limits in the *Compton Observatory* γ-ray survey of 'asynchronous rotators' (Schlegel *et al.* 1995) and in the 5-GHz radio survey of 'Polar and IPs' by Pavelin, Spencer & Davis (1994).

The high quality time-resolved optical spectroscopy, obtained during 7 nights in 1994 June using the 2.5 m *Isaac Newton Telescope* (INT, La Palma) and presented here, is an attempt to constrain further the precise nature of V795 Her. The optical data set is described in Section 2.2, and the nature of the complex inner-core and outer-wing structure in the Balmer emission lines is discussed in Section 2.3. Section 2.4 presents constraints based on Doppler imaging techniques, which are used to gain insight into possible locations for the complex line emission. An empirical interpretation of the optical data is presented in Section 2.5 and complementary INT FOS data examining the optical continuum properties are discussed in Section 2.6. Finally, in Section 2.7, the results are discussed in the context of recently proposed magnetic WD scenarios for V795 Her, and some disk-overflow simulations based on SW Sex-type models are presented. A comparison of the optical behaviour to the UV spectroscopic properties of V795 Her (obtained in a related program during the same week in 1994 June; see also Rosen *et al.* 1997) is carried out in Chapter 3.

2.2 Data acquisition and reduction

This study is based on observations secured over 7 nights between 1994 June 20 – 26 on the 2.5 m INT at La Palma. The principal data set comprises 241 individual exposures of V795 Her taken using the Intermediate Dispersion Spectrograph (IDS), with the EEV CCD and R1200B grating. The wavelength coverage amounts to $\lambda\lambda 4080 - 4970$ Å, with a spectral resolution of ~ 1 Å. Individual exposure times were ~ 300 sec. A log of the observations is shown in Table B.1. Mostly phase-binned spectra of improved signal-to-noise were used in this work (see Section 2.3.2).

These data are complimented by 37 spectra (see Table B.2 for the log of observations) secured on 1994 June 24 using the Faint Object Spectrograph (FOS) on the INT, taken in order to study the optical colour and continuum behaviour of V795 Her. The FOS data cover $\lambda\lambda 3740 - 10200$ Åin two orders, with a spectral resolution of ~ 10 Å.

The data were extracted, and wavelength and flux calibrated, according to standard procedures using the Starlink packages FIGARO (Meyerdierks 1993) and PAMELA (Horne 1986). The IDS and FOS data sets were treated separately. The data reduction of the IDS spectra was carried out entirely within FIGARO and DIPSO (Howarth *et al.* 1995). Sky regions on either side of the star were identified and the stellar background was removed. Cu-Ar arc spectra were taken approximately every 30 min in order to carry out the wavelength calibration. They were extracted from

the same positions on the slit as the objects and were then wavelength calibrated by fitting a fifth order polynomial to the arc lines. The wavelength scale was interpolated between neighbouring arc spectra. Over the course of a night's observations the wavelength scale shifted by 1.2 Å (equivalent to 80 km s^{-1} at 4500 Å). Several exposures were also made of flux and atmospheric standards. A spline fit was carried out to the flux standard continuum and the instrumental response corrected for by calibrating the spline fit with the tabulated fluxes of the standard star. As the observations were secured using a narrow slit, the flux estimates are not totally reliable and therefore the data are not strictly spectrophotometric.

The data reduction of the FOS spectra was carried out using both FIGARO and PAMELA. It followed the same basic procedure as the IDS data reduction, apart from the actual extraction of the two spectral orders. This required the use of the optimal extraction routines within PAMELA to trace the curved orders on each image. The two orders were extracted separately. Sky regions were identified either side of the order and subtracted from the image using a PAMELA subroutine. Optimal extractions were then performed, weighted to the centre of the object region. The subsequent data manipulation and analysis was carried out mostly using the DIPSO package.

2.3 The spectral line behaviour

This section presents the key observational characteristics of the Balmer and He line profiles of V795 Her apparent in the IDS spectra. The mean IDS spectrum from the full data set is shown in Figure 2.1. Emission is present in the 'double-peaked' lines of Hβ, Hγ and Hδ, plus He II λ4686, He I λ4921, the metal lines of C II λ4267, and C III/N III at $\sim\lambda\lambda$4645. He I λ4471 is seen in absorption.

2.3.1 Modulated spectral variability

In order to examine the incidence of temporal variations in these lines, a fractional variance spectrum was computed and is shown in the lower panel of Figure 2.1. The statistic plotted is σ^2_λ, where

$$\sigma^2_\lambda = \frac{1}{(N-1)[\bar{f}(\lambda)]^2} \sum_{i=1}^{N} [f_i(\lambda) - \bar{f}(\lambda)]^2 \qquad (2.1)$$

and N is the number of spectra, $\bar{f}(\lambda)$ is the mean flux at wavelength λ and $f_i(\lambda)$ is the flux of the i^{th} spectrum at that wavelength. There are substantial line profile variations in the Balmer emission

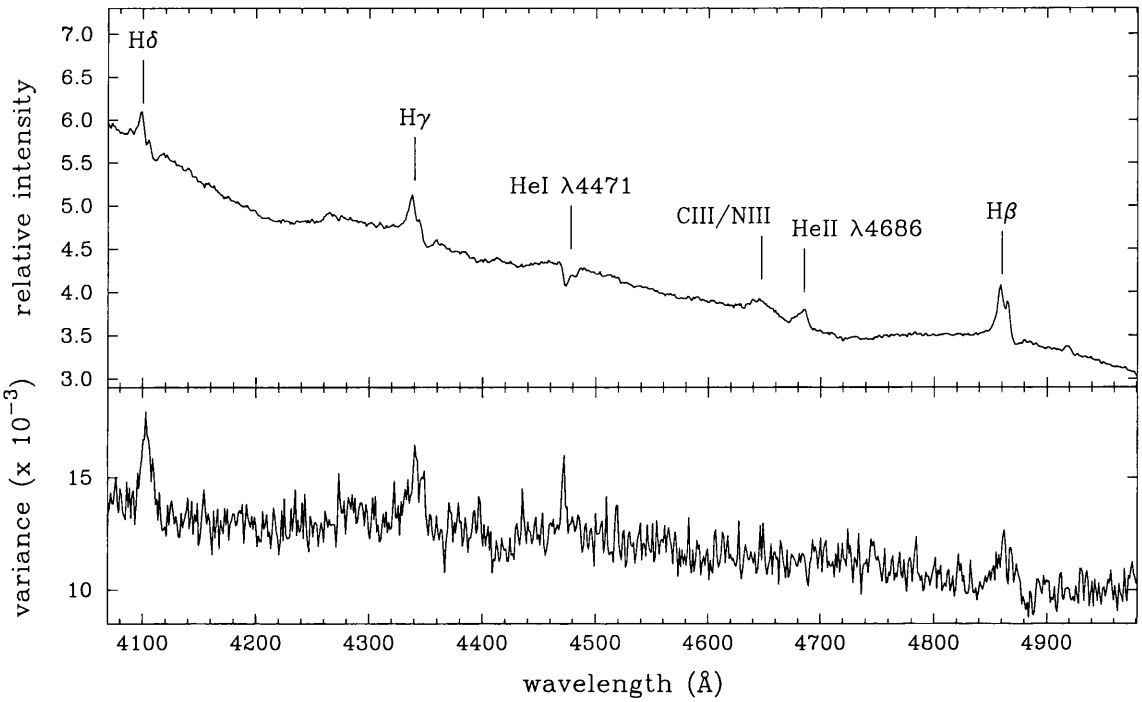

Figure 2.1: Mean IDS spectrum of V795 Her (upper panel) and the fractional variance (lower panel; Section 2.3.1).

lines, and in the He I λ4471 absorption. Relatively smaller scale fluctuations are also present in the (weaker) lines of He II λ4686 and He I λ4921.

In order to examine any systematic or cyclic behaviour of these line profile variations in V795 Her, a Fourier analysis based on individual measurements of the total observed Hβ flux and the absorption equivalent width of He I λ4471 was performed (Figure 2.2), employing the CLEAN techniques of Roberts, Lehár & Dreher (1987; with a gain of 0.8 and 200 iterations). Significant power spectrum peaks are present in both spectral lines at 2.59 ± 0.05 hr and 2.61 ± 0.03 hr (conservative errors are quoted based on the half-width at half-maximum of the power spectrum peaks). These results confirm previously established records that the optical lines of V795 Her modulate on the mooted orbital period of the system (see references in Section 2.1). Perhaps of further interest is the power evident in Figure 2.2 at $\sim 1.48 \pm 0.02$ hr (16.190 day^{-1}) in Hβ and, more tentatively, in He I λ4471 at $\sim 1.46 \pm 0.02$ hr. These peaks do not correspond to any simple (beat) relation between the 2.60 hr, 2.80 hr or 4.86 hr (UV *IUE*) periods. Their origin is uncertain. Note, however, that Rosen *et al.* (1997) also tentatively identify a peak at ~ 1.51 hr in their Fourier analysis of UV resonance lines in *HST* spectroscopy of V795 Her.

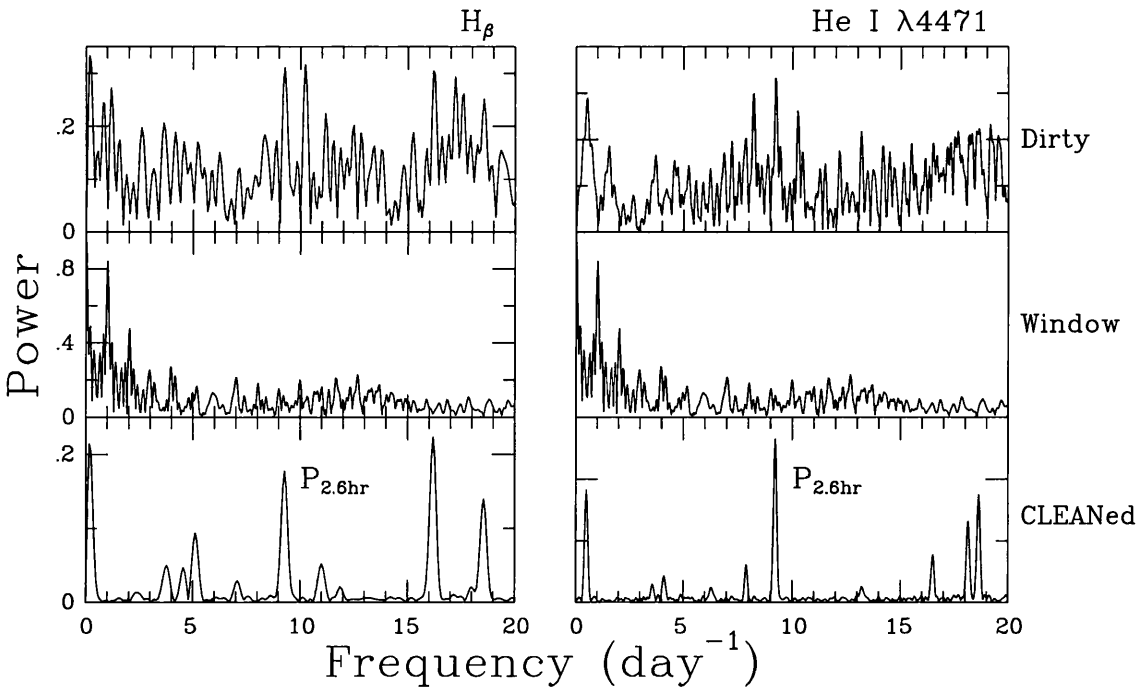

Figure 2.2: CLEAN Fourier analysis (Roberts, Lehár & Dreher 1987) of the Hβ emission and He I λ4471 absorption strengths in V795 Her. Strong frequency components associated with the 2.60 hr orbital period are present in both data sets.

2.3.2 Structure of the line profiles

Based on the results of Section 2.3.1, and to permit detailed studies of the nature of the cyclic optical line profile variations in V795 Her, the IDS spectra were folded into 20 phase bins. Typically about 15 individual spectra were added into each bin. Each phase bin was 0.05 phase units wide, with the first bin centred at phase 0.025. The orbital ephemeris of Shafter *et al.* (1990), which is more accurate than the similar period derived in Section 2.3.1, was adopted:

$$T_0 = HJD - 2\,447\,329.824 + 0.1082468N \tag{2.2}$$

The maximum redward and blueward radial velocity motion of the optical emission lines corresponds to quadratures at $\phi_{2.6} = 0.25$ and $\phi_{2.6} = 0.75$, respectively. The estimate of the accumulated phase uncertainty for observations taken in 1994 June is ± 0.06 (1σ). (Note, the radial velocity variations examined by Shafter *et al.* 1990 are not the same as the weak outer wing changes in the Balmer lines reported here).

A montage of the 20 phase-binned IDS spectra, covering $\lambda\lambda 4090-4980$ Å is shown in Figure 2.3. The overall line emission flux decreases around $\phi_{2.6} = 0.6-0.7$ (see below), and there are extensive differences in the morphology of the line profiles during the orbital cycle (see also Fig-

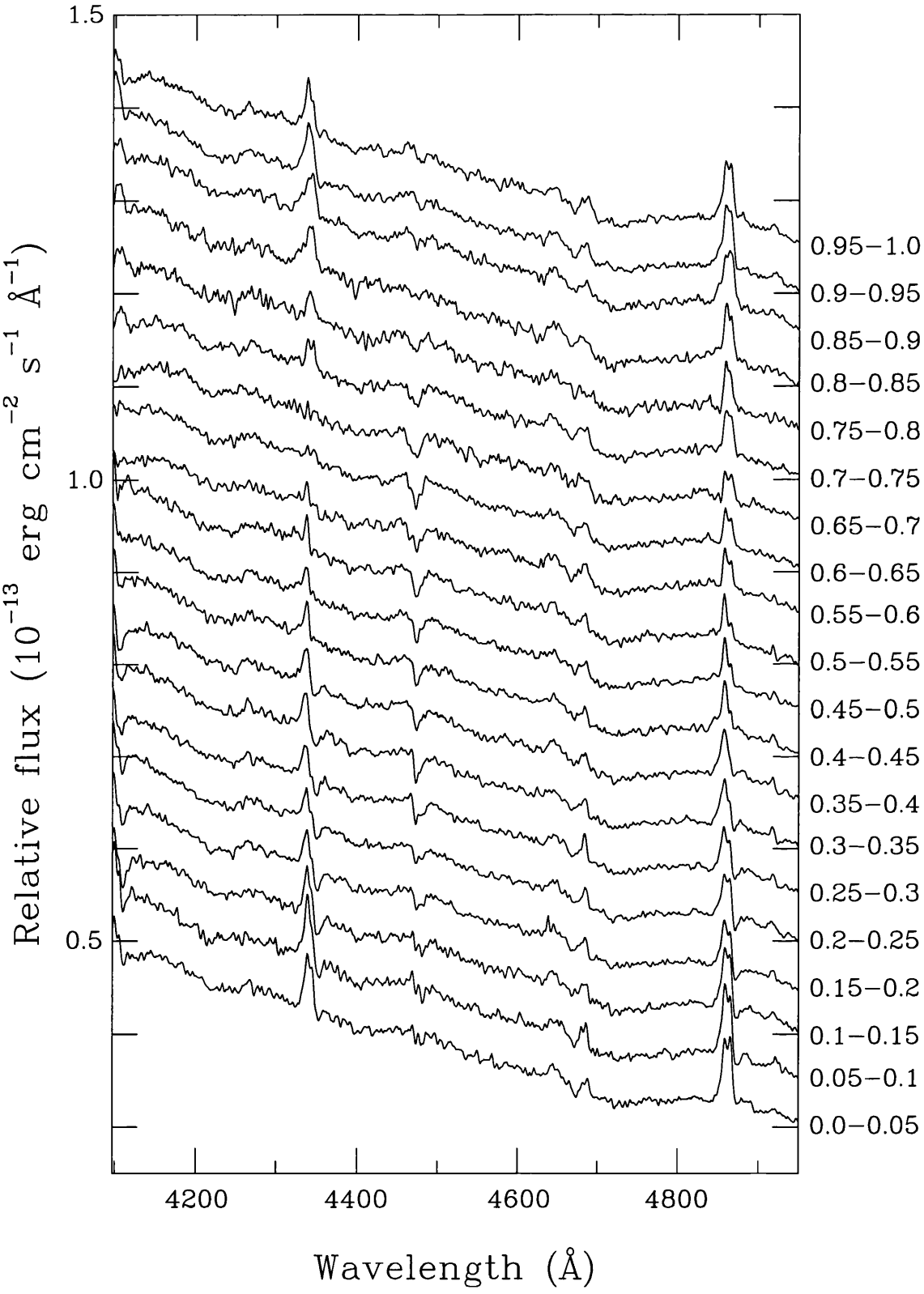

Figure 2.3: Montage of the phase-binned IDS spectra of V795 Her. Each spectrum is shifted from the next by 0.5 x 10^{-14} erg cm^{-2} s^{-1} Å^{-1}. The range of the phase bins are indicated for the 2.60 hr period.

ure 2.4 where the data from the phase bin centred at $\phi_{2.6} = 0.475$ has been plotted over the data from the bin centred at $\phi_{2.6} = 0.025$ for Hβ, Hγ, He I λ4471 and He II λ4686). The Balmer profiles in particular may be 'decomposed' into three variable constituents: a double-peaked emission core, shallow extended emission wings, and variable absorption which appears to be strongest in the first half of the cycle (it is still apparent however in later phase bins, *e.g.* $\sim 0.75 - 0.8$; see also Figures 2.8 and 2.12). Trailed spectrograms displaying the profile changes as a function of orbital phase over $\lambda\lambda 4200 - 4950$ Å are shown in Figure 2.5. The upper image in Figure 2.5 shows the observed phase-binned spectra (*c.f.* Figure 2.3), and the lower greyscale shows these data as residuals from the mean spectrum of the entire time series data set. The intensity scales are reversed such that enhanced emission is seen as *darker* shades.

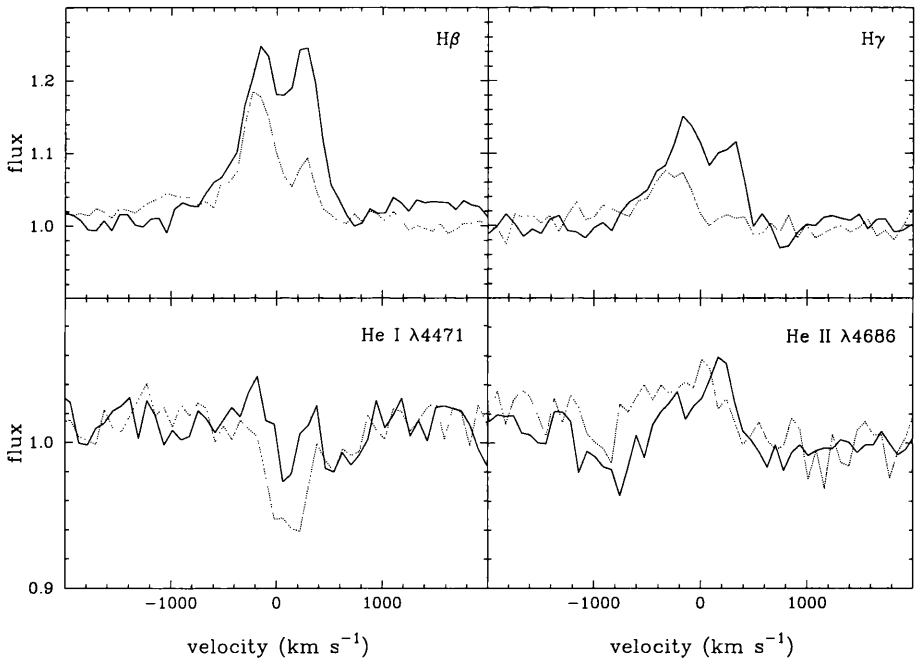

Figure 2.4: Line profile morphology changes over the orbital cycle for Hβ, Hγ, He II λ4471 and He II λ4686. In each panel, the solid line shows the line profile from the phase bin centred at $\phi_{2.6} = 0.025$ and the dotted line, the profile at $\phi_{2.6} = 0.475$.

The overall variations in the Balmer, He I λ4921 and He II λ4686 emission are in the same sense *i.e.* there is a maximum in the observed line flux at $\phi_{2.6} = 0.0$. The equivalent widths (EW) of these lines are plotted as a function of the 2.60 hr phase in Figure 2.6. Since the Balmer profiles of V795 Her are complex and affected by independent components due to variable absorption which is stronger on the redward side (Figure 2.3; also see Figures 2.8 and 2.12) and by systematic wing behaviour (Figures 2.5 and 2.7), this initial look at the overall trend of the variations in line strength

versus orbital phase samples only a limited range (in velocity space) of the line profiles. The blueward Hβ and Hγ core emission is sampled by measuring the EW between -500 and 0 km s^{-1}, the EW changes in the blueward Hβ wing are monitored between -1750 and -500 km s^{-1}, while the total He I λ4471 absorption EW was sampled. These measurements were made in line profiles normalised with respect to a local continuum. A more detailed examination of the behaviour of the line strengths is carried out in the next section (Figure 2.9). Figure 2.6 shows that the central core emission of the Balmer lines peaks at $\phi_{2.6} \sim 0$ and declines in strength toward a minimum at $\phi_{2.6} \sim 0.6-0.7$. In both Hβ and Hγ a 'secondary dip' in core emission strength is noted around $\phi_{2.6} = 0.2-0.25$. The maximum absorption strength of He I λ4471 correlates with the minimum in the Balmer core emission. The full-width at half-maximum (FWHM) of the He I absorption and He II λ4686 is also at its largest at $\phi_{2.6} \sim 0.7$ (*i.e.* ~ 1100 km s^{-1}). Finally, the strength of the (weak) fluctuations in the Hβ (and Hγ) wing does not modulate in any obvious manner, though as described below the central velocities are clearly cyclic.

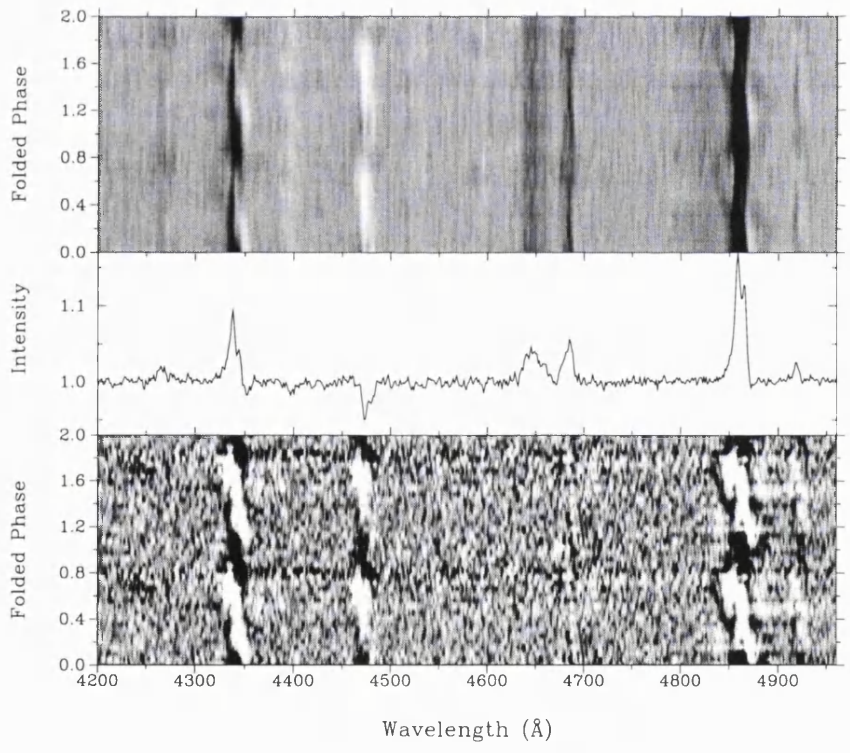

Figure 2.5: Trailed spectrograms displaying the optical line profile variations in V795 Her as a function of the 2.60 hr period. Darker shades show where line flux is greatest. The bottom panel is an image of the individual phase-binned spectra normalised by the mean spectrum (which is shown in the middle panel).

It is clear from Figure 2.5 that the inner cores and the wings of the Balmer lines vary in different ways. The outer wing modulation is characterised by the presence of a double wave pattern, with synchronised net blueshifted and redshifted humps. Similar profile changes have been reported by Haswell *et al.* (1994) and Casares *et al.* (1996). Section 2.5, however, argues that the variability in the wings is *not* due to the presence of separate waves on each wing. This behaviour of the outer wings is shown in close-up for the case of Hβ in the following section, which also examines in more detail the redward absorption feature noted above, the behaviour of the line strengths as a function of phase for the different velocity strips across the profile, and the results of a simple Gaussian fit to the Hβ lines. This section is then followed by a further two sections which examine the detailed behaviour of the other Balmer lines (Hγ and Hδ), and the helium lines (He II λ4686 and He I λ4471).

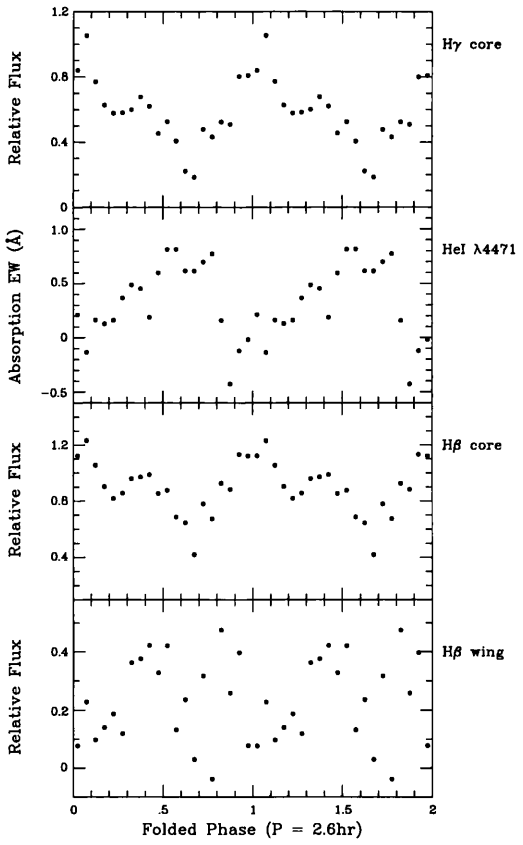

Figure 2.6: The EW of core emission in Hγ and Hβ, of outer wing fluctuations in Hβ, and of He I λ4471 total absorption, as a function of the 2.60 hr cycle.

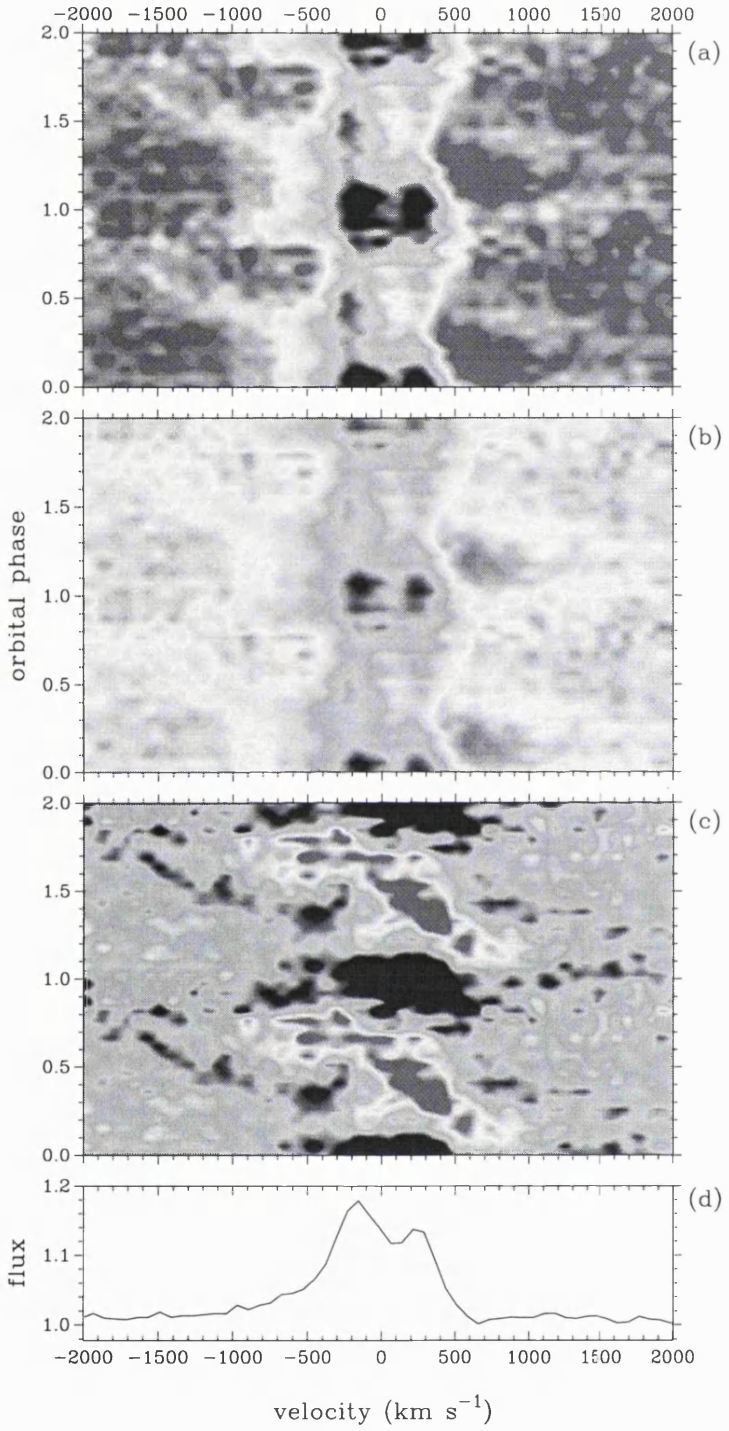

Figure 2.7: Trailed spectrograms of the phase-dependent variations in Hβ. Panel (a) shows the data with the contrast levels set to reveal the inner core details and panel (b) with the contrasts set to show the outer wing variations. Panel (c) shows data that has been normalised by dividing the raw data by a mean template and panel (d) contains the mean line profile.

Line profile behaviour of Hβ

As the strongest emission line present in this wavelength region Hβ provides the best opportunity to explore the complex behaviour of the Balmer line profiles. The inner core and outer wings are clearly varying in different ways (see Figure 2.5), and the trailed spectrograms shown in Figure 2.7 reveal this in greater detail. The top two panels show the flux variations of the rectified Hβ profiles as a function of the orbital phase, with the contrast levels of panel (a) scaled to reveal the inner core details and those of panel (b) scaled to show the outer wing variations. Panel (c) shows data that has been normalised by dividing the raw data by a mean template, which is shown in panel (d). The presence of a low-velocity s-wave is not detected, in contrast to earlier observations of V795 Her, although the enhancement of both peaks is noted at $\phi_{2.6} \sim 1.0$ and of the blue peak at $\phi_{2.6} \sim 0.4$. The weak emission features in the Hβ wings modulate as a double s-wave pattern, with synchronised net blueshifted and redshifted components. The velocity progression of the outer waves appears to be asymmetric, with the most rapid changes occurring between $\phi_{2.6} = 0.7 - 0.9$. The outer wing variations are much clearer on the blueward side of the line centre, owing to the presence of an absorption feature on the red wing. This redward absorption feature is stronger during the first half of the orbital cycle (Figure 2.8).

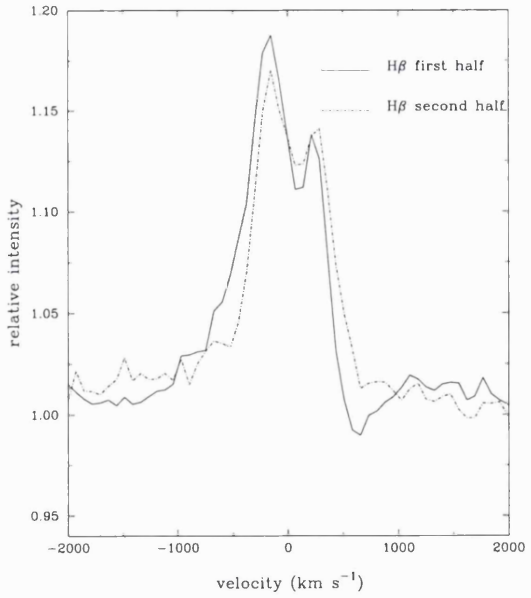

Figure 2.8: The redward absorption feature in Hβ. The solid line shows the mean Hβ profile from the first half of the orbital cycle ($\phi_{2.6} = 0.0 - 0.5$) and the dotted line shows the mean profile from the second half ($\phi_{2.6} = 0.5 - 1.0$).

The Hβ line profiles of V795 Her are very complex due to both the systematic wing behaviour (Figure 2.7) and the variable redward absorption (Figure 2.8). In an attempt to break down this behaviour and identify the major region of variability, the line profile was split into velocity strips and the line strength versus phase for each velocity strip was examined. The results of this analysis are presented in Figure 2.9. The line was split into 8 velocity bins across the line profile from $-2000\,\mathrm{km\,s^{-1}}$ to $+2000\,\mathrm{km\,s^{-1}}$, each velocity bin being $500\,\mathrm{km\,s^{-1}}$ wide.

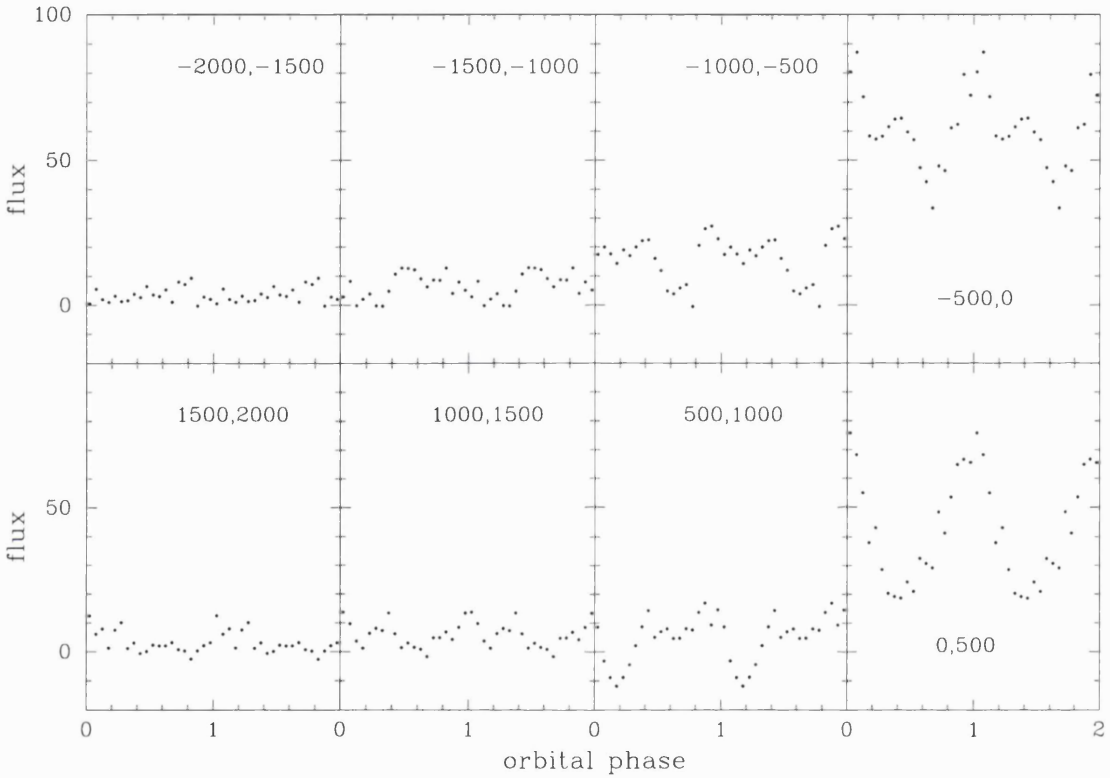

Figure 2.9: Light curves as a function of velocity within the Hβ line profile.

While the behaviour in the velocity bins $[-1000, -500\,\mathrm{km\,s^{-1}}]$ and $[500, 1000\,\mathrm{km\,s^{-1}}]$ are roughly anti-phased, the behaviour in bins $[-500, 0\,\mathrm{km\,s^{-1}}]$ and $[0, 500\,\mathrm{km\,s^{-1}}]$ differ significantly. In velocity bin $[-1000, -500\,\mathrm{km\,s^{-1}}]$ there is minimum flux at $\phi_{2.6} \sim 0.6-0.7$ and a secondary dip at around $\phi_{2.6} = 0.2-0.25$. For velocity bin $[500, 1000\,\mathrm{km\,s^{-1}}]$ the minimum is at $\phi_{2.6} \sim 0.2$ and the secondary dip is at $\phi_{2.6} \sim 0.6$. The behaviour in velocity bin $[-500, 0\,\mathrm{km\,s^{-1}}]$ mirrors that of velocity bin $[-1000, -500\,\mathrm{km\,s^{-1}}]$ with peak flux at $\phi_{2.6} \sim 0$, a decline in strength toward a minimum at $\phi_{2.6} \sim 0.6-0.7$ and a secondary dip in emission strength at around phase $\phi_{2.6} = 0.2-0.25$. Velocity bin $[0, 500\,\mathrm{km\,s^{-1}}]$ shows a maximum at $\phi_{2.6} = 0.9-1.0$, a minimum at $\phi_{2.6} = 0.4-0.5$ and no sign of a secondary dip.

The following summary describes the primary characteristics of the optical profile changes to the Hβ line in V795 Her. It is based in part on a simple Gaussian profile fit to the phase-binned data. (As demonstrated in the next section, these results apply equally to the other, weaker Balmer lines in the IDS spectra).

1. The central velocity of the perturbation on the wing of the Hβ profile reaches a maximum blueward value of ~ -1615 km s^{-1} at $\phi_{2.6} = 0.6 - 0.7$. This phase corresponds to the instance when the strength of the core emission is at its minimum (*e.g.* Figure 2.9).

2. The flux variations on the red wing are noticeably weaker than those on the blue wing (*e.g.* Figure 2.7).

3. The velocity progression of the outer 'wave' may be asymmetric. The increase in velocity as a function of phase is more gradual up to $\phi_{2.6} = 0.6 - 0.7$, compared to the more rapid changes between $\phi_{2.6} \sim 0.75$ and $\phi_{2.6} \sim 1.0$. This asymmetry was not recognised by Casares *et al.* (1996) although I believe it can also be discerned in their data set of V795 Her.

4. These INT data do not reveal any clear evidence for an s-wave modulation in the inner core Hβ components (*e.g.* Figures 2.7 and 2.9). This is in contrast, for example, to the findings of Casares *et al.* (1996) in data secured between 1994 February and July. The observed Hβ core emission variations in these INT data can be accounted for in terms of changes in the strengths and widths (in velocity space) of the blue and red components. The central velocities of the double peaks are essentially stable with mean observed velocities of ~ -165 km s^{-1} and $+280$ km s^{-1}, respectively (in the observer's frame).

5. The absorption component in Hβ is strongest during the first half of the orbital cycle (Figures 2.8 and 2.10). There is an apparent blueward progression from $\sim +770$ km s^{-1} (at $\phi_{2.6} = 0.0 - 0.05$) to $+400$ km s^{-1} (at $\phi_{2.6} = 0.35 - 0.4$) of the central velocity of the observed absorption trough. The absorption is severely blended with the red emission core component after this phase bin. The total observed absorption equivalent width decreases as a function of phase from ~ 0.3 Å to less than 0.02 Å. There is no evidence in these data for gross night-to-night differences in the shapes of phase-binned profiles (Figure 2.11; *c.f.* Figure 3 of Casares *et al.* 1996).

6. The FWHM of the blue and the red inner core components is also highly variable (see Figure 2.10). The Gaussian profile fits indicate a broader blue component with FWHM in the

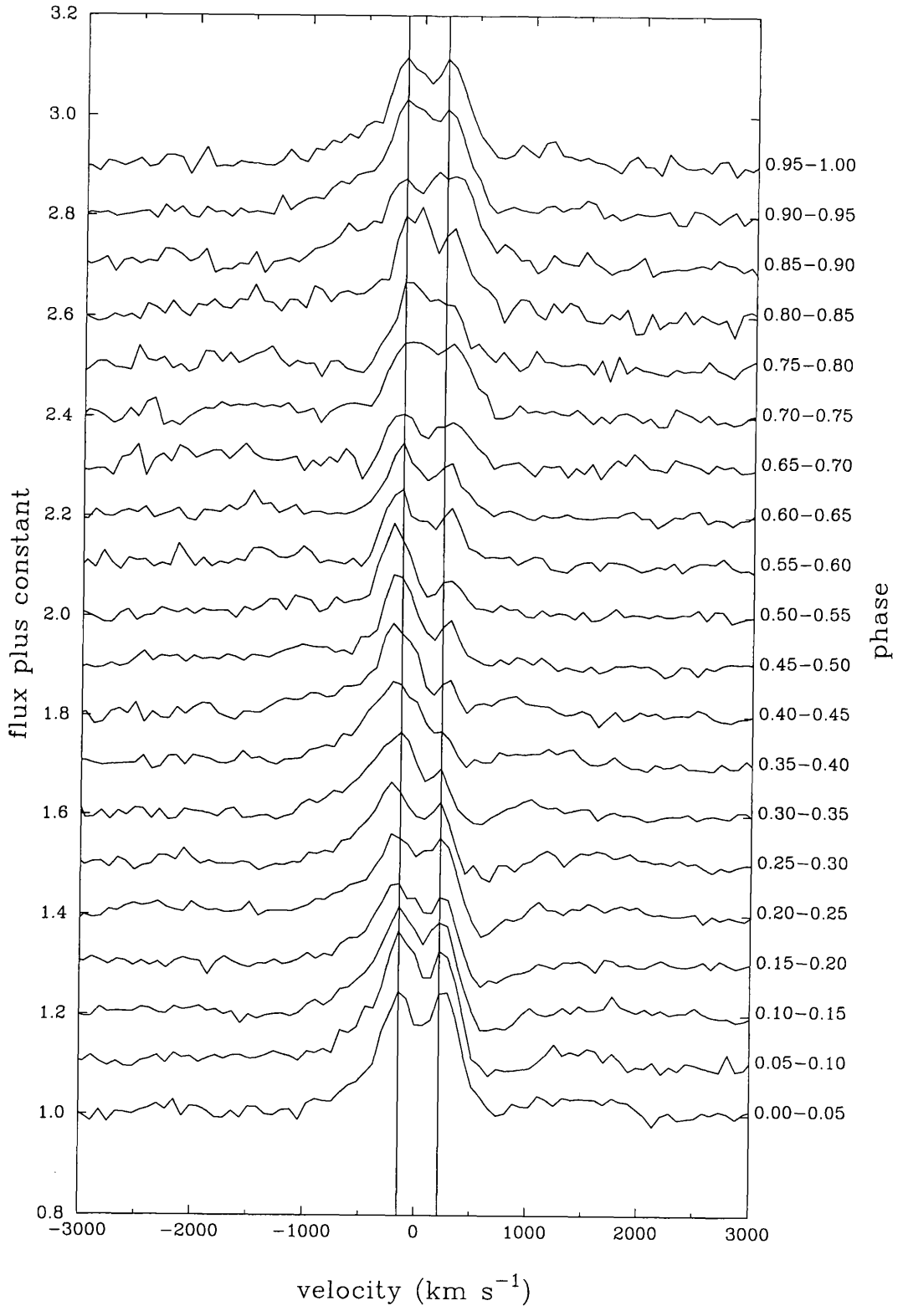

Figure 2.10: Montage of the phase-binned Hβ spectra of V795 Her. The range of the phase bins are indicated for the 2.60 hr period.

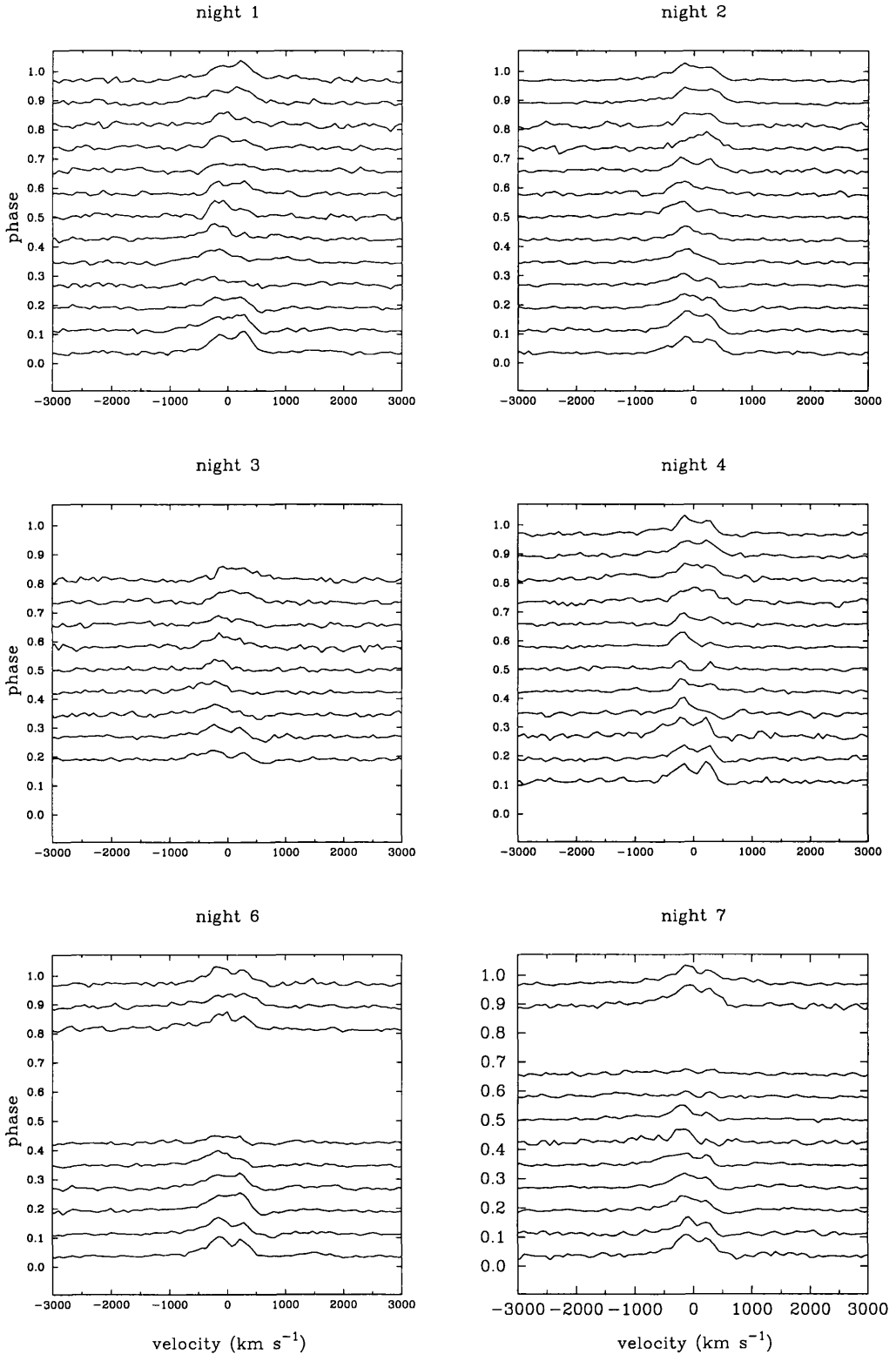

Figure 2.11: Montage of phase-binned Hβ profiles for individual nights. In this figure the data are folded into 13 phase bins. There is no evidence for gross night-to-night changes in the line profiles.

range $\sim 300-550$ km s^{-1}; the width of the red component is typically only $100-350$ km s^{-1}. This is also true late in the cycle when the redward absorption is much weaker and does not severely affect the red core emission component. Both components have larger velocity widths around phase $0.7-0.75$ (Figure 2.10).

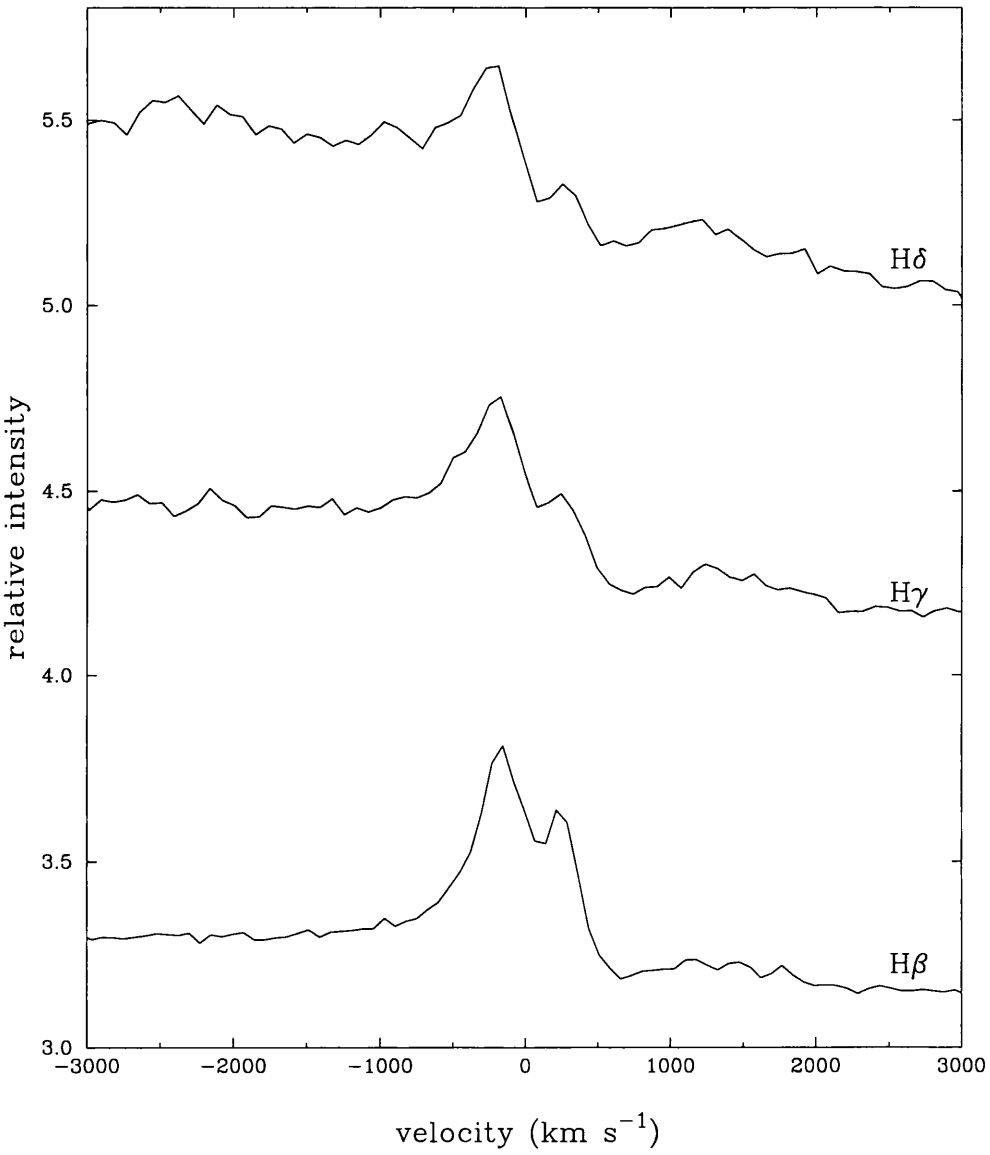

Figure 2.12: A comparison of the redward absorption feature in the Balmer lines. From top to bottom: Hδ, Hγ and Hβ.

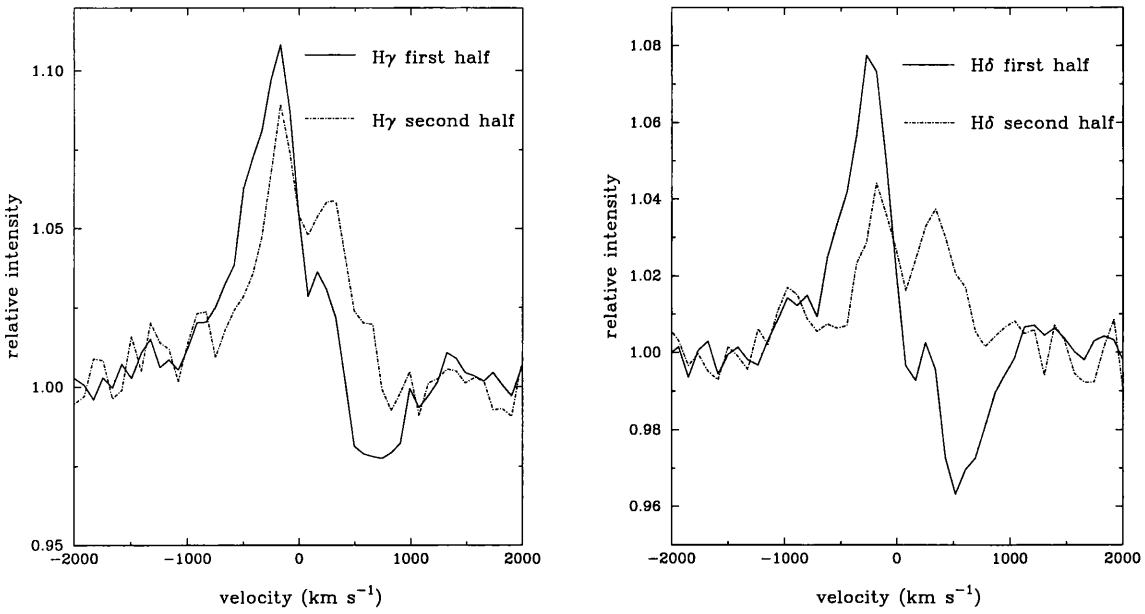

Figure 2.13: The redward absorption feature in Hγ and Hδ during the first (solid line) and second (dotted line) halves of the orbital cycle.

Line profile behaviour of Hγ and Hδ

Having examined the behaviour of the Hβ line profile this section moves on to look at the characteristics of the other Balmer lines sampled in this data set. The redward absorption feature seen in the Hβ line profile (Figure 2.8) is also present in the Hγ and Hδ line profiles. Figure 2.12 shows the mean line profiles for Hδ, Hγ and Hβ and reveals an increase in the absorption strength from Hβ to Hδ. Again, the absorption is clearly stronger during the first half of the orbital cycle (Figure 2.13).

Hγ and Hδ also display the same outer wing behaviour as Hβ. Figures 2.14 and 2.15 are trailed spectrograms that show the line profiles versus orbital phase. Again, variations are seen in the outer wings. Although these variations are weaker than those seen in the Hβ line, they seem to be behaving in the same manner. The maximum blueward central velocity of the blue wing variation is $\sim -1600\,\mathrm{km\,s^{-1}}$ and is reached at $\phi_{2.6} = 0.6 - 0.7$. The flux variations are weaker on the red wing than on the blue wing, and again there is some evidence that the velocity progression may be asymmetric. The most rapid changes occur between $\phi_{2.6} \sim 0.75 - 1.0$, while the changes between $\phi_{2.6} = 0.0 - 0.65$ are more gradual. The inner core components of the Balmer lines do not show any obvious s-wave modulation.

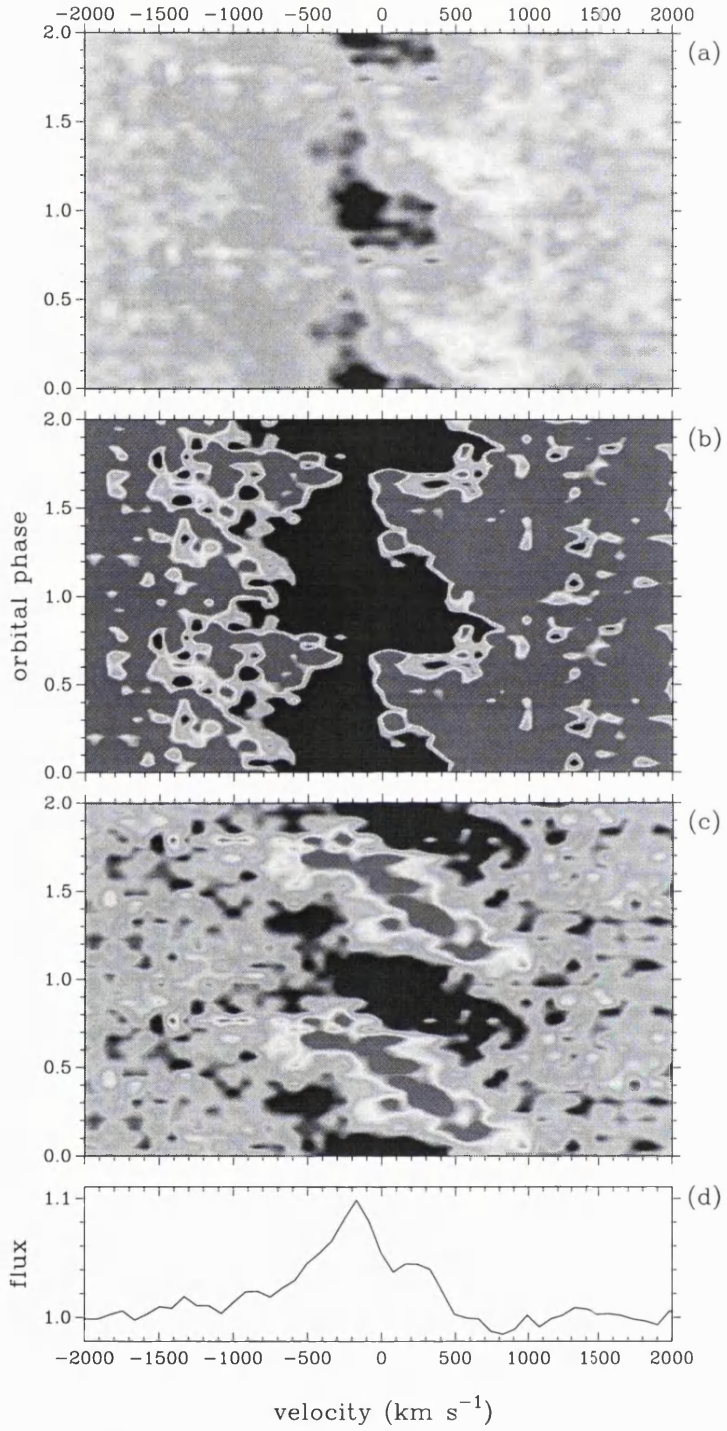

Figure 2.14: Trailed spectrograms of the phase-dependent variations in Hγ. Panel (a) shows the data with the contrast levels set to reveal the inner core details and panel (b) with the contrasts set to show the outer wing variations. Panel (c) shows data that has been normalised by dividing the raw data by a mean template and panel (d) contain the mean line profile.

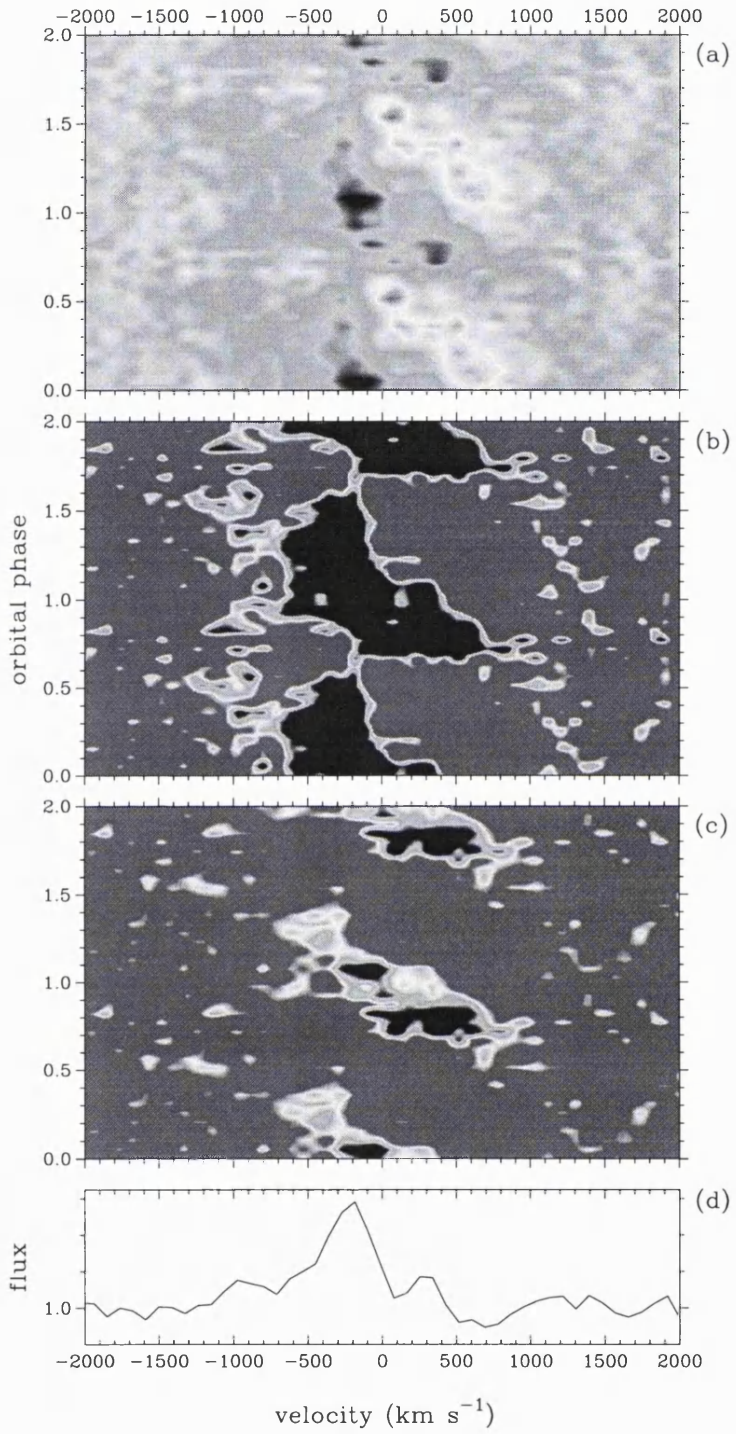

Figure 2.15: Trailed spectrograms of the phase-dependent variations in Hδ. Panel (a) shows the data with the contrast levels set to reveal the inner core details and panel (b) with the contrasts set to show the outer wing variations. Panel (c) shows data that has been normalised by dividing the raw data by a mean template and panel (d) contain the mean line profile.

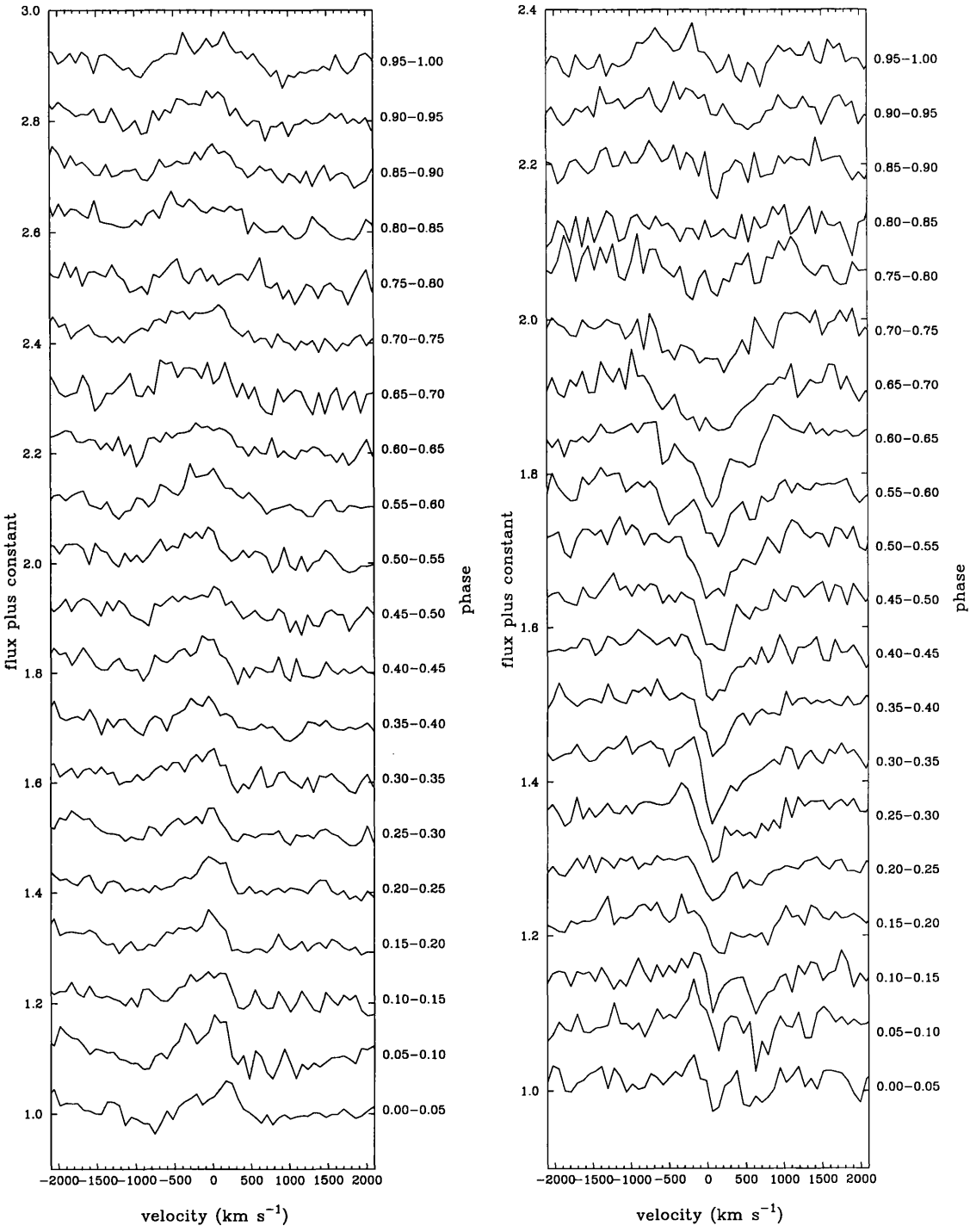

Figure 2.16: Montage of the phase-binned He II λ4686 and He I λ4471 spectra of V795 Her. The range of the phase bins are indicated for the 2.60 hr period.

Line profile behaviour of He II λ4686 and He I λ4471

The final part of this section on the spectral line behaviour of V795 Her examines the helium lines He II λ4686 and He I λ4471. Figure 2.16 shows the 20 phase-binned line profiles of both lines. The He II λ4686 line appears to be single-peaked for much of the orbital cycle and there is little evidence for a redward absorption feature in this line, looking only at the montage. Figure 2.17 shows the mean He II λ4686 line profiles for the first ($\phi_{2.6} = 0.0 - 0.5$; solid line) and second ($\phi_{2.6} = 0.5 - 1.0$; dotted line) halves of the orbital cycle. Although there is a reduction in flux in the first half of the cycle on the redward wing of the line profile, it is matched by a reduction in flux in the same velocity region blueward of the line centre. Looking at the trailed spectrograms of the flux variations versus orbital phase (Figure 2.18), and in particular at the image created using data normalised with the mean template, there is some suggestion that there may be reduced emission redward of the line centre for the first half of the orbital cycle. The detection of a redward absorption feature in the He II λ4686 line is therefore ambiguous.

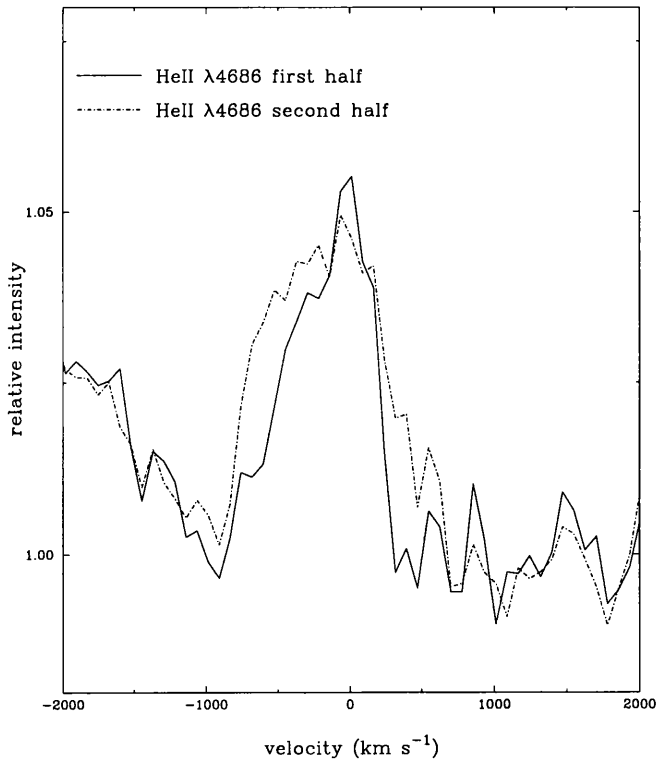

Figure 2.17: The redward absorption feature in He II λ4686. The solid line shows the mean He II λ4686 profile from the first half of the orbital cycle ($\phi_{2.6} = 0.0 - 0.5$) and the dotted line the mean profile from the second half ($\phi_{2.6} = 0.5 - 1.0$).

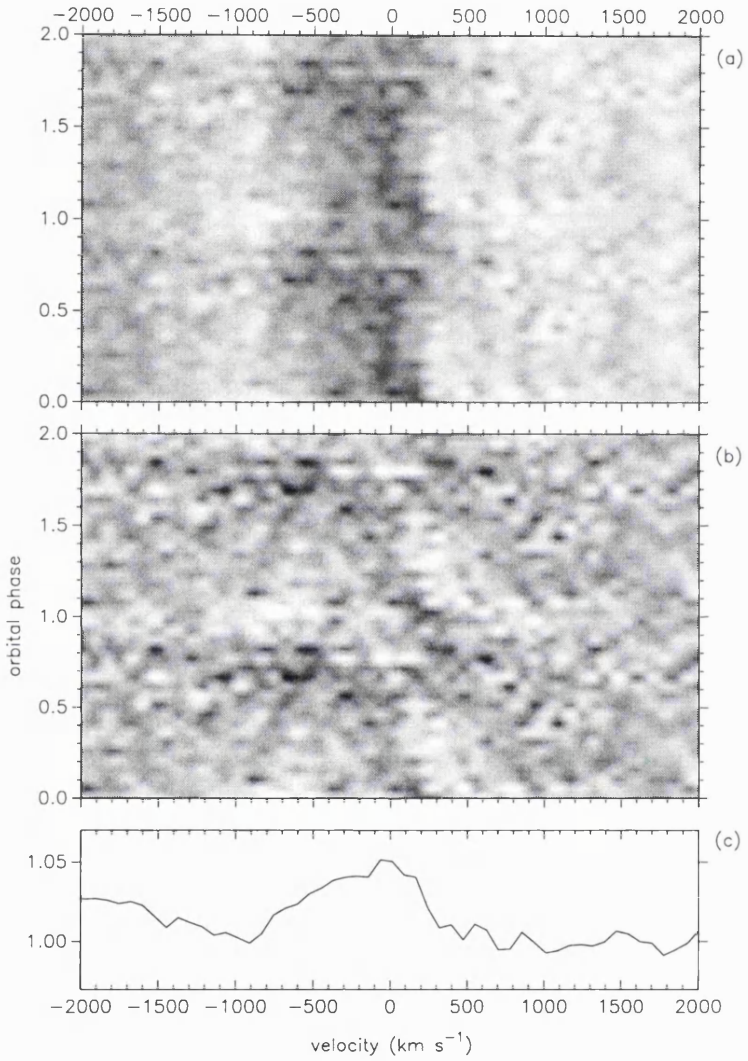

Figure 2.18: Trailed spectrograms of the phase-dependent variations in He II λ4686. Panel (a) shows the flux variations versus phase for the raw data, panel (b) shows data that has been normalised by dividing the raw data by a mean template and panel (c) contain the mean line profile.

The trailed spectrograms of the flux variations versus orbital phase for the He II λ4686 line (Figure 2.18) do not reveal any obvious sinusoidal radial velocity modulations. A simple fit to the He II λ4686 line was carried out using a single Gaussian profile, the results of which are shown in Figure 2.19. The radial velocity curve shows an asymmetric velocity progression: the line is at its maximum blueward velocity at $\phi_{2.6} = 0.0$, there is a gradual redward movement from $\phi_{2.6} = 0.0 - 0.7$ until the maximum redward velocity is reached, and then there is a much more rapid return blueward from $\phi_{2.6} = 0.7 - 1.0$.

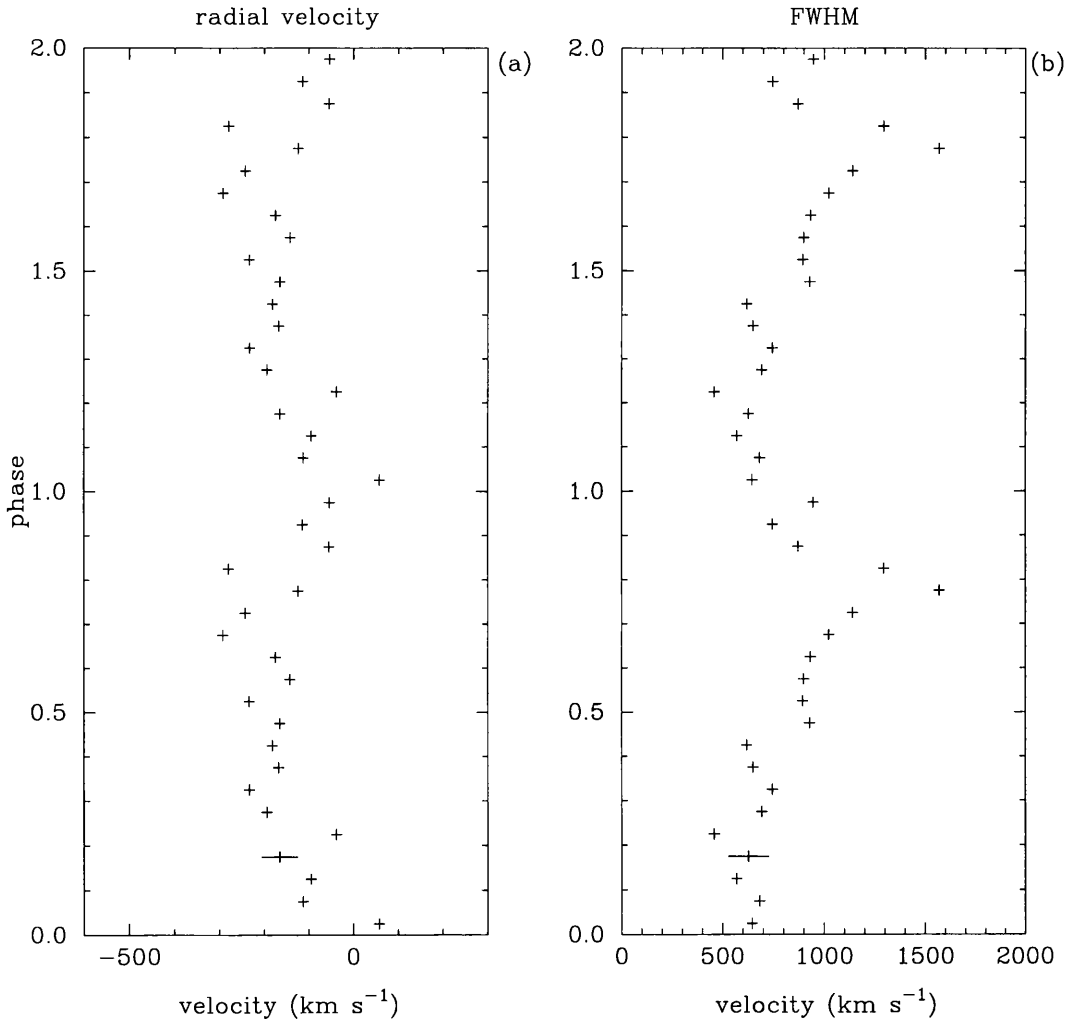

Figure 2.19: Simple Gaussian fit to the He II λ4686 line profiles. Panel (a) shows the central velocity of the Gaussian fit to the emission line and panel (b) the FWHM of the Gaussian fit. Typical error bars are shown.

The light curves as a function of velocity across the He II λ4686 line profile are shown in Figure 2.20. The flux was measured in 4 velocity bins across the line profile, each bin being 500 km s^{-1}

wide. The He II line clearly behaves differently in velocity space from the Balmer lines. The flux in velocity bins $[-1000, -500\,\mathrm{km\,s^{-1}}]$ and $[-500, 0\,\mathrm{km\,s^{-1}}]$ is minimum at $\phi_{2.6} \sim 1.0$ and for velocity bin $[0, 500\,\mathrm{km\,s^{-1}}]$ it is minimum at $\phi_{2.6} \sim 0.3$.

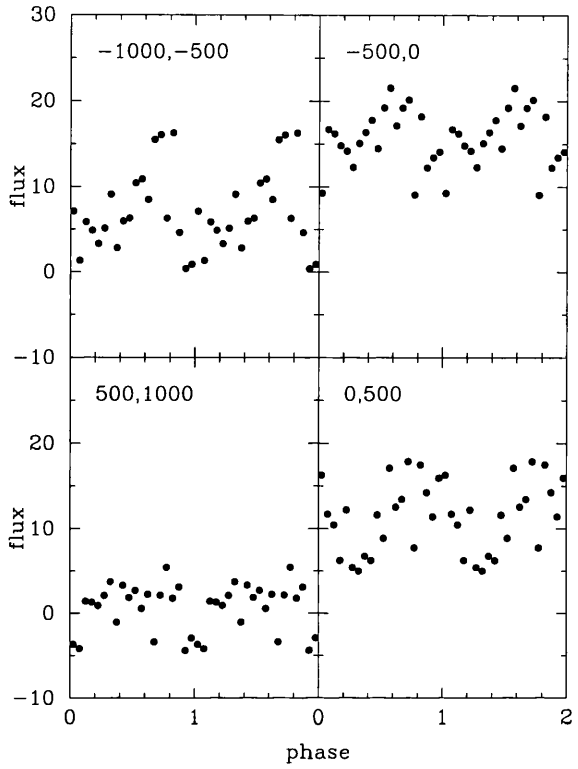

Figure 2.20: Light curves as a function of velocity within the He II λ4686 line profile.

A montage of the absorption line profiles of He I λ4471 is shown in the right-hand panel of Figure 2.16. The absorption widens and deepens over the orbital cycle until it reaches a maximum depth and width at $\phi_{2.6} \sim 0.65 - 0.70$. After this phase, the absorption declines in strength and appears to move redward. There is some indication of a blueward emission component, seen most clearly at $\phi_{2.6} = 0.25 - 0.35$ ($v \sim -400\,\mathrm{km\,s^{-1}}$). Figure 2.21 shows the trailed spectrograms for the He I λ4471 line. The absorption component clearly widens to a maximum at $\phi_{2.6} \sim 0.7$ and then rapidly disappears. The image in panel (b) has had the contrast levels changed to highlight a tentative identification of a redward absorption feature during the first half of the orbital cycle ($\phi_{2.6} \sim 0.9 - 1.3$). The contrast levels in panel (c) have been adjusted in order to examine the possible emission component identified in the montage (Figure 2.16), blueward of the line centre. This feature appears to correspond to the blueshifted outer s-wave seen in the Balmer lines (Figures 2.7, 2.14 and 2.15), as it migrates bluewards from $\sim -500\,\mathrm{km\,s^{-1}}$ to $\sim -1500\,\mathrm{km\,s^{-1}}$ between $\phi_{2.6} = 0.3$ and $\phi_{2.6} = 0.8$.

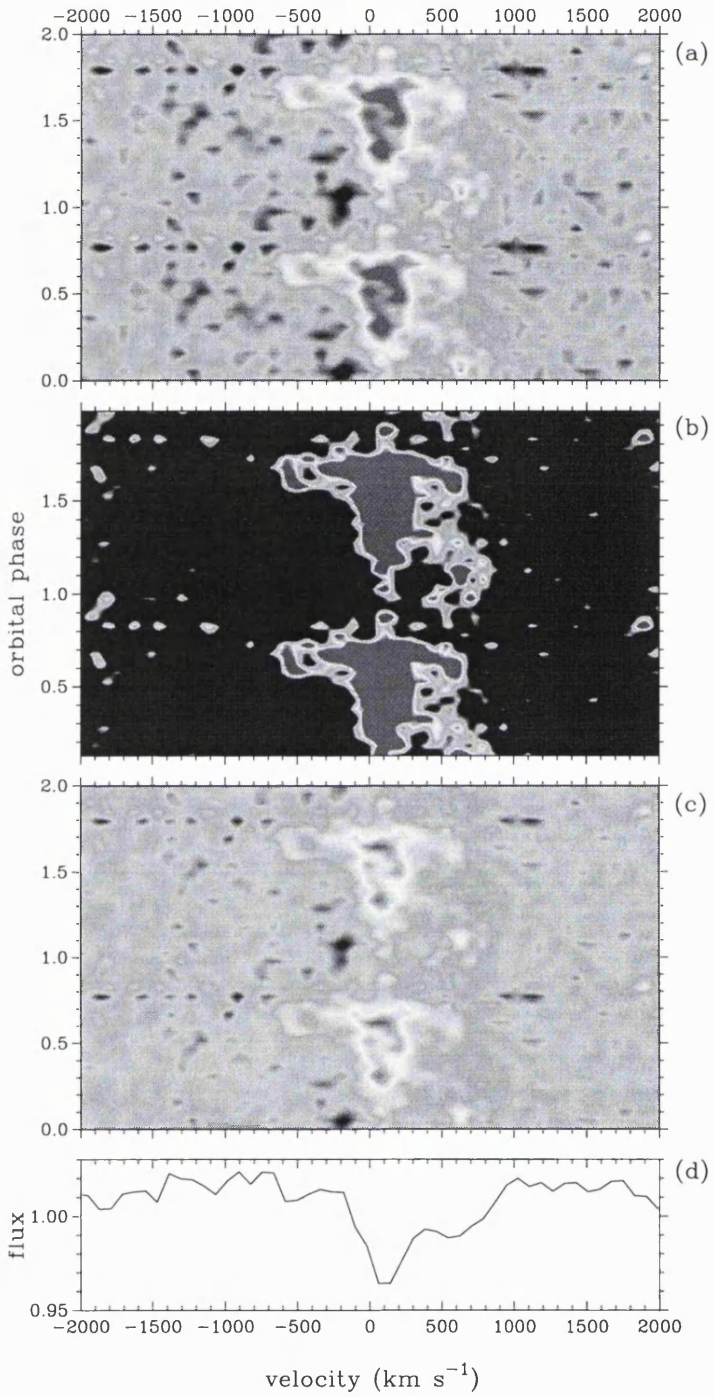

Figure 2.21: Trailed spectrograms of the phase-dependent variations in He I λ4471. Panel (a) shows the flux variations versus phase for the raw data and panel (b) shows the same raw data with the contrast levels set to show the possible identification of redward absorption. The contrast levels in panel (c) have been adjusted to examine the emission component identified in the montage of phase binned profiles (Figure 2.16). Panel (d) shows the mean line profile.

Figure 2.22 shows the light curves as a function of velocity across the He I λ4471 line profile. The flux was measured in 4 velocity bins, each of width 500 km s^{-1}, from -1000 km s^{-1} to 1000 km s^{-1}. For velocity bins [$-500, 0$ km s^{-1}] and [0, 500 km s^{-1}] the absorption is greatest at $\phi_{2.6} = 0.7$. Casares *et al.* (1996) suggest that the He I λ4471 absorption line is the best place to examine the behaviour of the absorption features seen in V795 Her. A simple Gaussian fit to the absorption profile was carried out and is shown in Figure 2.23 . Panel (a) shows the radial velocity behaviour of the absorption component, which seems markedly different from the behaviour reported by Casares *et al.* (see their Figure 7). The absorption feature that is fitted here is confined in velocity space to $-40 < v < +600$ km s^{-1}; *i.e.* for most of the orbital cycle (particularly in the phase interval 0.0 – 0.5) it is *redward* of the line centre. Casares *et al.* measured the radial velocity of the He I λ4471 line by cross-correlation with the mean profile. They identify a narrow, high amplitude absorption feature (semi-amplitude $\sim$ 500 km s^{-1}) that is roughly centred on the rest velocity, and a broad, low amplitude absorption that deepens near their phase 0.5 (corresponding to $\phi_{2.6} = 0.66$ in our phase convention).

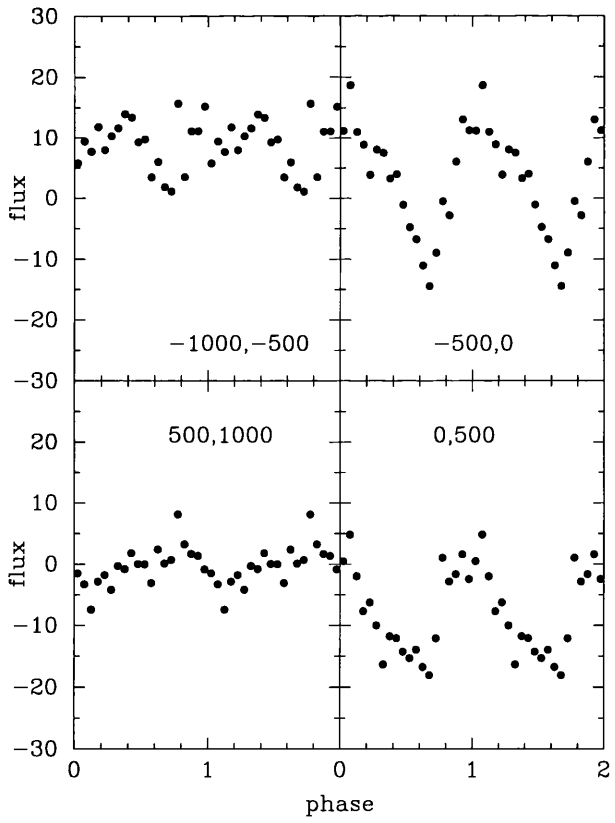

Figure 2.22: Light curves as a function of velocity within the He I λ4471 line profile.

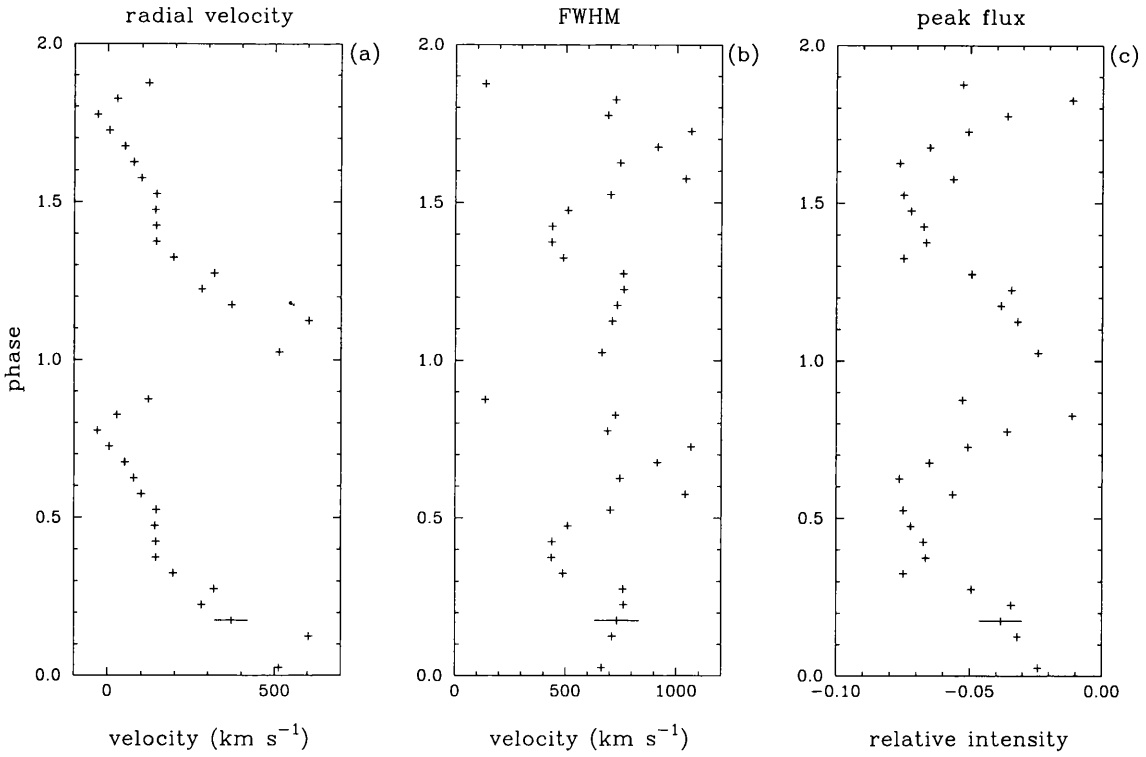

Figure 2.23: Simple Gaussian fit to the He I λ4471 line profiles. Panel (a) shows the central velocity of the Gaussian fit to the absorption profile, panel (b) the FWHM of the Gaussian fit and panel (c) the peak flux of the fit. Typical error bars are shown.

2.4 Doppler imaging

Doppler imaging methods (described in Section 1.3 and Appendix A) generally provide a powerful handle on the line emission distribution in CVs. The techniques assume, however, that the emission sources are essentially in planar motion on an accretion disk, and therefore may not be ideally suited to mapping the outer wing perturbations seen in the Balmer lines of V795 Her. Nevertheless the Doppler mapping may help constrain the likely location of the outer wing emission source, and shed light on the nature of the changes in the inner cores of the Balmer line (Section 2.3.2).

Doppler maps of the Hβ emission were computed based on 39 phase-binned profiles (Figure 2.24), using Fourier-filtered back projection (see *e.g.* Kaitchuck *et al.* 1994). Projecting the map in different directions yields a model velocity profile that fits the observed velocity profile at the corresponding binary phases. The map therefore resolves the Hβ emission line regions in Doppler coordinates (V_X, V_Y). The orbital phase of inferior conjunction of the secondary in V795 Her is not known, and thus the Doppler maps can be rotated arbitrarily.

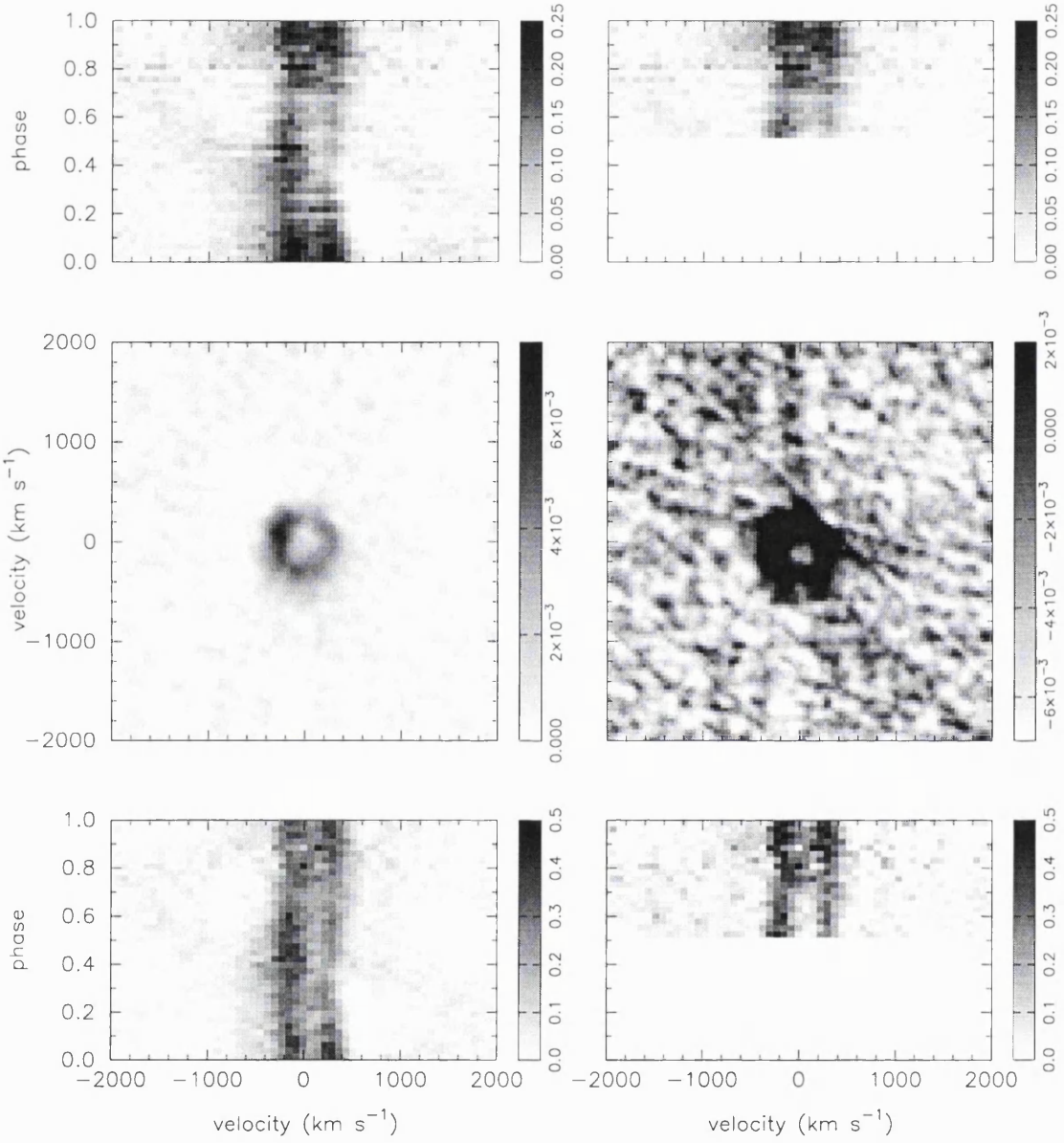

Figure 2.24: Doppler imaging of the Hβ emission. The panels show, from top to bottom, the observed data as a trailed spectrogram, the computed Doppler image and the predicted data. The left-hand panels show the inner-core emission. The right-hand panels use data from the second half of the orbital cycle only (where absorption effects are less).

Low velocity patterns corresponding to the inner core Hβ regions are shown in the left-hand panels of Figure 2.24. The Doppler map, together with the observed morphology of the line profiles (*e.g.* Figures 2.3, 2.7), suggest that the inner core Balmer emission arises from a ring of planar material located in the outer region of the accretion disk (*i.e.* at velocities $\sim 150-250\,\mathrm{km\,s^{-1}}$). Enhanced H$\beta$ emission is seen as a darker region in the upper left quadrant of the central ring in the tomogram (Figure 2.24). However, this enhancement may not uniquely correspond to an inner s-wave feature, since an increase in strength and (velocity) width at phase 0.4 and 0.9, without radial velocity motion, would also mimic such a behaviour in the maps.

In an attempt to trace the high velocity outer wave in the Balmer wings, a second Doppler map of the Hβ emission was constructed (right-hand panels of Figure 2.24), based on data from the second half of the orbital cycle only. This minimises the contaminating effect of the variable absorption feature, since it dominates when redward, *i.e.* between phases 0.0 – 0.5 (Figure 2.10). There is no strong indication in Figure 2.24 for a high velocity emission source. A very weak pattern may be present at $\sim 1600\,\mathrm{km\,s^{-1}}$, up and slightly left of the centre of the map. (The low signal levels used mean that the inner core changes are 'saturated' and spoke-like artifacts, due to incomplete phase coverage, are now seen in the background).

Figure 2.25 shows the Doppler maps of the Hγ and He II λ4686 emission. The Hγ map strongly resembles the Hβ Doppler image (Figure 2.24). Again, the inner core emission appears to arise from the outer regions of the accretion disk ($v \sim 200\,\mathrm{km\,s^{-1}}$). There is no trace of the higher velocity outer wave(s) in the tomogram. The right-hand panels show the He II λ4686 Doppler imaging, which looks very different from the maps of the Balmer lines. There is little evidence of disk emission and instead there appears to be stationary low velocity emission ($v \sim 100\,\mathrm{km\,s^{-1}}$).

The Doppler maps (Figures 2.24, 2.25) interpret the observed trailed spectrogram as a sum of emission components following sinusoidal velocity curves with different semi-amplitudes and phases but all centered on the rest wavelength of the emission line. This representation is most appropriate for emission lines from gas moving with velocities V_X, V_Y in the orbital plane of a binary system, but with no net velocity ($V_Z \sim 0$) perpendicular to the orbital plane. The absence of a clear structure in Figure 2.24 corresponding to the outer wing emission features at velocities of $\sim 1600\,\mathrm{km\,s^{-1}}$ implies that the wing emission is not well represented by this model. Inspection of the trailed spectrogram (Figure 2.7) suggests that when the red and blue wing features are interpreted as arising from a single emission component, then this component must jump rapidly across

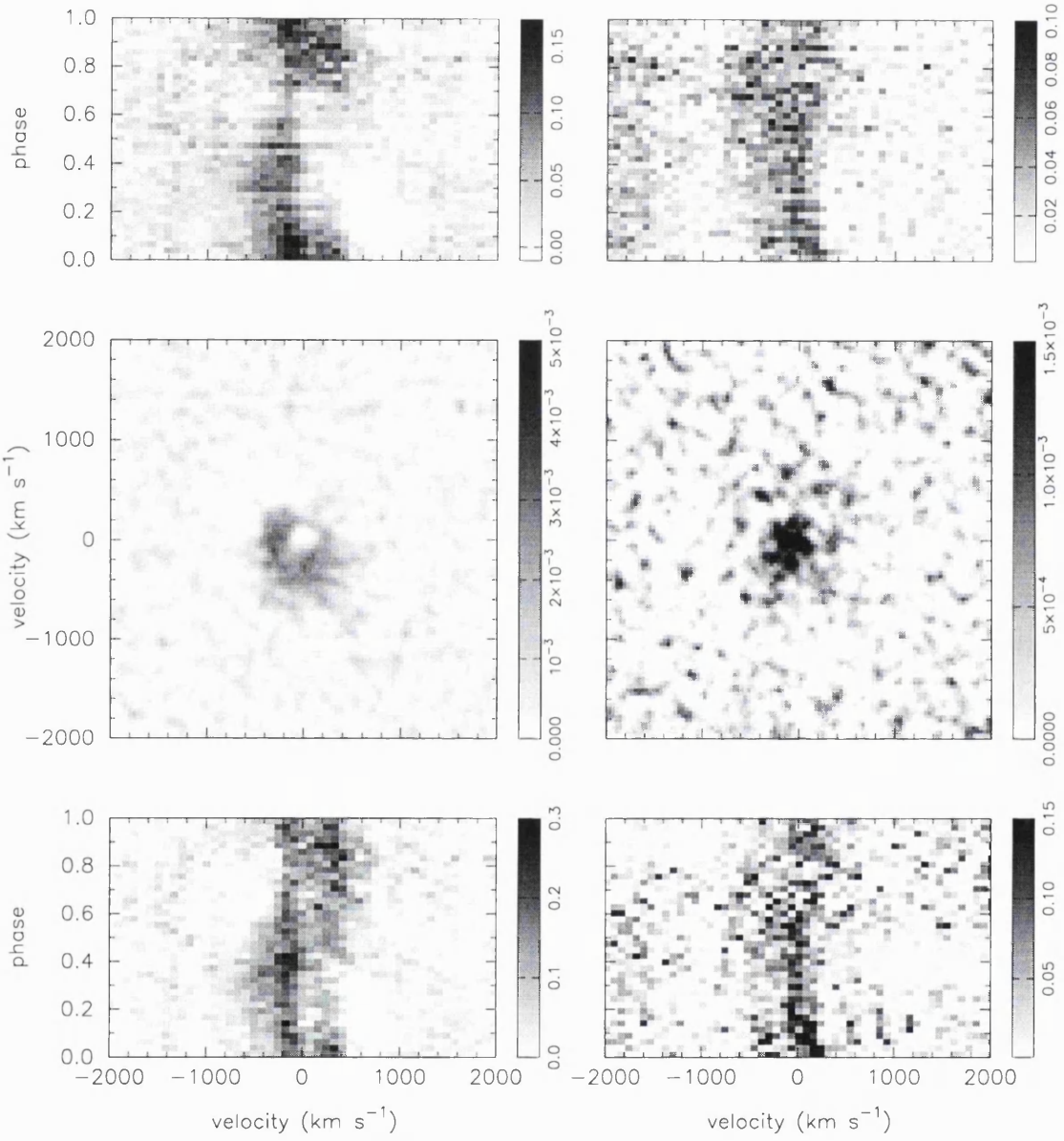

Figure 2.25: Doppler imaging of the Hγ and He II λ4686 emission. The panels show, from top to bottom, the observed data as a trailed spectrogram, the computed Doppler image and the predicted data. The left-hand panels show the Hγ emission and the right-hand panels show the He II λ4686 emission.

the centre of the line from red to blue around $\phi_{2.6} = 0.4$ and from blue to red around $\phi_{2.6} = 0.9$. This behaviour can be mimicked by a sum of centered sinusoids, but only if components at velocities much larger than 1600 km s^{-1} are included. The data around phases 0.2 and 0.7 do not support the presence of such high velocity components. This explains why the wing features visible in the data (*e.g.* Figure 2.7) do not produce a signature in the Doppler map.

2.5 An empirical interpretation: single broad emission plus superposed absorption

The empirical interpretation of the outer wing variations in the Balmer lines adopted by Casares *et al.* (1996) invokes two *separated*, but phased, emission components. The components result therefore in net blueshifted and net redshifted s-waves with maximum velocities reaching $\pm$ 1800 km s^{-1} (which may relate to magnetic accretion columns on the WD). It is argued in this section that an (at least) equally viable empirical interpretation of the data is that based on the study of the emission line behaviour of PX And and other SW Sex-type systems reported by Hellier & Robinson (1994).

The principal notion considered is that of a single broad emission feature which follows a high velocity s-wave, but which also has a superimposed, sympathetically phased absorption component; this then yields an overall double-humped profile. It is the motion of these 'humps' that should then be associated with the double outer wing s-waves seen in Figure 2.7. An *ad hoc* demonstration of this interpretation is presented here, postponing until Section 2.7.2 some disk-overflow simulations based on the SW Sex-type models of Hellier & Robinson (1994).

For a broad emission s-wave with a *central* 'self-absorption', the observed flux at low velocities (*e.g.* between -500 and 500 km s^{-1}) would be a minimum when the wave crosses zero velocity amplitude (*i.e.* $\phi_{2.6} = 0$ and $\phi_{2.6} = 0.5$; note that the *absolute* phasing of V795 Her is unknown). However, in the case of V795 Her the central emission flux is at a minimum when the 'outer wave' has a *maximum* blueward shift (*i.e.* $\phi_{2.6} = 0.7$; *e.g.* see Figures 2.6 and 2.7). To account for this difference, the superimposed absorption must be redshifted with respect to the emission centre.

A simple simulation of this interpretation was attempted by adopting (i) a Gaussian emission profile of FWHM = 2800 km s^{-1}, (ii) a FWHM = 1250 km s^{-1} absorption which is redshifted from the emission centre by 800 km s^{-1}, (iii) an 800 km s^{-1} full amplitude s-wave velocity motion, and (iv) central double-peaked core profiles which are stationary in velocity and fixed in strength. A

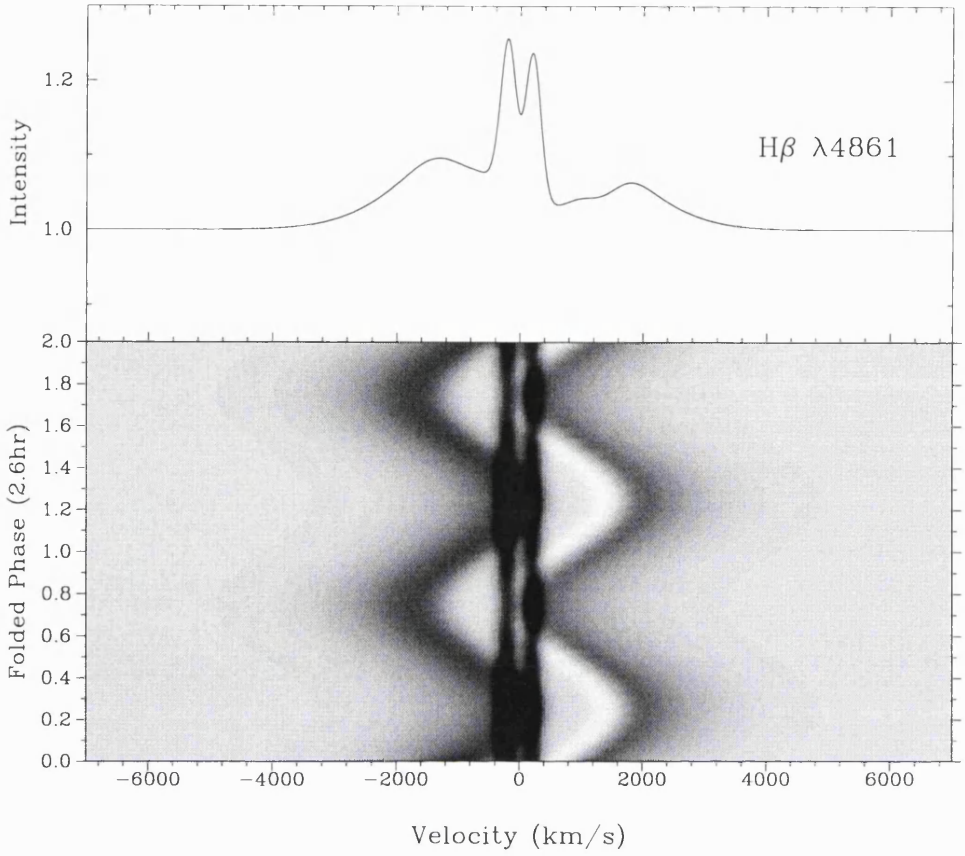

Figure 2.26: Simulations of the Hβ variations in V795 Her, combining a single broad emission feature plus a sympathetically phased, net redshifted, superimposed absorption (Section 2.5). The mean spectrum from the models is shown in the upper panel.

trailed spectrogram of this simulation is shown in Figure 2.26. The 'single broad emission plus redshifted absorption' interpretation successfully reproduces the four basic observational characteristics of the V795 Her Balmer lines: (i) it provides synchronised outer wing double s-wave structures, (ii) a minimum in observed core flux is evident at $\phi_{2.6} = 0.7$ (see below), (iii) the observed strength of the redward outer s-waves is less than the blueward one, and (iv) it accounts for the presence of redshifted absorption around $\phi_{2.6} = 0.25$ and possibly after $\phi_{2.6} = 0.75$ (*e.g.* Figure 2.3).

The mean flux between -500 and $0\,\mathrm{km\,s^{-1}}$ in the simulated data is shown in Figure 2.27 as a function of orbital phase. Whilst this is not intended as a match to the Hβ core behaviour in Figure 2.6 (also see Figure 2.9), it is interesting to note in Figure 2.27 the 'flattening' in total flux at $\phi_{2.6} = 0.25$, in addition to the obvious minimum at $\phi_{2.6} = 0.7$. A further interesting comparison may be made between the Doppler maps of the Hβ line (Figure 2.24) and a Doppler image of the simulated data (Figure 2.28). This image was created by adding noise (of a similar level to

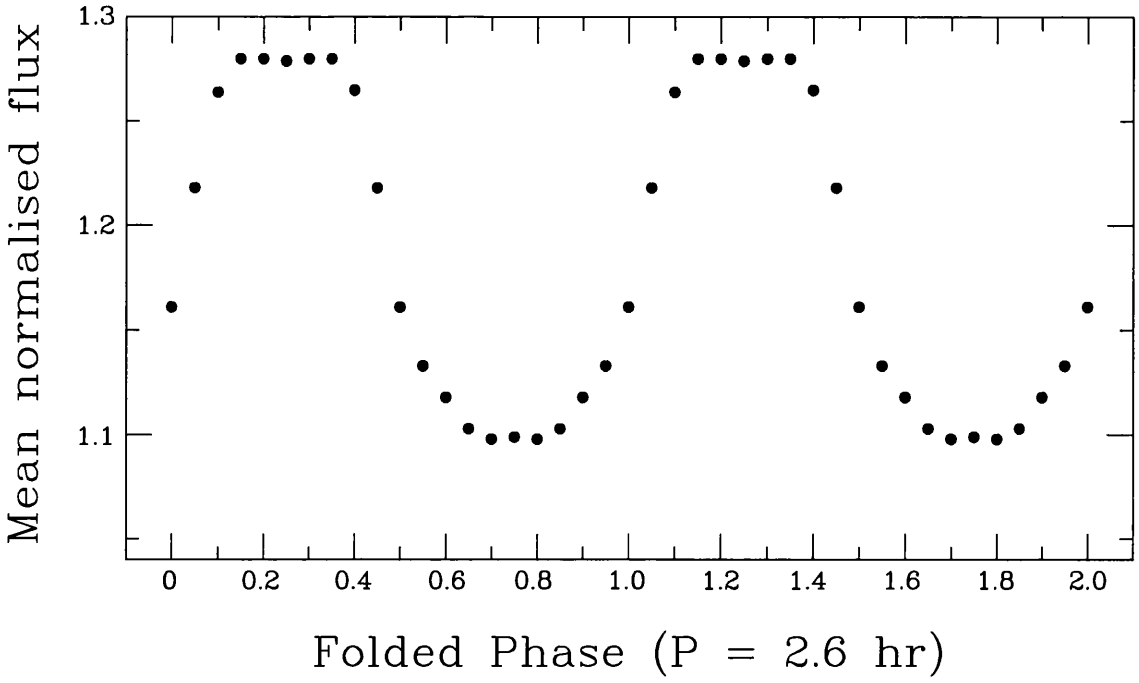

Figure 2.27: The mean flux measured between -500 and $0\,\mathrm{km\,s^{-1}}$ in the simulated Hβ profiles shown in Figure 2.26 (Section 2.5; also *c.f.* Figure 2.6).

the noise present in the observed data set) to the simulated data described above (and presented in Figure 2.26). The two maps are broadly similar, but the empirical model has not reproduced the enhancement in emission on the accretion disk (at $V_X \sim -300\,\mathrm{km\,s^{-1}}$, $V_Y \sim +300\,\mathrm{km\,s^{-1}}$).

It must be acknowledged that this interpretation also results in a somewhat contrived picture for the physical origin of the different line components. The basic notion is that the gas stream overflows the outer rim of the accretion disk and re-impacts somewhere on the inner disk. The inner bright spot – with high Keplerian velocities – might then produce the broad emission feature. The superimposed absorption would then be due to the portion of the stream that falls back on to the disk, prior to the re-impact, and is projected against the bright disk. Since the stream feeds the bright spot, this provides an absorption component that traces the velocity motion of the emission feature. A major unresolved issue in this simple demonstration, however, is the physical origin of the requisite net redshift of the absorption source. Some more physically based simulations using disk-overflow models are attempted in Section 2.7.2.

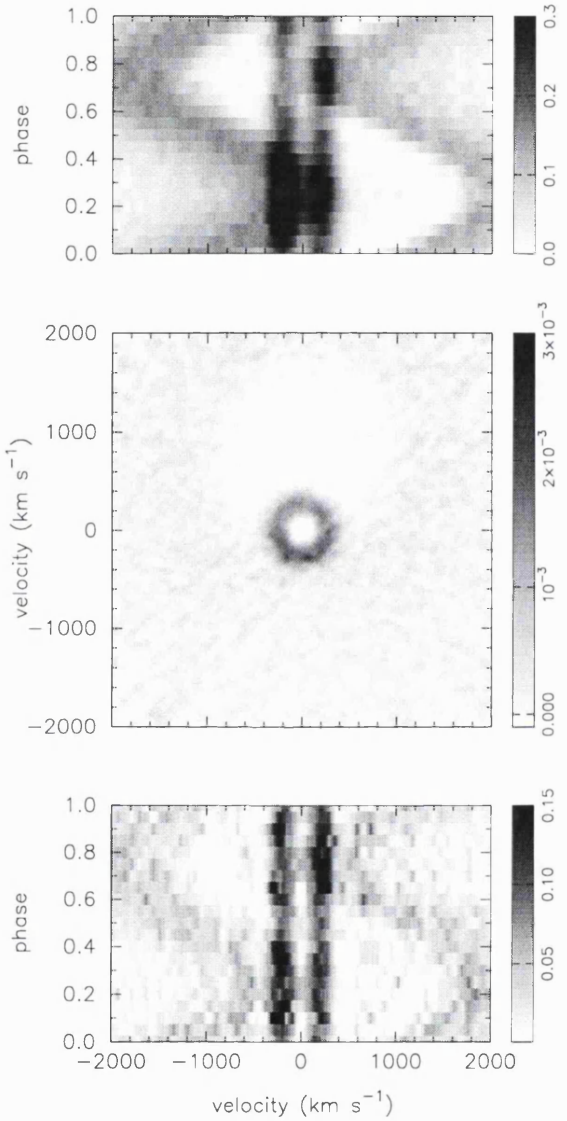

Figure 2.28: Doppler image of the simulated Hβ variations (Figure 2.26). The top panel shows the simulated data (with additional noise), the middle panel shows the Doppler image and the bottom panel the predicted data.

2.6 FOS data and the continuum properties

Previous UV low resolution *IUE* studies have indicated that the continuum flux of V795 Her is not substantially variable *i.e.* above approximately the 15 % level (*e.g.* Prinja, Rosen & Supelli 1991). In addition, Rosen *et al.* (1997) did not find any evidence for coherent modulations in the *HST* FOS continuum data. These optical IDS and FOS data of V795 Her provide some indication for variations in the continuum fluxes at approximately the 10 % level. The mean continuum flux over $\lambda\lambda 4720-4800$ Å is shown in Figure 2.29 for 20 phase bins. (This 'band' is line free, *e.g.* Figure 2.1, and it is covered in the IDS data and in the FOS second order data). There is a sharp drop of ~ 10 % in the continuum flux covering about 25 % of the cycle. The flux minimum is at $\phi_{2.6} \sim 0.7$ and is in phase with the decrease in the core flux of the Balmer lines (*e.g.* Figure 2.6). Ratios of integrated fluxes in broad wavelength bands placed at the blue and red regions of the FOS data do not provide any compelling indication of large (or modulated) colour changes in V795 Her.

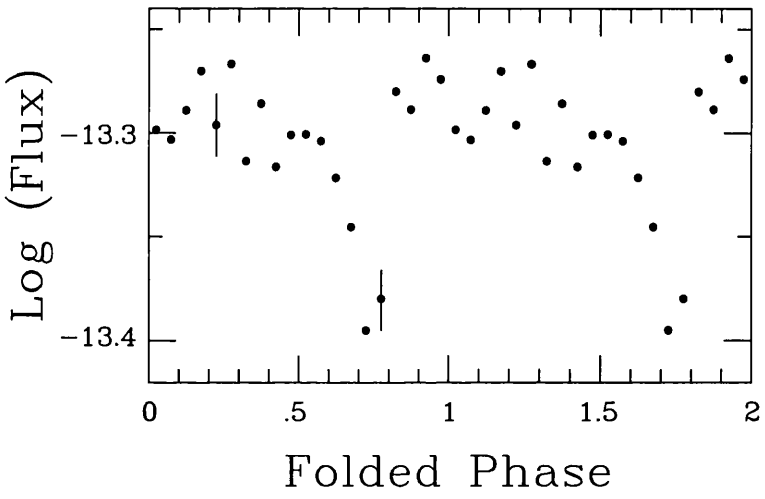

Figure 2.29: The mean flux in phase-binned data for the (line-free) band $\lambda\lambda 4720-4800$ Å is shown as a function of the 2.6 hr period.

The mean spectrum of V795 Her from ~ 1150 Å to 2μ is shown in Figure 2.30, where data is combined from *IUE* (Prinja, Drew & Rosen 1992), *HST* (Rosen *et al.* 1997), INT IDS and FOS (this study) and UKIRT CGS4 (obtained in 1994 by Rosen, private communication). Since a detectable 2200 Å feature due to interstellar reddening in not apparent (suggesting $E_{(B-V)} < 0.05$), no reddening corrections have been applied. The overall continuum distribution of V795 Her is remarkably well traced from UV to IR by a 15 000 K, $\log g = 3.0$ Kurucz LTE (local thermal equilibrium) model atmosphere (Figure 2.30). The model corresponds approximately, for example, to

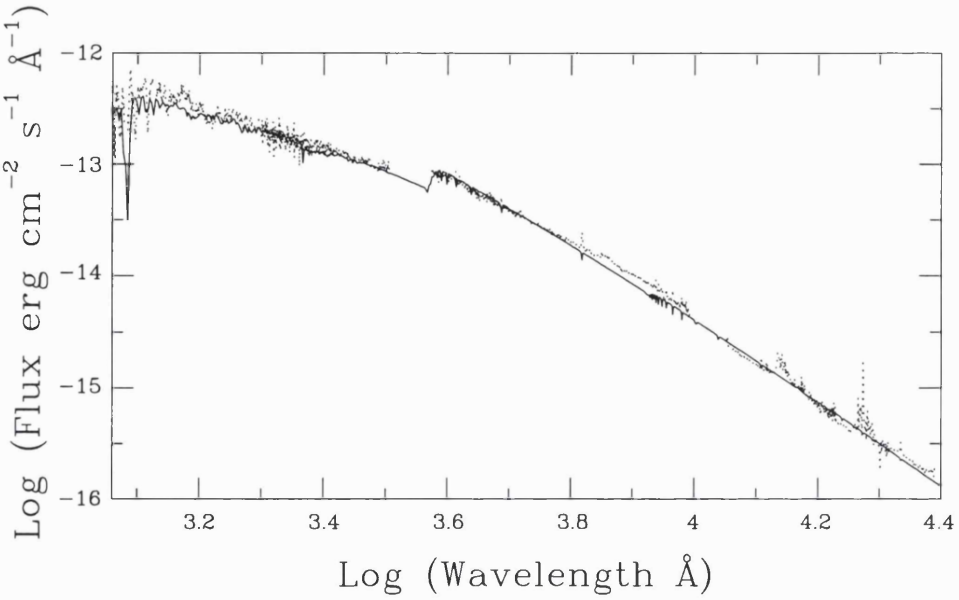

Figure 2.30: The UV, optical and IR spectrum of V795 Her is shown (dotted line; Section 2.6), and is compared with a Kurucz LTE model atmosphere for $T_{\rm eff} = 15\,000$ K and $\log g = 3.0$ (solid line; normalised at the visual magnitude).

a mid-B stellar spectral type.

A variable, strong Hα emission line is present in the FOS data, with FWHM $\sim 1250\,{\rm km\,s^{-1}}$, together with the presence of 'underlying' absorption (see also Section 2.3.2). Fluctuations are also seen in the He I λ7076 emission line. There are, however, no clear indications for TiO bands at for example λ7150 Å or λ7600 Å, which may have betrayed the presence of the M-dwarf secondary. It seems that the observed flux in the red optical region of V795 Her is dominated by the accretion disk emission sources.

2.7 Discussion

The rather complex nature of the optical (and UV; see Chapter 3) spectral behaviour of V795 Her must naturally have implications for any geometric and physical model of this system. Ultimately the precise classification of V795 Her must be consistent with the key observational constraints. The principal spectroscopic properties of V795 Her apparent in this optical data set are summarised below:

1. The overall strengths of the Balmer and He emission lines modulate on the mooted orbital period of V795 Her (~ 2.6 hr). However, the variations are *asymmetric* in that although the maximum observed flux occurs at $\phi_{2.6} = 0$, the minimum line flux corresponds to $\phi_{2.6} \sim 0.6 - 0.7$, with a much smaller decrease in strength at $\phi_{2.6} \sim 0.2 - 0.25$.

2. The extreme emission wings of the Balmer lines exhibit *very weak* phase modulated humps which are net blueshifted and redshifted, covering an observed central velocity range between 550 km s^{-1} and 1615 km s^{-1}. The 'wave' traced by this modulation may also be asymmetric with a considerably more gradual blueward progression between $\phi_{2.6} = 0 - 0.7$, compared to the redward motion between $\phi_{2.6} = 0.75 - 1.0$. The overall (weak) double-humped behaviour is simulated in terms of a single broad emission source tracing out a high-velocity s-wave, plus superimposed redshifted absorption.

3. The inner core of the Balmer emission lines (*i.e.* between $\sim \pm 500$ km s^{-1} dominates the characteristics outlined in item 1 above. In contrast to the interpretation of Casares *et al.* (1996), a distinct inner s-wave is not apparent in the time series of the Balmer lines. The blue and red components of the observed double-component structure are instead relatively stable in velocity, with substantial changes in strength and width.

4. The Balmer lines are also affected by an absorption component, which may extend out to approximately $\pm$ 1000 km s^{-1}. This feature is stronger during the first half of the cycle when it appears redwards.

5. A small (at the ~ 10 % level) variation is apparent in the optical continuum flux of V795 Her. The changes are restricted to less than ~ 25 % of the orbital cycle, with a minimum in continuum flux corresponding to the phase of minimum emission line strength. The overall continuum distribution of V795 Her, from UV to IR, is well reproduced by a Kurucz LTE model atmosphere with $T_{\rm eff} = 15\,000$ K and $\log g = 3.0$.

In the following sections two different scenarios for V795 Her are discussed: (i) channeled accretion columns in a magnetic WD which is phased-locked with the accretion disk (see *e.g.* Casares *et al.* 1996), and (ii) a disk-overflowing gas stream based on the SW Sex models of Hellier & Robinson (1994), which is favoured by this study as a more realistic and compatible description of the line structure and behaviour of V795 Her.

2.7.1 A magnetic model for V795 Her?

An ongoing debate has been taking place concerning the exact nature of V795 Her. Although it displays the credentials of a nova-like system, the discovery of distinct photometric and spectroscopic periods (Shafter *et al.* 1990) led to it being proposed as a possible intermediate polar candidate, *i.e.* a binary in which the accreting compact star possesses a strong magnetic field ($B \sim 10^6 - 10^7$ G) and rotates asynchronously with respect to the companion star. However, the lack of a strong, coherent X-ray modulation in V795 Her (Rosen *et al.* 1995) and a catalogue of other observational properties led these authors to conclude that a magnetic interpretation was inappropriate. Nevertheless, the recent study of the optical spectral lines motivated Casares *et al.* (1996) to resurrect the idea of a magnetized accretor. In their model, they go beyond conventional magnetic scenarios and suggest that V795 Her might in fact be a system in which the WD and companion star are phase-locked, as in the strongly magnetic AM Her (polar) binaries, but in which a partial accretion disk persists. They argue that the sympathetically phased blueshifted and redshifted high velocity s-waves that they observe (see also Haswell *et al.* 1994 and Section 2.3.2) could arise in the magnetically entrained plasma that is falling along field lines onto the WD. The model assigns the two components to the flows above and beneath the binary plane (but on the same field lines) so that their mean motions are opposed, thus producing the blue and redshifted offsets. Given the remarkable hybrid nature of this picture and the archive of observational information that exists for this star, the model of Casares *et al.* (1996) is examined here, both in the context of the parameters that could lead to such phase-locking, and in terms of the constraints that can be imposed by the observations.

The first consideration is how such a phase-locked geometry could arise. The requirement for phase-locking in the Casares *et al.* (1996) model comes about because only one radial velocity variation is observed in V795 Her, *i.e.* the 2.6 hr period. There is no convincing evidence for an asynchronous rotator. The magnetic field in this 'polar-with-a-disk' binary has the effect of truncating the circulation and funnelling material along the field. The very presence of a disk or disk-like structure means that there is an accretion torque acting on the WD. This can be expressed as

$$G_{acc} = \dot{M}(GM_{WD}R_A)^{\frac{1}{2}} \tag{2.3}$$

where $\dot{M}$ is the accretion rate, M_{WD} is the WD mass, G is the gravitational constant and R_A is the Alfvén radius which, to first order, defines the inner edge of the accretion disk. To maintain synchronicity (*i.e.* phase-locking), requires $G_{lock} \geq G_{acc}$ where G_{lock} is the locking torque. The

locking torque presumably involves the interaction of the WD's magnetic field with either an intrinsic or an induced field on the companion star. The most likely interaction is a dipole-dipole (d-d) torque (*e.g.* King, Frank & Whitehurst 1990; hereafter KFW) which leads to

$$G_{lock} = \frac{\mu_1 \mu_2}{a^3} g_1(\theta_1, \theta_2) \tag{2.4}$$

where μ_1 and μ_2 are the magnetic moments of the WD and companion star respectively, a is the binary separation and $g_1(\theta_1, \theta_2) = 3 \sin\theta_1 \cos\theta_2 - \sin(\theta_1 - \theta_2)$ is a geometric factor which depends on the azimuthal orientations of the dipole moments with respect to the line of centres for the WD (θ_1) and the companion star (θ_2) respectively. It should be noted that the torque is weakened by a factor $\sim (R_{WD}/a) \lesssim 10^{-2}$ if quadrupole or higher multipoles are invoked. KFW demonstrate that $g_1(\theta_1, \theta_2) \leq 2$ for all values of the arguments. They also argue that if rotational braking of the companion plays a role and/or the geometry is to remain stable, $g_1(\theta_1, \theta_2)$ is probably $\lesssim 0.3$. For torque balance, Equations 2.3 and 2.4 require that

$$\frac{\mu_1 \mu_2}{a^3} g_1 = \dot{M} (G M_{WD} R_A)^{\frac{1}{2}} \tag{2.5}$$

The accretion rate can be estimated from the system luminosity. The integrated continuum flux between 1200 Å and 2 μ (Figure 2.30) is 6.7 x 10^{-10} ergs s^{-1} cm^{-2} which converts to a luminosity of 7.6 x 10^{32} D_{100}^2 ergs s^{-1} where D_{100} is the distance in units of 100 pc. Assuming most of this (unmodulated) luminosity is generated in a disk, it should be less than or comparable to the energy available for radiation at the WD's surface, which is presumably hidden from the observer since a modulated X-ray signal is not seen. In other words, the total system luminosity is at least twice that produced in the disk. Since $G M_{WD} \dot{M} / R_{WD} = L$, this implies (for $M_{WD} = 0.8\, M_\odot$ and $R_{WD} = 7$ x 10^8 cm) that $\dot{M} \gtrsim 10^{16}\, D_{100}^2$ g s^{-1}. This estimate is very much a lower limit since the measured flux excludes a substantial fraction of the disk emission that arises in the EUV. Thus with all factors considered, the total accretion rate is probably closer to 10^{17} g s^{-1}.

Assuming a WD mass of 0.8 $M_\odot$ and a modest accretion rate of 10^{16} g s^{-1}, the smallest value for the right-hand side (RHS) of Equation 2.5 (~ 4.6 x 10^{33}) occurs for the smallest adopted Alfvén radius, which is taken to be 2 x 10^9 cm ($\sim 2\, R_{WD}$ above the stellar surface). However, for a given accretion rate, R_A is dictated by μ_1 (*e.g.* Equation 3b of Hameury, King & Lasota 1986), and for the chosen values, this implies that $\mu_1 \propto R_A^{7/4} \dot{M}^{1/2} \sim 10^{31}$ G cm^3. Taking an exceptionally large value of $\mu_2 \sim 10^{34}$ G cm^3 (see KFW and references therein), the maximum possible value of $g_1 = 2$ and a binary separation of 6.6 x 10^{10} cm, the LHS of Equation 2.5 is 7.7 x 10^{32} so the accretion torque substantially exceeds the locking counter-torque and synchronism is not possible.

Allowing R_A to be as large as the circularization radius, $R_c \sim 1.2 \times 10^{10}$ cm (formally, if $R_A > R_c$ a disk will not form), requires $\mu_1 \sim 2.2 \times 10^{32}$ G cm^3, and the LHS of Equation 2.5 ($\propto \mu_1$) then just exceeds the RHS ($\propto \mu_1^{2/7}$ because $R_A \propto \mu_1^{4/7}$) so that locking becomes possible in principle. Nevertheless, several factors, particularly in combination, are likely to ensure that in fact the accretion torque always exceeds the synchronizing torque. For example, an accretion rate above 10^{16} g s^{-1}, $g_1 < 2$, as is expected, and/or $\mu_2 < 10^{34}$ G cm^3, will all effectively act to enable the accretion torque to overwhelm the locking torque. *This examination therefore concludes that it is essentially impossible for the WD's rotation to be locked to the binary motion in V795 Her.*

One caveat to the above argument concerns the expectation that once the Alfvén radius exceeds the circularization radius, disk formation is prevented. This might be circumvented in principle if a disk were able to persist over evolutionary time scales. However, disks are likely to be relatively transient components in any CV, disappearing during periods of low mass transfer, so one would expect there to be a point when, with $R_A > R_C$, it could no longer reform following a low state. This situation is believed to be illustrated in some established IP binaries such as RXJ 1712 – 24 (Buckley *et al.* 1995) where a disk is believed to be absent and accreting material interacts directly with the magnetosphere. Thus the expectation is that this basic argument against synchronicity in V795 Her is valid.

This theoretical argument is compounded by several observational and technical objections. An apparently important aspect of the Casares *et al.* (1996) model is that accretion proceeds towards both poles along *the same set* of field lines; accretion onto the upper pole from one side of the disk and onto the lower pole from the opposite side of the disk would introduce anti-phased s-wave behaviour, contrary to observation. However, such a picture probably requires material accreting towards the more distant pole to overcome a substantial potential barrier as it is initially forced outward by the field geometry. This problem might be avoided if the dipole moment was nearly parallel to the spin axis, but such close alignment would not then permit the large velocity amplitude of the s-wave that is observed. Alternatively, one might be able to invoke a distorted field, perhaps involving higher multipoles, to permit ready access to both poles. However two further, and probably more serious, concerns for any IP interpretation are the weakness of the X-ray signal and the lack of a clear X-ray modulation, although it is acknowledged that only rather modest constraints are formally imposed on any pulsed component by current X-ray data (Rosen *et al.* 1995).

2.7.2 A disk-overflow model?

The empirical interpretation of the optical line profile changes in V795 Her presented in Section 2.5 relates then to a qualitative physical interpretation which invokes a disk-overflowing gas stream. V795 Her has many similarities to SW Sex stars, a subclass of nova-likes delineated by Thorstensen *et al.* (1991). Although it does not meet two of Thorstensen *et al.*'s characteristics, that SW Sex stars are eclipsing and have orbital periods of 3 – 4 hrs, these are likely to be selection effects. The more important characteristics are high velocity *s*-waves dominating the line wings and peculiar absorption features. The absorption features vary in velocity and depth over the orbital cycle, being most prominent at $\phi = 0.5$ (where inferior conjunction of the primary is at $\phi = 1.0$). Hellier & Robinson (1994) and Hellier (1997) have proposed a model in which SW Sex stars are explained by a disk-overflow scenario. The general picture is of an accreting gas stream which overflows the outer rim of the disk, producing absorption when projected against the bright accretion disk. The stream then re-impacts in the inner disk regions, resulting in a broad emission line and a high velocity *s*-wave. The combination of disk emission plus stream absorption results in the observed double-humps in the wings of the Balmer lines. The stationary inner core double-peaks observed in the case of V795 Her may then arise independently from a ring of planar material in the outer disk.

As noted by Casares *et al.* (1996), V795 Her's emission line behaviour resembles that of the SW Sex stars, showing both the high velocity *s*-waves and the complex absorption features. There are some differences though. Principally, the absorption is not confined to the line core, as is common in SW Sex stars, but also extends into the line wings, at the same phase as the high velocity *s*-wave. Casares *et al.* (1996) therefore interpreted the high velocity changes as two *s*-waves, separated by a shift in γ-velocity (*e.g.* their Figure 12). However, since the absorption is often below the local continuum, the data cannot be explained by two *s*-waves alone; extra absorption is needed between them. Since single high velocity *s*-waves are the main characteristic of SW Sex stars, an alternative is to regard the emission as a single broad component, cut into by a narrower absorption feature, creating a double-humped profile (see *e.g.* the demonstration in Section 2.5).

The SW Sex model of Hellier & Robinson (1994) had emission only from the point where the stream re-impacts the disk, as required to reproduce the emission lines of PX And. Since the absorption in V795 Her has the same phase and velocity as the high velocity emission, it must also, in this model, come from the re-impact point. This requires that this region in V795 Her produces

a self-absorbed emission profile with central absorption, compared to pure emission in the other SW Sex stars. No explanation for these differences is offered here, except to note that V795 Her, not being eclipsing, is at a lower inclination.

In the disk-overflow model, the stream also produces absorption features while flowing between the site of its initial impact with the disk and its re-impact site. The velocity and phasing of this material is correct to reproduce the characteristic SW Sex absorption, which starts redward of the line center at $\phi \sim 0.1$ and progresses blueward, becoming deepest at ϕ - 0.5. Such features are obvious in V795 Her (*e.g.* Figure 2.5); note, however, that the phasing in V795 Her is not yet established, and the data would be closer to SW Sex-type behaviour if $\sim 0.2-0.3$ in phase was subtracted from Figure 2.5 and, for example, Figure 2.7; see also Casares *et al.* (1996). A problem with this model however, both in V795 Her and in SW Sex stars, is that it predicts comparable absorption moving back redwards between $\phi = 0.6-1.0$ (Hellier & Robinson 1994). This is either not seen, or is at best much weaker. This problem has so far not been resolved, although Hellier & Robinson (1994) suggest that disk flaring could provide an answer, *i.e.* the visibility of the stream depends on whether it is on the near or the far side of the disk.

To illustrate the similarities of V795 Her with SW Sex stars, Hellier kindly provided a simulation of the line profiles from a stream overflowing the disk, using the modelling code described in Hellier & Robinson (1994) and Hellier (1997). The major difference with the previous modelling is the inclusion of absorption along the length of the stream from the initial disk impact to its re-impact, whereas previous simulations had absorption only from the first section of the stream. The re-impact point also produces emission. This simulation is shown in Figure 2.31. It is phased with inferior conjunction of the secondary at $\phi = 1.0$; this is not the same as for the data, since the absolute phasing is not known for V795 Her (*i.e.* the data can be shifted arbitrarily). The simulation gives a reasonable schematic reproduction of the high velocity emission, the absorption in the line wings, and the absorption running from the red side of the core at $\phi = 0$ to the blue side at $\phi = 0.5$. However, it has not reproduced the reduction in absorption at $\phi = 0.5-1.0$. As a whole, the model takes no account of changes in intensity of the components round the orbit, so these are not well reproduced.

To summarise, the emission lines in V795 Her behave similarly to those in SW Sex stars, suggesting a similarity in their physical origin. The disk-overflow model proposed by Hellier & Robinson (1994) can account for a number of the observed dynamical features of V795 Her. However,

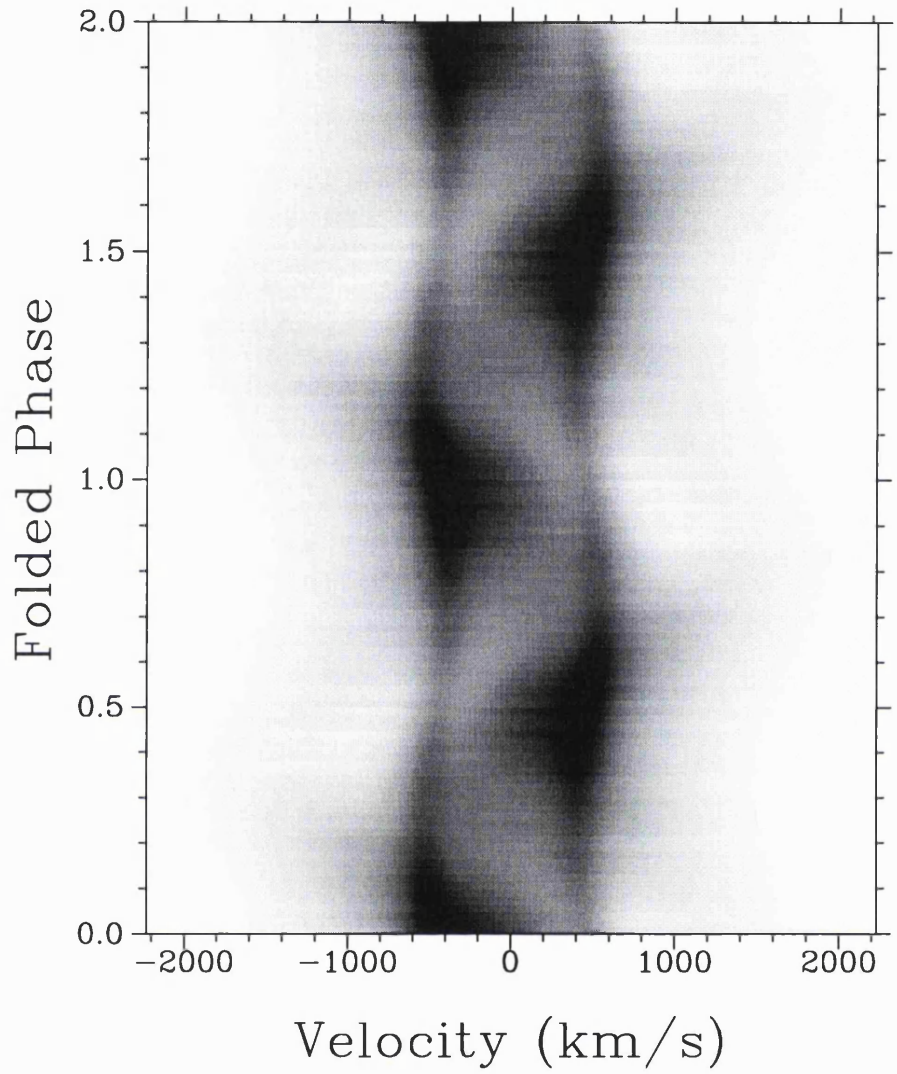

Figure 2.31: A simulation of the V795 Her optical behaviour using modified versions of the disk-overflow models of Hellier & Robinson (1994) and Hellier (1997). High velocity s-wave emission is reproduced (darker shades), plus phased self-absorption (lighter shades). The model is not sensitive to (reasonable) adopted values of the orbital parameters for V795 Her. The high velocity emission comes from the stream re-impact, assuming that the velocity is mid-way between that of the stream and the local disc. The emission is represented by a broad Gaussian with a FWHM equal to half the local velocity. The absorption, arising from the full length of the stream, has a narrower width (FWHM = 25 % of the local velocity) to give a double-humped profile.

several discrepancies remain, which need to be investigated by a more physically realistic model of disk-overflow.

Chapter 3

A comparison of the UV *HST* and optical INT properties of V795 Herculis

3.1 Introduction

The optical INT spectra of V795 Her described in Chapter 2 are accompanied by contemporaneous *HST* UV data secured during 1994 June. The multi-wavelength spectroscopic properties of V795 Her afforded by these unique data sets are compared and contrasted in this chapter in order to provide further physical constraints on the system.

Until the UV *HST* data set used in this chapter was obtained in 1994 June, V795 Her had previously only been studied at UV wavelengths using the *IUE* satellite. The first systematic UV spectroscopic study of V795 Her was presented by Prinja, Rosen & Supelli (1991) and is based on 11 low resolution *IUE* spectra taken on 1989 October 12 – 13, plus 3 observations from 1984. The presence of a moderate wind is indicated by the broad, asymmetric blueshifted absorption trough seen in the C IV λ1550 resonance line doublet. They noted extensive variability in this (partially) wind-formed feature on timescales as short as a few hours but did not find any simple correlation between these changes and the orbital period. A follow-up study by Prinja, Drew and Rosen (1992) combined these spectra with 16 new observations from 1990 August. Again, extensive variability is observed in the C IV $\lambda\lambda$1550 absorption, and is also seen in the Si IV $\lambda\lambda$1400 line. The line profile changes do not appear to be related to the 2.60 hr spectroscopic period but their time series analysis suggests the presence of a 4.86 hr periodic modulation that had never previously been

reported. To investigate this, a further 23 observations were secured in 1992 August by Prinja & Rosen (1993). A 4.86 hr modulation was again found, which they found to be consistent with a coherent period over the 3 year time span of the data. Patterson & Skillman (1994) contend that this coherency should not be accepted unquestioningly as the cycle count of such a sparse data set is very unreliable.

It is clear from previous studies that there is strong evidence for an outflowing wind in V795 Her: in particular, the morphology of the C IV line at certain phases is that of a P Cygni-type profile which is typically associated with mass loss (Section 1.2.1). Despite concerns expressed above about the coherency of the signal, there have certainly been variations in the C IV line profile on a 4.86 hr timescale. At the same time, no detection of the then accepted 2.60 hr orbital period has been made. Rosen *et al.* (1997) obtained the first UV observations of V795 Her to be made using the *HST*, and it is this data set which is compared to the optical spectroscopy that was obtained in the same week in 1994 June and described in Chapter 2 . *This is the first time that it has been possible to compare directly UV and optical spectroscopy of V795 Her and be confident that the system was in the same state when both sets of observations were made.* A key issue is to determine whether the changes in the UV resonance lines are entirely due to wind changes, or whether additional non-wind emission sources (*e.g.* the accretion disk) are also variable and thus 'contaminating' the UV lines. It is hoped that these unique data sets may resolve this issue. Section 3.2 describes the *HST* data set, while Section 3.3 summarises the main UV properties of V795 Her. Section 3.4 discusses two empirical interpretations of the data and Section 3.5 goes on to compare in detail the *HST* data set and the UV properties with the quasi-simultaneous optical spectroscopy of Chapter 2. The implications of this comparison are discussed in Section 3.6.

3.2 The *HST* data set

UV *HST* data of V795 Her was obtained during three closely-separated runs in 1994 June (Rosen *et al.* 1997). This data set is quasi-simultaneous with the optical spectroscopy described in Chapter 2. A shortened log of the observations is given in Table B.3, and Table 3.1 indicates the degree of simultaneity between the data sets (also see Section 3.5). Each of the three closely spaced runs spanned approximately 8.5 hr, with the on-source exposure time totalling 8.1 hr. To achieve an unprecedented time resolution of this source the data were recorded using the blue digicon of the Faint Object Spectrograph (FOS) operated in RAPID mode. This mode permitted a total of 1458

spectra to be collected, with repetitive 20 s exposures and a minimal (< 1 s) dead time between integrations. The 0.9″ aperture and the G130H grating were used to obtain a wavelength coverage of $\lambda\lambda 1150 - 1605$ Å at a resolution of ~ 1 Å.

For much of the analysis the *HST* spectra were folded into 20 phase bins using the orbital ephemeris of Shafter *et al.* (1990) that was applied when phasing the INT data in Chapter 2 (Section 2.3.2):

$$T_0 = HJD - 2\,447\,329.824 + 0.1082468N \tag{3.1}$$

The maximum redward and blueward radial velocity motion of the optical emission lines corresponds to quadratures at phase 0.25 and 0.75 respectively, and the estimate of the accumulated phase uncertainty for observations taken in 1994 June is ± 0.06 (1 σ). Typically about 70 individual spectra were added into each bin. Each phase bin was 0.05 phase units wide, with the first bin centred at phase 0.025.

Table 3.1: Overlap of the UV *HST* data and optical INT data for V795 Her. The phase was calculated with the ephemeris used in Chapter 2 (see Equation 3.1).

HJD − 2 449 000	*HST* file number	INT file number	phase
525.3678	739		0.760
525.3863 – 525.4074		153 – 158	0.930 – 0.125
525.4111 – 525.4114	740 – 741		0.160 – 0.162
525.4115		159	0.163
525.4116 – 525.4192	742 – 776		0.164 – 0.234
525.4194		161	0.236
525.4194 – 525.4234	777 – 795		0.236 – 0.273
525.4235		162	0.274
525.4237 – 525.4268	796 – 810		0.275 – 0.304
525.4276 – 525.4605		163 – 171	0.312 – 0.616
525.4756 – 525.4868	811 – 861		0.756 – 0.859
525.4882		176	0.872
525.4901 – 525.4922	862 – 872		0.889 – 0.909

continued on next page

continued from previous page

HJD − 2 449 000	*HST* file number	INT file number	phase
525.4923		177	0.910
525.4925 – 525.4963	873 – 890		0.911 – 0.946
525.4964 – 525.5314		178 – 187	0.947 – 0.271
525.5422 – 525.5424	892 – 893		0.370 – 0.373
525.5425		190	0.373
525.5426 – 525.5464	894 – 911		0.375 – 0.410
525.5466		191	0.411
525.5467 – 525.5507	912 – 930		0.412 – 0.449
525.5507		192	0.449
525.5509 – 525.5547	931 – 948		0.451 – 0.486
525.5548		193	0.487
525.5549 – 525.5589	949 – 967		0.488 – 0.525
525.5589		194	0.525
525.5591 – 525.5600	968 – 972		0.527 – 0.535
525.5994		201	0.899
527.3740	1376		0.293
527.3831 – 527.4161		511 – 519	0.377 – 0.682
527.4188 – 527.4201	1378 – 1384		0.706 – 0.719
527.4202		520	0.720
527.4203 – 527.4312	1385 – 1434		0.721 – 0.822
527.4314		522	0.823
527.4315 – 527.4355	1435 – 1453		0.824 – 0.861
527.4355		523	0.861
527.4357 – 527.4366	1454 – 1458		0.863 – 0.871
527.4397		524	0.900

3.3 The UV resonance line properties

A study of the *HST* data set is presented by Rosen *et al.* (1997). The main UV characteristics of V795 Her are described in this section. The most prominent lines displayed in the mean spectrum (Figure 3.1) are N V $\lambda\lambda$1240, Si IV $\lambda\lambda$1400 and C IV $\lambda\lambda$1550. Also present are the C III λ1176 line, the Si II/Si III/O I blend around $\lambda\lambda$1300 Å and the C II λ1335 line. It had been suspected previously that the spectrum is affected by substantial line blanketing and this higher resolution data set provides conclusive evidence for this (*e.g.* immediately redward of the C IV line). The C IV doublet ($\lambda\lambda$1548.19, 1550.76, v_{sep} = 498 km s^{-1}) is not resolved due to the intrinsic line broadening being greater than the separation but the Si IV doublet components are separated ($\lambda\lambda$1393.76, 1402.77, v_{sep} = 1939 km s^{-1}).

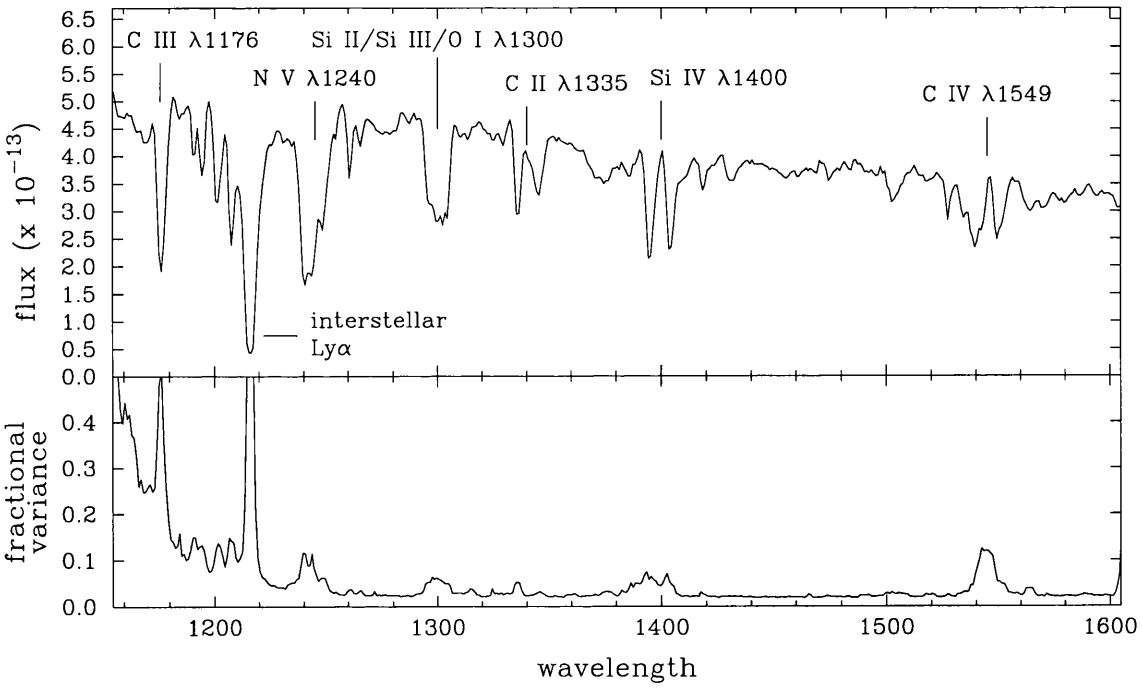

Figure 3.1: Mean *HST* spectrum of V795 Her (upper panel) and the fractional variance (lower panel).

The bottom panel of Figure 3.1 shows the fractional variance. The statistic plotted is σ^2_λ, where

$$\sigma^2_\lambda = \frac{1}{(N-1)[\bar{f}(\lambda)]^2} \sum_{i=1}^{N} [f_i(\lambda) - \bar{f}(\lambda)]^2 \tag{3.2}$$

as used and described in Section 2.3.1 (Equation 2.1). The overall variability of the spectrum is dominated by the strong resonance lines. (The increase in the statistic below 1200 Å is caused by contributions from statistical noise which are introduced by the rapid decline in the sensitivity of

the instrument).

Rosen *et al.* carried out a Fourier analysis of the data set in order to examine the photometric behaviour of both the continuum and the absorption lines. For the first time in a UV data set of V795 Her, a clear modulation in the line fluxes is seen on the 2.60 hr (orbital) period. They find no evidence of variations occurring on the 4.86 hr period reported previously in *IUE* studies (Prinja, Drew & Rosen 1992; Prinja & Rosen 1993). The continuum is not seen to vary on either the 2.60 hr period or the 2.80 hr optical photometric period (Mironov, Moshkalev & Sugarov 1983). A montage of the phase-binned spectra is shown in Figure 3.2.

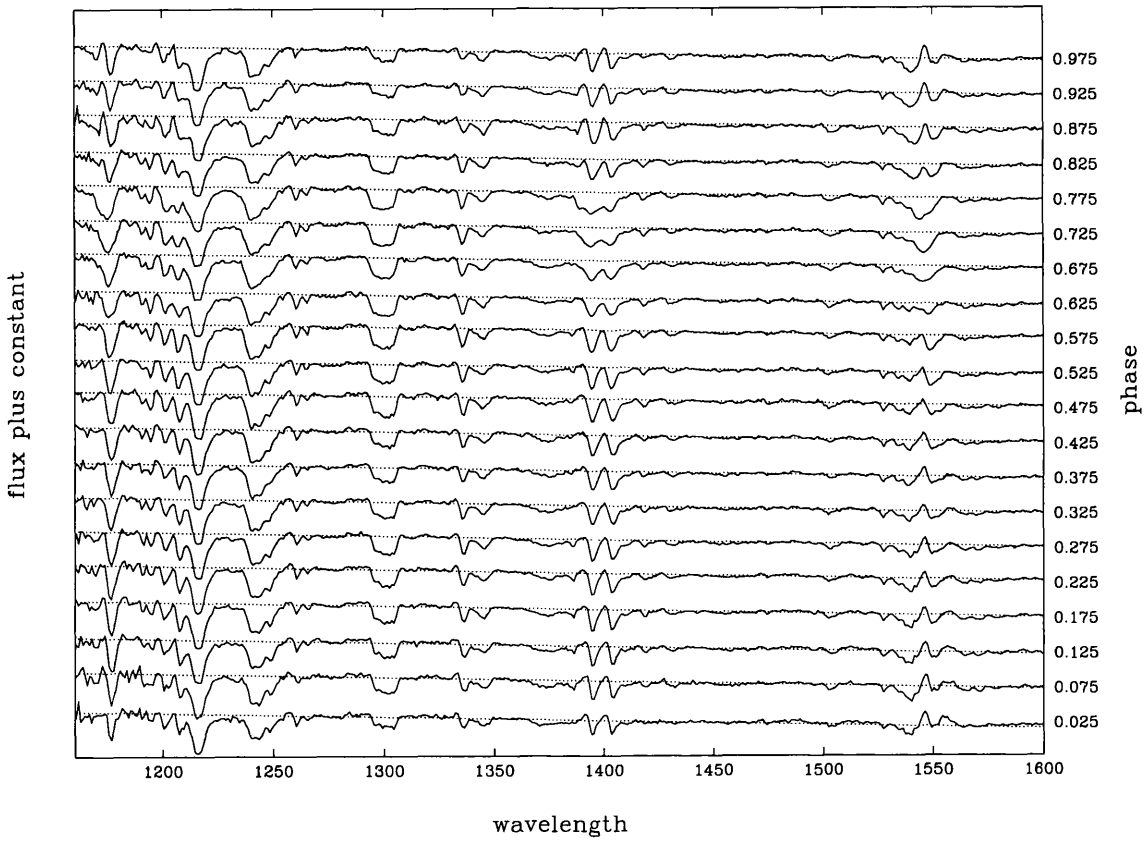

Figure 3.2: Montage of the phase-binned V795 Her *HST* spectra. The dotted line provides a common reference level to aid the eye.

3.3.1 The 4.86 hr period and the *IUE* spectra

The non-detection of a 4.86 hr signal in this *HST* data set brings into question its previous detection in *IUE* studies. Prinja & Rosen (1993) discount the possibility that the 4.86 hr period may be due to a sampling problem because it was detected in two independent data sets that were sampled in

different ways. Patterson & Skillman (1994) discuss the validity of describing the 4.86 hr period as 'coherent'. The two independent *IUE* data sets were taken $\sim$ 1 year apart and each covers $\sim$ 5 days. This means that the data set is very sparse and it is possible that the detection of the 4.86 hr periodicity in both data sets is due to the chance sampling of a non-coherent signal.

Figure 3.3 shows the *HST* data set folded into 20 phase bins on the 4.86 hr 'period'. The total integrated flux below the Si IV line (between $\lambda\lambda 1387 - 1407$ Å) was measured in each bin within DIPSO. The *HST* data do not show a clear modulation on the 4.86 hr period (*c.f.* Figure 3 of Prinja & Rosen 1993).

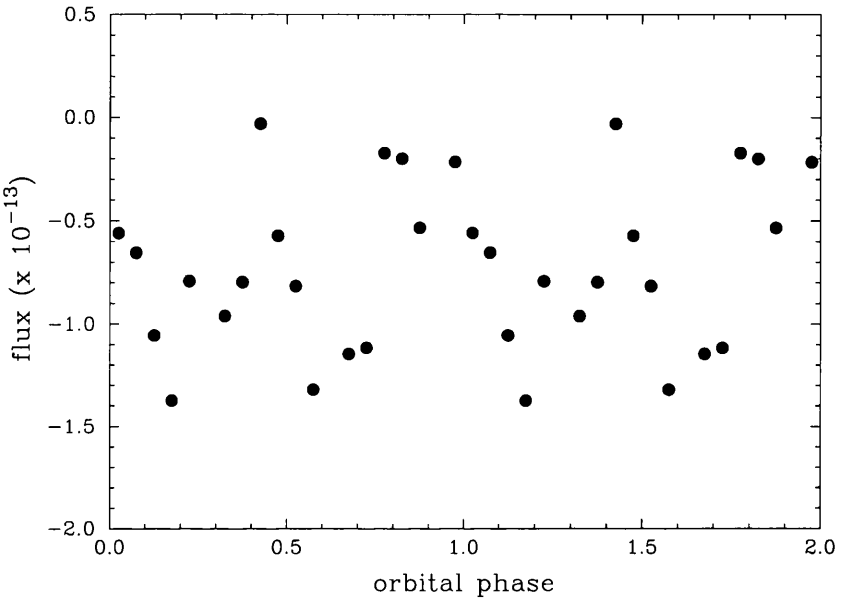

Figure 3.3: The total integrated flux below the Si IV line folded on the 4.86 hr 'period'.

The sampling of the earlier *IUE* studies should have been sufficient to detect a 2.60 hr signal if it were present at the level currently seen in the *HST* data set. A plausible explanation is that when the *HST* observations were made, V795 Her was in a somewhat different state from the state it was in when observed with *IUE*. This hypothesised change of state is backed up by other observations from the two epochs.

Earlier optical studies of V795 Her detected a 2.80 hr photometric period (Mironov, Moshkalev & Sugarov 1983; Rosen *et al.* 1989; Shafter *et al.* 1990; Zhang *et al.* 1991). Patterson & Skillman's (1994) study finds that this signal has essentially disappeared, and the optical INT data set examined in Chapter 2 also shows no sign of a 2.80 hr periodicity. Furthermore, Patterson & Skillman report

a possible brightening of V795 Her coincident with the disappearance of the 2.80 hr period. The mean brightness in 1983 (Mironov, Moshkalev & Sugarov 1983) was $\langle V \rangle = 13.22$ while the mean brightness from 1992 to 1994 was $\langle V \rangle = 12.90$. The typical flux level in the UV continuum has also increased: the level in the *IUE* studies is approximately 25% lower than the level in this *HST* data set (Rosen *et al.* 1997). Changes in the UV line profile shapes have also occurred between the epochs of the *IUE* and *HST* observations (Rosen *et al.* 1997). The relative strength of the C IV $\lambda\lambda$1550 emission peak is much greater in the *IUE* data set.

3.3.2 Line profile structure

The mean C III, Si IV and C IV line profiles are shown in velocity space in Figure 3.4. The velocity scales are with respect to the rest velocity of the weighted mean of the multi-component C III line (1175.66Å), with respect to the blueward component of the Si IV doublet (1393.76 Å), and with respect to the rest velocity of the weighted C IV doublet (1549.05 Å). This velocity scale convention is used throughout this chapter. (The C III λ1176 line is made up of a 6 component multiplet, but may essentially be treated as a singlet here). Figure 3.4 also shows the deepest absorption profile and the maximum emission profile for each line to give a feel for the degree of variability within the data set.

The C IV line extends from about -3500 to $+1000$ km s^{-1}. The deepest absorption profile ($\phi_{2.6} = 0.775$) clearly shows an asymmetric, blueward absorption trough which has its minimum near -1000 km s^{-1}. This absorption is filled in by an apparently narrow emission component at other phases, that is situated near -600 km s^{-1}. Two shallow Si II absorption features are superposed on the blue wing of the C IV line profile (Si II λ1527 at -4270 km s^{-1} and Si II λ1533 at -3110 km s^{-1}).

The C III line does not show any evidence for an extended blueward absorption wing between -3500 and -2000 km s^{-1}, although an absorption component is seen which, in the mean profile, is roughly centred on the rest wavelength. The absorption is much broader in the deepest absorption profile ($\phi_{2.6} = 0.775$) and extends from -1500 km s^{-1} to $+1200$ km s^{-1} with the minimum occurring at ~ -200 km s^{-1}. For much of the orbital cycle, the blueward wing appears to be filled in by an emission feature. The Si IV doublet is well separated and both components essentially behave like the C III line.

It appears that these three lines share a common absorption component. Figure 3.5 shows the

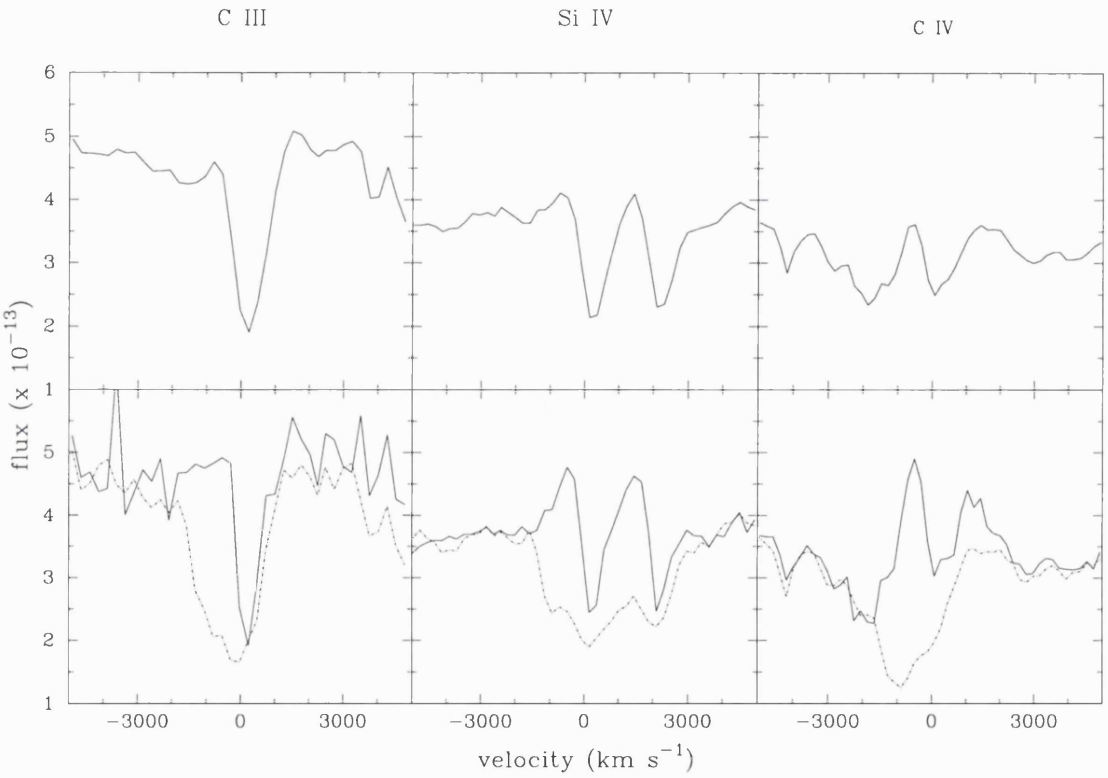

Figure 3.4: The mean spectra (upper panel), deepest absorption profiles (dotted line, lower panel) and maximum emission profiles (solid line, lower panel) of C III, Si IV and C IV in velocity space. The deepest absorption profiles correspond to $\phi_{2.6} = 0.775$ and the maximum emission profiles to $\phi_{2.6} = 0.025$. The velocity scales are with respect to the rest velocity of the C III line (1175.66 Å), with respect to the blueward component of the Si IV doublet (1393.76 Å), and with respect to the rest velocity of the weighted C IV doublet (1549.05 Å).

C III, Si IV and C IV profiles at $\phi_{2.6} = 0.775$. At this phase the emission noted on the blue wing is at its weakest. The absorption component is clearest in the C III profile where it can be seen to extend from -1500 km s^{-1} to $+1200$ km s^{-1}. It is also quite obvious in each of the doublet components of the Si IV line, but in the C IV line profile it is harder to see as this absorption is blended with the asymmetric blueward absorption trough. This will also contaminate the position of the minimum of the C IV profile, pulling it further bluewards than for C III and Si IV.

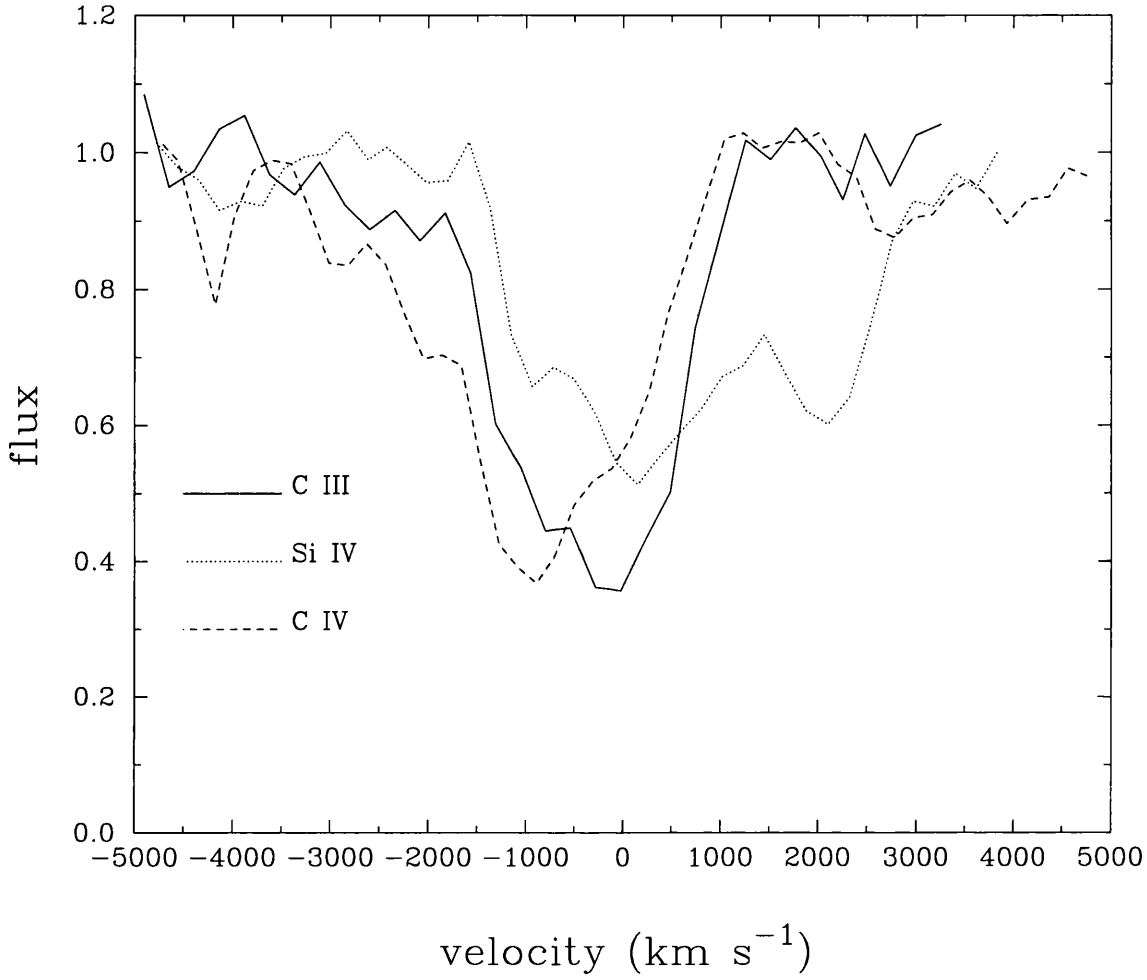

Figure 3.5: The common absorption component in the C III (solid line), Si IV (dotted line) and C IV (dashed line) line profiles (at $\phi_{2.6} = 0.775$). The profiles have been normalised to the local continuum level and the velocity scales are with respect to the rest velocity of the C III line (1175.66 Å), with respect to the blueward component of the Si IV doublet (1393.76 Å), and with respect to the rest velocity of the weighted C IV doublet (1549.05 Å).

The fractional variance plot (Figure 3.1) shows that there are stronger changes occurring on the blue wing than on the red wing for the Si IV and C IV lines. A clearer indication of which parts of

the line profiles are varying is gained by plotting the fractional variance over the mean spectrum for these two lines (Figure 3.6). The changes occur blueward of the rest velocity, are confined to the velocity regime -1500 to 0 km s^{-1}, and correlate well with the emission peak that fills in part of the absorption trough. Figure 3.7 shows the two-dimensional colour representations of the flux variations in the C IV, C III and Si IV line profiles versus orbital phase and reveal that the variability is mostly evident in the phase interval $0.55-0.85$. (Blue shades indicate the most intense emission and red shades the deepest absorption).

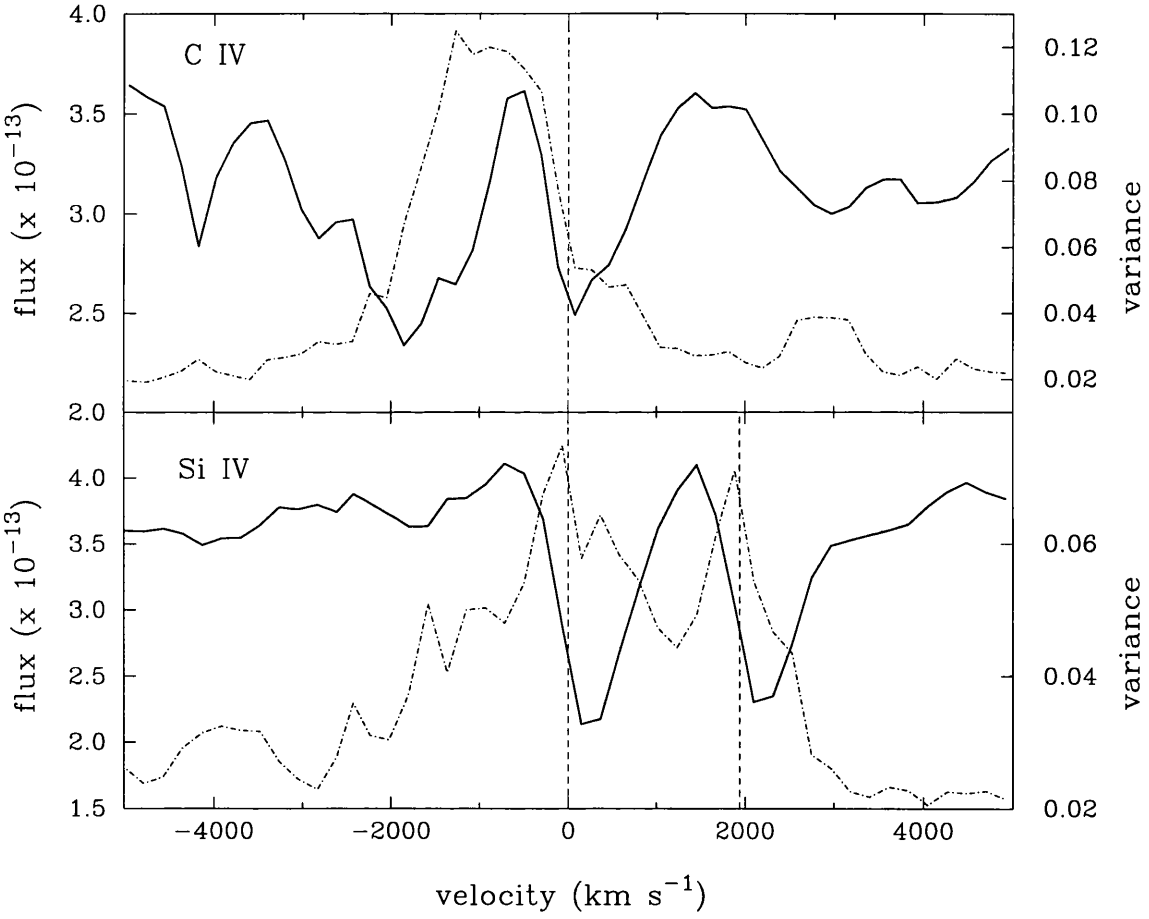

Figure 3.6: Fractional variance (dot-dashed line) plotted over the mean spectrum (solid line) for C IV (top panel) and Si IV (lower panel). The velocity scales are with respect to the rest velocity of the weighted C IV doublet (1549.05 Å) and with respect to the blueward component of the Si IV doublet (1393.76 Å), with dashed lines marking these rest velocities. In the lower panel a second dashed line shows the rest velocity of the red component of the Si IV doublet.

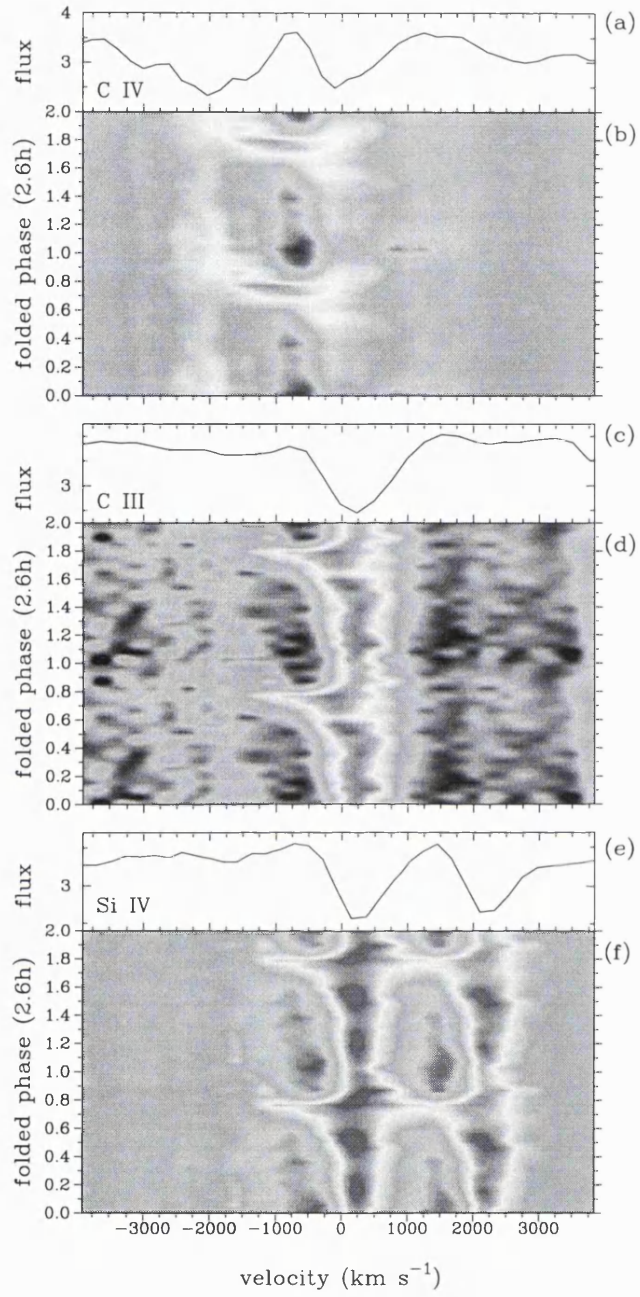

Figure 3.7: The flux variations of C IV, C III and Si IV as a function of orbital phase. Panel (a) shows the mean C IV line profile and panel (b) the corresponding two-dimensional colour representation of the flux variations versus orbital phase. Panels (c) and (d) show the C III profile and trailed spectrogram and panels (e) and (f) those for the Si IV profile. The velocity scales are with respect to the rest velocity of the weighted C IV doublet (1549.05 Å), with respect to the rest velocity of the C III line (1175.66 Å), and with respect to the blueward component of the Si IV doublet (1393.76 Å). Blue shades indicate the most intense emission and red shades the deepest absorption.

The emission feature in the C IV line appears to fade after $\phi_{2.6} = 0.55$ until the profile is pure absorption at $\phi_{2.6} \sim 0.75$, and then it reappears by $\phi_{2.6} = 0.85$. The extended blue wing (-3500 to -2000 km s^{-1}) and the red wing ($+500$ to $+1000$ km s^{-1}) are largely stable throughout the orbital cycle. The variability in the C III line is confined to roughly the same phase interval. The absorption broadens at $\phi_{2.6} \sim 0.55$, has extended blueward as far as -1500 km s^{-1} by $\phi_{2.6} \sim 0.75$ and returns to its original shape by $\phi_{2.6} \sim 0.85$. Again, the red wing remains roughly constant through the orbit. This pattern of variability is repeated for the two components of the Si IV line.

Rosen *et al.* also examined the possible radial velocity motions of the emission and absorption components. They found that the emission peak is substantially blueshifted from the rest velocity to ~ -650 km s^{-1}, but that the radial velocity motion that they measure (semi-amplitude $\sim 120-150$ km s^{-1}) could also be accounted for by intensity changes in a multi-component line profile structure. They found a radial velocity motion of ~ 95 km s^{-1} in the absorption lines at λ1419 Å and λ1430 Å but were unable to detect any motion of the absorption line at λ1345 Å. (These absorption lines were chosen as they were uncontaminated by the emission feature seen in the more prominent lines).

The main UV line properties of V795 Her are summarised below:

1. The UV line fluxes modulate on the mooted orbital period of V795 Her (2.60 hr). There is no indication of the 4.86 hr period that was observed previously in *IUE* data (Prinja, Drew & Rosen 1992; Prinja & Rosen 1993), and the continuum is not seen to vary on either the 2.60 hr spectroscopic period or the 2.80 hr optical photometric period (Mironov *et al.* 1983).

2. The only evidence for a wind-formed feature in the UV resonance line profiles is the asymmetric, blueward absorption trough seen in the C IV line. The blueward side of this absorption trough (-3500 to -2000 km s^{-1}) does not appear to vary throughout the orbital cycle, implying that there is little asymmetry in the wind outflow (or that it is observed at a low inclination).

3. The variations in the UV resonance lines on the 2.60 hr orbital period are largely confined in both velocity space ($-1500 < v < 0$ km s^{-1}) and in phase ($0.55 < \phi_{2.6} < 0.85$). They appear to be dominated by an apparently narrow emission feature, ~ 600 km s^{-1} blueward of the line centres, which disappears and reappears over this phase interval.

4. The UV resonance lines appear to share a common absorption component which is roughly

centred on the rest velocity. At its maximum ($\phi_{2.6} = 0.775$) it extends from -1500 km s^{-1} to $+1200$ km s^{-1}.

5. A possible radial velocity motion has been detected in the blueward emission feature (semi-amplitude $\sim 120-150$ km s^{-1}), but this motion could also be accounted for solely by intensity changes if the profile comprised a multi-component structure.

3.4 Empirical interpretations of the UV line properties

The complex nature of the UV line profile behaviour allows a large number of possible empirical interpretations. The simplest model interprets the variability in terms of a narrow, blueshifted emission component. A second interpretation invokes a broad, fairly stable emission component plus a constant absorption feature and then attributes the variability to a second, variable absorption component. These two ideas are discussed below.

3.4.1 A narrow blueshifted variable emission component?

Figure 3.6 shows that most of the variability in the C IV line profile is occurring between -2000 and 0 km s^{-1}, coincident with the narrow emission component seen in the mean profile. The simplest interpretation of the UV line behaviour attributes all of the variability to a narrow, blueshifted emission component. During the phase interval $0.55 < \phi_{2.6} < 0.85$, the emission gradually fades, is minimum at $\phi_{2.6} = 0.775$ and then reappears. The emission peak is blueshifted to ~ -600 km s^{-1} and has a possible radial velocity motion of semi-amplitude ~ 130 km s^{-1}.

Although, on the face of it, appealing to a narrow emission component to explain the 2.60 hr variations is an attractive idea, there is no part of the binary system that can convincingly produce such emission. The large blueshift of the line (~ -600 km s^{-1}) makes a conventional bright spot emission source implausible. An alternative emission source at a re-impact site near the WD, caused by an overflow of the infalling gas stream, also hits difficulties. Such a source cannot be being observed at high inclination angles because no substantial radial velocity variations of the emission component are observed. However, adopting a low inclination doesn't work either: the emission component is blueshifted implying an *upward* flow. As the emission declines at $\phi_{2.6} \sim$ 0.75, further material is also needed to hide the emission source over the relevant velocity region.

3.4.2 Broad emission plus superposed absorption?

The basic empirical interpretation of the optical emission line behaviour described in Chapter 2 invoked a single, broad emission feature (FWHM ~ 2800 km s^{-1}) following a high velocity s-wave and a superposed, sympathetically phased absorption component (Section 2.5). This empirical interpretation may relate to a physical picture in which the gas stream overflows the accretion disk and re-impacts on the inner disk regions (Section 2.7.2). Could there be a UV counterpart to the broad feature observed in the optical data that is somehow masked in the *HST* data?

A broad emission component is not immediately obvious in the UV data (but neither was it obvious in the optical data: its presence was inferred from the outer wing behaviour). The broad emission could manifest itself as the narrow blueshifted emission peak, narrow because its wings having been cut into by absorption components. Some evidence for a broad emission component may come from the bump seen redward of the C IV line profile ($+1000$ to $+2000$ km s^{-1}) between phases $0.0-0.5$, and which is strongest at $\phi_{2.6} \sim 0.0$. The filling in of the blue wing (-2000 to -1000 km s^{-1}) between phases $0.3-0.6$ in the C III and Si IV lines may provide further evidence of this broad emission.

If a broad component is present, its mean position is near the rest velocity, while the variance plots show that most of the variability occurs in a narrow region blueward of the line centre. Rather than being caused by changes in the broad emission component, the variations seen in the line profiles between phases $0.55-0.85$ must be caused by a variable blueshifted absorption in the velocity range $-2000 < -1000$ km s^{-1}.

To summarise, this empirical model requires (i) a wind outflow to produce the asymmetric high velocity (-3500 to -1500 km s^{-1}) absorption component in the C IV line, (ii) a broad (FWHM $\sim$ $1300-2000$ km s^{-1}) emission component, (iii) a variable, blueshifted absorption in the velocity range $-2000 < -1000$ km s^{-1} that acts in the phase interval $0.55-0.85$, and (iv) a relatively constant absorption component, centred near the rest velocity, to produce the stable red wing seen in the C III, Si IV and C IV lines. Possible physical locations of these emission and absorption sources are discussed in Section 3.6.

A detailed comparison of the UV and optical line behaviour is carried out in the next section in order to gain more information on possible correlated behaviour and to work towards a unified model that explains both the UV and the optical spectroscopic properties of V795 Her.

3.5 Comparison to the optical emission line behaviour

The INT and *HST* data sets provide a unique opportunity to study V795 Her simultaneously at optical and UV wavelengths and to be confident that the system was in the same state when both sets of observations were made. Table 3.1 shows how the two data sets overlap. The windows in which the optical and UV data are genuinely simultaneous are very small, as revealed by Figure 3.8 which shows the continuum flux for the two data sets plotted against time. The flux was measured in the line free continuum region $\lambda\lambda 1440-1490$ Å for the *HST* spectra and in the continuum region $\lambda\lambda 4372-4401$ Å for the INT spectra. (This figure is intended to show clearly the overlap between the two data sets rather than to compare directly the optical and UV continuum behaviour. It was shown in Chapter 2 that the optical continuum flux of V795 Her does not modulate on the orbital period, and Rosen *et al.* 1997 showed that the UV continuum does not display a 2.60 hr periodicity).

The *HST* spectra were recorded in groups of 80 exposures, each exposure being 20s long (see Section 3.2). Only 4 groups out of a total of 23 are simultaneous with INT spectra. Each group took $\sim$ 1600s to record, whereas the exposure time for each INT spectrum was $\sim$ 300s. Therefore only 5 INT spectra were recorded for each group of 80 *HST* spectra. It is clear that little useful information can be gleaned from a direct temporal comparison of the optical and *HST* data sets. Instead the signal-to-noise of the INT data must be improved by phase binning. The remainder of this section will concentrate on comparing the phase-binned optical and UV data, in the main using 20 phase bins. One may still be confident of making a fair comparison as the two data sets are quasi-simultaneous, the coverage of the optical data set spans the UV data set, and because no significant changes were seen in the optical spectra from night to night (*e.g.* Figure 2.11). All these imply that the system was in the same state when both the optical and the UV observations were made.

It was shown in Chapter 2 that the overall strengths of the Balmer and He emission lines modulate on the mooted orbital period of V795 Her (2.60 hr). However, the variations are *asymmetric* in that although the maximum observed flux occurs at $\phi_{2.6} = 0$, the minimum line flux corresponds to $\phi_{2.6} \sim 0.6-0.7$, with a much smaller decrease in strength at $\phi_{2.6} \sim 0.2-0.25$ (*e.g.* see Figure 2.6). As shown in Figure 3.9, this behaviour is also broadly reproduced in the total observed fluxes of the resonance lines C IV $\lambda\lambda 1550$ and Si IV $\lambda\lambda 1400$. This figure also shows the behaviour of the total Hβ flux.

A more detailed comparison was made between the optical and UV line properties by mea-

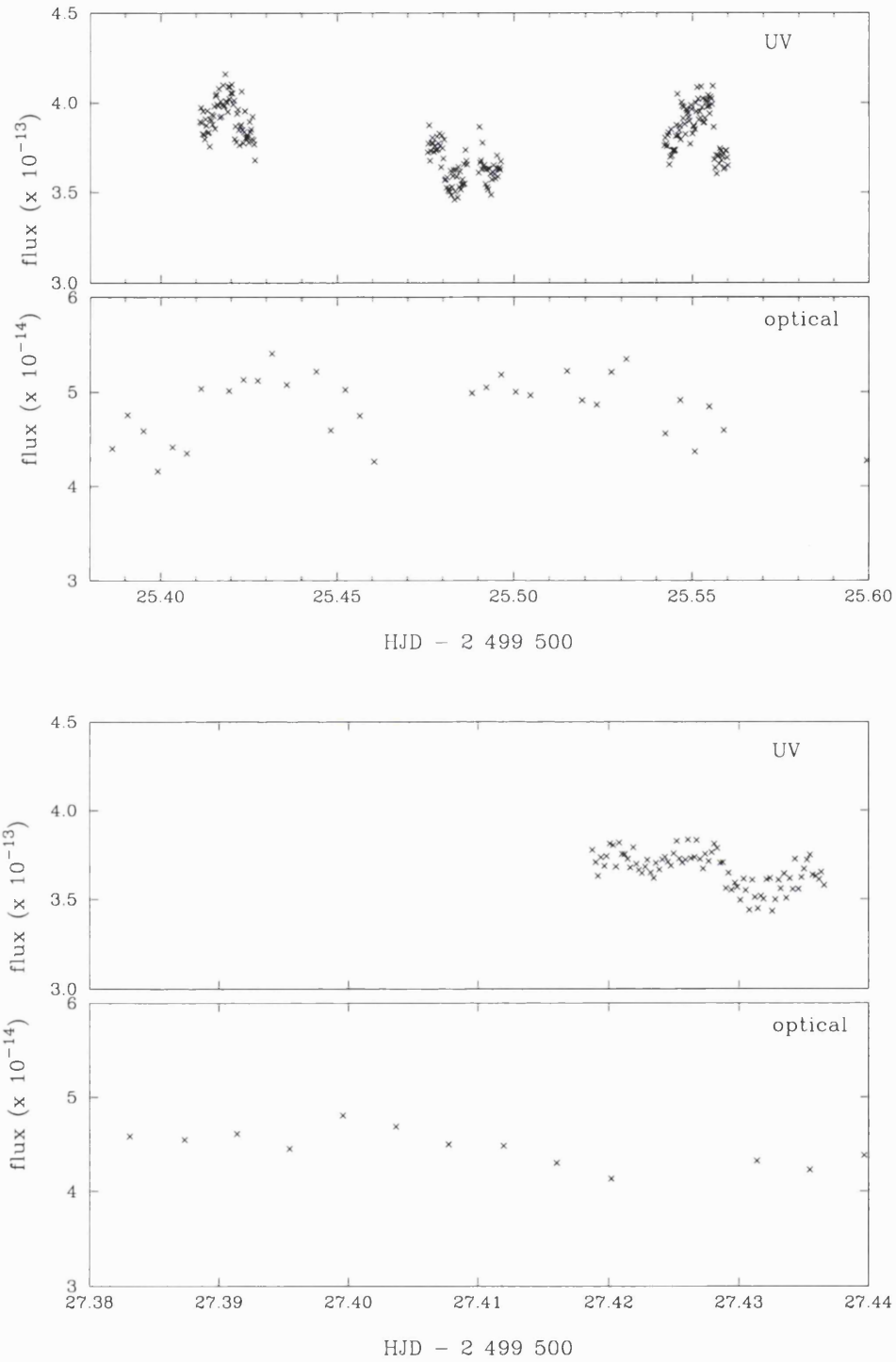

Figure 3.8: Comparison of the optical and UV continuum levels for the two sets of INT and *HST* spectra which overlap in time (see Table 3.1). The top panel of each set shows the flux in the UV continuum region $\lambda\lambda 1440-1490$ Å and the bottom panel shows the flux in the optical continuum region $\lambda\lambda 4372-4401$ Å.

suring the flux in 8 velocity bins, each of width 500 km s^{-1}, across the line profile. The resultant light curves for C IV $\lambda\lambda$1550, Si IV $\lambda\lambda$1400 and Hβ are shown in Figure 3.10. (The correlation between velocity bins [$-$1000, $-$500 km s^{-1}] and [1000, 1500 km s^{-1}] in the Si IV line is due to the doublet nature of this line; the same modulations are repeated in both the blueward and redward components. Zero velocity is with reference to the rest wavelength of the blue component and the velocity separation of the two components is $\sim$ 2000 km s^{-1}).

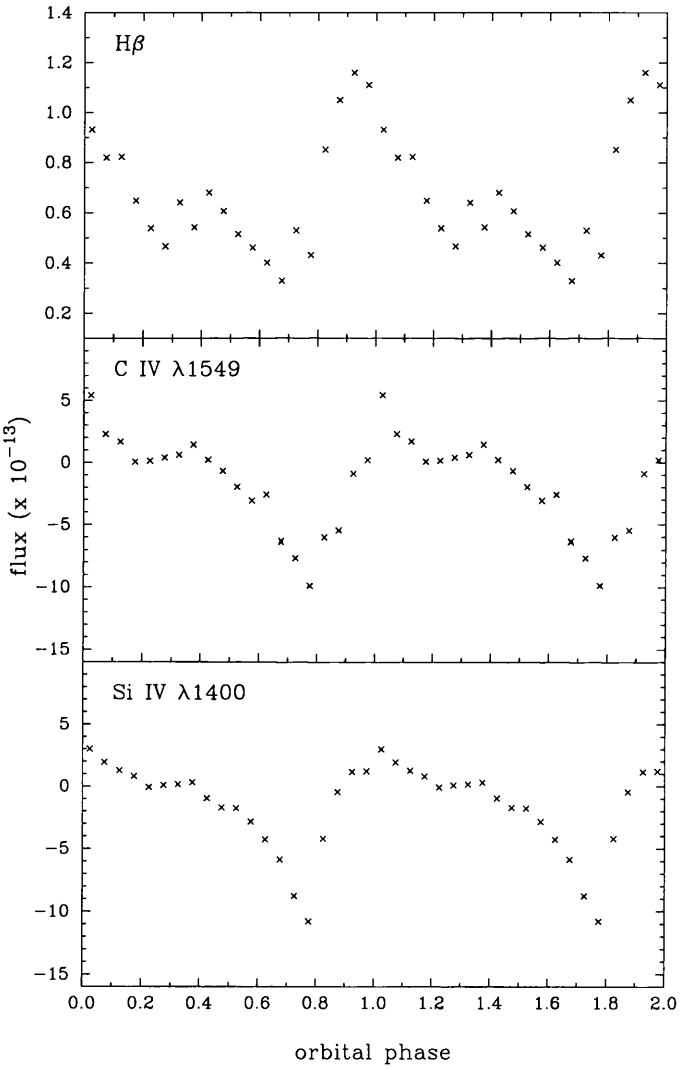

Figure 3.9: The total observed fluxes of the C IV $\lambda\lambda$1550 and Si IV $\lambda\lambda$1400 resonance lines compared to the total Hβ flux.

From Figure 3.10 it is clear that the optical (Hβ) and the UV (C IV, Si IV) line behaviour in velocity bins [$-$1000, $-$500 km s^{-1}] and [$-$500, 0 km s^{-1}] is correlated. Maximum flux is at $\phi_{2.6}$ = 0.0, minimum flux is at $\phi_{2.6}$ = 0.7 $-$ 0.8, and a secondary dip in the flux levels is seen at

$\phi_{2.6} \sim 0.2$ for all these lines. However, where the Hβ line is clearly affected by the redward absorption feature (velocity bin [500, 1000 km s^{-1}], $\phi_{2.6} = 0-0.5$) no corresponding reduction in flux is seen in the UV lines.

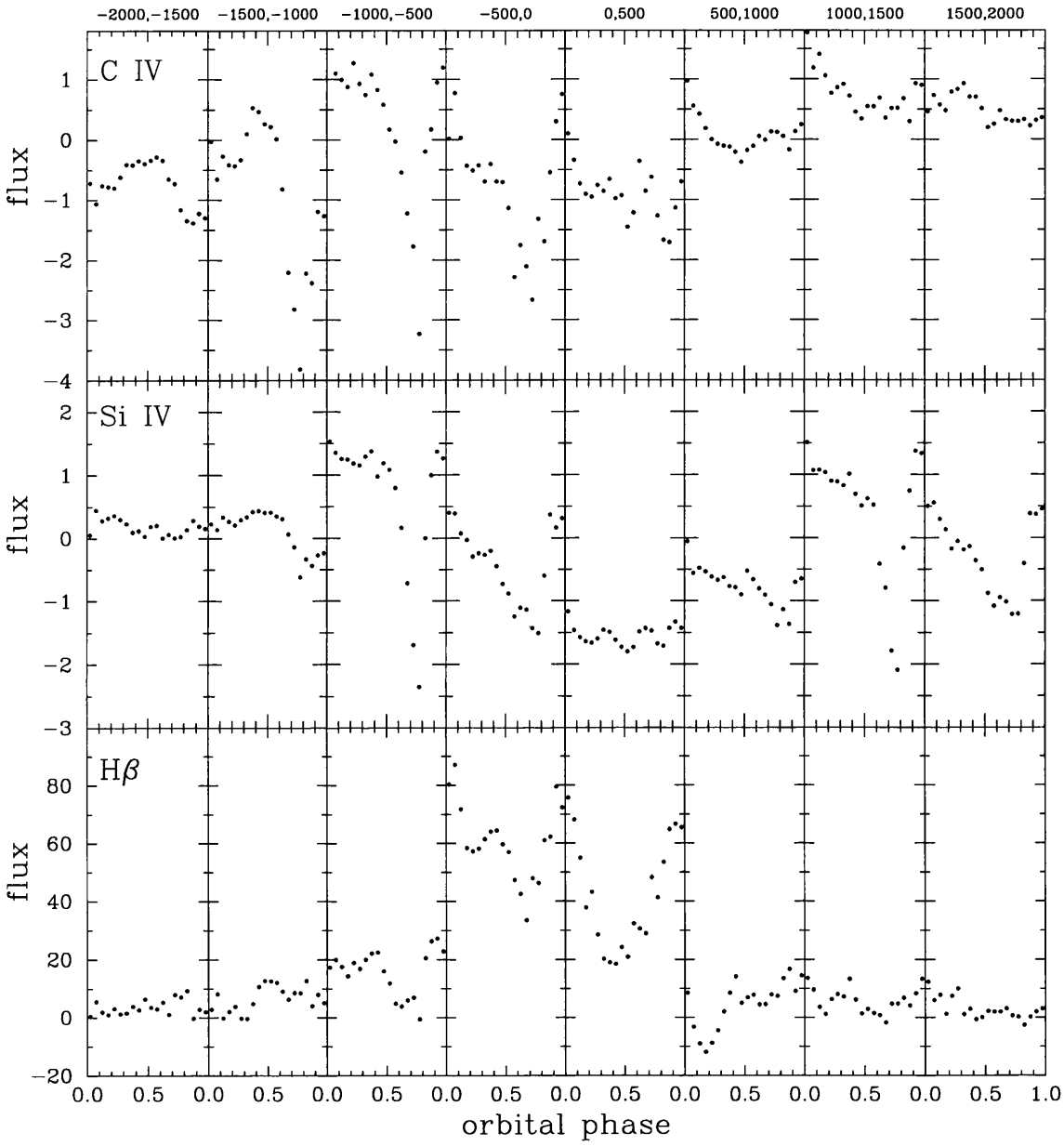

Figure 3.10: Light curves of C IV $\lambda\lambda$1550, Si IV $\lambda\lambda$1400 and Hβ as a function of velocity within the line profile. The velocity bins are shown at the top of each column.

The optical absorption line He I λ4471, examined in Section 2.3.2 (Figures 2.16 and 2.21), appears to behave in a manner that is similar to the UV resonance line behaviour. Figure 3.11 shows the trailed spectrograms of the flux variation versus orbital phase for the UV resonance line C III λ1176 and for the optical absorption line He I λ4471. The optical absorption line He I λ4471

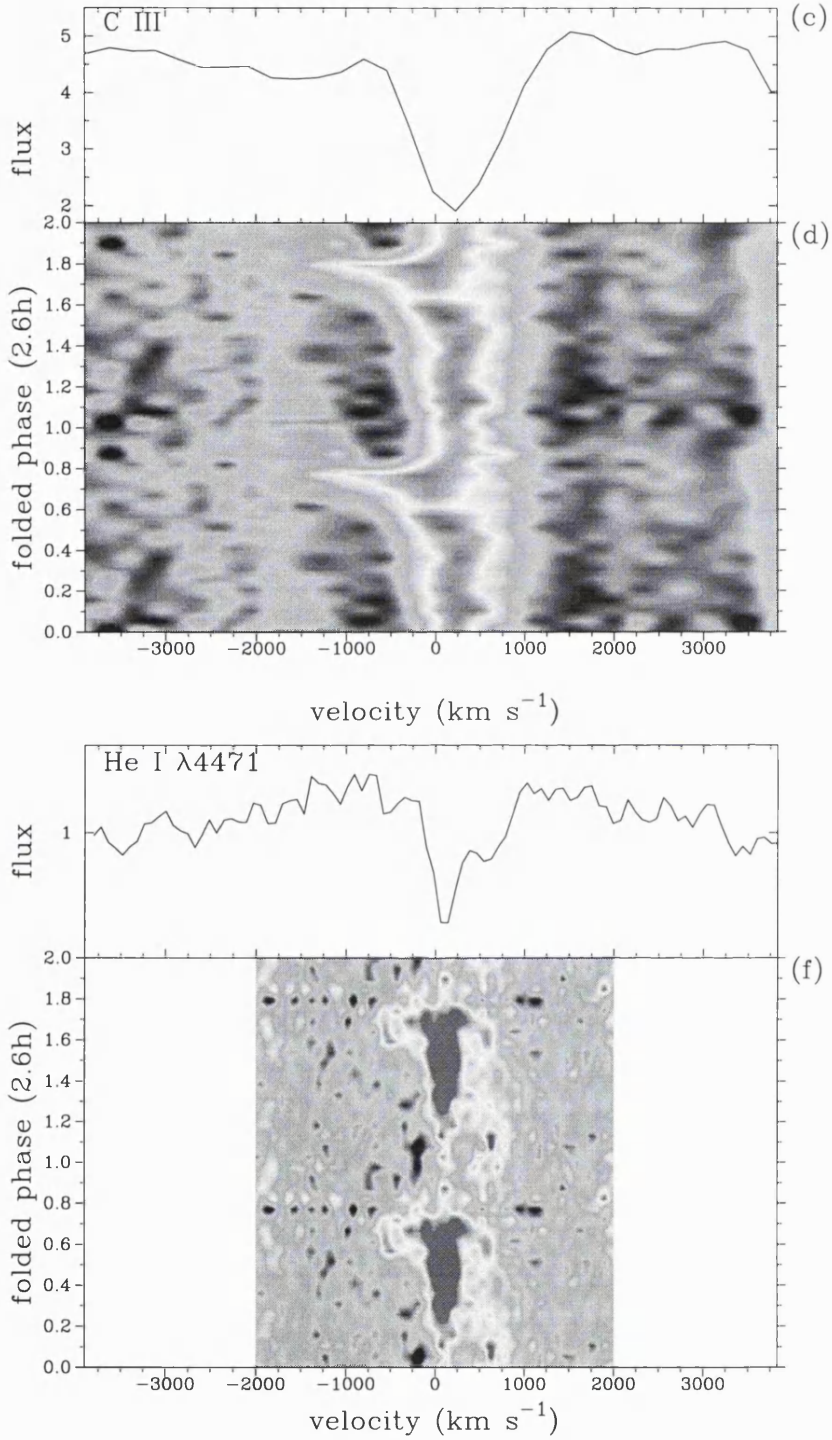

Figure 3.11: Trailed spectrograms of the C III λ1176 (top panel) and He I λ4471 (bottom panel) lines.

widens and deepens over the orbital cycle until it reaches a maximum depth and width at $\phi_{2.6} \sim 0.65-0.70$. After this phase, the absorption declines in strength. There is some indication of a blueward emission component ($v \sim -300$ km s^{-1}) in the phase interval $0.25-0.35$ in the montage of phase binned profiles (Figure 2.16). The trailed spectrogram of the He I λ4471 flux variations (Figures 3.11 and 2.21) suggests that this emission may be the blueward outer s-wave seen in the Balmer lines (Section 2.3.2). The velocity range of the blueward emission feature is -1200 to -200 km s^{-1} and it reaches its maximum blueward velocity at $\phi_{2.6} \sim 0.5$ and its maximum redward velocity at $\phi_{2.6} \sim 0.1$. In comparison, the variations in the UV resonance lines are largely confined in velocity space to $-1500 < v < 0$ km s^{-1} and in phase to $0.55 < \phi_{2.6} < 0.85$. They appear to be dominated by an apparently narrow emission feature, ~ 600 km s^{-1} blueward of the line centres, which disappears and reappears over this phase interval.

The light curves as a function of the velocity across the line profile are shown for C III λ1176 and He I λ4471 in Figure 3.12. The profile has been split into 4 velocity bins, each 500 km s^{-1} wide, and the flux variations versus orbital phase plotted for each velocity bin. Again, a degree of correlated behaviour is seen blueward of the line centre in velocity bin [-500, 0 km s^{-1}], where maximum flux occurs at $\phi_{2.6} \sim 1.0$, minimum flux occurs at $\phi_{2.6} \sim 0.7$ and a secondary minimum is seen at $\phi_{2.6} \sim 0.25$. The UV (C III λ1176) and optical (He I λ4471) behaviour redward of the line centre, in velocity bin [0, 500 km s^{-1}], is not correlated.

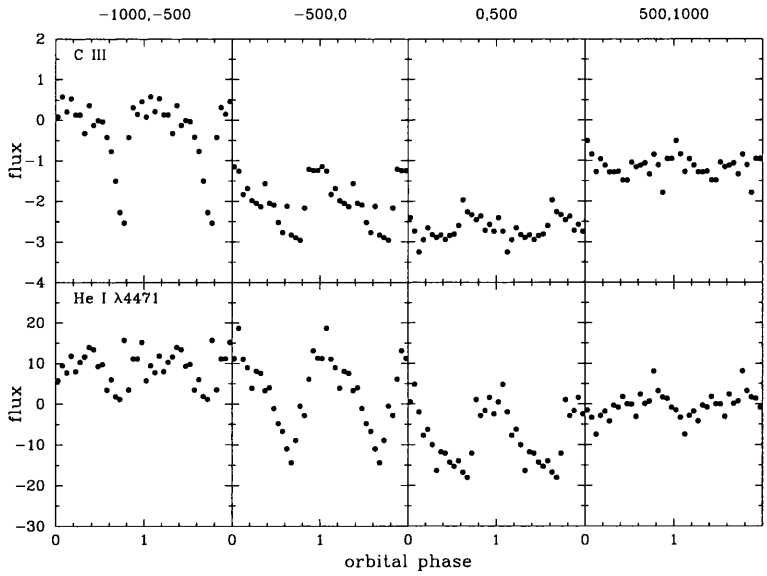

Figure 3.12: Light curves of the C III λ1176 and He I λ4471 line profiles as a function of velocity. The velocity bins are shown at the top of each column.

3.6 Discussion

Analysis of the first UV *HST* data set of the nova-like variable V795 Her has revealed modulations on the mooted orbital period (2.60 hr). Previous *IUE* studies found no correlation between the line variability and the orbital period and instead detected a 4.86 hr variation (*e.g.* Prinja & Rosen 1993). These *HST* data do not show any modulation on the 4.86 hr period and suggest that V795 Her was in a different state when these observations were made. This change is supported by the optical INT observations described in Chapter 2: a prominent 2.80 hr photometric modulation (Mironov, Moshkalev & Sugarov 1983; Rosen *et al.* 1989; Shafter *et al.* 1990; Zhang *et al.* 1991) has essentially disappeared (Patterson & Skillman 1994; also see Section 2.3.1). Patterson & Skillman report that these changes may also be accompanied by a small increase in the system's brightness. In addition, the typical UV continuum flux levels measured in the *IUE* studies was $\sim 25\%$ lower than the *HST* level, and there have been changes to the line profile shapes (Section 3.3.1).

The C IV $\lambda\lambda$1550 line is the only UV resonance line to show clear evidence of a wind-formed feature. The asymmetric blueward absorption trough extends to at least -1500 km s^{-1} and may extend as far as -3500 km s^{-1}. (The blue limit is difficult to determine due to line blanketing effects and contamination by the two absorption lines Si II λ1526.7 and Si II λ1533.5). The absorption is approximately constant over the entire orbital cycle.

The 2.60 hr variability is largely confined to the phase interval 0.525 – 0.875 and to the velocity range $-1500 < v < 0$ km s^{-1}. The simplest interpretation, namely that of invoking a narrow and variable blueshifted emission component, is rejected as there is no part of the binary system which could, convincingly, produce such emission (Section 3.4.1). An alternative model which includes a self-absorbed, broad emission component was examined as it may be possible to tie this model in with the disk-overflow scenario used to explain the optical emission line behaviour in Chapter 2 (see Sections 2.5 and 2.7.2). This empirical model and its relation to the disk-overflow scenario are discussed below (Section 3.6.1).

A comparison of the optical INT and UV *HST* line behaviour was carried out. Some evidence of correlated behaviour was found but it is confined to the velocity region blueward of the line centre ($-1000 < v < 0$ km s^{-1}). The pattern of modulation in the overall strengths of the Balmer and He emission lines is broadly reproduced in the UV resonance lines (Figure 3.9). When this type of comparison is broken down into velocity bins and the flux variations across the line profile are studied, the optical and UV line behaviour is correlated in velocity bins [-1000, -500 km s^{-1}] and

[-500, 0 km s^{-1}], but the behaviour immediately redward of the line centre (velocity bin [0, 500 km s^{-1}]) does not match (Figure 3.10). The UV resonance lines do not reveal any obvious red-shifted absorption, which is what is responsible for the flux variations versus phase in the [0, 500 km s^{-1}] Hβ velocity bin.

The following sections exmaine two physical models which attempt to explain the UV, and the optical, line properties of V795 Her. Section 3.6.1 looks again at the disk-overflow scenario, initially proposed to explain the optical behaviour in Chapter 2 (Section 2.7.2) and Section 3.6.2 considers briefly the possible relation of V795 Her to T Tauri stars.

3.6.1 Disk-overflow?

The empirical model which invokes a broad emission feature to explain the variability of the UV resonance lines in V795 Her (Section 3.4.2) also requires some other components. The observational properties may be explained with (i) an asymmetric blueward absorption feature that extends out to high velocities (-3500 to -1500 km s^{-1}), (ii) a relatively constant absorption component (that produces the stable red wing seen in the C III λ1176, Si IV $\lambda\lambda$1400 and C IV $\lambda\lambda$1550 lines), (iii) a broad emission component (FWHM $\sim 1300-2000$ km s^{-1}) and (iv) a variable blueshifted absorption component ($-2000 < v < -1000$ km s^{-1}) that acts in the phase interval $0.55-0.85$. This section considers possible physical origins for these absorption and emission sites and examines them in the context of the disk-overflow model suggested in Chapter 2 to explain the optical INT emission line behaviour (Section 2.7.2).

The asymmetric, blueward absorption (seen only in the C IV $\lambda\lambda$1550 resonance line) is a wind-formed feature. The extent of the line blanketing and the contamination by the Si II absorption lines (Si II λ1526.7 and Si II λ1533.5) prevent an accurate measurement of the wind profile, and therefore preclude any attempts to model the wind properties of V795 Her. There appears to be very little variation of the blueward side of the absorption throughout the orbital cycle which implies that there is little asymmetry in the wind outflow.

The absorption component common to all the resonance lines is seen most clearly in the C III λ1176 line at $\phi_{2.6} = 0.775$. Again, this appears to be a fairly constant feature throughout the orbital cycle, as evidenced by the invariance of the redward wing of this feature ($v \sim 1200$ km s^{-1}). From examination of the C III line, the absorption has a FWZI ~ 2700 km s^{-1} and a central velocity near to the rest velocity. These properties are all compatible with an accretion disk origin. Both

this underlying absorption and the line blanketing could originate in a disk photosphere.

The broad emission component (FWHM $\sim 1300-2000$ km s^{-1}) could have a physical origin consistent with the disk-overflow model. It may be the UV counterpart of the broad feature seen at optical wavelengths and produced at the re-impact site of an overflowing gas stream. To reproduce the 2.60 hr variability, a variable blueshifted absorption component is required. As it is clearly tied to the 2.60 hr orbital period it is unlikely to have a wind origin. This component acts largely in the velocity range $-2000 < v < -1000$ km s^{-1} and in the phase range $0.55-0.85$. In the disk-overflow model, the broad optical emission is self-absorbed, producing double-humped line profiles. Additional absorption arises in the gas stream as it flows from its intital impact site to the re-impact site. This optical absorption is only obvious when it is redward of the line centre in the first half of the orbital cycle. The relation between the optical and the UV absorption, if any, is not clear. The variable blueshifted absorption seen in the UV resonance lines could be the UV counterpart of the optical absorption component, being observed at its maximum blueshift. However, the UV component must be more variable than the optical absorption to show such different behaviour between the first and second halves of the orbital cycle. It must be much stronger around $\phi_{2.6} = 0.75$ and much weaker when it is redshifted at early phases in the cycle.

3.6.2 A connection to T Tauri stars?

T Tauri stars are thought to be recently formed solar mass stars. The classical T Tau stars are surrounded by a disk whereas naked T Tau stars are not. As young stellar objects, T Tau stars are in the process of ridding themselves of the circumstellar material associated with star formation. In a classical T Tau star, material accretes onto the star through a disk and a wind carries away the excess angular momentum thus permitting the relatively slow rotation observed. The narrow band of rotation periods observed in classical T Tau stars, compared to the wide range reported in naked T Tau stars (Edwards *et al.* 1993), suggests that the disk is coupled to the star in some way, most likely via a magnetic field (Camenzind 1990; Königl 1991).

The classical T Tau star SU Aur has been observed extensively by Johns & Basri (1995). They report variability in the blue Hα wing and in both wings of the Hβ line on the stellar rotation period ($\sim$ 3 days). Johns & Basri explain these observations using an 'egg-beater' model. In this model the inner edge of the disk is disrupted by the star's magnetic field. At the inner disk regions, the accretion flow divides in two, with one portion following the magnetic field lines onto the star and

the other becoming a centrifugally driven outflow. The magnetic axis is at an angle to the stellar rotation (and disk) axis, breaking the azimuthal symmetry and resulting in variations on the rotation period. The blue wing variations are then associated with the outflow and the red wing variations with the accretion flow.

Rosen *et al.* (1997) suggest that the blue wing variations observed in the UV resonance lines of V795 Her may be analagous to the Hα variations seen in SU Aur. The shifting of the phenomenon from the optical to the UV may be explained by the deeper gravitational potential surrounding the WD in V795 Her. The biggest problem within this analogy is the identification of the 2.60 hr periodicity with the rotation period of the WD rather than with the orbital period of the system. As argued in Section 2.7.1, it is very unlikely the the WD spin period and the orbital period in V795 Her are synchronous. This model can therefore only be correct if the orbital period of V795 Her is not 2.60 hr after all.

3.7 Summary

The first detection of the modulation of the UV resonance lines on the mooted orbital period of V795 Her has been made in this *HST* data set. The lack of the 4.86 hr periodicity that was reported in earlier *IUE* studies, the disappearance of the 2.80 hr photometric period at optical wavelengths, the small increase in brightness of the system and the changes in the UV spectral shapes all indicate that V795 Her is in a different state than when observed previously.

The UV resonance line C IV $\lambda\lambda$1550 shows evidence for an outflow in V795 Her, namely a wind-formed, asymmetric, blueward absorption trough. The constancy of the trough's blueward edge does not point to the wind as being responsible for the orbital variability seen in the UV resonance line profiles. One of the key motivations in simultaneously studying V795 Her at optical and UV wavelengths was to discover the source of the variability of the UV resonance lines. This study suggests that UV line profile variability, at least in V795 Her, is not associated with the wind-formed features.

The common absorption component of the UV resonance lines (see Section 3.3.2) is assumed to arise from the accretion disk, quite likely in the disk photosphere. It is clearly a significant component of the overall line profile and the implications of this for CV wind modelling are quite significant. Current synthesis codes do not include the potential contribution of disk emission and

absorption to the UV line profiles. This study suggests that, in the case of modest wind outflows, an important contribution is being neglected.

The UV observations of V795 Her are broadly compatible with the disk-overflow scenario discussed in relation to the optical work (Chapter 2) but there remain several discrepancies. A tentative identification of a broad emission feature in the UV lines that is the counterpart of the broad optical emisson, responsible for the outer wing variations, has been made. The s-wave produced by the optical emission appears to have a semi-amplitude of ~ 400 km s^{-1}. If the motion of the proposed broad UV emission has a similar semi-amplitude, it is not clear why the red absorption wing (assumed to arise in the disk) is apparently unaffected by this feature. The optical and UV line properties differ on the redward side of the lines. The proposed UV counterpart of the optical absorption component must be more variable, being strong at $\phi_{2.6} \sim 0.75$ and much weaker between $\phi_{2.6} = 0.0 - 0.5$ when it is redshifted.

As the lines being studied in the UV are generally of a higher ionization state than the optical lines, the UV emission and absorption sites will not necessarily be coincident with the optical ones. It is therefore reasonable to expect only a *broad* agreement between the optical and UV line behaviour, rather than a detailed correlation. Clearly further work is needed (see Chapter 6) to ascertain if the disk-overflow model is a viable explanation of the spectroscopic properties of V795 Her or if, in the light of the analogies drawn with classical T Tau stars, a magnetic model should be re-examined.

Chapter 4

Time-resolved optical spectroscopy of SS Cygni during outburst

4.1 Introduction

SS Cyg is a U Gem-type dwarf nova (*i.e.* it brightens by several magnitudes at regular intervals) with an orbital period of 6.6 hr. In quiescence it has a visual magnitude of $\sim$ 11.8 mag, and in outburst it brightens to $\sim$ 8.1 mag. Outbursts generally last for 13 – 22 d, and the recurrence time ranges between 21 and 126 d, with a mean recurrence time about 50 d. Figure 4.1 shows a typical portion of SS Cyg's light curve, displaying an example of each of the different outburst types as described by Howarth (1978). Outbursts can be classified as long or short, and as symmetric or asymmetric, which gives rise to four distinct groupings. Symmetric outbursts are also known as anomalous due to the atypical, long rise to maximum.

SS Cyg is a well studied system. The review by Giovanelli & Martínez-Pais (1991) describes the observational properties discovered up to that date and discusses them in the context of CV theories. Before describing the most recent spectroscopic studies by Steeghs *et al.* (1996) and by Martínez-Pais *et al.* (1994; 1996), I will summarise what is known about SS Cyg, concentrating in the main on spectroscopic work.

Following its discovery as a variable star in 1896, SS Cyg has been monitored almost continuously resulting in a light curve that spans over 100 years. Statistical work on this light curve (Howarth 1978; Bath & van Paradijs 1983) provided the outburst classification scheme described

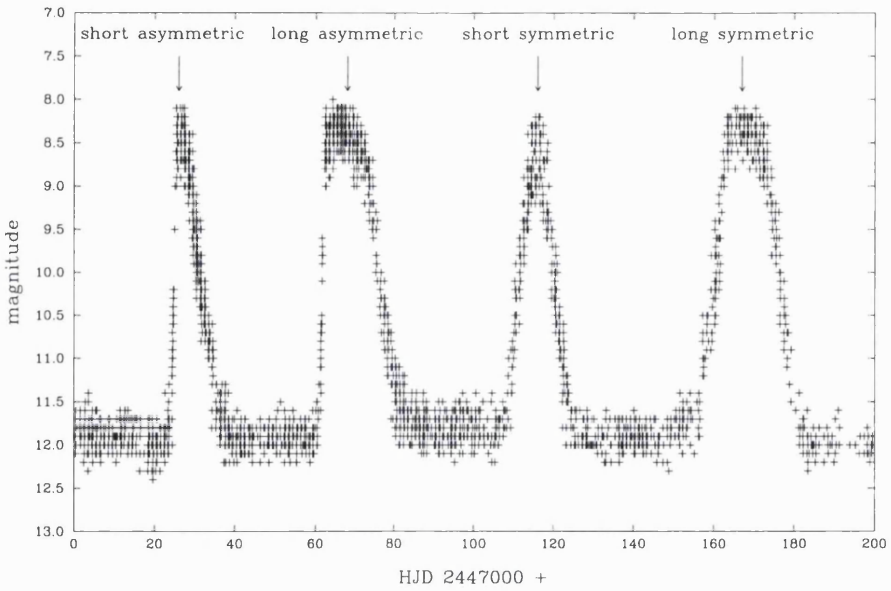

Figure 4.1: A typical portion of the SS Cyg light curve showing the different outburst types. This light curve was created using data from the International Database of the American Associoation of Variable Star Observers (AAVSO), based on observations submitted to the AAVSO by variable star observers worldwide.

above and gave reliable estimates of the outburst properties (also described above). In the early 1970s SS Cyg was both discovered to be an X-ray emitter (Rappaport *et al.* 1974) and studied for the first time at UV wavelengths (Holm & Gallagher 1974).

In quiescence the optical spectrum of SS Cyg has a strong, blue continuum with strong, wide Balmer emission lines. Emission from the He II λ4686 line is virtually absent. Absorption features from the late-type secondary star are also visible during quiescence. In outburst the Balmer lines are seen in absorption, with a narrow emission core. As the outburst progresses the He II λ4686 line increases in strength. The strength of the emission core of the Balmer lines increases as the system goes into decline until the absorption is no longer visible and the profiles return to their quiescent appearance. At the same time the strength of the He II λ4686 emission decreases and then finally disappears. (See Figure 4.3 which shows the evolution of the line profiles from quiescence to outburst maximum.)

The quality of the data in spectroscopic studies from the early 1980s (Stover *et al.* 1980; Hessman *et al.* 1984) exceeded that of earlier work and these authors were able to correct erroneous measurements of the fundamental physical parameters of the system. The orbital period and ephemeris used currently is the one derived by Hessman *et al.* (see Table 4.1). Studies from this time

concentrated on establishing the radial velocity motions of the late-type secondary and the WD, both in outburst and quiescence.

System Parameter	Value	Reference
P_{orb} (d)	0.275 129 73	Hessman *et al.* 1984
T_0 (HJD)	2 444 841.868 24	Hessman *et al.* 1984
M_1 ($M_\odot$)	0.97	Giovanelli *et al.* 1983
M_2 ($M_\odot$)	0.56	Giovanelli *et al.* 1983
K_1 (km s^{-1})	92	Martínez-Pais *et al.* 1994
K_2 (km s^{-1})	155	Martínez-Pais *et al.* 1994
i	37°	Ritter 1990

Table 4.1: The system parameters of SS Cyg adopted in this study.

The motivation behind many studies of SS Cyg has been the desire to distinguish between the competing models of dwarf nova outbursts, namely the secondary instability model (where an instability on the secondary star causes enhanced mass transfer and thus increased mass accretion through the disk onto the WD) and the disk instability model (where an instability in the accretion disk itself causes the mass transfer onto the WD to increase). (See Section 1.1.3 for a discussion of the theory of dwarf nova outburst mechanisms). Clarke, Capel & Bowyer (1984) carried out the first spectroscopic study that followed the evolution of the system over a complete outburst cycle. Their aim was to 'map' the temperature and density changes in different regions of the accretion disk in order to discriminate between an onset of outburst due to viscosity changes in the disk and an onset due to an increased rate of mass transfer from the secondary. They tabulate the sequence of pronounced spectral changes in the Balmer and helium lines and examine their phasing with respect to the continuum brightening.

Cheng & Lin (1992) modelled the spectra recorded by Hessman *et al.* (1984) at the maximum, and during the decline, of a short symmetric outburst in 1981. To explain some of the observed features of SS Cyg (*e.g.* the coexistence of H and He I emission and the absence of a significant Balmer jump at maximum light), they modified a disk atmosphere model used previously by introducing a corona above the disk photosphere. Their model implies that the outburst was initiated from the inner disk regions. This result is compatible with the disk instability model of dwarf nova outburst theory, but does not agree with predictions made by the mass transfer instability model.

Mansperger *et al.* (1994) have also studied SS Cyg in the hope of examining the different outburst mechanism theories. They aimed to catch the system in a pre-outburst state at both optical and UV wavelengths (during the pre-outburst state, normally up to five days before the rapid rise to maximum, the optical continuum is seen to rise gradually while the emission lines weaken and/or become narrower). The disk instability model of dwarf nova outbursts interprets this pre-outburst state as the relatively slow passage of a warm front through the disk prior to the passage of a hot front which triggers the rapid rise of the outburst (Mineshige 1988). Although Mansperger *et al.*'s data suggest that significant changes were occurring in the disk, consistent with SS Cyg being in a pre-outburst state, there was no outburst until 30 days after their observations were made. There may be other explanations for the optical continuum brightening and the large drop in emission line strength observed, such as gas stream irregularities or magnetic disruption, but the occurrence of some type of disk instability is the most favoured interpretation. They do not suggest a reason why this particular instability failed to result in a full outburst.

Martínez-Pais and co-workers have published two optical, time-resolved spectroscopic studies of SS Cyg, the first looking at the quiescent properties (Martínez-Pais *et al.* 1994) and the second at the properties when the system is in outburst (Martínez-Pais *et al.* 1996). In their first study they derive some of the orbital and geometrical parameters of the system (see Table 4.1). They also detect strong emission from the secondary star, which is being heated, even during quiescence, by irradiation from the inner regions of the accretion disk. Their later study covers the decline from a long, asymmetric outburst and the rise to a long, symmetric outburst. (They also report on some data taken at the maximum of the long, asymmetric outburst, but these spectra have no orbital resolution; see Table 4.2). They find some evidence that the symmetric outburst may be caused by an increase in the mass transfer rate from the secondary star, as the outburst is seen to begin in the outer disk regions, and the size of the hot spot increases and possibly brightens during the rise to outburst.

Fewer studies of SS Cyg have been carried out at UV wavelengths. SS Cyg is known to drive a wind when in outburst, as evidenced by the P Cygni-type profiles of the C IV $\lambda\lambda$1550 and He II λ1640 lines, and the extended absorption in the N V $\lambda\lambda$1240 line (Prinja & Rosen 1995). A study by Lombardi, Giovanelli & Gaudenzi (1987) of 37 low resolution *IUE* spectra of SS Cyg, recorded in quiescence, revealed orbital modulations of the continuum flux and of the emission line flux. They claim that the shape of the modulation is dependent on whether the period of quiescence follows a long or a short outburst. Baluta, Nousek & Mansperger (1995) have examined 20 low resolution

IUE outburst spectra of SS Cyg. Again, a wind is evidenced by a prominent P Cygni-type C IV $\lambda\lambda$1550 profile, and by velocity shifted absorption in the N V $\lambda\lambda$1240 and Si IV $\lambda\lambda$1400 lines. Both the C IV emission and absorption line strengths were measured and variations as large as a factor ~ 2 revealed, on timescales as short as ~ 30 min. These variations are not correlated with the orbital period for the emission strengths but the absorption strengths do show evidence of orbital modulation.

The most recent spectroscopic work on SS Cyg is a time-resolved optical study by Steeghs *et al.* (1996) which examines the system one week after maximum light of a long symmetric outburst. All the emission lines have a double-peaked structure, with the Balmer lines showing the most extended disk. Fine structure within the peaks indicates non-axisymmetric disk emission and therefore non-Keplerian motion. The broad absorption wings of the Balmer line profiles indicate a hot, optically thick accretion disk. In most of the lines (except He II λ4686) they see an s-wave feature phased with the secondary star. Doppler imaging (an imaging tool described in Section 1.3) reveals this to be caused by strong emission from the front side of the Roche lobe. They report the presence of stationary, low velocity emission in the Hα and He II λ4686 lines, which is difficult to interpret as there is no obvious part of the binary system that exhibits the observed motion.

Table 4.2 provides a summary of the major spectroscopic studies of SS Cyg, including the study presented here. It lists the outburst type and indicates whether the data set used was orbitally resolved. A new, time-resolved orbital study of SS Cyg is reported on in this chapter. The spectra were recorded over 6 nights in 1994 June at the 2.5m INT at La Palma as SS Cyg underwent a long asymmetric outburst. As can be seen from Table 4.2, few spectroscopic studies with orbital resolution have been carried out when SS Cyg is at maximum light. To the best of my knowledge, this is the first time-resolved data set to be recorded at the maximum of a long asymmetric outburst. The data set is described in Section 4.2, Section 4.3 presents the optical line properties and Section 4.4 presents Doppler imaging of SS Cyg. Possible origins of the low velocity, stationary emission are discussed in Section 4.5. Section 4.6 presents an *IUE* data set which was recorded during the same outburst in 1994 June, but a week after the optical observations were made. The conclusions of this study are discussed in Section 4.7.

observation date	outburst stage†	spectral coverage (Å)	resolution (Å)	integration time (min)	orbital resolution
1993 Aug[a]	D, LSy	4200 – 5000 6390 – 6850	0.7	2	yes
1992 Nov[b]	Q	4100 – 5000	1.9		yes
1987 Jun[c]	R, LSy	3970 – 4950	1	10 – 15	yes
1987 Oct[c]	D, LA	3980 – 4900	1	10 – 15	yes
1985 Jul[c]	M, LA & D, LA	3540 – 5230	3	5 – 20	no
1987 Jul[d]	Q	4000 – 5000 6480 – 6750	1	10 – 15	yes
1992 May[d]	Q	6400 – 6750	0.6	8	yes
1984 Jul[e]	D (end), SA	3940 – 4920	0.6	6	yes
1983 Jul/Aug[f]	SA (full cycle)	3900 – 5000	4	32	no
1981 Aug[g]	Q	4000 – 5300	?	15	yes
1981 Oct[g]	M, SA	4000 – 5300	?	15	yes
1978 Jul/Aug[h]	Q	3700 – 5300	3.8	5 – 10	yes
1994 Jun[i]	R, LA	4000 – 5000	1	5	yes
1994 Jun[i]	near M, LA	4000 – 5000	1	1	yes
1994 Jun[i]	near M, LA	4000 – 10000	10	0.5	yes
1994 Jun[i]	near M, LA	4000 – 5000	1	4	yes

† L = long, S = short, A = asymmetric, Sy = symmetric, Q = quiescence, R = rise, M = maximum, D = decline

Table 4.2: Summary of spectroscopic studies of SS Cyg. ([a]: Steeghs *et al.* 1996 [b]: Mansperger *et al.* 1994 [c]: Martínez-Pais *et al.* 1996 [d]: Martínez-Pais *et al.* 1994 [e]: Echevarria *et al.* 1989 [f]: Clarke, Capel & Bowyer 1984 [g]: Hessman *et al.* 1984 [h]: Stover *et al.* 1980 [i]: this study)

4.2 The optical data set of SS Cyg

The data used in this study were obtained over 6 nights between 1994 June 22 – 27 on the 2.5m INT at La Palma and were taken using the IDS with the EEV CCD and R1200B grating. The wavelength coverage amounts to $\sim \lambda\lambda 4080 - 4970$ Å, with a spectral resolution of ~ 1 Å. Table B.4 gives the log of observations. The data were taken at the start of a long asymmetric outburst of SS Cyg. Figure 4.2 shows the position of the observations over the outburst cycle and Table 4.3 gives the phase coverage of each night's data. One spectrum (data set C) was taken using the FOS on the INT and covers $\lambda\lambda 3740 - 10200$ Å in two orders, with a spectral resolution of ~ 10 Å.

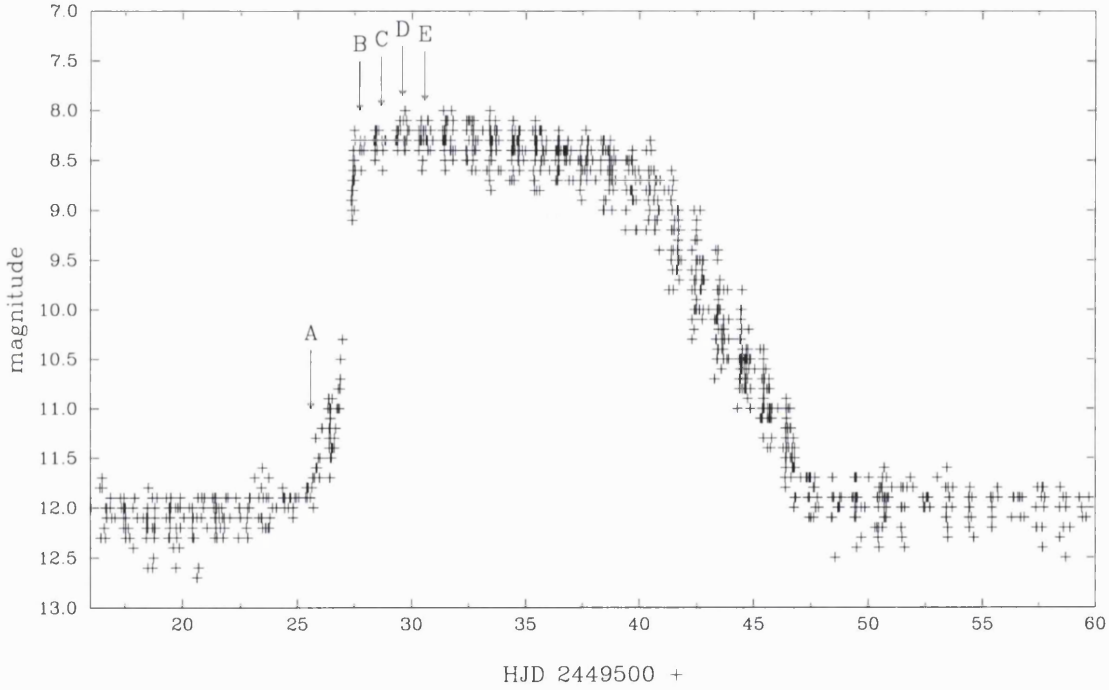

Figure 4.2: The position of the optical observations on the SS Cyg light curve. The labels A – E refer to the 5 data sets described in Table 4.3. This light curve was created using data from the AAVSO International Database, based on observations submitted to the AAVSO by variable star observers worldwide.

Data reduction followed the same procedures as used for V795 Her (Chapter 2). Several exposures of flux and atmospheric standards were recorded in addition to the stellar exposures. The FIGARO (Meyerdierks 1993) and PAMELA (Horne 1986) *STARLINK* packages were used to extract the data and carry out the wavelength and flux calibrations. Most of the subsequent data manipulation and analysis was carried out using the DIPSO package (Howarth *et al.* 1995). As the seeing

data set	date	file number(s)	number of spectra	phase coverage (%)	comment
A	94-JUN-22	199	1	–	pre-outburst spectrum
B	94-JUN-24	592 – 602	11	6	
C	94-JUN-25	717	1	–	FOS spectrum
D	94-JUN-26	812 – 853	35	53	
E	94-JUN-27	938 – 977	29	61	

Table 4.3: Phase coverage of SS Cyg observations

disk was larger than the aperture, these spectra are not strictly spectrophotometric.

4.3 The optical spectroscopic properties

The mean IDS spectrum from each night (data sets A, B, D and E; see Table 4.3) is shown in Figure 4.3 and the evolution of the lines over the outburst is clear. The first spectrum (data set A) was taken while SS Cyg was still in a pre-outburst state; there is strong Balmer and He I λ4471 emission and the He II λ4686 line is absent. Data set B was taken 2 days later and there has been a dramatic change to the line profiles; the emission lines have evolved into wide absorption lines and a narrow emission feature can just be noted in the core of each line. The slope of the continuum steepens considerably between the quiescent (set A) and outburst (set B) data sets. When data set D was recorded a further 2 days later the 'outburst line' He II λ4686 is clearly visible, and the emission feature in the core of the Balmer and He I lines has increased greatly.

The Hβ line profiles clearly show a multi-component structure. The asymmetry seen between data sets D and E, *i.e.* that the blue peak is stronger in data set D and that the red peak is stronger in data set E, may be the result of the different phase coverage of the two data sets. Data set D spans the range $\phi = 0.45 - 1.00$ and data set E spans the range $\phi = 0.95 - 0.65$.

The analysis presented here concentrates on the data from sets D and E where in both cases there is more than one half of an orbital cycle of phase coverage (Table 4.3). For much of the analysis these two data sets can be combined; the resultant data set then covers a complete orbital cycle.

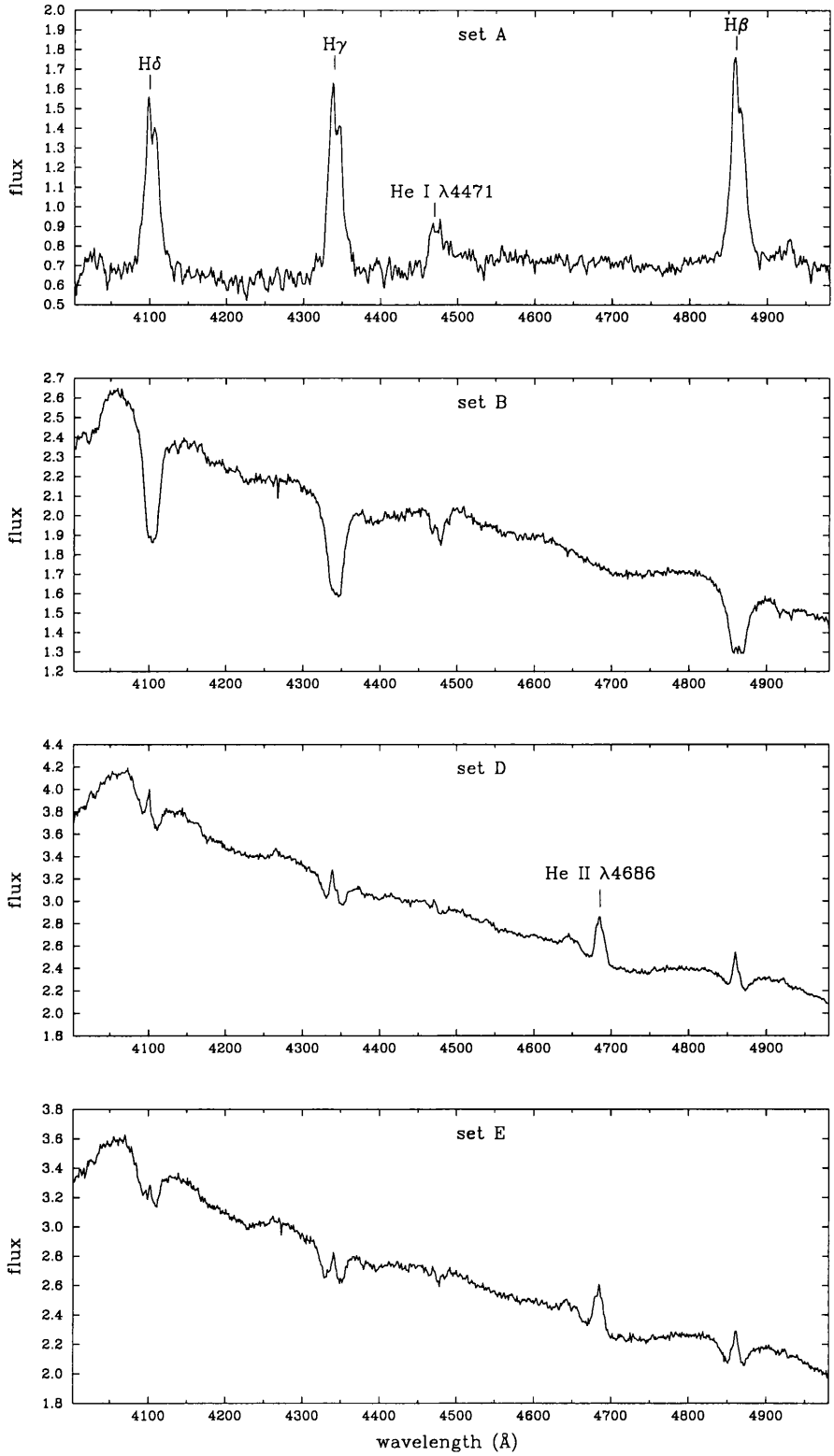

Figure 4.3: The mean spectra from data sets A, B, D and E (see Table 4.3).

4.3.1 Orbital variability

Figure 4.4 show the mean IDS spectrum for data sets D and E (Table 4.3) and the corresponding fractional variance. The statistic σ^2_λ is plotted, where

$$\sigma^2_\lambda = \frac{1}{(N-1)[\bar{f}(\lambda)]^2} \sum_{i=1}^{N} [f_i(\lambda) - \bar{f}(\lambda)]^2 \tag{4.1}$$

as used and described in Section 2.3.1 (Equation 2.1). There are substantial variations occurring in the Balmer lines and the He II λ4686 line and the variance appears to be greatest on the blueward side of the line centre. All the lines show a 'dip' in the variance at the rest velocity, which could be an indication of the stationary, low velocity emission component reported by Steeghs *et al.* (1996).

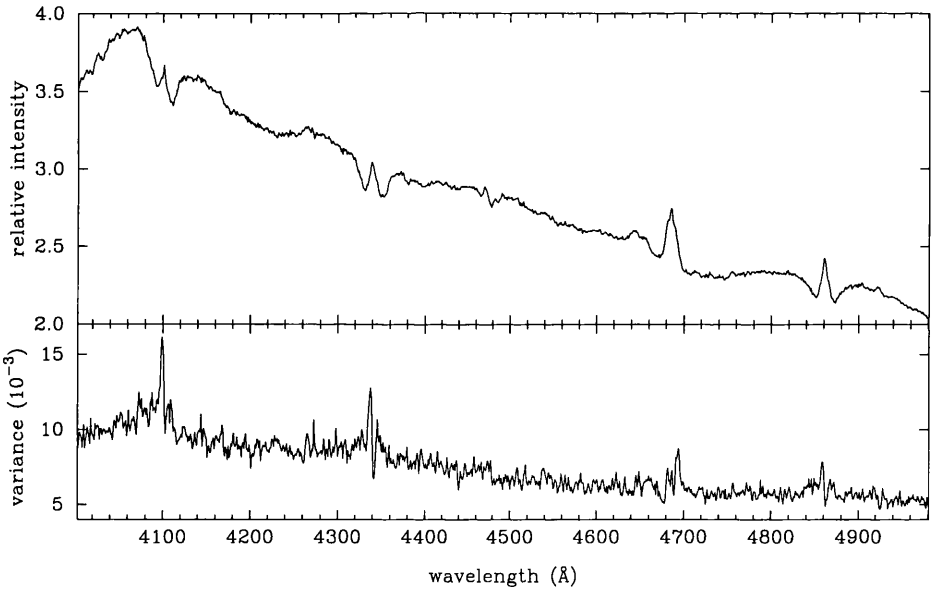

Figure 4.4: The mean IDS spectrum for data sets D and E (see Table 4.3) and the corresponding fractional variance (Equation 4.1).

To examine more closely which part of the line profile is changing, the mean profiles (from the combined data sets D and E) for the Hβ, Hγ and He II λ4686 lines are plotted in velocity space (Figure 4.5), and superposed on these are the corresponding fractional variance spectra (Equation 4.1). Most of the variability is confined to the velocity regime $-500 < v < 0$ km s^{-1} in the Balmer lines,

and to the regime $-500 < v < 500$ km s^{-1} in the He II λ4686 line. There is some weaker variability in the Balmer line wings, between -1500 and $+1000$ km s^{-1}. There appears to be a 'dip' in the variance of all three lines at $v \sim +100$ km s^{-1}.

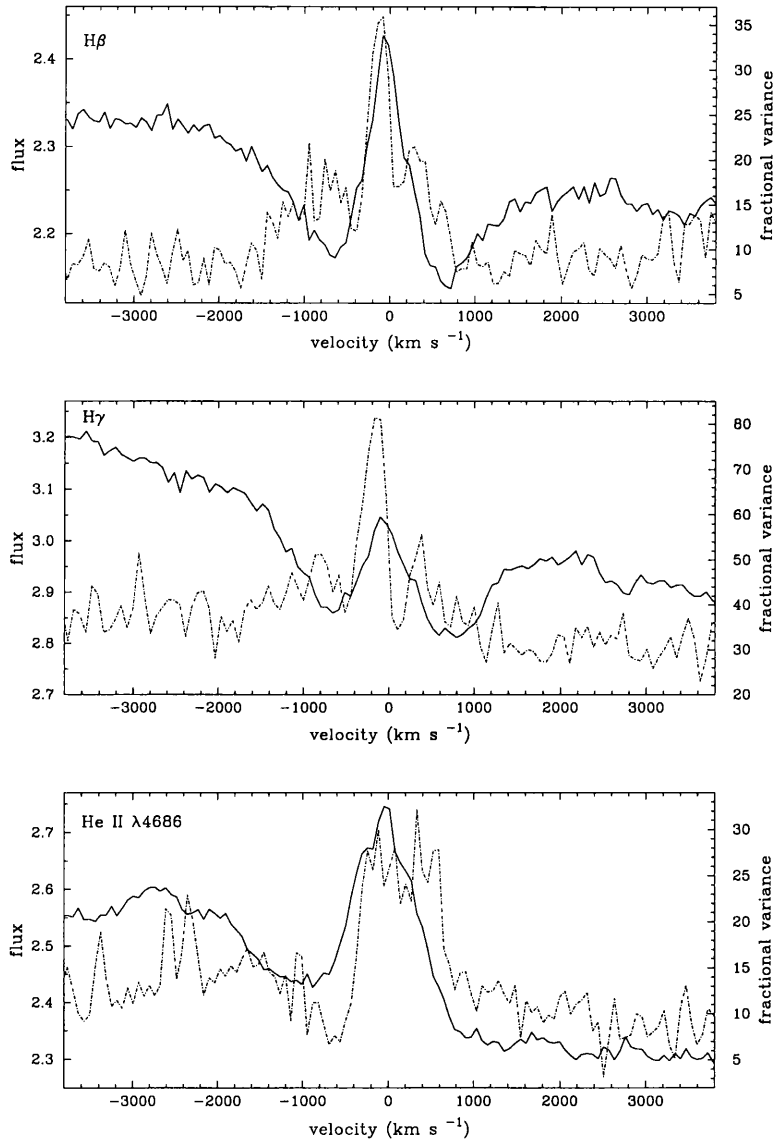

Figure 4.5: The fractional variance plotted over the mean Hβ (top panel), Hγ (middle panel) and He II λ4686 (bottom panel) line profiles, in velocity space, for the combined data sets D and E. The solid line shows the mean profile and the dotted line shows the fractional variance.

4.3.2 Line profile structure

The data from sets D and E were folded into 20 phase bins using the orbital ephemeris of Hessman *et al.* (1984; this choice of ephemeris is discussed by Martínez-Pais *et al.* 1994):

$$T_0 = HJD - 2\,444\,841.86824 + 0.27512973N \tag{4.2}$$

and

$$\phi = \frac{t - 2\,444\,841.86824}{0.27512973} + 0.25. \tag{4.3}$$

$\phi = 0.0$ corresponds to the inferior conjunction of the secondary star. There are typically 4 individual spectra per phase bin. Two montages of the 20 phase bins covering the Hβ line and the He II λ4686 line are shown in Figure 4.6. Some changes in the line profiles can be seen between set D (solid line) and set E (dotted line) in the phase bins that are covered by both data sets. In particular there is increased emission redward of the line centre at $\phi = 0.475$, and increased emission from -800 to $+800$ km s^{-1} at $\phi = 0.525 - 0.625$ in both the Hβ and the He II λ4686 lines. In view of such changes, the combination of these two data sets to gain a complete orbital cycle of coverage must be carried out with caution.

The Hβ line profiles (left-hand panel of Figure 4.6) show variable emission sitting on a broad, shallow absorption feature. The double-peaked nature of the line is less obvious than in the mean profiles (Figure 4.4) and there is clearly some radial velocity motion of the emission taking place. The He II λ4686 line profiles also appear to have a multi-component structure, possibly with a low velocity emission component filling in the gap between two peaks.

Figures 4.7, 4.8 and 4.9 are trailed spectrograms of the Hβ, Hγ and He II λ4686 profiles versus orbital phase for the combined data sets D and E. They show both the raw data and spectra which have been normalised in an attempt to reveal any small scale variations (in a manner similar to the way normalised data revealed small scale variations more clearly for V795 Her; *e.g.* see panel (c) of Figure 2.7). From top to bottom, the panels show greyscales of the raw data, the raw data divided by a minimum flux template, the raw data divided by the mean flux, and a greyscale of the difference spectra, created by subtracting the mean template from the individual spectra. In Figures 4.7 and 4.8 (Hβ and Hγ) the left-hand panels show the velocity regime $-3000 < v < 3000$ km s^{-1} and the right-hand panels show a close-up of the behaviour in the region $-1300 < v < 1300$ km s^{-1}.

The Hβ greyscales (Figure 4.7) display a clear s-wave feature that is phased with the secondary

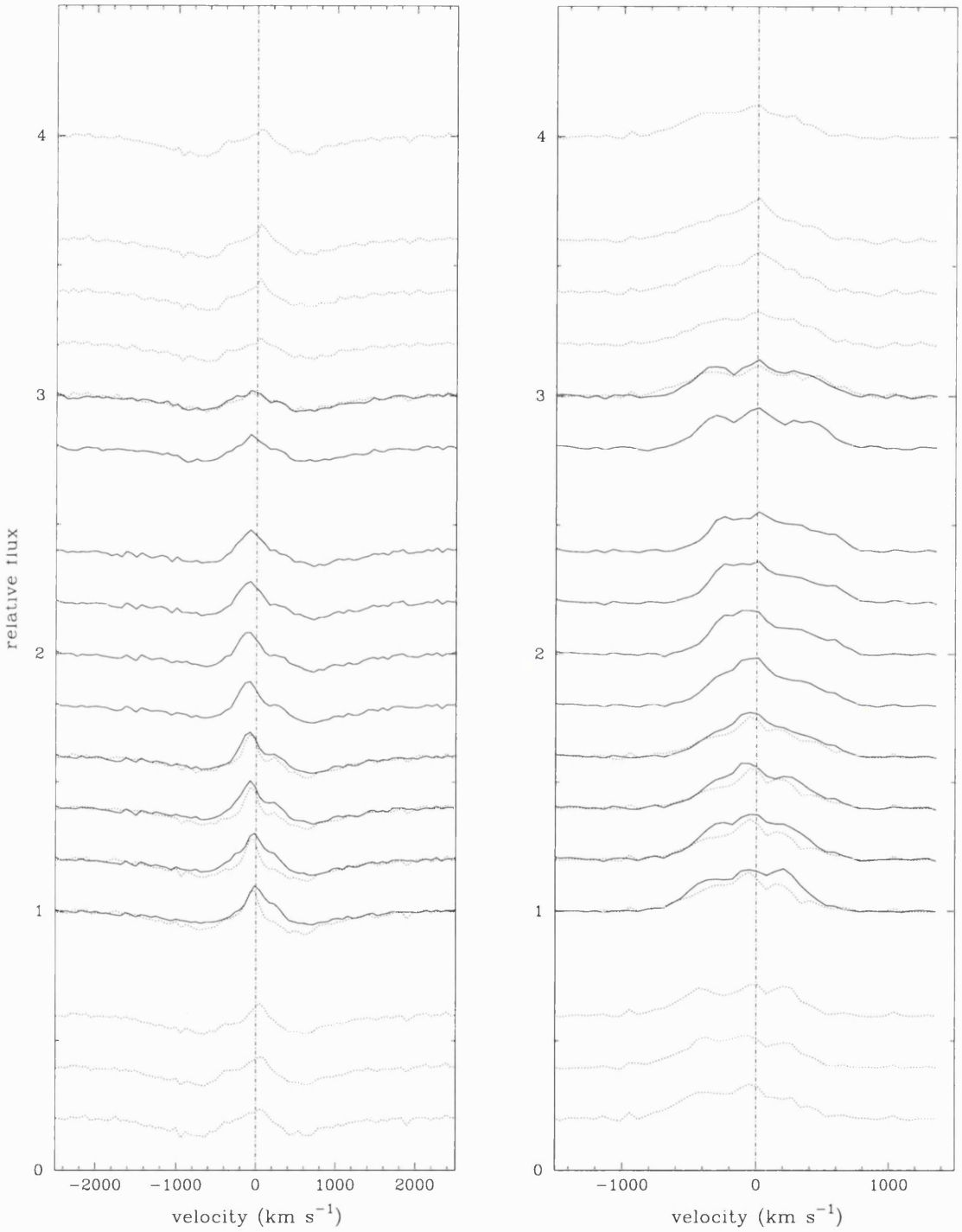

Figure 4.6: Montage of 20 phase bins for Hβ (left) and He II λ4686 (right). Data from set D is shown with the solid line and from set E with the dotted line. The dot-dash line indicates the rest velocities of the respective lines.

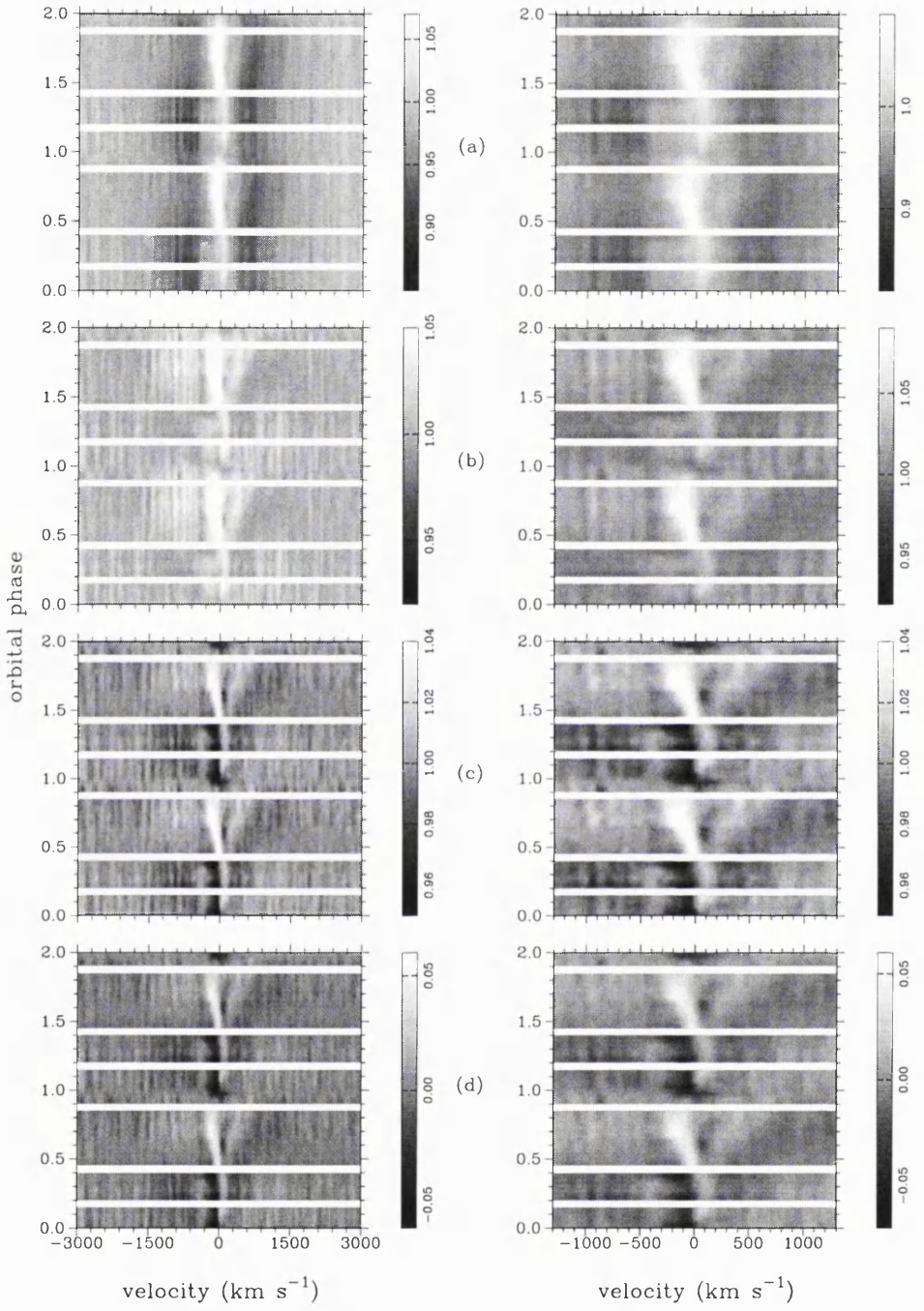

Figure 4.7: Trailed spectrograms of the Hβ line profile changes as a function of orbital phase. The left-hand panels shows the velocity range -3000 to $+3000$ km s^{-1} and the right-hand panels show a close-up of the behaviour in the velocity range -1300 to $+1300$ km s^{-1}. From top to bottom, panel (a) shows the raw data, panel (b) shows the data normalized by dividing the raw data by a minimum flux template, panel (c) shows the data normalized by dividing the mean flux and panel (d) shows the difference spectra, created by subtracting the mean template from the individual spectra.

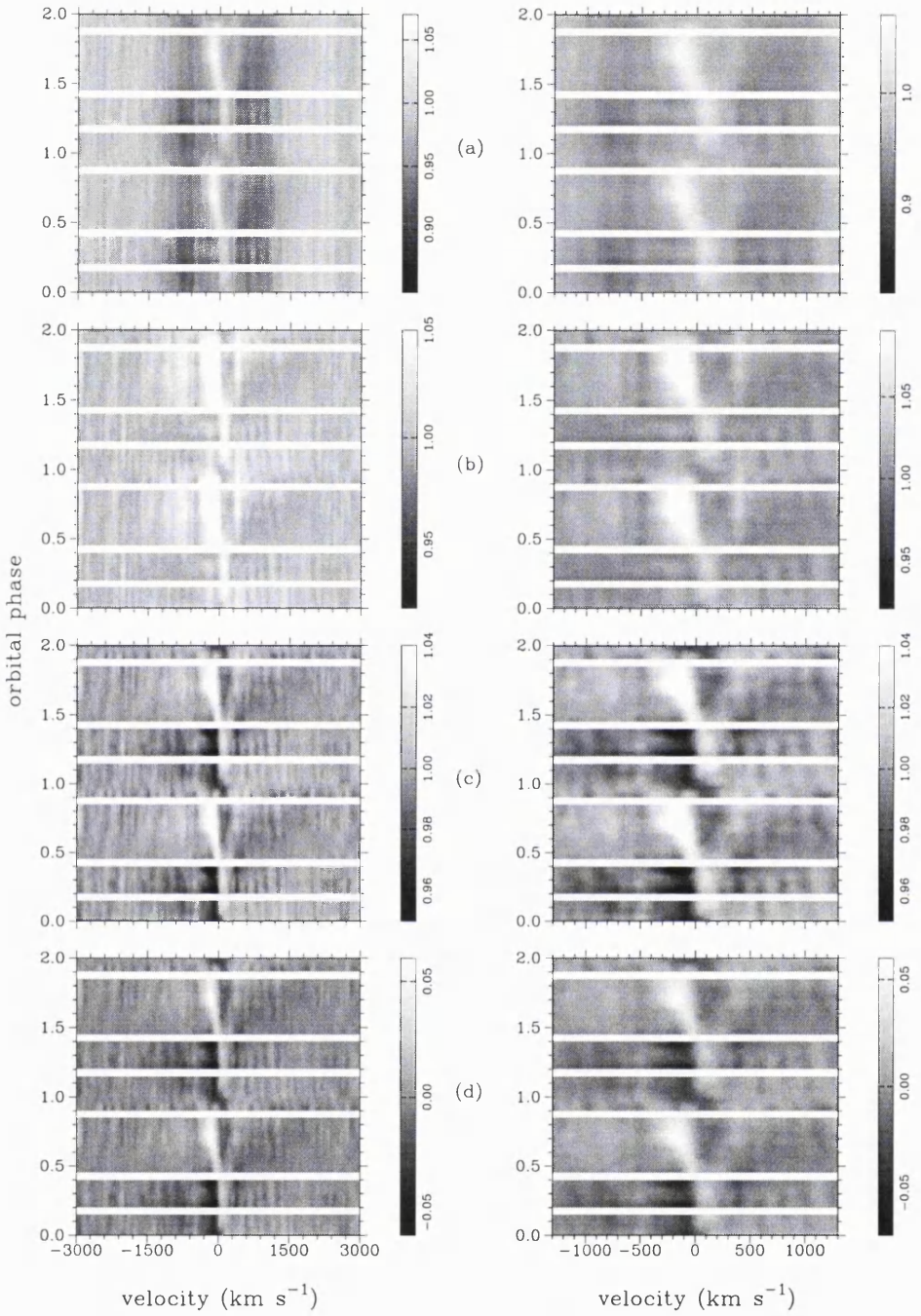

Figure 4.8: Trailed spectrograms of the Hγ line profile changes as a function of orbital phase. The left-hand panels shows the velocity range -3000 to $+3000$ km s^{-1} and the right-hand panels show a close-up of the behaviour in the velocity range -1300 to $+1300$ km s^{-1}. From top to bottom, panel (a) shows the raw data, panel (b) shows the data normalized by dividing the raw data by a minimum flux template, panel (c) shows the data normalized by dividing the raw data by the mean flux and panel (d) shows the difference spectra, created by subtracting the mean template from the individual spectra.

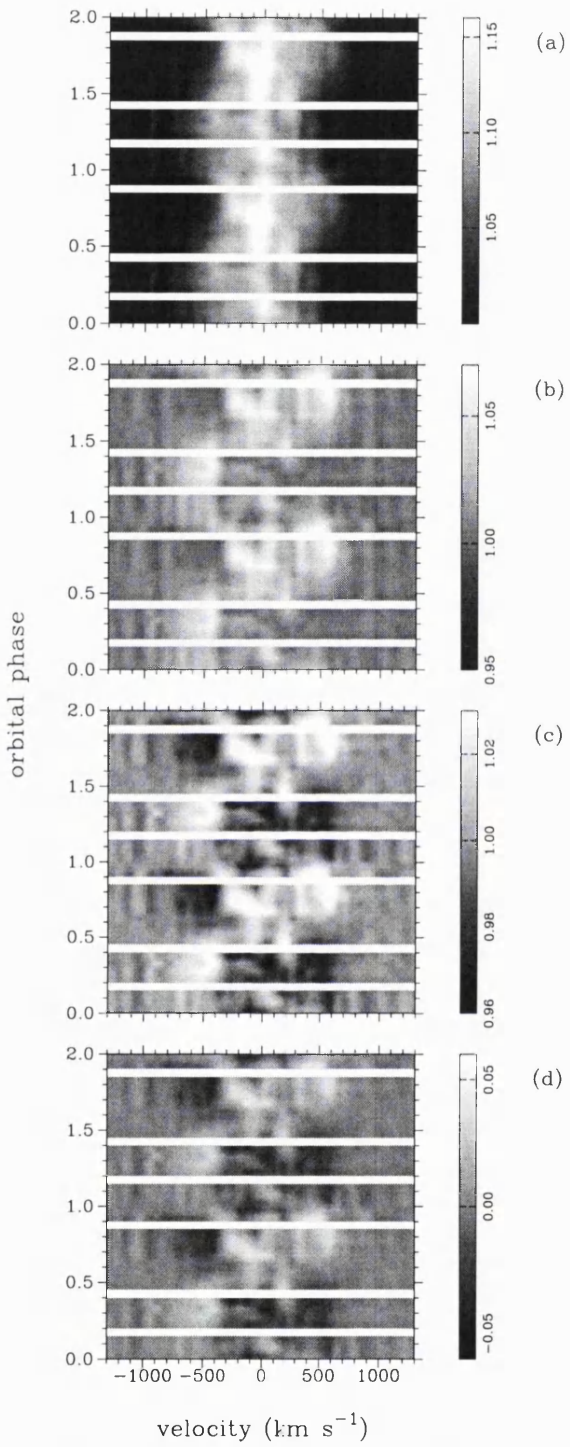

Figure 4.9: Trailed spectrograms of the He II λ4686 line profile changes as a function of orbital phase. From top to bottom, panel (a) shows the raw data, panel (b) shows data normalized by a minimum template, panel (c) shows data normalized by the mean and panel (d) shows the difference spectra.

star and that has a systematic velocity shift from the line centre, $\gamma \sim -15$ km s^{-1}, and a semi-amplitude of ~ 160 km s^{-1}. From the greyscales covering the wider velocity range (left-hand panels) it appears that the edges of the absorption feature (at ± 600 km s^{-1}) exhibit a radial velocity motion (semi-amplitude ~ 100 km s^{-1}) that is in anti-phase with the motion of the secondary star. There is little evidence in the greyscales created with the normalised spectra of the type of high velocity ($|v| > 1000$ km s^{-1}) variations such as were seen in V795 Her (*e.g.* Figure 2.7). The greyscales produced by the Hγ line profiles (Figure 4.8) closely follow the behaviour of the Hβ greyscales. Again, there is clearly an *s*-wave that is phased with the secondary star, and an anti-phased radial velocity motion in the Hγ absorption feature. The greyscales of the He II λ4686 line (Figure 4.9) indicate the presence of stationary low velocity emission centred on ~ -50 km s^{-1} and of width ~ 100 km s^{-1}. This feature appears to be stronger at $\phi = 0.1$ and $\phi = 0.6$. The greyscales of the raw data (top panel) also display emission between ± 600 km s^{-1}, which shows a clear radial velocity motion (semi-amplitude ~ 100 km s^{-1}) that may arise from the accretion disk.

4.3.3 Velocity characteristics

Simple Gaussian fittting was carried out to both the Hβ and the He II λ4686 profiles to examine the velocity characteristics of the lines. For the Hβ line double Gaussian profiles were used, one to fit the wide, shallow absorption component and the other to fit the emission core. In the case of He II λ4686, only one Gaussian was fitted to the profile. The central velocity of the Gaussian, its width and its strength were all free parameters. The results of these fits are shown in Figures 4.10 and 4.11. The Hβ absorption component clearly maps the radial velocity of the primary ($K_1 = 92$ km s^{-1} from Table 4.1), which suggests it has a disk origin. As would be expected, the fit to the emission component is less clear-cut: this component is likely to be made up by contributions from both secondary star and disk emission. There appears to be some behaviour that is anti-phased with respect to the behaviour of the absorption and is probably due to the secondary star emission (see Figure 4.15). The radial velocity changes revealed by the one component Gaussian fit to the He II λ4686 line are in phase with the motion of the primary star, indicating a disk origin for at least some component of this line. The values obtained for the FWHM of the profile fits to the Hβ emission component does not show any obvious systematic behaviour. The Hβ absorption component may be varying in strength, with minimum FWHM at $\phi \sim 0.2$ and maximum FWHM at $\phi \sim 0.7$. The He II λ4686 emission may also show strength modulations, with minimum at $\phi \sim 0.6$ and maximum at $\phi \sim 1.0$.

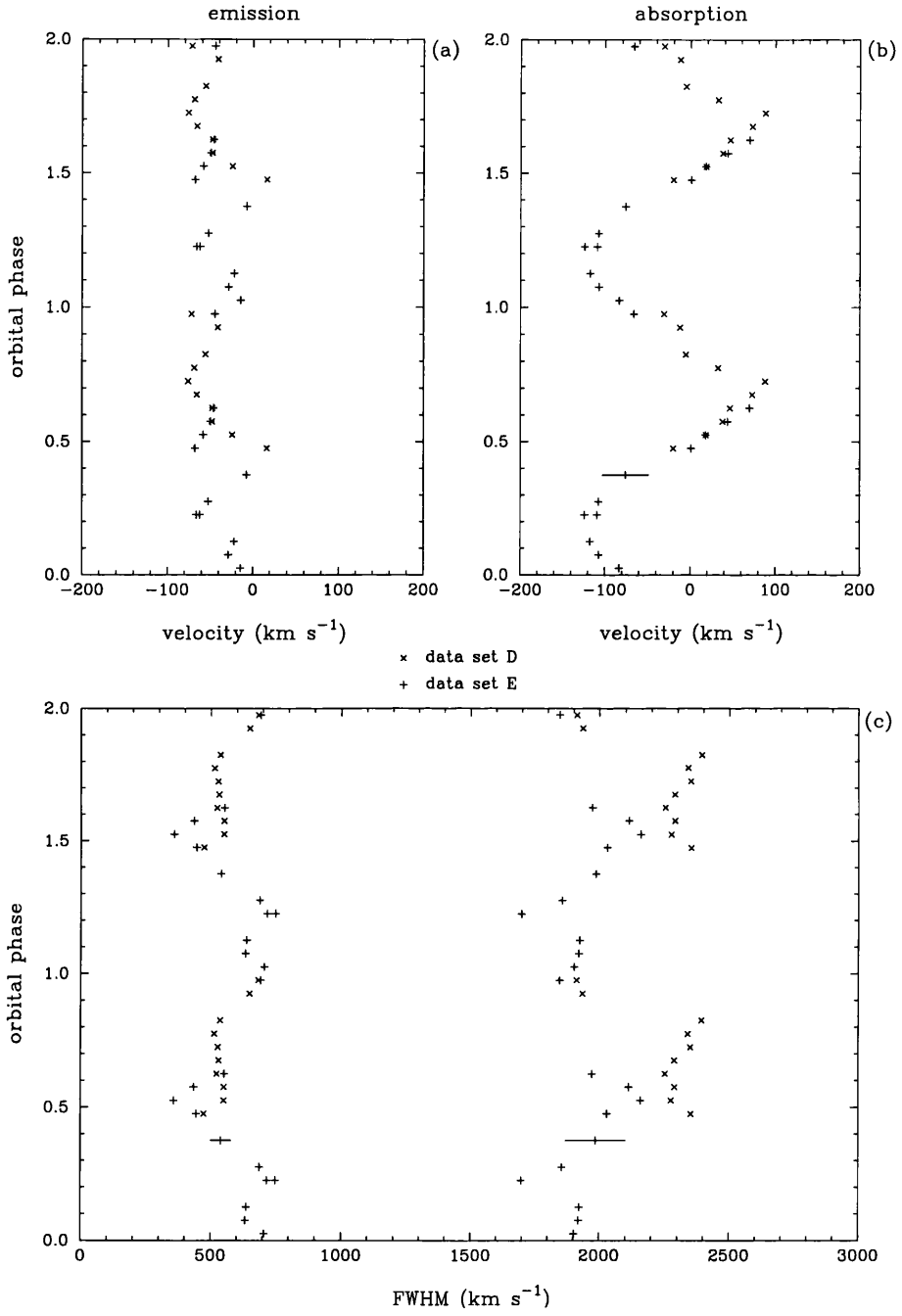

Figure 4.10: Simple double Gaussian fit to the Hβ line profiles. Panel (a) shows the central velocity of the fit to the emission component, panel (b) the central velocity of the fit to the absorption component, and panel (c) the FWHM of the fits. Data set D is represented by crosses and data set E by plus signs. Typical error bars are marked in panels (b) and (c) for the points at $\phi = 0.375$. (The error bars for panel (a) are less than the size of the symbols used to mark the points).

The values obtained for the radial velocities from the fit to the Hβ absorption component clearly show that data sets D and E are compatible. The smooth transition seen in Figure 4.10 justifies their combination into a data set with full phase coverage. The measurements of the FWHM show a poorer compatibility between data sets D and E. This is due to the increased emission noticed in Figure 4.6 in the phase interval $\sim 0.5-0.6$. It would appear that it is the overall flux level, and not the velocity characteristics themselves, that are changing between the two data sets.

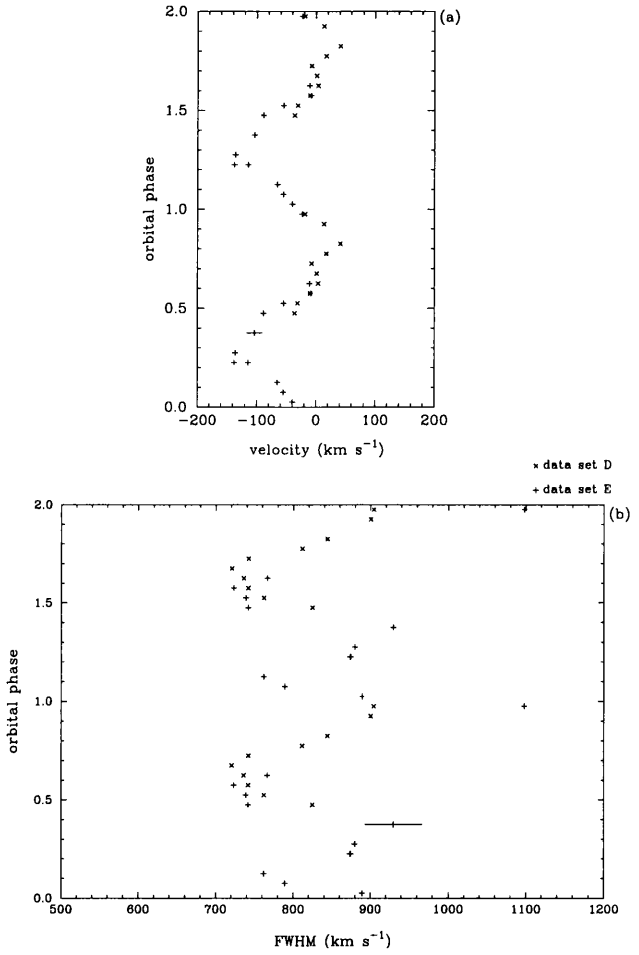

Figure 4.11: Simple Gaussian fit to the He II λ4686 line profiles. Panel (a) shows the central velocity of the fit to the emission component and panel (b) the FWHM of the fit. Data set D is represented by crosses and data set E by plus signs. Typical error bars are marked for the points at $\phi = 0.375$.

It is worth noting here that any conclusions drawn from this very simple profile fitting should be considered in light of the Doppler mapping presented in Section 4.4 (see Figures 4.15 and 4.16), which is able (subject to the constraints discussed in Section 1.3) to reveal the complex multi-component behaviour in greater detail.

Figure 4.12 shows the light curves as a function of velocity within the Hβ line profile. The profile was split into velocity strips 500 km s^{-1} wide and the flux in each velocity bin measured for each phase bin. The velocity bins [-1500, -1000 km s^{-1}], [-1000, -500 km s^{-1}], [500,1000 km s^{-1}] and [1000, 1500 km s^{-1}] show the most obvious modulations. The two bins blueward of the line centre ([-1500, -1000 km s^{-1}] and [-1000, -500 km s^{-1}]) behave in a correlated manner, and in anti-phase to the corresponding redward bins. This behaviour can be interpreted as being due to the motion of an absorption feature of approximately constant depth and width. The absorption would then be blueshifted at $\phi = 0.25$ and redshifted at $\phi = 0.75$. This modulation is phased with the WD (and therefore the accretion disk), and this interpretation is favoured because the absorption is thought to arise in the hot, inner regions of the accretion disk. Velocity bin [-500, 0 km s^{-1}] also shows modulated behaviour, with maximum flux at $\phi \sim 0.7$ and minimum flux at $\phi \sim 0.2$. This variation is likely to be caused by a combination of the motion of the absorption feature, described above, and the radial velocity motion of emission from the secondary star. The secondary is redshifted at $\phi = 0.25$ and blueshifted at $\phi = 0.75$. There is no clear modulation in the [0, 500 km s^{-1}] velocity bin.

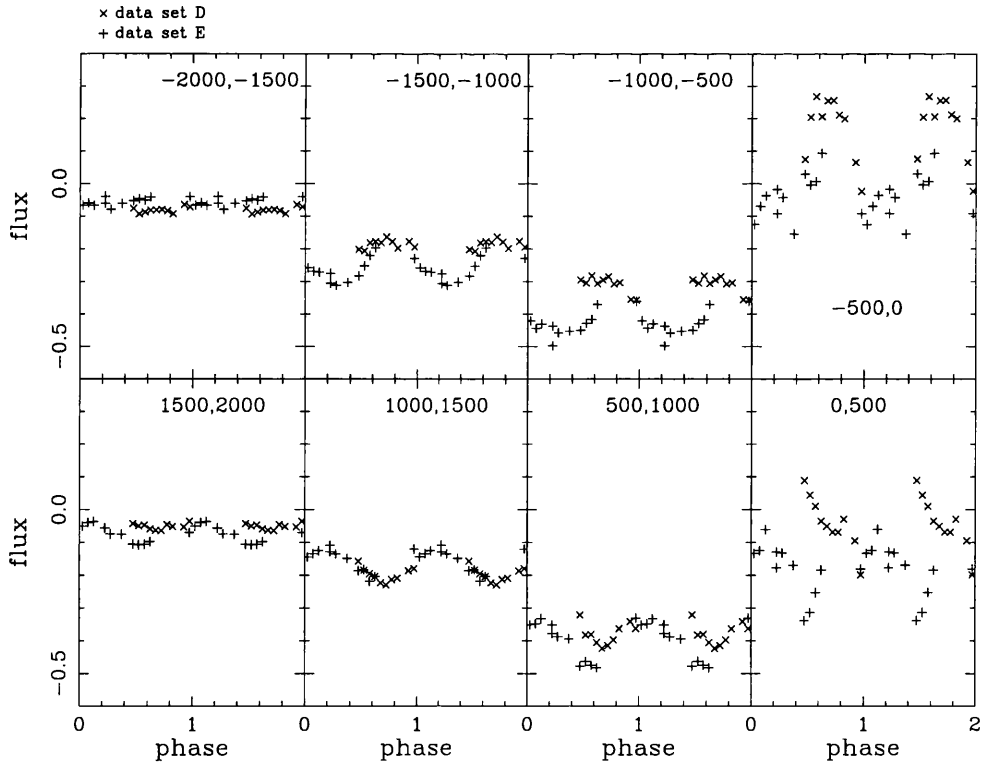

Figure 4.12: Light curves as a function of velocity within the Hβ line profile.

The light curves as a function of velocity across the He II λ4686 line profile were also measured and are shown in Figure 4.13. The modulations seen in velocity bins [-750, -500 km s^{-1}] and [-500, -250 km s^{-1}] are correlated, with maximum flux at $\phi \sim 0.3$ and minimum flux at $\phi \sim 0.8$. These modulations are in anti-phase with the modulations in velocity bins [250, 500 km s^{-1}] and [500, 750 km s^{-1}] and are probably caused by the radial velocity motion of emission from the accretion disk. The variations are phased with the primary star which is blueshifted at $\phi = 0.25$ and redshifted at $\phi = 0.75$.

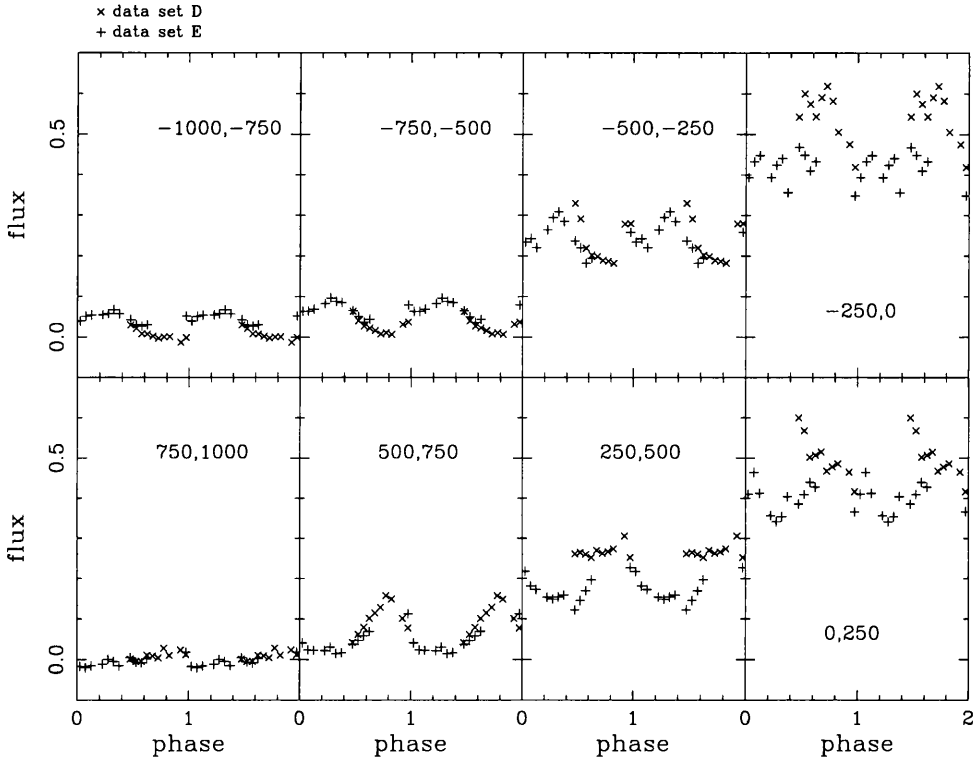

Figure 4.13: Light curves as a function of velocity within the He II λ4686 line profile.

The most central velocity bins ([-250, 0 km s^{-1}] and [0, 250 km s^{-1}]) of the He II λ4686 line may be affected by low velocity stationary emission (Steeghs *et al.* 1996). Figure 4.14 compares the emission in the central velocity bin [0, 250 km s^{-1}] with the behaviour of velocity bin [250, 500 km s^{-1}]. The modulations in velocity bin [250, 500 km s^{-1}] have been interpreted as being due solely to accretion disk emission. If there is low velocity stationary emission present in velocity bin [0, 250 km s^{-1}], the only difference between the two velocity bins should be the addition of a constant amount of flux, as the low velocity is 'stationary' and therefore exhibits no radial velocity motion. It is clear from Figure 4.14 that once a constant has been added to the flux in velocity bin

[250, 500 km s^{-1}], the flux changes are well correlated with the flux changes in velocity bin [0, 250 km s^{-1}]. This correlation supports the presence of low velocity stationary emission.

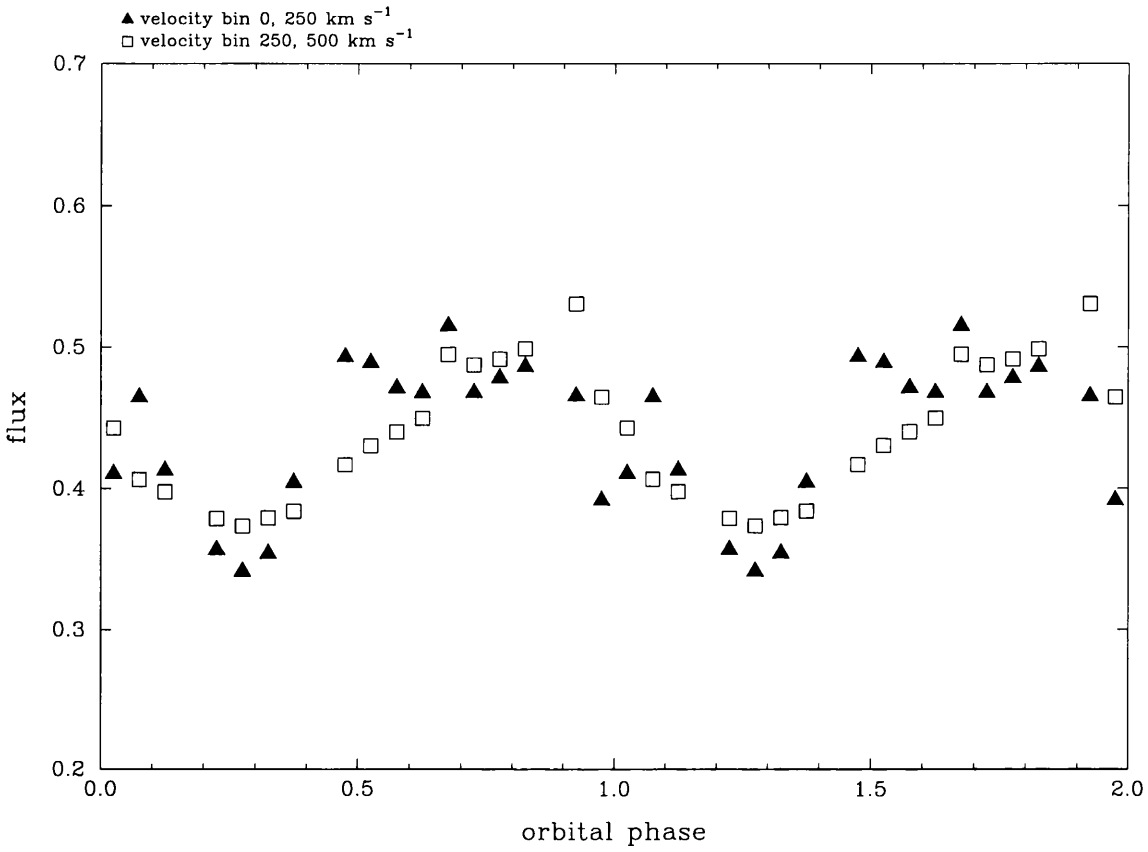

Figure 4.14: Comparison of the flux levels in velocity bins [0, 250 km s^{-1}] and [250, 500 km s^{-1}] within the He II λ4686 line profile. The solid triangles show data from the velocity bin [0, 250 km s^{-1}] and the open squares show data from the velocity bin [250, 500 km s^{-1}] to which a constant amount of flux has been added.

The key findings of Section 4.3 are summarised below.

1. The success of the profile fitting shows that data sets D and E *can* be combined to provide a full orbital cycle of coverage. It appears that it is only the overall flux level (rather than than the velocity characteristics themselves) that change between data sets D and E.

2. The Hβ and Hγ lines show a multi-component emission feature sitting on an absorption feature. The absorption feature extends to $\pm$600 km s^{-1} and its radial velocity motion has a semi-amplitude of $\sim$ 100 km s^{-1}. This motion follows the radial velocity motion of the primary star, and is suggestive of a disk origin. The emission seems to consist of contributions

from the secondary star and from the accretion disk. The trailed spectrograms show a distinct s-wave feature that is phased with the secondary star.

3. The He II λ4686 line displays emission that extends to ± 600 km s^{-1} and which has a radial velocity motion of semi-amplitude ~ 100 km s^{-1}, phased with the primary star. This is suggestive of an accretion disk origin. The trailed spectrograms reveal a stationary, low velocity emission feature centred on ~ -50 km s^{-1} and of width ~ 100 km s^{-1}, that appears to be strongest at $\phi = 0.1$ and $\phi = 0.6$. A comparison of the flux levels versus orbital phase for the central velocity bins of the He II λ4686 line confirms the presence of this stationary low velocity emission feature.

4.4 Doppler imaging

Doppler images of the optical emission lines were constructed to aid the interpretation of the line profile changes. The technique of Doppler imaging is discussed in Section 1.3 and Appendix A. Figure 4.15 shows the Doppler map for the Hβ line, constructed with the combined data sets D and E, using 39 phase bins. Caution must be applied when interpreting these Doppler maps as there may be some contamination by the underlying, possibly Stark broadened, absorption component. The Hβ Doppler map reveals a ring of accretion disk emission. The smoothness, in intensity, of the ring suggests that there is little azimuthal structure. Emission from the Roche lobe of the secondary star ($V_X, V_Y \sim 0, 150$ km s^{-1}) is also present. It is concentrated on the front part of the Roche lobe and is probably caused by the illumination of the secondary star by the outburst-brightened accretion disk. Some emission is seen near the centre of mass, outside the Roche lobe ($V_X, V_Y \sim -50, 0$ km s^{-1}). This is the stationary, low velocity emission reported by Steeghs *et al.* (1996).

The stationary, low velocity emission is seen much more clearly on the Doppler map of the He II λ4686 line (Figure 4.16). In this case there is almost no emission coming from inside the Roche lobe of the secondary. Non-axisymmetric disk emission is indicated by the enhanced emission in the upper right and lower left regions of the ring. This feature was again reported by Steeghs *et al.* (1996).

The third set of Doppler images (Figure 4.17) shows the mapping of the Hγ line. This map is similar to the Hβ map: there is a smooth ring of emission from the accretion disk and there is emission from the front part of the Roche lobe. There does not appear to be any low velocity stationary

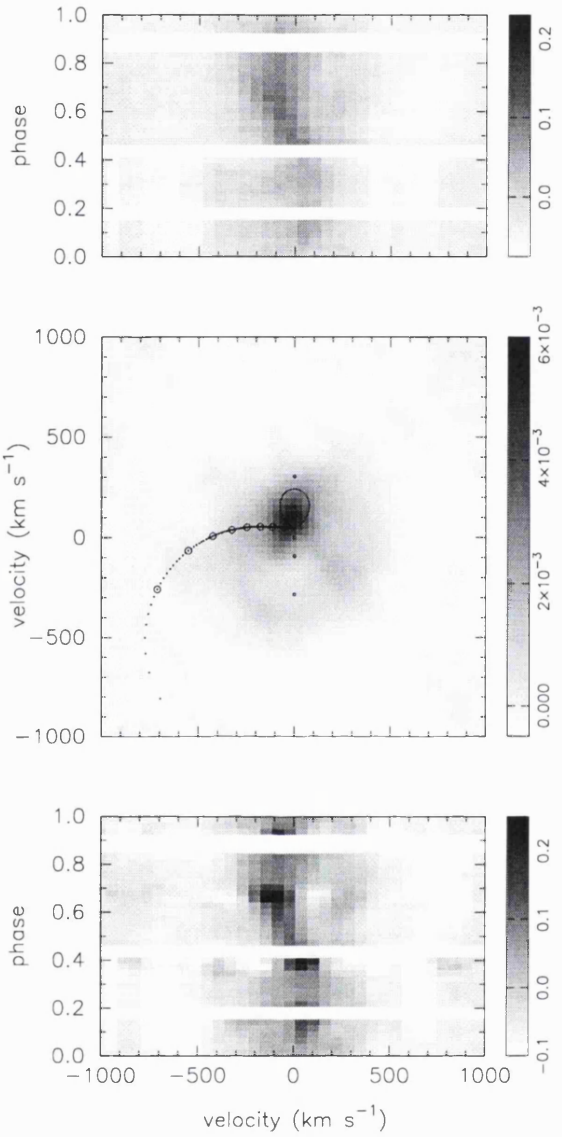

Figure 4.15: Doppler imaging of the Hβ line. From top to bottom, the panels show the trailed spectrogram of the input data, the Doppler map, and the predicted trailed spectrogram. The Roche lobe of the secondary star and the gas stream have been plotted on the tomogram, as has the centre of mass (the cross at the origin) and the position of the WD (the dot at 0, -155 km s^{-1}). The Roche lobe is calculated using the system parameters (see Table 4.1), and the gas stream is calculated from the ballistic trajectory of a single particle.

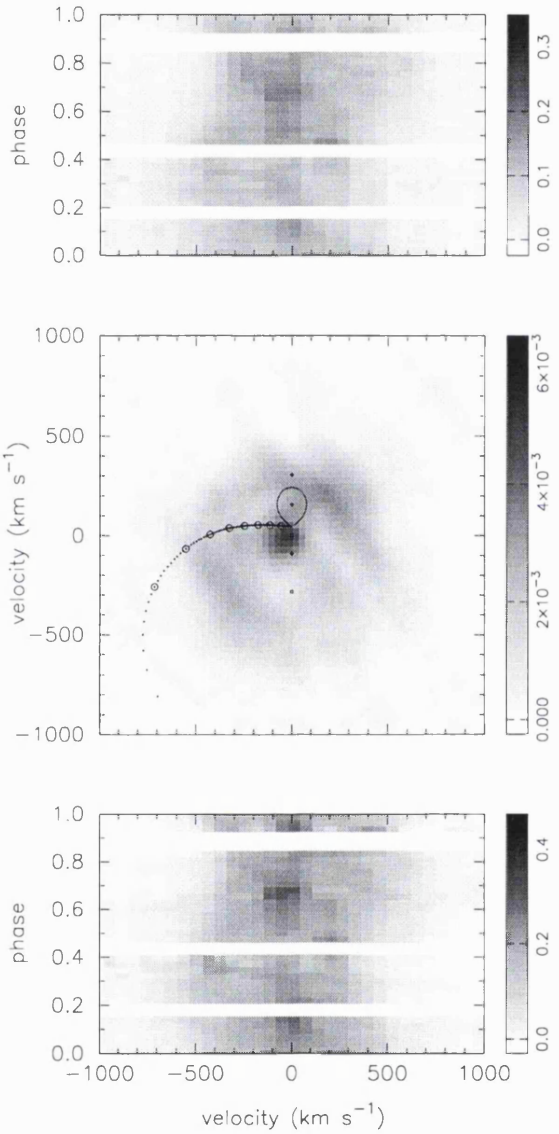

Figure 4.16: Doppler imaging of the He II λ4686 line. From top to bottom, the panels show the trailed spectrogram of the input data, the Doppler map, and the predicted trailed spectrogram.

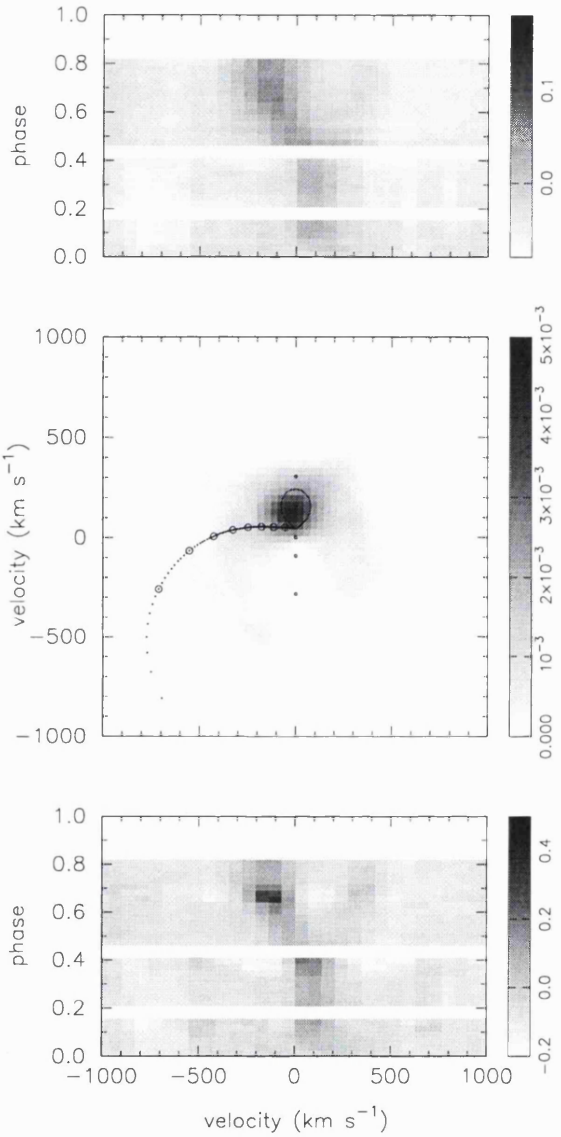

Figure 4.17: Doppler imaging of the Hγ line. From top to bottom, the panels show the trailed spectrogram of the input data, the Doppler map, and the predicted trailed spectrogram.

emission in this line. Once more, these maps are very similar to those produced by Steeghs *et al.* (1996).

This analysis aids the interpretation of the simple Gaussian fits, carried out on the Hβ and He II λ4686 lines in Section 4.3.3. The origin of the Hβ emission is obviously complex. There are contributions from the accretion disk, from the Roche lobe of the secondary star and from a stationary, low velocity component. Clearly these different components will have different phasings and therefore one would not expect to be able to fit them particularly well with one Gaussian profile (as used in Section 4.3.3; see also Figure 4.10). Unfortunately the different components cannot be distinguished due to line broadening, and it is impossible to decouple their behaviour.

4.5 The stationary, low velocity emission

This study confirms the presence of the stationary, low velocity emission component in SS Cyg, reported on recently by Steeghs *et al.* (1996). It is recognized most easily in the He II λ4686 line (Figure 4.16). Low velocity emission has also been noted in IP Peg (Steeghs *et al.* 1996; Marsh & Horne 1990), previously in SS Cyg (Clarke, Capel & Bowyer 1984) and in several other CVs (Smak 1981). Several possible sources for such stationary, low velocity emission have been postulated. Suggestions include gas stream emission (Shafter, Hessman & Zhang 1988), inflowing magnetic accretion or an outflowing wind (Marsh & Horne 1990), and emission from material held in place by magnetic loops that co-rotate with the secondary star (Steeghs *et al.* 1996). These different scenarios are discussed below.

4.5.1 Gas stream emission?

Low velocity emission has been seen to fill in the centre of the Balmer and He I lines in the eclipsing nova-like variable DW UMa. Shafter, Hessman & Zhang (1988) suggest that this emission may arise in the vicinity of the hot spot or in the gas stream. The behaviour of DW UMa does differ somewhat from that of SS Cyg: the Balmer and He I line profiles appear to be single-peaked for most of the orbital cycle and then become doubled between phases 0.4 and 0.6. These observations of SS Cyg show multi-component Balmer lines, while the He II λ4686 line exhibits a low-velocity emission component that fills in the gap between the double peaks for the entire orbital cycle. Shafter, Hessman & Zhang postulate that either the hot spot or the mass transfer stream

(or both) contribute significantly to the Balmer and He I emission in DW UMa, thus filling in the normally double-peaked disk profiles. The doubling seen around phase 0.5 is then caused by the occultation of this extra emission source.

This idea does not, however, seem to provide a plausible explanation for the low velocity emission in SS Cyg, where the emission is seen to be stationary (Figure 4.16). If the emission source is indeed the gas stream or the hot spot, then it should exhibit a radial velocity motion. As there is no part of the gas stream which is at rest with respect to the centre of mass of the system it seems unlikely that the gas stream can be responsible for the low velocity stationary emission.

4.5.2 Inflowing magnetic accretion?

The dwarf nova IP Peg was observed during outburst by Marsh & Horne (1990). In addition to emission from the accretion disk, they also observe an emission feature which fills in the gap between the disk peaks. On the Doppler map, this feature is situated inside the ring of emission from the accretion disk and does not fall along the gas stream trajectory. The velocity of the stationary emission is < 100 km s^{-1}. A further constraint may be placed on this emission source from the fact IP Peg is an eclipsing system: Marsh & Horne are able to confine the emission to within a radius of $0.1a$ from the WD (where a is the binary separation).

Marsh & Horne (1990) suggest a magnetic inflow along the rotation axis as one possible mechanism to explain the stationary low velocity emission. In this model the WD's magnetic field captures the inner part of the accretion flow. If this model is correct then one may expect to observe events which occur on the WD spin period. Such events are observed in DQ Her stars (a subset of the IPs: magnetic systems in which the WD rotates asynchronously with respect to the binary and the accretion flow within a certain radius is governed by the WD's magnetic field). The WD rotation period in an IP is typically 350 – 4000 s and is usually determined from X-ray observations. Marsh & Horne do not favour magnetic inflow to explain the stationary emission they observe in IP Peg because no such events occur on IP Peg's WD spin period. This problem is also encountered when this model is applied to SS Cyg, whose WD spin period is unknown. Periods other than the 6.6 hr orbital period detected in this system include DNOs (dwarf nova oscillations: low amplitude periodic brightness modulations observed in DN during outburst) in the range 7.3 – 10.9 s (Patterson, Robinson & Kiplinger 1978; Horne & Gomer 1980; Hildebrand, Spillar & Stiening 1981) and QPOs (quasi-periodic oscillations: brightness oscillations with low coherency) with periods 32 –

36 s and 730 s (Bartolini *et al.* 1985; Arévalo, Solheim & Lazaro 1989).

A further problem in applying this model to both IP Peg and SS Cyg arises from the velocity of the stationary emission observed. In both systems the velocity observed is <100 km s^{-1}, whereas the inner portion of the accretion disk, and the accretion flow, are expected to be at much higher velocities.

4.5.3 Slingshot prominences?

Steeghs *et al.* (1996) were the first to suggest 'slingshot prominences' as an interpretation of the stationary, low velocity emission seen in SS Cyg. Prominences have been observed extensively in many single, rotating stars (*e.g.* Collier Cameron & Robinson 1989) and also in the Sun (*e.g.* Pneuman & Kopp 1971). In single, rotating dwarf stars clouds of mainly neutral material form in coronal loops and are tied to the confining field by collisions between neutral H atoms and protons. The summits of the coronal loops extend to just beyond the Keplerian co-rotation radius. The density of the cloud increases as material is fed from the loop footpoints, which in turn increases the outward centrifugal force acting on the loop. To balance this, the magnetic tension in the confining loop must also increase and so the entire loop structure bulges outwards. The clouds are seen to be moving radially outwards, with acceleration rates that are slower than that of a cloud allowed to move freely in an open, radial field. The coronal field confines the cloud both radially and longitudinally. Clouds are formed and destroyed on timescales of a few days. (Slingshot prominences in single rotating stars, *e.g.* the KO dwarf star AB Dor (Collier Cameron *et al.* 1990), have been detected as transient *absorption* features produced when the clouds pass between the observer and the stellar disk).

The geometry of a CV is clearly more complicated than that of a single star. Steeghs *et al.* (1996) suggest that the region between the inner Lagrangian point (see Section 1.1.1) and the WD would be able to maintain a stable magnetic loop. A dense clump of gas may form at the summit of the loop, confined by the magnetic field. If this clump is illuminated by the disk and the secondary star, an emission source will be observed that co-rotates with the secondary, resulting in low velocity, stationary emission.

Some supporting evidence for magnetic activity on the secondary star comes from a study by Bianchini (1987) on the detection of solar-type cycles in CVs. SS Cyg shows a variation on a timescale that is greater than the outburst timescale. Bianchini's study suggests that the presence of

a solar-type cycle in the late-type secondary star can modulate the mass transfer rate. This modulation then manifests itself as a periodic variation of the quiescent luminosity and also as a periodic variation in the time interval between successive outbursts. Bianchini (1987) reports variations in SS Cyg on a period of ~ 7.3 yr, which would then be the candidate timescale of the solar-type cycle of SS Cyg's secondary star. The 22 yr cycle of solar activity seen in the Sun (*e.g.* sunspot activity) is explained using a magnetic model. It is therefore reasonable to assign the presence of such solar-type cycles in the secondary stars of CVs to magnetic activity. Further evidence of magnetic activity comes from a study of IP Peg, carried out by Wood *et al.* (1989). They examine the high rate of increase of the orbital period and suggest that magnetic activity on the secondary star may be responsible for this increase.

Low velocity stationary emission has been observed on at least three occasions in SS Cyg (Clarke, Capel & Bowyer 1984; Steeghs *et al.* 1996; this study). If this theory of slingshot prominences is the correct explanation, one must now question why emission has not been reported that may arise from prominences on other parts of the secondary star. The prominences can in principle appear anywhere on the surface of the secondary. Even if the region between the inner Lagrangian point and the WD is a particularly favoured site for the existence of stable magnetic loops, one must also question why the stationary, low velocity emission has been seen only when SS Cyg is in outburst. The inner face of the secondary star is illuminated even when the system is in quiescence (Martínez-Pais *et al.* 1994), presumably by the inner accretion disk regions. There seems to be no reason why the inner accretion disk shouldn't illuminate a slingshot prominence during quiescence, nor is there any evidence to suggest that the surface of the secondary star is only likely to exhibit magnetic activity during an outburst.

The clouds seen in single, rotating stars are formed and destroyed on timescales of a few days. The data presented in this study do not provide particularly useful constraints on the temporal behaviour of the low velocity emission. The data from sets D and E (combined to produce the main data set analysed in Section 4.3) were recorded on two consecutive nights which means that the stationary low velocity emission persisted for at least 24 hours. The data of Steeghs *et al.* (1996) were recorded over only a 6 hour period. These time scales are at least consistent with the behaviour of single star prominences. In the observations of Clarke, Capel & Bowyer (1984) the 'low-velocity filling component' that they report on decays much more slowly than the rest of the disk. It appears to be present for ~ 10 days.

4.5.4 A wind origin?

As an alternative explanation for the stationary, low velocity emission displayed by IP Peg, Marsh & Horne (1990) suggest a wind origin. They propose that the WD in IP Peg drives a spherical wind. To satisfy the constraints imposed by the eclipse of the stationary emission by the secondary star, the spherical expansion must be fairly rapid in order for the density, and therefore the He II emission rate, to decrease sufficiently rapidly with radius such that He II emission is confined to within $\sim 0.1\,a$. The wind, however, must be relatively slow and steady because the velocity dispersion of the emitting material is very low.

As SS Cyg is already known to drive a wind during outburst (*e.g.* Prinja & Rosen 1995), it seems reasonable to attempt to apply this model to explain the low velocity, stationary emission observed in this system. The outburst UV wind properties of SS Cyg during this outburst are discussed in Section 4.6.3.

4.6 UV *IUE* outburst properties of SS Cyg

The UV data set was compiled after searching the *IUE* final archive and discovering 22 spectra of SS Cyg which were recorded *during the same outburst* covered by the optical data, in 1994 June/July (see Section 4.2 and Figure 4.2). The timings of the UV observations on the light curve are shown in Figure 4.18, which also shows the position of the optical INT observations.

The spectra in the *IUE* final archive have all been treated in a uniform manner which allows data from different epochs over the lifetime of *IUE* to be compared in a consistent manner (Nichols *et al.* 1993). The 11 images of SS Cyg retrieved from the archive were taken with the short wavelength (SWP) camera in low dispersion mode. They cover the wavelength range $\lambda\lambda 1150 - 1980$ Å with a resolution of ~ 6 Å. Each image was exposed in both the large and small apertures, which gives 22 spectra in total. The image numbers are given in Table 4.4, along with the labels (F – K) used in this study to identify the different groups of spectra (see Figure 4.18). A log of the *IUE* archive spectra is given in Table B.5.

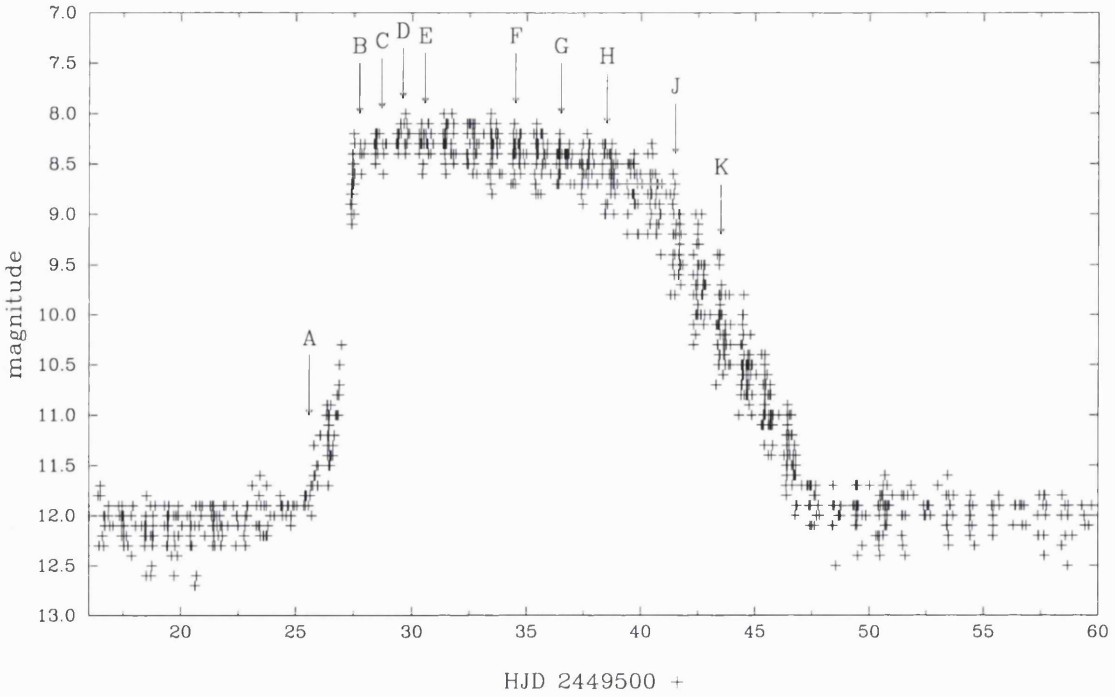

Figure 4.18: The position of the UV *IUE* observations on the SS Cyg light curve. Labels F – K refer to the 5 UV data sets described in Table 4.4, and labels A – E to the 5 optical data sets described in Table 4.3. This light curve was created using data from the AAVSO International Database, based on observations submitted to the AAVSO by variable star observers worldwide.

image number	date	number of spectra	data set label
SWP 51280 – 51282	94-JUL-01	4	F
SWP 51304 – 51306	94-JUL-03	4	G
SWP 51325 – 51327	94-JUL-05	4	H
SWP 51372 – 51373	94-JUL-08	4	J
SWP 51391 – 51393	94-JUL-10	6	K

Table 4.4: The *IUE* observations of SS Cyg.

4.6.1 The UV line and continuum properties

The mean spectrum from each group of spectra F – K (see Table 4.4) is shown in Figure 4.19. The overall flux level decreases from F to K as the system begins its decline from outburst (see Figure 4.18). The C IV $\lambda\lambda$1550 and N V $\lambda\lambda$1240 resonance lines are present in the mean spectrum of each group. The C IV line clearly shows a P Cygni-type profile, indicative of mass loss (see Section 1.2.1). UV *IUE* observations of SS Cyg in quiescence do not show any evidence of P Cygni-type profiles (Lombardi, Giovanelli & Gaudenzi 1987). This profile shape persists even up to group K, by which time the visual magnitude has decreased to mid-way between its outburst and quiescent values (see Figure 4.18). The He II λ1640 line decreases in strength from F to J and is not present in the mean spectrum of group K. A weak detection of the Si II / Si III / O I blend around $\lambda\lambda$1300 Å is made but the Si IV doublet ($\lambda\lambda$1400) is not detected in this data set. The shape of the continuum slope does not appear to change from F to K.

Figure 4.20 shows the behaviour of the continuum, and of the He II λ1640 and C IV $\lambda\lambda$1550 lines as the outburst progresses. The mean flux in the line-free continuum band $\lambda\lambda$1419 – 1470 Å was measured for each individual spectrum and plotted against the mid-exposure time. The continuum level shows a steady decline. (The levels recorded in the large and small apertures are significantly different, and have been plotted using different symbols; the filled triangles show data from the large aperture and the open squares show data from the small aperture. It should be noted that the flux levels recorded are very unreliable, even when carrying out relative photometry). The same behaviour is seen for the He II λ1640 line, where the total integrated flux above the continuum was measured. The total integrated flux below the C IV $\lambda\lambda$1550 resonance line was also measured for each individual spectrum. There is a decline in absorption strength from F to K. Finally, the flux ratio between the continuum bands $\lambda\lambda$1419 – 1470 Å and $\lambda\lambda$1742 – 1801 Å was measured. The flux ratio is fairly constant, confirming the earlier observation that the continuum slope is not varying from F to K (Figure 4.19).

The mean, rectified C IV $\lambda\lambda$1550 resonance line profiles for each group F – K are shown in Figure 4.21. The profiles were rectified by the division of a first order polynomial that was fitted to the continuum regions on either side of the line profile. There do not seem to be any gross changes in the line profile shape over the course of the observations. The blueward absorption extends to $\sim -4500\,\mathrm{km\,s^{-1}}$ (the velocity scale is with respect to the weighted mean of the C IV doublet, 1549.05 Å). This value is probably an overestimate of the wind's terminal velocity as the

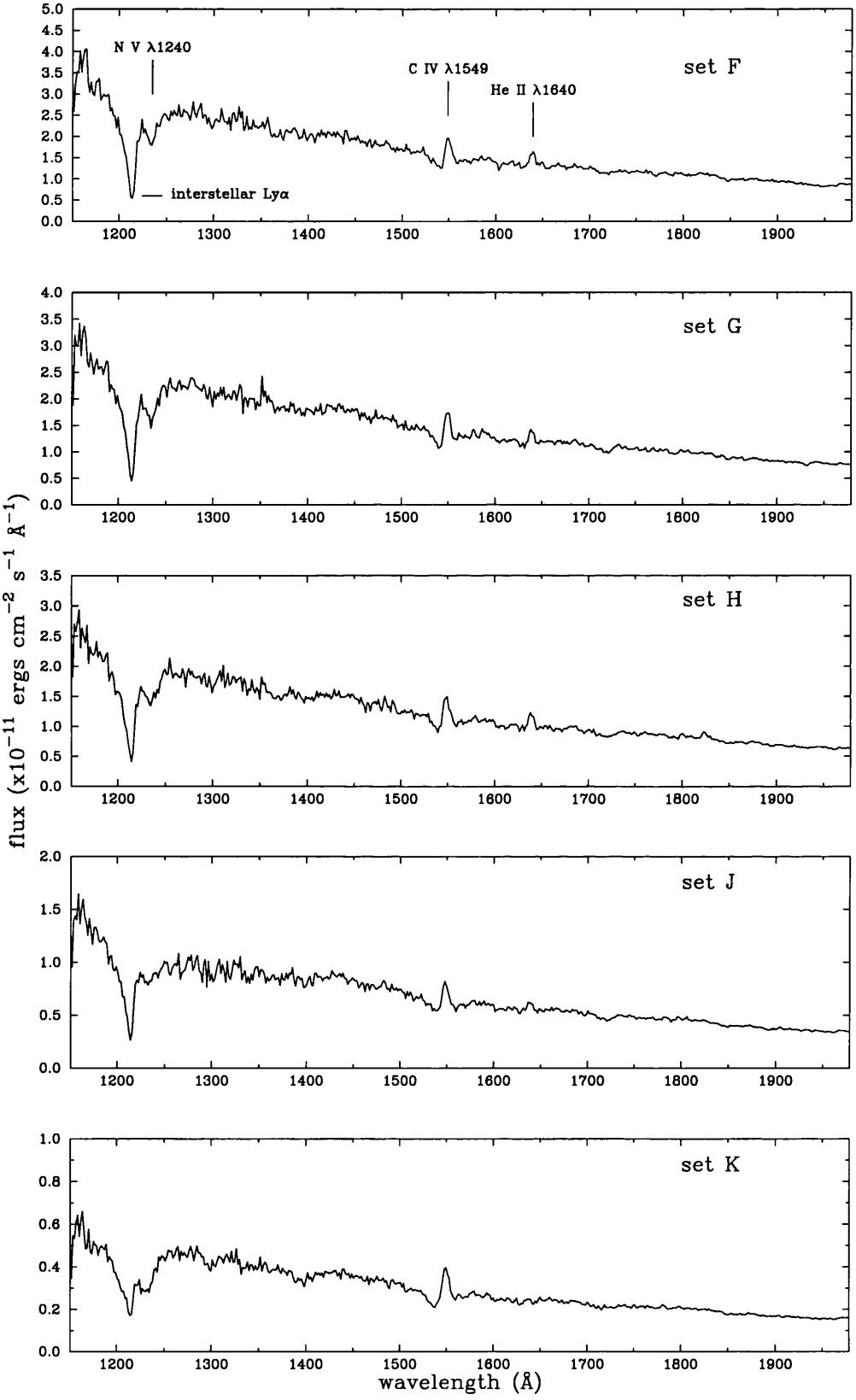

Figure 4.19: The mean spectra from data sets F – K (see Table 4.4).

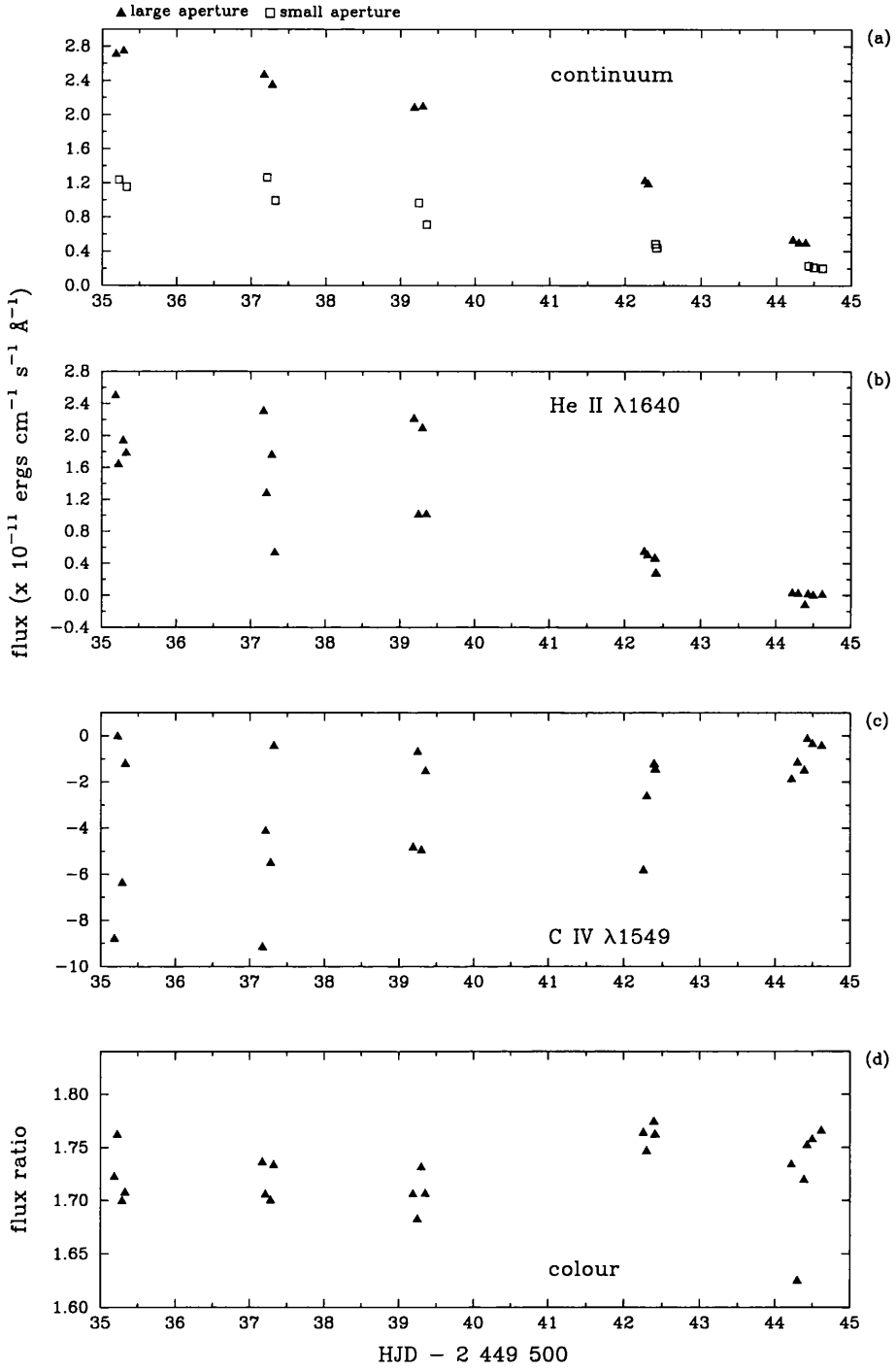

Figure 4.20: The UV line and continuum behaviour against time. Panel (a) shows the flux in the continuum band $\lambda\lambda 1419-1470$ Å, with the measurements from the large aperture spectra shown by filled triangles and those from the small aperture spectra shown by open squares. Panel (b) shows the flux in the He II $\lambda 1640$ line, panel (c) shows the flux in the C IV $\lambda\lambda 1550$ line and panel (d) shows the ratio of the flux in the $\lambda\lambda 1419-1470$ Å continuum band to the flux in the $\lambda\lambda 1742-1801$ Å continuum band.

absorption is likely to be contaminated by blending, *e.g.* potentially with Si II absorption features (Si II λ1527 at -4270 km s^{-1} and Si II λ1533 at -3110 km s^{-1}).

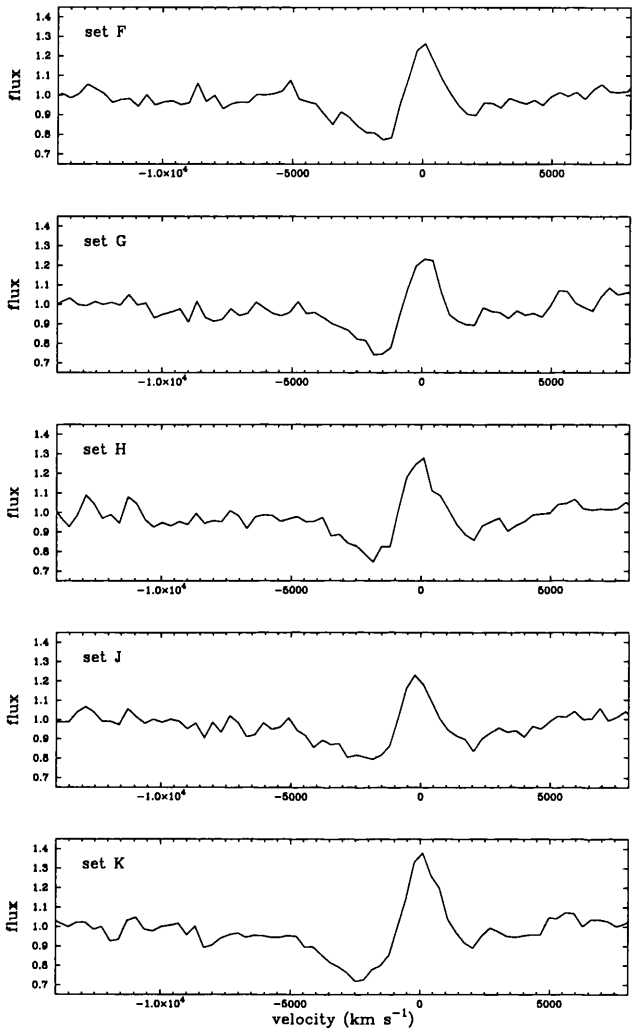

Figure 4.21: The mean, rectified C IV $\lambda\lambda$1550 line profiles are shown for data sets F – K (Table 4.4 and Figure 4.18). The velocity scale is with respect to the weighted mean of the C IV doublet (1549.05Å).

4.6.2 Orbital modulation?

There is little evidence in this *IUE* data set for any orbital variation although, as Table 4.5 shows, the orbital resolution of the data is poor, especially if group F is discounted (*e.g.* in the analysis of any orbital variability in the He II λ1640 line). When this is coupled with the low spectral resolution, the scope for detection of any orbital variability is expected to be low.

image number	aperture†	orbital phase	group
SWP 51393	L	0.007	K
SWP 51282	S	0.082	F
SWP 51325	L	0.109	H
SWP 51391	S	0.153	K
SWP 51306	L	0.181	G
SWP 51372	L	0.266	J
SWP 51306	S	0.331	G
SWP 51325	S	0.331	H
SWP 51391	L	0.394	K
SWP 51392	S	0.406	K
SWP 51373	L	0.425	J
SWP 51327	L	0.521	H
SWP 51280	L	0.556	F
SWP 51392	L	0.679	K
SWP 51280	S	0.703	F
SWP 51327	S	0.713	H
SWP 51372	S	0.765	J
SWP 51304	L	0.784	G
SWP 51373	S	0.818	J
SWP 51393	S	0.848	K
SWP 51282	L	0.934	F
SWP 51304	S	0.935	G

† L = large aperture, S = small aperture

Table 4.5: The orbital phase of the *IUE* archive spectra of SS Cyg. Labels F – K refer to the 5 UV data sets described in Table 4.4 (see Figure 4.18).

Figure 4.22 shows the EW of the C IV $\lambda\lambda$1550 line profiles between -4500 and 1500 km s^{-1}. Before the EW was measured, the profiles were rectified by the division of a first order polynomial that was fitted to the continuum on either side of the line. The EW does not show a distinct modulation, although there may be a minimum at $\phi = 0.70 - 0.85$.

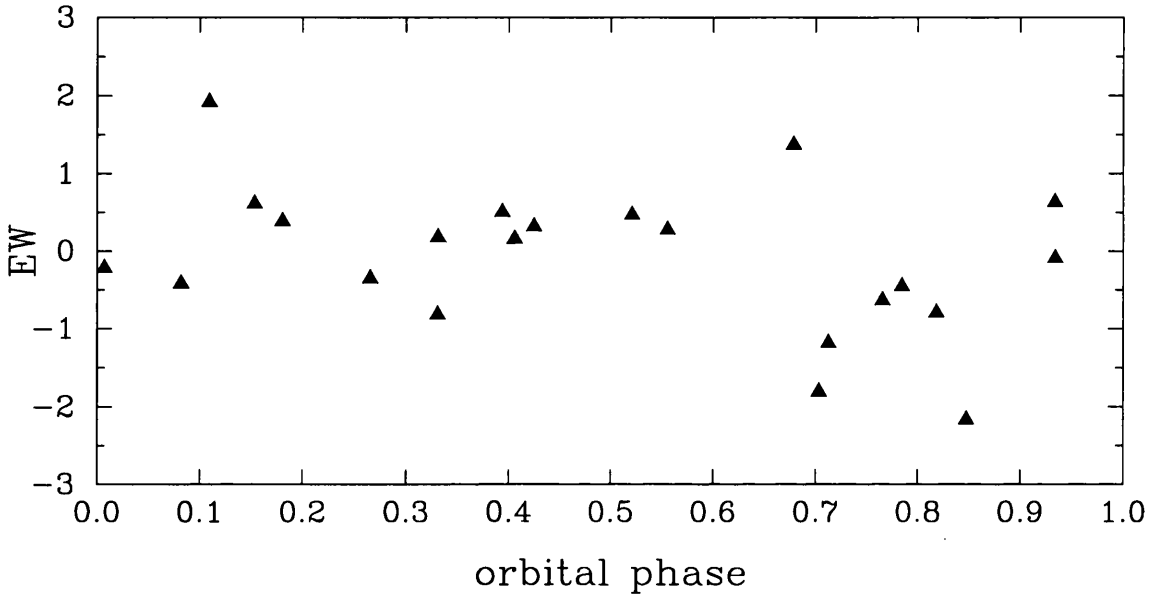

Figure 4.22: The C IV $\lambda\lambda$1550 EW versus orbital phase.

4.6.3 The UV wind properties

The limited spectral resolution and phase coverage of the *IUE* data set restricts the amount that can be said about the UV wind properties of SS Cyg. As evidenced by the P Cygni-type profile of the C IV line, SS Cyg is clearly driving a wind. The blueward edge of the absorption trough is measured to be at ~ -4500 km s^{-1}, although this is probably an overestimate of the wind's terminal velocity. The reduction in the absorption strength of this line between groups F and K implies that the outflow is decreasing in strength as the system declines from outburst. The rectified C IV line profile is not observed to undergo any gross changes from F to K but the data set is too limited to examine profile changes over the orbital cycle.

The presence of a wind outflow at UV wavelengths at least raises the possibility of a corresponding optical wind component. This optical component may then relate to the stationary low velocity emission (see Section 4.5.4). However, unambiguous optical wind signatures are gener-

ally difficult to detect in observations of non-magnetic CVs. For example, even in the cases of RW Sex and V3885 Sgr, which drive strong UV outflows (*e.g.* Prinja & Rosen 1995), no corresponding signatures are evident in the optical lines (*e.g.* Beuermann, Stasiewski & Schwope 1992; Haug & Drechsel 1985). This fact is likely to reflect the low density, high ionization nature of CV outflows. A wind origin may be the favoured interpretation of the low velocity stationary emission observed in IP Peg (Marsh & Horne 1990). In the case of SS Cyg, however, the inclination angle of 37° (Ritter 1990) is considerably lower than that of the eclipsing system IP Peg. For an outflow to be seen in emission in SS Cyg, the observed portion of the wind must be considerably further from the WD. This scenario would not seem to be compatible with the low velocity of the stationary emission observed at optical wavelengths. It therefore seems unlikely that the low velocity stationary emission can be due to a wind in this case.

4.7 Summary

This chapter examines new time-resolved optical observations of SS Cyg made during an outburst. Also presented here are archive UV *IUE* spectra obtained during the same outburst. The analysis confirms the presence of low velocity, stationary emission in the He II λ4686 and Hβ lines that was reported on recently by Steeghs *et al.* (1996). The observations presented here were recorded near the maximum of a long, asymmetric type outburst whereas Steeghs *et al.* observed a long, *symmetric* type outburst. Several explanations for the low velocity, stationary emission are discussed (Sections 4.5 and 4.6.3), the most feasible being emission from slingshot prominences.

There are some potential problems with the slingshot prominence model. Low velocity, stationary emission has now been reported in SS Cyg on at least three occasions, and has also been observed at comparable velocities in at least one other system (IP Peg). As the proposed prominences can in principle appear anywhere on the surface of the secondary star, why have stationary components arising from such sites not been observed at different velocities? Also, if the slingshot prominence model is correct, by now one might also hope to have observed low velocity, stationary components during quiescence. This problem clearly requires further work (see Chapter 6).

Chapter 5

Optical and UV spectroscopy of BZ Camelopardalis

5.1 Introduction

BZ Cam (0623+71) is a poorly studied nova-like CV which was discovered in 1981 by Bond (Ritter 1984). It is an obvious target in a study of wind-driving CVs because it has shown unambiguous evidence for a wind in its optical spectrum (*e.g.* Patterson *et al.* 1996). It is also of interest because it is located at the southern edge of a 'bow-shock' nebula (see Figure 5.1), discovered during a search for faint planetary nebulae on Palomar Sky Survey prints by Ellis, Grayson & Bond (1984) and designated 'EGB 4'.

The first spectroscopic study of BZ Cam, carried out by Lu & Hutchings (1985), covered the spectral range $\lambda\lambda$ 4000 – 4900 Å. They report narrow, weak Balmer emission and very weak He I, He II and C II emission. Measuring the radial velocities of the Balmer line wings and of the Balmer line peaks, they determine the most probable orbital periods as 0.1390 d and 0.1535 d (see Table 5.1). Their paper shows the mean spectra at $\phi = 0.25$ and $\phi = 0.75$. The mean spectrum at $\phi = 0.75$ appears to exhibit a P Cygni-type profile in the Hγ line, although this identification (not made by Lu & Hutchings) is only tentative because the Hβ line does not display such a profile so clearly.

BZ Cam was observed with *IUE* by Woods, Drew & Verbunt (1990) in a study of dwarf novae and nova-like variables. The targets were chosen such that the SWP images could be recorded with exposure times that were less that one quarter of the orbital cycle. The C IV $\lambda\lambda$1550, Si IV $\lambda\lambda$1400

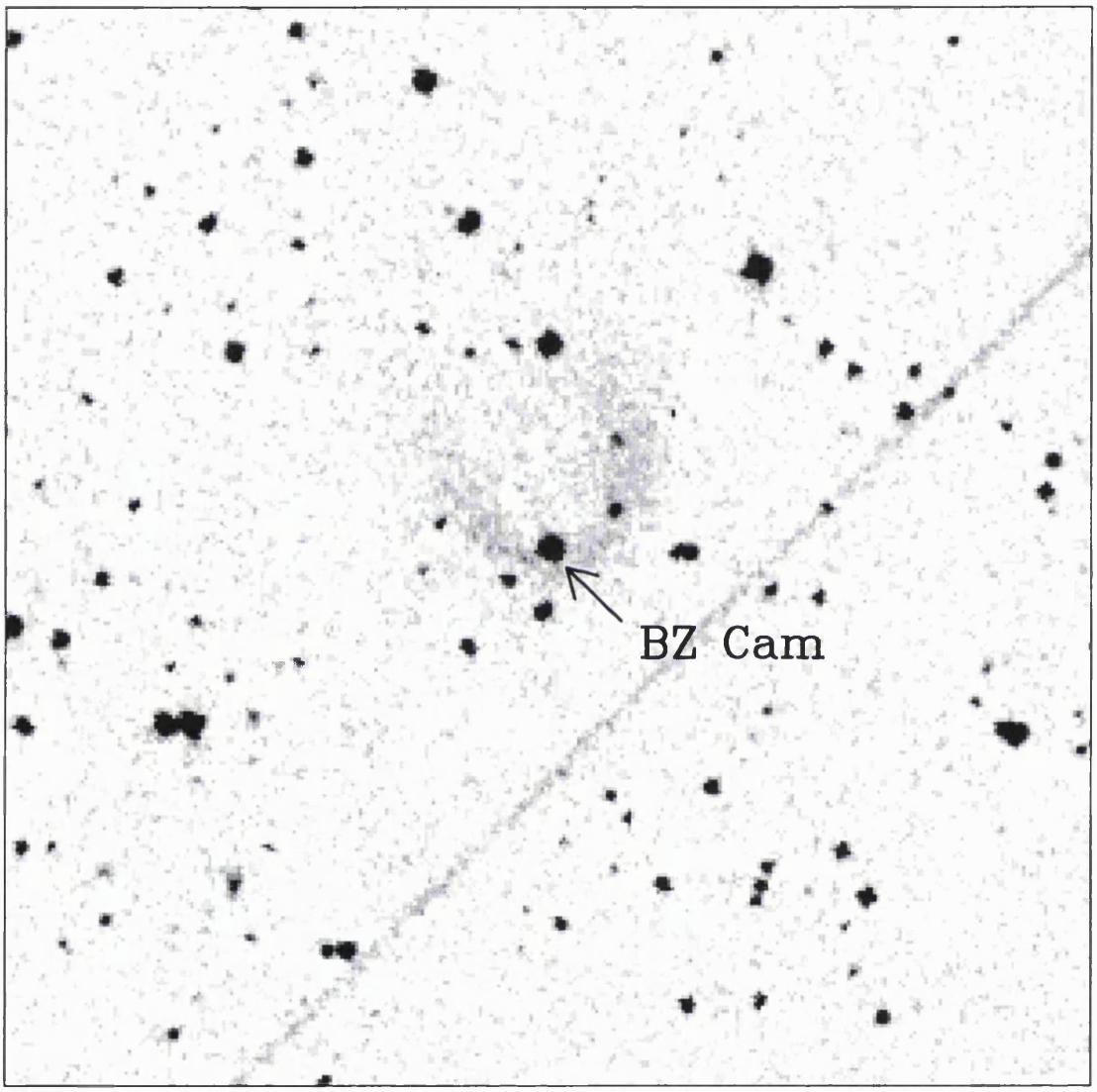

Figure 5.1: The 'bow-shock' nebula associated with BZ Cam. This image is taken from the Digitized Sky Survey and is based on photographic data obtained using the Oschin Schmidt Telescope on Palomar Mountain.

Period (hr)	Type	Reference
3.46	photometric	Ritter (1984)
3.34	spectroscopic	Lu & Hutchings (1985)
3.68	spectroscopic	Lu & Hutchings (1985)
3.684	spectroscopic	Thorstensen, Thomas & Patterson (1994)
3.67	spectroscopic	Patterson *et al.* (1996)
3.689	photometric	Patterson *et al.* (1996)

Table 5.1: Reported periods of BZ Cam

and N V $\lambda\lambda$1240 lines all show P Cygni-type profiles. They report dramatic changes in all the line profiles, although measurements of the equivalent widths do not show any clear periodicity.

Griffith, Fabian & Sion (1995) analysed the 15 low resolution SWP spectra of BZ Cam contained in the *IUE* archive (including those recorded by Woods, Drew & Verbunt 1990). Although these spectra span the years 1981 – 1989, 8 spectra were recorded in a 28 hour period in 1988 and it is these spectra that afford the best opportunity[1] (albeit a limited one) for an analysis of the UV line properties versus orbital period. The spectra show large and rapid variations in the C IV $\lambda\lambda$1550 P Cygni profile and in the strong absorption of the N V $\lambda\lambda$1240, Si IV $\lambda\lambda$1400, He II λ1640 and N IV λ1718 lines. The observed strengths of the C IV and Si IV line profiles is correlated. Despite the limited extent of the data set, the properties of the 8 spectra recorded over 28 hours in 1988 were examined against (relative) orbital phase (using the ephemeris of Thorstensen, Thomas & Patterson 1994). Plots of the equivalent widths versus orbital phase suggest that the strongest absorption occurs at $\phi \sim 0.2$, with weaker evidence for minimum absorption at $\phi \sim 0.3$ and for a secondary maximum at $\phi \sim 0.5$. The terminal velocity of the wind was estimated by measuring the blueward edge of the absorption for each line. The lower temperature ion species (C IV $\lambda\lambda$1550 and Si IV $\lambda\lambda$1400) have average terminal velocities of ~ -5000 km s^{-1}, while they measure the average terminal velocities of the higher temperature ion species (N V $\lambda\lambda$1240 and He II λ1640) as ~ -3000 to -4000 km s^{-1}. It should be noted that measurements of the terminal velocity in low resolution *IUE* data is likely to be in error by as much as 1000 km s^{-1}. Griffth, Fabian & Sion suggest that this may be evidence of a differentially expanding wind where the higher temperature ionization species are being formed closer to the ionizing source (*e.g.* the inner disk or the boundary layer).

[1] *HST* FOS spectra of BZ Cam have been recorded but are not public at the time of writing this thesis

The most detailed optical study of BZ Cam to date (Patterson *et al.* 1996) presents both spectroscopy and photometry which reveal periodic and quasi-periodic variations in radial velocity (underlying period ~ 0.153 d) and brightness. Twelve (weak) candidate signals are identified, with semi-amplitude $\sim < 0.03$ mag. They also report unusual and complex line profiles. The spectroscopy covers $\sim \lambda\lambda 4300 - 7100$ Å with a resolution of 3.5 Å and detects emission from the Balmer lines, He I and probably He II $\lambda 4686$. The Balmer lines contain narrow emission cores and the Hα line displays a broad, red emission wing which extends out to 2400 km s^{-1} from the line centre. In some observations a strong absorption is seen in the blue wing of the He I $\lambda 5876$ line. In one sequence of spectra, the P Cygni-type trough initially extends out to 2000 km s^{-1} bluewards of the line centre and over the following 40 minutes of observations the trough is seen to decrease in width and strength. Such rapid motion is seen on separate occasions in the observations but with no readily identified periodicity. Combining this observation with evidence of the P Cygni-type profiles reported by Woods, Drew & Verbunt (1990) from their UV spectroscopy and with the emission seen in the red Hα wing, there is strong evidence for a disk outflow from BZ Cam. A radial velocity study of Hα, Hβ and He I $\lambda 5876$ was carried out. Although the velocity curves obtained are not particularly sinusoidal they reveal a period near 0.153 d, which is thought to be the orbital period. Patterson *et al.* also report on 192 h of photometry obtained in 31 nights over a 4 month period in 1994/5. Very complex light curves were obtained that may arise from the superposition of several periodic signals. Using their photometry, their radial velocity study and some previous radial velocity measurements Patterson *et al.* measure the orbital period as 0.153693(7) d (see Table 5.1).

Ringwald & Naylor (1997) have carried out the most recent spectroscopic study of BZ Cam, recorded over 2 nights using the ISIS spectrograph on the 4.2m William Hershel Telescope (WHT). They observed P Cygni events in the He I $\lambda 5876$ and Hα lines. The data were recorded with a 30 second time resolution and reveal the appearance of the P Cygni events over time intervals of $6 - 20$ minutes. The events typically last for $\sim 30 - 40$ minutes. The absorption troughs of the profiles are seen to move redward over time. Again, no correlation of the P Cygni events with orbital phase is noted.

The properties of the nebula (see Figure 5.1) associated with BZ Cam were examined in a study by Krautter, Klaas & Radons (1987). They carried out both direct CCD imaging and long slit spectroscopy. Direct images were obtained both through an Hα filter and through a Strömgren y filter (which served as a continuum filter). The parabolic 'bow-shock' structure of the nebula is revealed by the Hα image whereas no sign of the nebulosity is seen in the Strömgren y continuum image.

This indicates that there is no reflection nebulosity and that the entire nebulosity observed is emission nebulosity. The surface brightness of the nebula is only a small amount above the sky background, and the nebula itself extends approximately $105''$ in both the north-south and east-west directions. Krautter, Klaas & Radons also recorded a long slit spectrum, centred $6''$ south of the star and running approximately east-west. The wavelength coverage was $\lambda\lambda 4720-7200$ Å. The intensity contour map shows emission from the lines Hα and Hβ, and from the forbidden lines [N II] $\lambda\lambda$6548, 6584, [Si II] $\lambda\lambda$6717, 6731 and [O III] $\lambda\lambda$4959, 5007. The [O III] emission is much stronger in the east than in the west, but the other lines do not show this asymmetric behaviour. Using the long slit spectrum they measured the emission line ratios for [Si II] $\lambda\lambda$6717, 6731 in the east (1.32) and the west (1.15), from which they calculated electron densities of 100 cm^{-3} (east) and 250 cm^{-3} (west). Finally they calculated the nitrogen to sulphur abundance ratio, which is N/S = 6.4 (east) and N/S = 5.7 (west). These values are close to the solar value of 5.12.

The bow-shock nebula has also been examined by Hollis *et al.* (1992). They present deep radio continuum and narrow-band optical emission line images of the system, and some optical long slit spectroscopy. The radio nebula is extremely weak and extended, and its properties are consistent with thermal bremsstrahlung. The total 6 cm continuum flux scales as expected with the Hα emission and there is no detectable radio polarization. Three sets of filters were used in the optical imaging: Hα, [N II] and [O III]. The images all reveal a bow-shock nebula morphology. The optical spectroscopy sampled the apex emission and the east and the west limbs of the nebula covering the spectral range $\lambda\lambda 3400-7400$ Å. The spectra are dominated by strong [O III] $\lambda\lambda$4959, 5007 and [O II] $\lambda\lambda$3727, 3729 emission. Also seen is weaker Hα, Hβ, [N II] $\lambda\lambda$6548, 6584 and [Si II] λ6717, 6731 emission. The [O III] emission is stronger in the east than in the west, in agreement with the observations of Krautter, Klaas & Radons (1987). A discussion of the origin of the bow shock nebula, and the theories proposed by Hollis *et al.* and by Krautter, Klaas & Radons is postponed until Section 5.6.

New spectroscopic data, obtained at the Dominion Astrophysical Observatory (DAO) in 1997 February, is presented in this chapter, along with a study of the full set of archive *IUE* spectra of BZ Cam. Section 5.2 presents the optical and UV data sets. The evidence for a wind is presented in Section 5.3 which considers both the optical (Section 5.3.1) and the UV (Section 5.3.2) observations. Section 5.4 considers the constraints these data offer on the inclination angle of BZ Cam and Section 5.5 makes an estimate of the wind mass loss rate. The implications of these observations on both the wind properties and the origin of the bow-shock nebula are discussed in Section 5.6.

5.2 Observations

5.2.1 Optical DAO spectroscopy

The optical data were recorded over 10 nights between 1997 February 4 – 13 on the 1.85m Plaskett telescope at the DAO in Canada. The Cassegrain spectrograph was used with the SITe-3 CCD and the 2161G grating. The long observing run was drastically reduced by poor weather conditions and a total of 109 spectra were secured over 3 nights. The wavelength coverage amounts to $\lambda\lambda$4276 – 5060 Å, with a spectral resolution of $\sim$ 1.3 Å. Individual exposure times were $\sim$ 300 sec. A log of the observations is shown in Table B.6.

The data were extracted and wavelength calibrated according to standard procedures using the *STARLINK* packages FIGARO (Meyerdierks 1993) and DIPSO (Howarth *et al.* 1995). Sky regions on either side of the star were identified and the stellar background was removed. Fe-Ar arc spectra were taken approximately every 30 min in order to carry out the wavelength calibration. They were extracted from the same positions on the slit as the objects and were then wavelength calibrated by fitting a fifth order polynomial to the arc lines. The wavelength scale was interpolated between neighbouring arc spectra. Over the course of a night's observations the wavelength scale shifted by 0.1 Å (equivalent to 6 km s^{-1} at 4500 Å). Due to the poor seeing conditions, the data were not flux calibrated.

5.2.2 Archive *IUE* spectra

The UV data set was compiled from the *IUE* final archive, from which all the available spectra of BZ Cam were retrieved. The final archive spectra have all been treated in a uniform manner which allows data from different epochs over the lifetime of *IUE* to be compared in a consistent manner (Nichols *et al.* 1993). A total of 15 images of BZ Cam were recovered, taken with the short wavelength (SWP) camera in low dispersion mode. They cover the wavelength range $\lambda\lambda$1150 – 1980 Å with a resolution of $\sim$ 6 Å. One image (SWP 13372) was exposed in both the large and small apertures, which gives 16 spectra in total. The image numbers and observation dates are given in Table 5.2 and a log of the *IUE* archive spectra is given in Table B.7.

image number	date	number of spectra
SWP 13372	81-FEB-26	2
SWP 21251	83-OCT-07	1
SWP 21948	84-JAN-06	1
SWP 22458	84-MAR-10	1
SWP 34774 – 34777	88-NOV-19	4
SWP 34784 – 34787	88-NOV-20	4
SWP 35975 – 35977	89-APR-10	3

Table 5.2: The *IUE* observations of BZ Cam.

5.3 The wind of BZ Cam

This section examines the spectroscopic properties of BZ Cam, and in particular the evidence for a wind. Section 5.3.1 looks at the optical data from the DAO and Section 5.3.2 studies the archive *IUE* spectra.

5.3.1 Optical observations

The mean spectrum from the optical DAO observations is shown in Figure 5.2. Before the mean spectrum was created, the individual spectra were normalised by the division of a first order polynomial that was fitted to the continuum regions. The mean spectrum shows single-peaked Hβ and Hγ emission features which possibly sit on some underlying absorption. Also shown in Figure 5.2 (dotted line) is an average of five individual exposures of BZ Cam that show P Cygni-type Balmer line profiles. The simultaneous occurrence of this profile shape in both the Hβ and the Hγ lines make this an unambiguous identification. Optical P Cygni-type profiles have been observed previously in the He I λ5876 line and in Hα (Patterson *et al.* 1996).

The orbital phase of the observations was calculated using the ephemeris that Patterson *et al.* (1996) derived from their photometric data:

$$T_0 = HJD - 2\,449\,746.686 + 0.153693N \tag{5.1}$$

The accumulated phase uncertainty for observations taken in 1997 February is $\pm$ 0.21 (1σ). Using

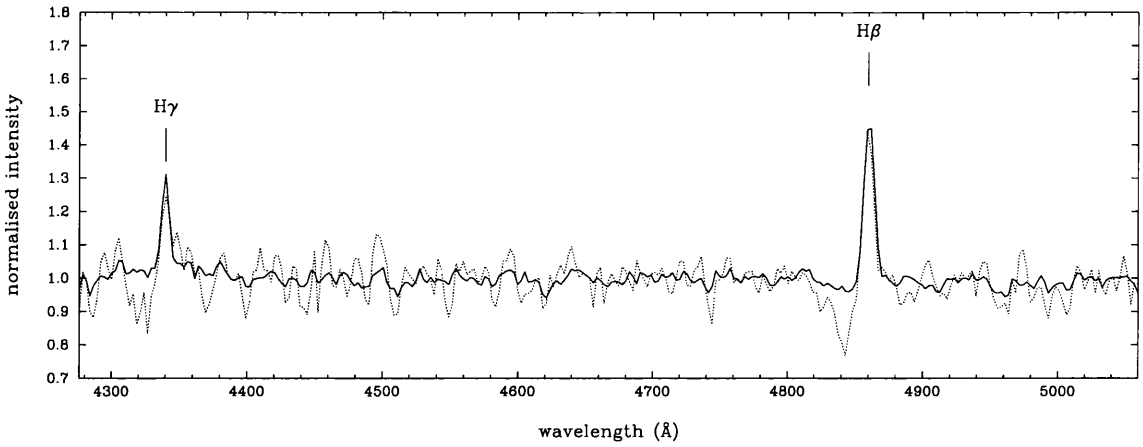

Figure 5.2: The mean optical DAO spectrum of BZ Cam (solid line) and an average of five individual exposures (files 624, 642, 672, 785 and 802; see Table B.6) that show P Cygni-type Hγ and Hβ line profiles (dotted line). The spectra have been normalised to the continuum level.

this ephemeris, a trailed spectrogram of the individual Hβ profiles was created. Figure 5.3 shows the resulting two-dimensional colour representation of the flux variations versus orbital phase. The Hβ line core clearly exhibits an s-wave, with a semi-amplitude of ~ 100 km s^{-1}. The s-wave is at its maximum redward velocity at $\phi \sim 0.25$ and at its maximum blueward velocity at $\phi \sim 0.75$.

A simple Gaussian fit to the Hβ emission was carried out, and the central velocity of the emission peak was measured. Figure 5.4 shows a plot of the radial velocity of the Hβ emission versus the orbital phase. The plot reveals an orbital modulation with maximum redward velocity at $\phi \sim 0.2-0.3$, maximum blueward velocity at $\phi \sim 0.7-0.8$ and a semi-amplitude of ~ 100 km s^{-1}. In the radial velocity curves of Patterson *et al.* (1996), the Hβ emission is at maximum redward velocity at $\phi \sim 0.1$ and at maximum blueward velocity at $\phi \sim 0.6$. This difference arises from the uncertainty in the cycle count between these observations and the observations of Patterson *et al.* (the estimated phase uncertainty from using the ephemeris of Patterson *et al.* for this data set is 0.21). Plotting the EW of the Hβ line between -600 and $+600$ km s^{-1} against the orbital period (Figure 5.5) does not reveal any modulated behaviour. The Hβ emission profile therefore appears to move in velocity space over the orbital cycle but with no variations in strength.

The signal-to-noise of this data set is not very high and there are only a few individual spectra which show optical P Cygni-type line profiles. Figure 5.6 shows the Hβ and Hγ profiles of one of the individual spectra which does exhibit such line profiles (file 785; see Table B.6). The profiles have been plotted in velocity space and the blueward edge of the Hβ absorption measured to be

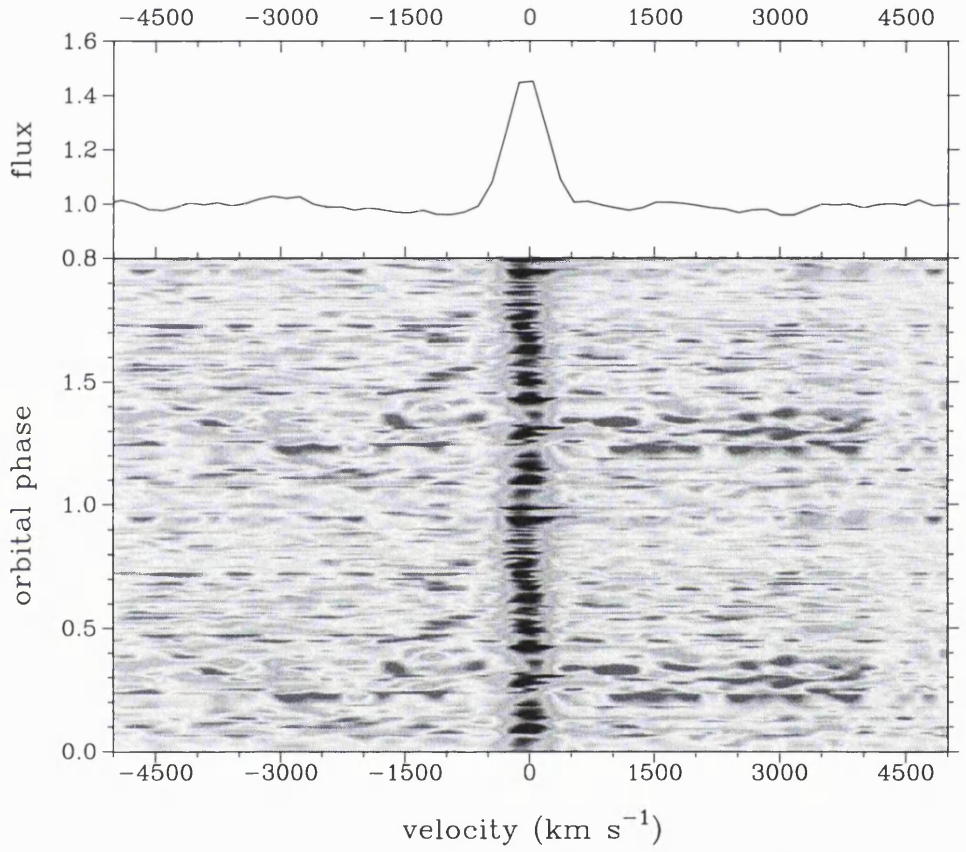

Figure 5.3: Trailed spectrogram of the Hβ line profiles (bottom panel). The top panel shows the mean Hβ profile. The blue shades show where the line flux is greatest and the red shades show where it is smallest.

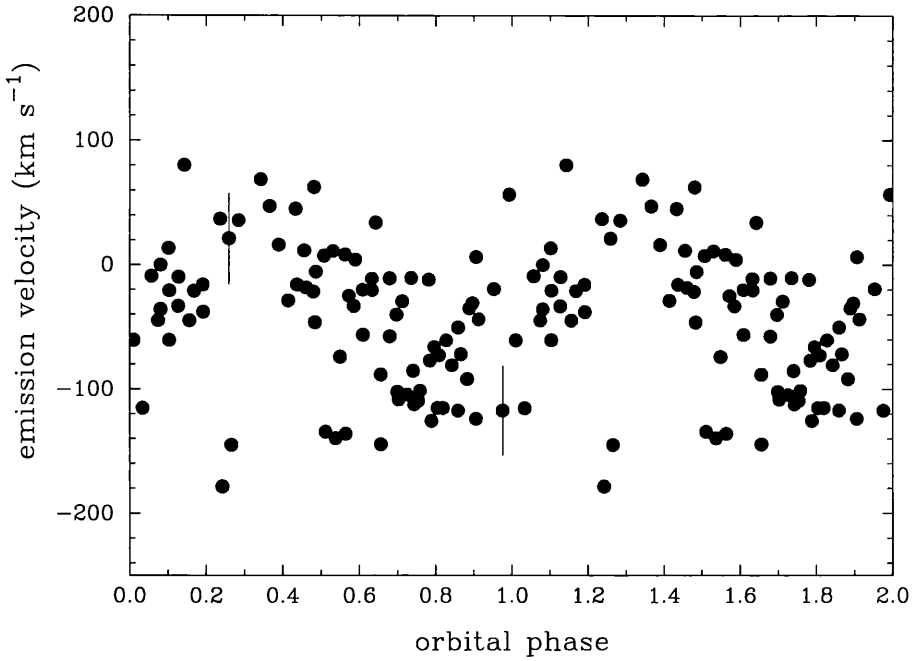

Figure 5.4: The Hβ radial velocity curve. The central velocity of the Hβ emission was measured using a simple Gaussian fit. Typical error bars are shown.

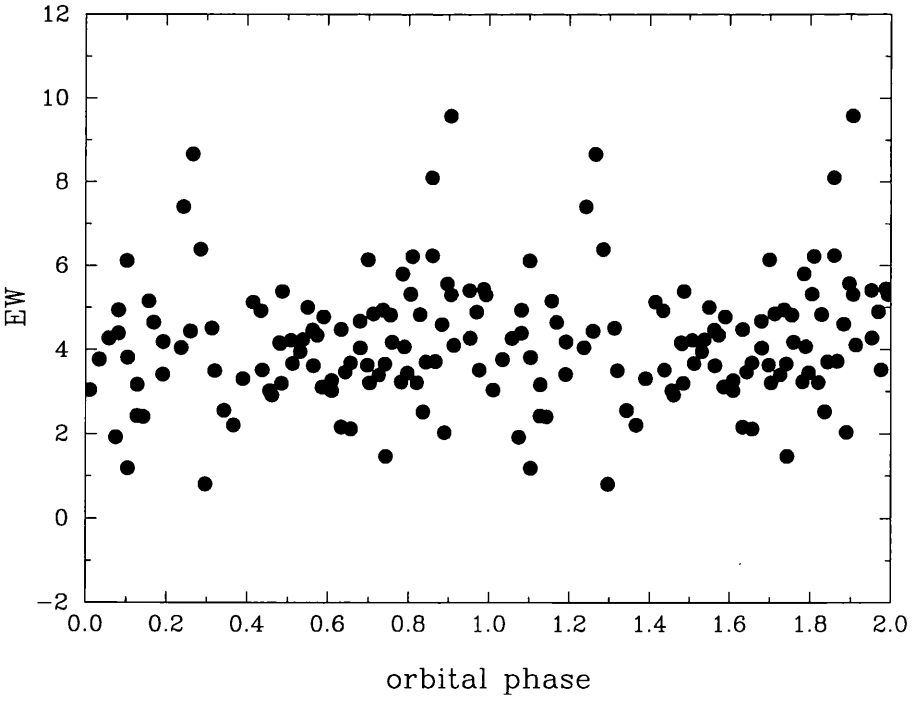

Figure 5.5: The Hβ EW plotted against orbital phase.

~ -1600 km s^{-1}. This value is comparable to the -2000 km s^{-1} found by Patterson *et al.* (1996) for the He I λ5876 blueward edge. To ascertain whether these profiles are genuinely wind-formed or whether they appear to be P Cygni shaped due to the coincidence of a broad absorption feature and a narrow emission feature, an analysis of the Hβ line profiles was carried out. (A 'P Cygni-type' line profile could be formed when the radial velocity motion of a broad absorption feature has brought it to its most blueward velocity and a narrow emission feature is at $\sim$ the rest velocity).

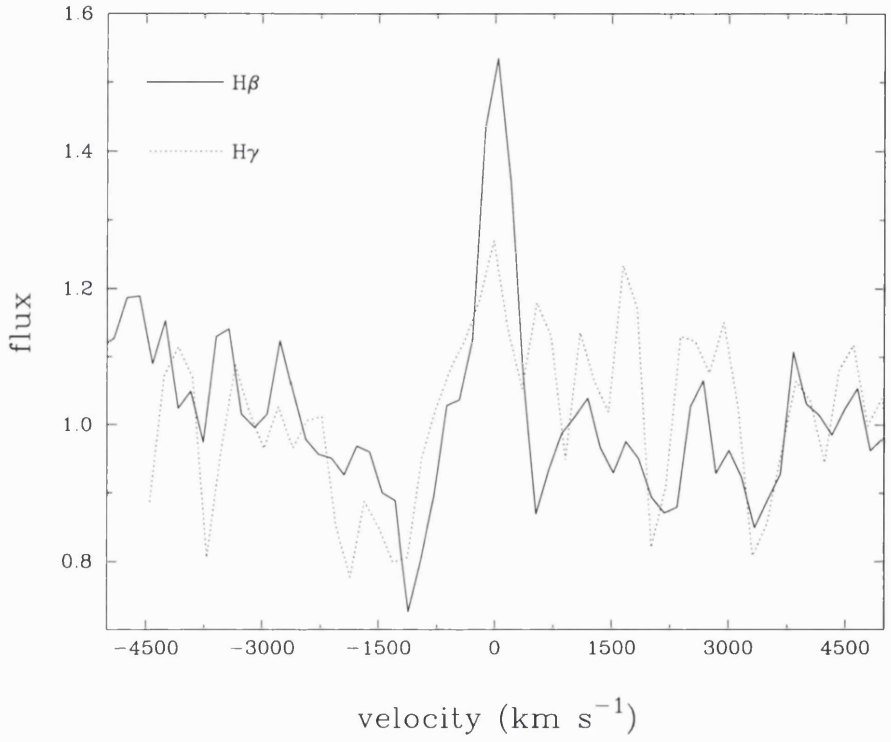

Figure 5.6: The P Cygni-type Hβ (solid line) and Hγ (dotted line) profiles of BZ Cam (from file 785).

For each Hβ profile, the equivalent width (EW) in two velocity bins either side of the line centre (EW_{blue} from -1600 to -650 km s^{-1} and EW_{red} from 650 to 1600 km s^{-1}) was measured. If the radial velocity motion of a broad absorption feature is being sampled, the behaviour in the two velocity bins should be *anti-correlated* (*i.e.* when the EW in the blue velocity bin is maximum, the EW in the red velocity bin should be minimum). The EW in the red velocity bin is plotted against the EW in the blue velocity bin in Figure 5.7. The dotted line shows one-to-one correlation (*i.e.* if the EWs are anti-correlated, the points should lie on a line perpendicular to the dotted line). According to Figure 5.7, the EWs blueward and redward of the line centre do not show correlated behaviour. The mean values of the EWs are $\langle EW \rangle_{blue} = 0.49$ Å and $\langle EW \rangle_{red} = 0.12$ Å. The

greater value for the $\langle EW \rangle_{blue}$ suggests that there is greater absorption blueward of the line centre for the complete orbital cycle. This *blueshifted* absorption suggests that this is a wind-formed feature.

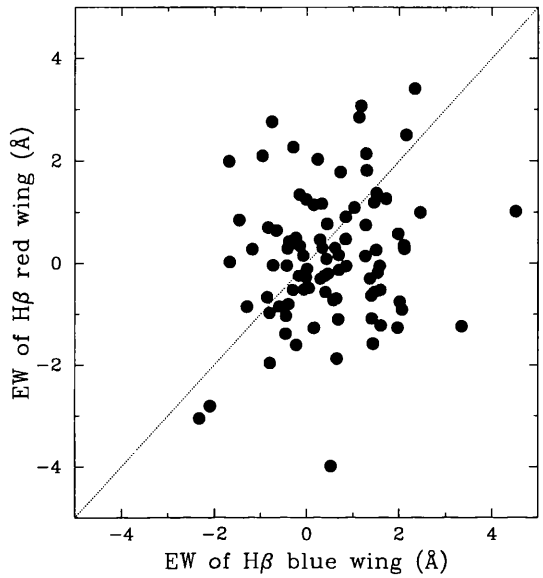

Figure 5.7: The equivalent width of the red wing of the Hβ line between 650 and 1600 km s^{-1} plotted against the equivalent width of the blue wing between -1600 and -650 km s^{-1}. The dotted line shows a one-to-one correlation.

A further check on this assertion may be carried out by plotting the radial velocity of the Hβ emission against the EW in the blue velocity bin (Figure 5.8). If the P Cygni-type profiles are made up of a broad absorption component (centred on the rest velocity) and a narrow emission component (variable in velocity), one might expect the EW in the blue velocity bin to be correlated with the radial velocity of the Hβ emission. Figure 5.8 shows that the two quantities are not correlated, suggesting that the absorption feature does indeed have a wind origin.

Having argued above that the optical P Cygni-type absorption line profiles are wind-formed, the EW of the blue velocity bin (-1600 to -650 km s^{-1}) was plotted against the orbital period (Figure 5.9). There is no obvious correlation between the wind strength and the orbital phase. This is consistent with the P Cygni events reported by Patterson *et al.* (1996) which also showed no obvious periodicity.

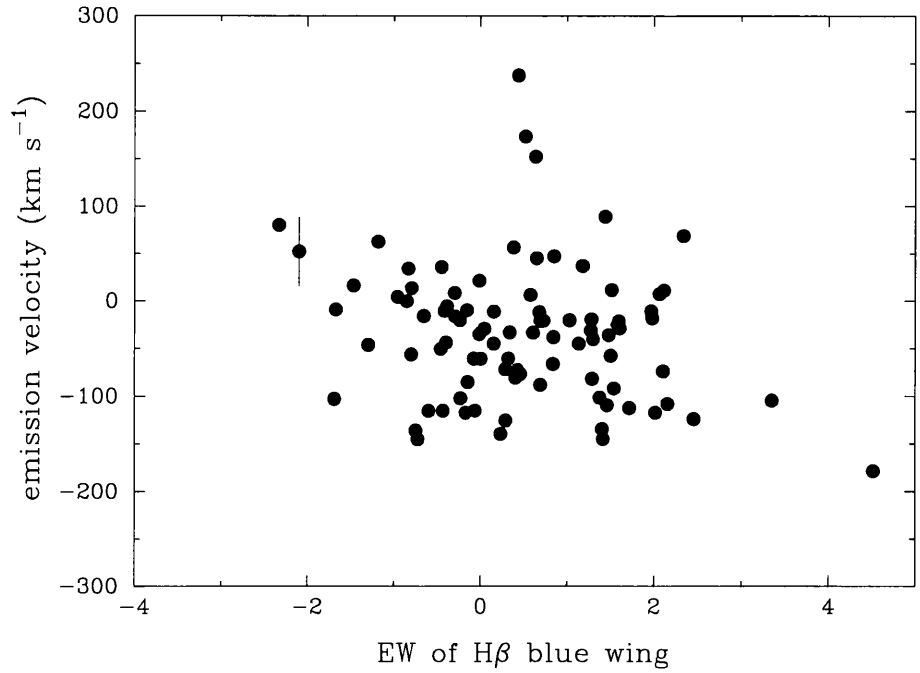

Figure 5.8: The velocity of the Hβ emission plotted against the EW of the blue wing between -1600 and -650 km s^{-1}. Typical error bars are shown.

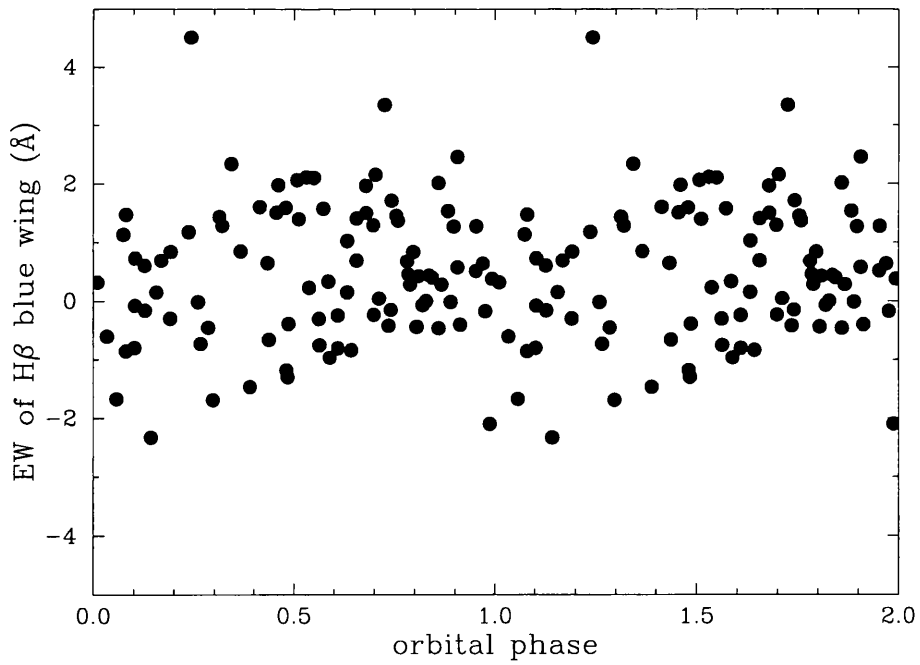

Figure 5.9: The equivalent width of the blue wing of the Hβ line between -1600 and -650 km s^{-1} plotted against the orbital phase.

5.3.2 UV observations

The *IUE* archive spectra of BZ Cam have been examined previously by Griffith, Fabian & Sion (1995). In this section the archive spectra are re-examined with the aim of constraining the wind mass loss rate (Section 5.5) and the inclination angle of the system. These properties affect the interpretation of the observations in the context of the origin of the bow-shock nebula associated with BZ Cam, which is discussed in Section 5.6.

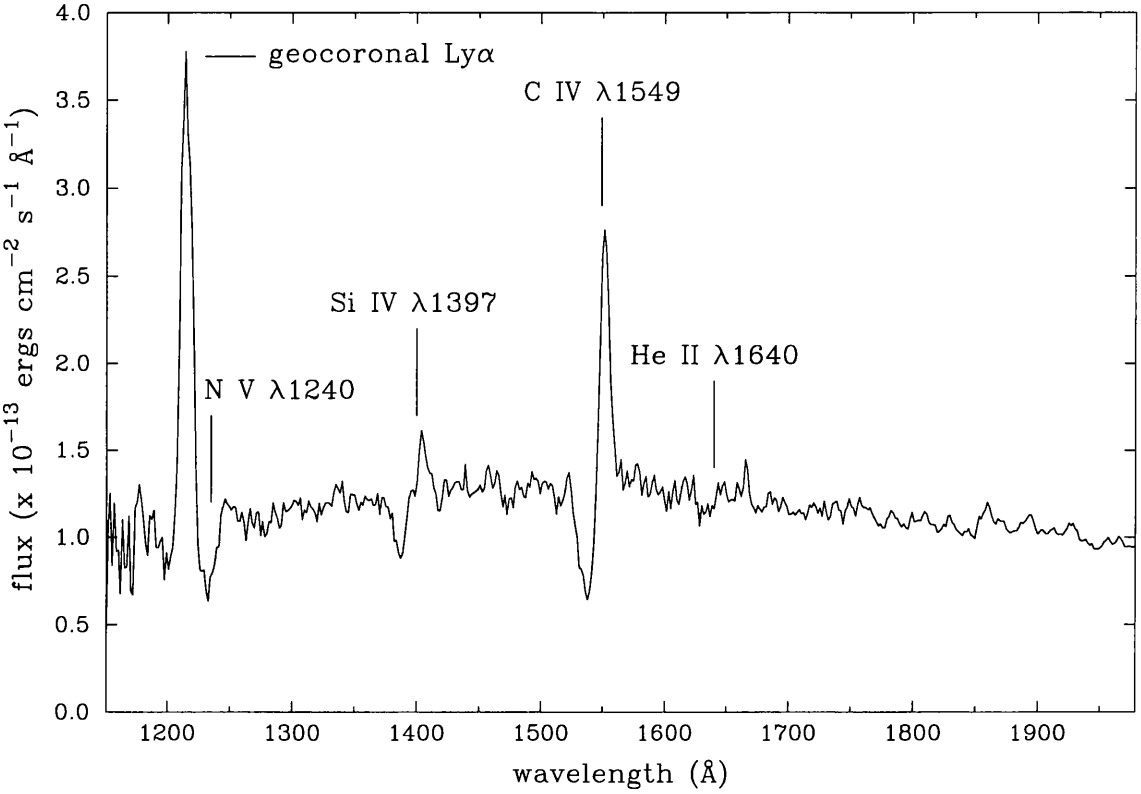

Figure 5.10: The mean *IUE* spectrum from the group of 8 spectra recorded in 1988 (see Table 5.2).

The mean *IUE* spectrum from the group of 8 spectra that were taken over a 28 hr period in 1988 (see Table 5.2) is shown in Figure 5.10. The Si IV $\lambda\lambda$1400 and C IV $\lambda\lambda$1550 show distinct P Cygni profiles, and the N V $\lambda\lambda$1240 and He II λ1640 lines are in absorption. Figure 5.11 shows the C IV $\lambda\lambda$1550 profiles for 12 of the 18 *IUE* archive spectra. Large changes in the strength and in the shape of the profile are evident over time. The spectrum extracted from image SWP 34785 (ϕ = 0.84), for example, is almost pure emission, whereas the spectrum from image SWP 34777 (ϕ = 0.36) shows a very obvious P Cygni profile with a strong absorption trough. The absorption is

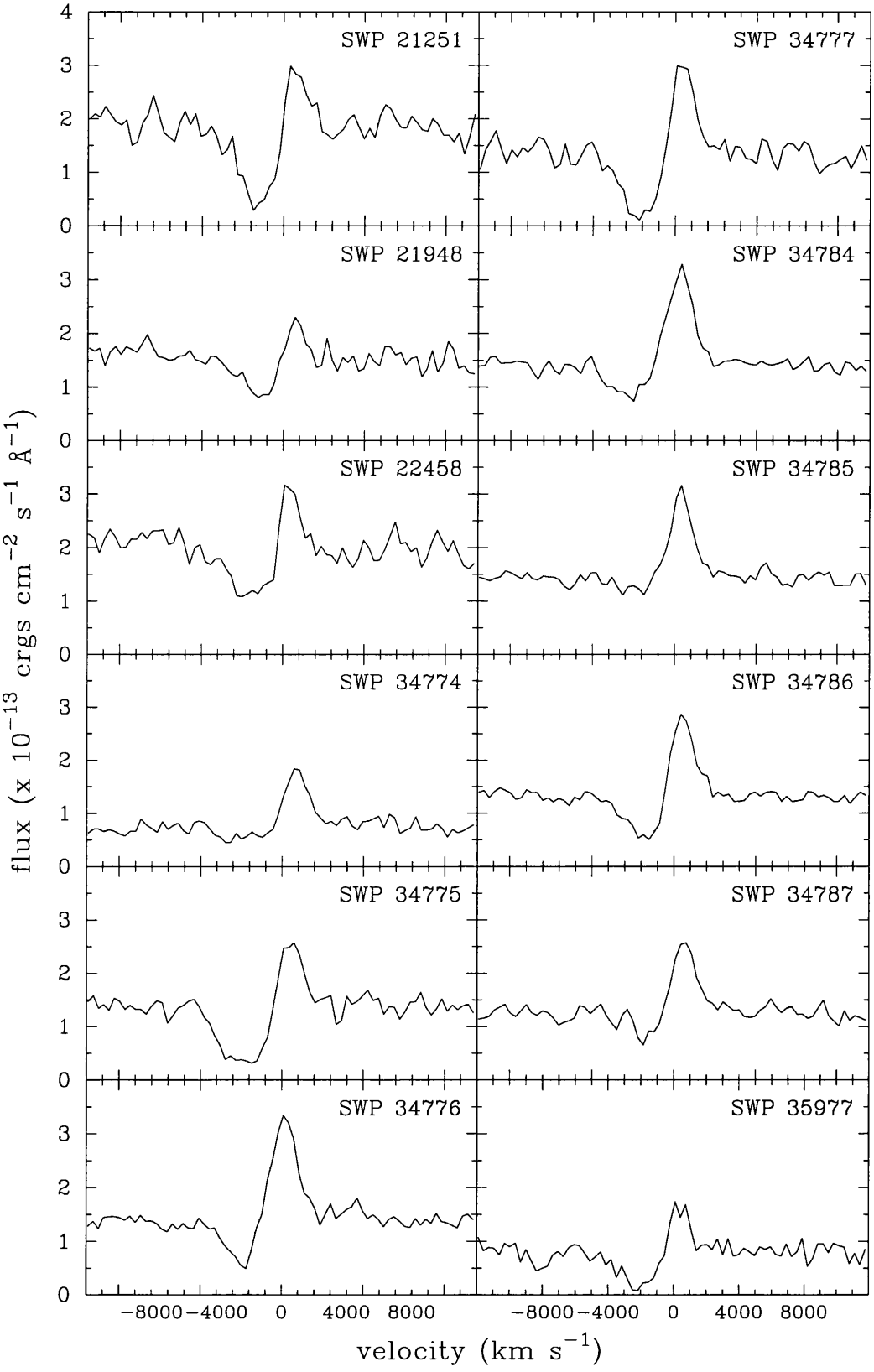

Figure 5.11: A selection of the archive *IUE* C IV $\lambda\lambda$1550 profiles.

highly variable over short timescales, as a comparison of the spectra from images SWP 34786 and SWP 34787 reveals. These spectra were recorded only 40 minutes apart. This timescale is similar to the timescale over which the optical wind features are seen to vary (Patterson *et al.* 1996).

The terminal velocity of the wind is estimated by measuring the blueward edge of the C IV $\lambda\lambda$1550 absorption trough. The mean C IV $\lambda\lambda$1550 P Cygni profile is shown in Figure 5.12 (solid line) along with the deepest absorption profile (SWP 34775; dashed line). From model fits to the deepest absorption profile (see Section 5.5) the edge is measured to be at -4300 km s^{-1}. This value could well be an overestimate of the true terminal velocity because the absorption is likely to be contaminated by blending, for example with Si II absorption features (Si II λ1527 at -4270 km s^{-1} and Si II λ1533 at -3110 km s^{-1}). Figure 5.12 also shows a typical C IV profile of the nova-like variable RW Sex ($i = 43°$), a system that is known to drive a strong outflow. From this comparison it can be seen that the absorption features of the two systems have similar strengths.

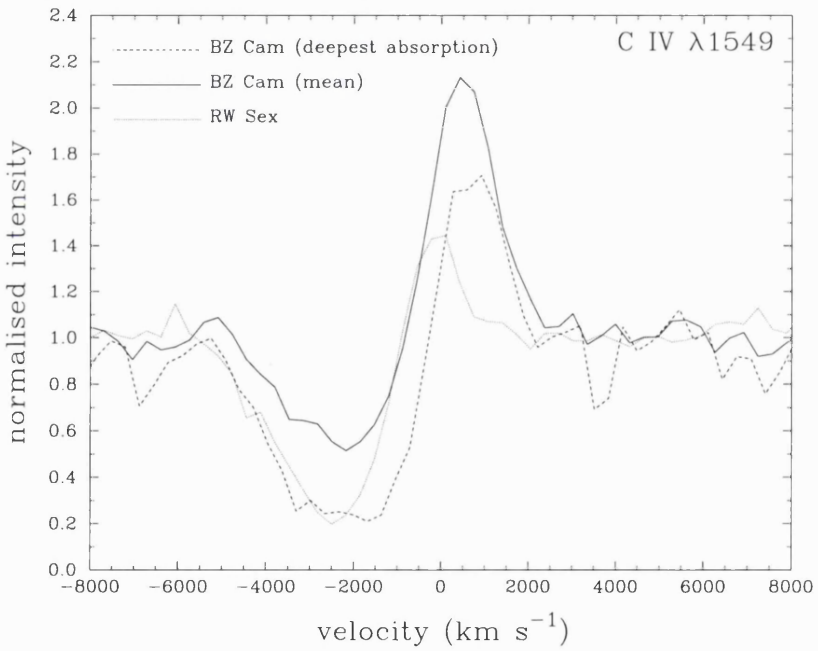

Figure 5.12: A comparison of the mean (solid line) and deepest absorption (dashed line) C IV $\lambda\lambda$1550 P Cygni profiles of BZ Cam to the C IV profile of the nova-like variable RW Sex (dotted line).

The properties of the 8 *IUE* archive spectra that were recorded over the 28 hr period in 1988 (see Table 5.2) were examined against orbital phase. The exposures were phased using the orbital period from the ephemeris of Patterson *et al.* (1996), relative to the mid-exposure time of the first file (SWP

34774). The orbital phases are shown in Table 5.3. The first thing to note is the (unexplained) discrepancy between the phases calculated here and those of Griffith, Fabian & Sion (1995). This study calculates the phases of each spectrum at mid-exposure time, relative to the mid-exposure time of SWP 34774, using a period of $P_{orb} = 0.153693$ d.

file number	mid-exposure time	relative phase
SWP 34774	13:37	0.00
SWP 34775	15:19	0.46
SWP 34776	16:53	0.89
SWP 34777	18:37	0.36
SWP 34784	12:46	0.28
SWP 34785	14:51	0.84
SWP 34786	16:46	0.36
SWP 34787	17:26	0.54

Table 5.3: The relative orbital phase of the *IUE* spectra from 1988 November 19–20. The phasing uses the orbital period from the ephemeris of Patterson *et al.* (1996) and is carried out relative to the mid-exposure time of the first file.

Figure 5.13 shows the UV properties of the 8 spectra versus orbital phase. The mean flux in the line-free continuum band $\lambda\lambda 1419-1470$ Å and the total flux of the N V $\lambda\lambda 1240$, C IV $\lambda\lambda 1550$, Si IV $\lambda\lambda 1400$ and He II $\lambda 1640$ lines was measured. There are no obvious modulations of the flux levels, although there is possibly a dip in flux at $\phi \sim 0.4$ in the C IV line. This cannot be confirmed without a larger data set. Griffith, Fabian & Sion (1995) tentatively identify both a minimum and a maximum in the equivalent width measures taken from the same data set.

5.4 The inclination angle

There is a strong dependence of the wind properties of a CV on the system's inclination angle (see Section 1.2.1). To find the mass loss rate from the wind (an important parameter when considering the origin of the bow-shock nebula) it is necessary to input the inclination angle into a wind modelling code. In this section the inclination angle of BZ Cam is estimated.

No photometric eclipses are observed for this object, which implies that $i < 65°$. By examin-

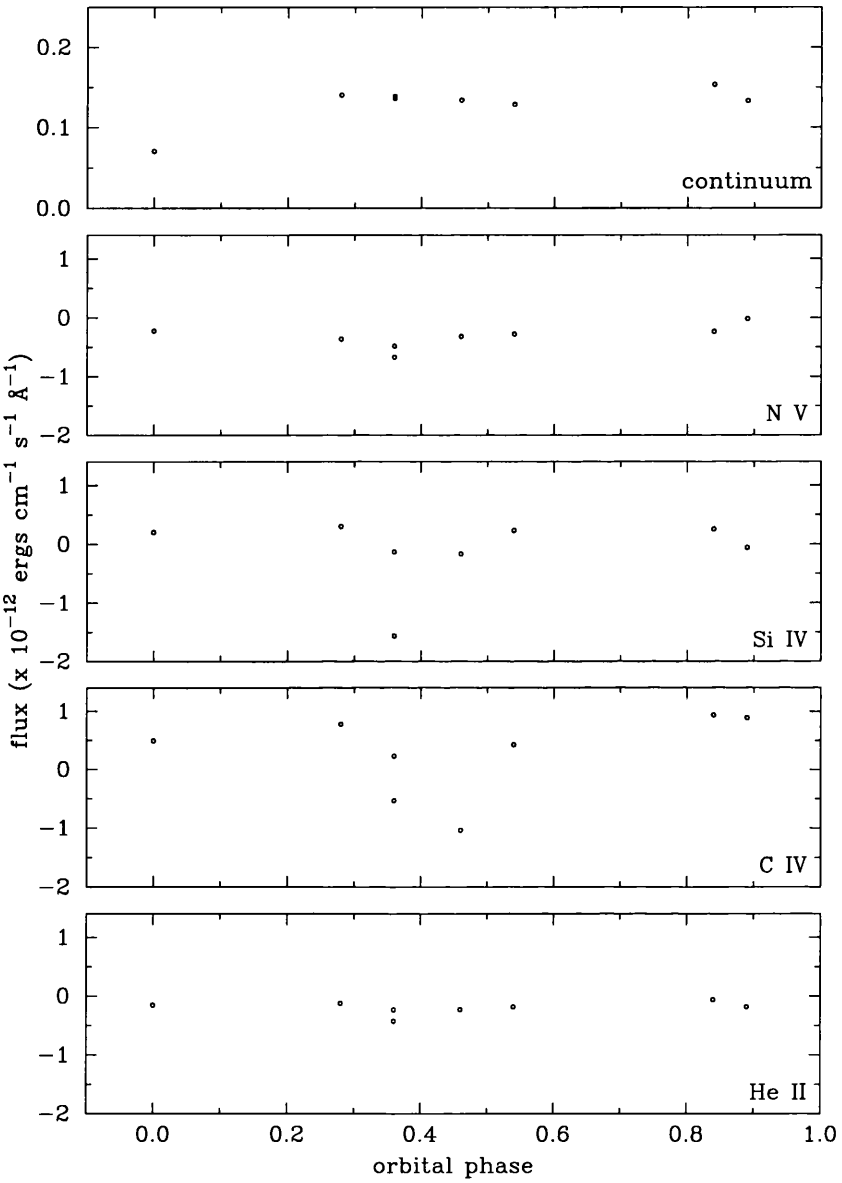

Figure 5.13: The UV *IUE* properties versus orbital phase. The panels show, from top to bottom, the mean continuum flux in the line-free band $\lambda\lambda 1419 - 1470$ Å and the total flux of the N V $\lambda\lambda 1240$, C IV $\lambda\lambda 1550$, Si IV $\lambda\lambda 1400$ and He II $\lambda 1640$ lines.

ing the narrowness of the Balmer emission lines, the study by Lu & Hutchings (1985) suggests that $i < 40°$. This study looks again at the Hβ emission line profile to constrain the inclination angle. Horne & Marsh (1986) examined the formation of emission lines in accretion disks and computed both optically thin and optically thick line profiles for a range of inclination angles. Figure 5.14 shows the Hβ profile of BZ Cam and synthetic profiles of optically thin emission lines for inclination angles of $i = 15°$ and $i = 0°$, taken from Horne & Marsh. (At these low inclination angles there is no discernible difference between the optically thin and optically thick cases. The difference becomes apparent only at higher inclinations. This is due to the introduction of an anisotropic component into the local line broadening by the disk's Keplerian velocity field. Shear broadening occurs because it is easier for line photons trapped in an optically thick emission layer to escape in directions along which the Keplerian shear flow provides large Doppler gradients. In the optically thin case, the shear broadening has little effect because the line photons are able to escape from the emission line region in all directions).

The synthetic profiles in Figure 5.14, taken from Figure 4 of Horne & Marsh (1986), were calculated with a Keplerian velocity at the inner accretion disk of 2200 km s^{-1} and a Keplerian velocity at the outer disk of 700 km s^{-1}. The profiles were convolved with a Gaussian to simulate an instrumental response of FWHM = 150 km s^{-1}. The model peaks, and the observed Hβ profile, were normalised to a peak value of 10. Although these synthetic profiles were not calculated with the intention of modelling the emission profiles of BZ Cam, they allow the inclination angle of the system to be estimated. A reasonable value to place on the inclination is $i \leq 15°$.

This argument is supported by X-ray observations of BZ Cam. In a study of the X-ray source in non-magnetic CVs, van Teeseling, Beuermann & Verbunt (1996) analysed all the available *ROSAT* PSPC observations and found an anti-correlation between the observable emission measure and the inclination angle. The emission measure EM is defined as

$$EM = \int n_e^2 dV \tag{5.2}$$

where n_e is the electron density and V is the emitting volume. The same anti-correlation was found when using the quantity $count\ rate \times distance^2$. Using a mean count rate of 0.075 counts per second (van Teeseling & Verbunt 1994) and an estimated distance of 500 pc (Krautter, Klaas & Radons 1987), the inclination angle is constrained from van Teeseling, Beuermann and Verbunt's Figure 5 to be $i < 20°$.

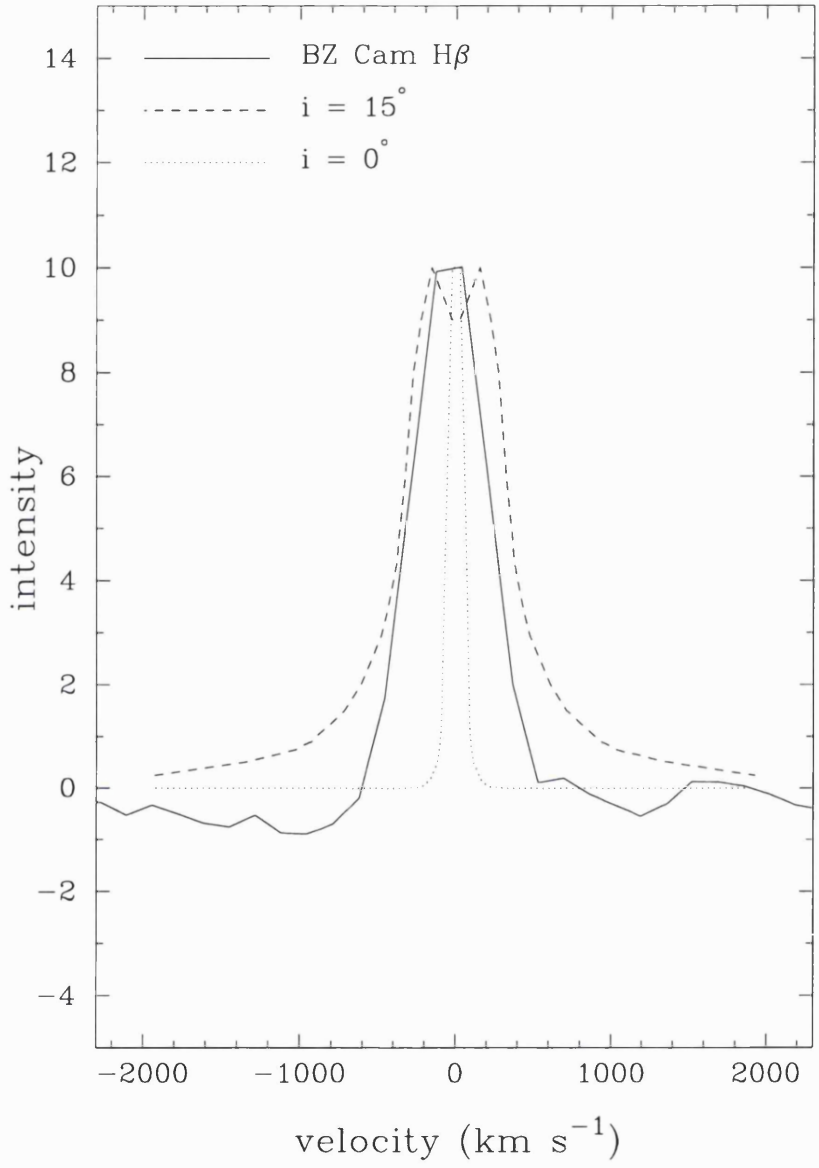

Figure 5.14: Synthetic profile fits to the Hβ emission. The solid line shows the observed Hβ profile, the dashed line shows the synthetic profile for i = 15° and the dotted line shows the synthetic profile for i = 0°. The synthetic profiles were taken from Figure 4 of Horne & Marsh (1986). The Keplerian velocities of the inner and outer accretion disk were 2200 km s^{-1} and 700 km s^{-1} respectively. The profiles were convolved with a Gaussian to simulate an instrumental response of FWHM = 150 km s^{-1}. The model peaks, and the observed Hβ profile, were normalised to a peak value of 10.

5.5 The disk-driven mass loss rate

Model wind line profiles were synthesised using the code described by Drew (1987). The profiles are calculated for a wind flowing radially from the centre of an accretion disk. The ionization law of the wind is assumed to be constant, a constant acceleration velocity law is used, and the line transfer effects calculated according to the prescription of Castor (1970). The wind temperature was fixed arbitrarily at 50 000 K and the disk temperature at 100 000 K. The degree of bipolarity of the outflow was chosen to be $l = 2$ (see Drew 1987). A WD radius of $R_{WD} = 0.014\ R_{\odot}$ and a disk radius of $R_{disk} = 30\ R_{\odot}$ were adopted. The remaining input parameters are the inclination angle and the maximum wind velocity. The value measured in Section 5.3.2 of the maximum blueward edge of the C IV $\lambda\lambda$1550 absorption, 4300 km s^{-1}, was used as the maximum wind velocity. The product of the mass loss rate and the C^{3+} ion fraction ($\dot{M}q_{C^{3+}}$) was then constrained by choosing the best model fit to the line profile from a grid of different values of the product of the mass loss rate and the ion fraction. The model profiles were convolved to the resolution of the *IUE* spectra before comparing them to the observed data.

The initial modelling approach was to assume that both the absorption and the emission are entirely wind-formed, leaving the inclination angle i as a free parameter. The best fit to the observed profile was for an inclination angle of $i = 60°$ and $\dot{M}q_{C^{3+}} = 1$ x $10^{-10} M_{\odot} yr^{-1}$. This fit is shown in Figure 5.15 as the dotted line. From the constraints derived in the previous section (Section 5.4), models were also run using a (probably more realistic) inclination angle of $i = 15°$. The best fit has $\dot{M}q_{C^{3+}} = 0.3$ x $10^{-10} M_{\odot} yr^{-1}$, and is shown as a dashed line in Figure 5.15. Using this value of the inclination angle, it is impossible to fit the emission part of the line profile. This may indicate the presence of significant contributions to the emission in C IV from non-wind sources, such as a bright spot on the accretion disk. This study shows that the potential contribution of non-wind emission sources to the UV line profiles can be significant, as in the case of V795 Her (see Chapter 3 and Section 3.7).

To derive an actual mass loss rate from the expression $\dot{M}q_{C^{3+}} = 0.3$ x $10^{-10} M_{\odot} yr^{-1}$, a value for the ion fraction is needed for the C^{3+} ion. Mauche & Raymond (1987) adopted ion fractions of $q_{C^{3+}} \sim 3$ x 10^{-3} in a study of the the C IV profiles of HL CMa that they compared to a shock-compressed wind model. The adopted value compares reasonably with values derived for O star winds (~ 1 x 10^{-3}; Howarth & Prinja 1989) and gives an estimate for the wind mass loss rate of $\dot{M} = 1$ x $10^{-8} M_{\odot} yr^{-1}$. It should be noted that any estimate of the ion fraction $q_{C^{3+}}$ must be treated

with much caution; even the values estimated for O star winds (which are better understood than the winds of CVs) are quite uncertain.

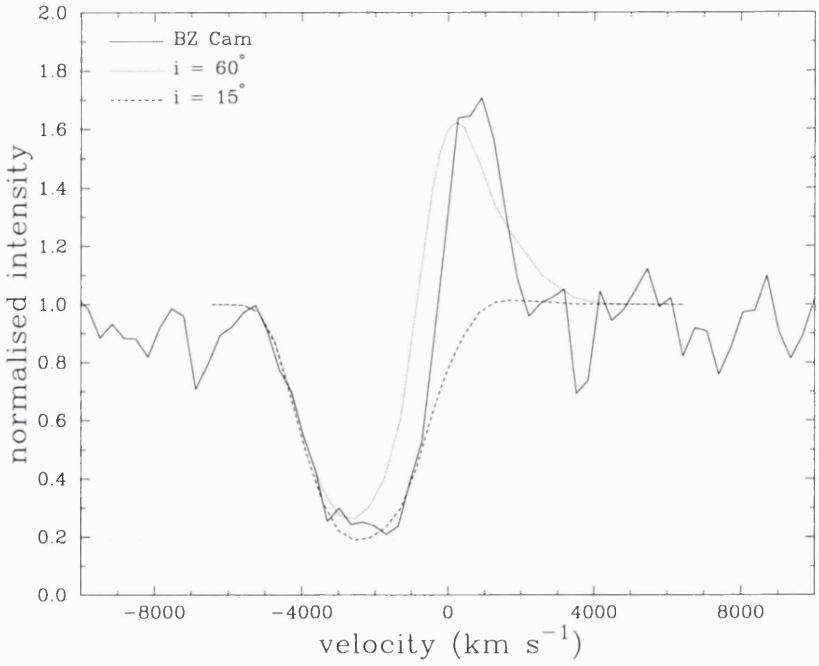

Figure 5.15: Model profile fits to the C IV $\lambda\lambda$1550 line. The wind model and the parameters used in the fits are described in the text. The solid line shows the observed C IV profile, the dotted line shows the best fit to both the emission and the absorption (inclination angle i = 60°, $\dot{M}q_i$ = 1 x $10^{-10} M_{\odot} yr^{-1}$), and the dashed line shows the best fit for an inclination angle of i = 15° ($\dot{M}q_i$ = 0.3 x $10^{-10} M_{\odot} yr^{-1}$).

5.6 Discussion

Analysis of a new optical data set, presented in this chapter, has revealed P Cygni-type features in the Balmer lines. An examination of archive UV *IUE* spectra has provided constraints on the wind mass loss rate. Neither data set has shown convincing evidence for any orbital variability of the wind-formed features, although admittedly the UV data set is somewhat limited in this respect. A short summary of the system parameters that have been derived or adopted during this study are given in Table 5.4. Section 5.6.1 discusses the optical wind properties of BZ Cam and Section 5.6.2 goes on to consider the origin of the bow-shock nebula.

system parameter	value	source
i	≤ 15 °	this study
v_∞ (C IV) (km s^{-1})	4300	this study
$\dot{M}q_{C^{3+}}(M_\odot yr^{-1})$	0.3 x 10^{-10}	this study
$q_{C^{3+}}$	3 x 10^{-3}	Mauche & Raymond (1987)
$\dot{M}(M_\odot yr^{-1})$	1 x 10^{-8}	this study
d (pc)	500	Krautter, Klaas & Radons (1987)

Table 5.4: Summary of the system parameters derived or adopted during this study.

5.6.1 The wind properties of BZ Cam

BZ Cam is one of very few CVs to show *optical* P Cygni-type line profiles. To make a qualitative comparison between this wind and other hot star winds seen at optical wavelengths, it is necessary to turn to massive early-type stars. Wolf-Rayet stars drive extremely strong outflows but optical P Cygni profiles are seen only in the He lines; the Balmer lines have pure emission (scattered) profiles due to dense winds. Optical P Cygni profiles in the Balmer lines are seen for O stars. Figure 5.16 compares the Hβ P Cygni profiles of BZ Cam and an example Of star, HD 151804 (spectral type O8 If). The two spectra have the same spectral resolution. The maximum velocity of the Hβ profile of BZ Cam has been measured as -1600 km s^{-1}, while the blue wing of the Hβ profile of HD 151804 extends only to ~ -500 kms. It is clear that the O star wind does not reach such high velocities as the wind in BZ Cam. It should also be noted that, in comparison to other O stars, HD 151804 shows extreme behaviour. A further difference between these wind-formed profiles is the ratio of the absorption and emission strengths, although the greater emission strength seen in BZ Cam will be due in part to contamination by a disk source.

These comparisons, and the fact BZ Cam is one of very few CVs to exhibit optical P Cygni profiles, suggest that the wind of BZ Cam is very unusual. It is not obvious how such high velocity P Cygni profiles can be formed in both the optical Balmer and He lines. This brings into question the assumption that CV winds are driven solely by radiation pressure, at least in the case of BZ Cam. A further unusual property of BZ Cam's wind is its high time variability. Patterson *et al.* (1996) observed rapid motion of the absorption trough in a time interval of 40 minutes. Ringwald & Naylor (1997) have reported similar rapid variability in WHT ISIS spectroscopy. The P Cygni

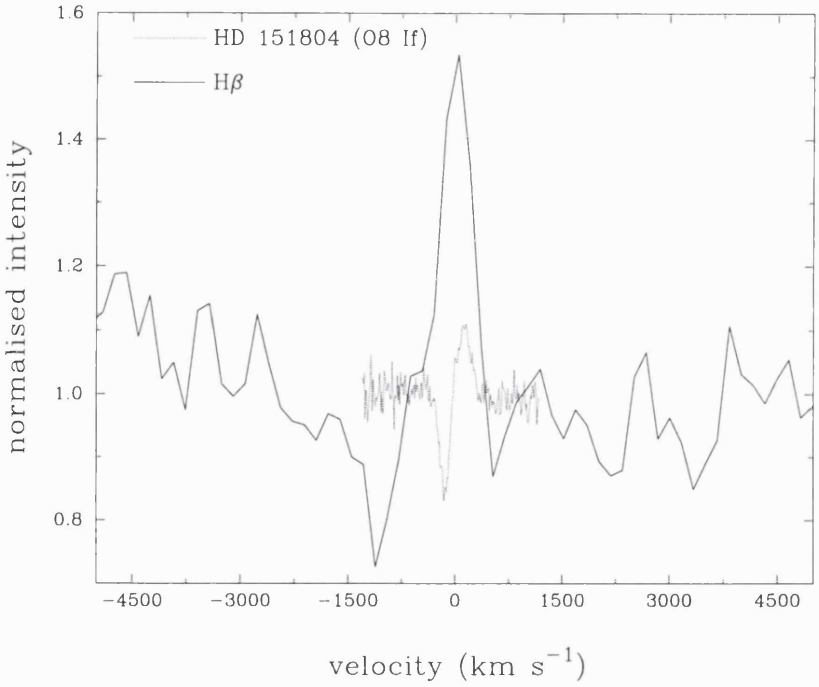

Figure 5.16: A comparison of the Hβ P Cygni profiles of BZ Cam (solid line) and an O star (HD 151804, spectral type O8 If; dotted line).

events appear over a timescale of 6 – 20 minutes and typically last for $\sim$ 30 – 40 minutes. During this time the troughs are observed to move redwards. In neither set of observations do the optical wind changes appear to be related to the orbital phase.

It is an interesting exercise to establish some constraints on the brightness of BZ Cam, and to estimate a lower limit to the mass accretion rate. Spectra covering the full wavelength range from the EUV to the IR do not exist for this system, so in order to estimate the total integrated flux, a Kurucz model atmosphere was fitted to a combined SWP and LWR *IUE* spectrum. The model fit had $T_{\rm eff}$ = 14 000 K and log g = 3.0 and was normalised at 3000 Å. The total integrated flux from $\sim \lambda\lambda$270 Å – 0.8 μ, calculated using the model fit, is $F = 6.5 \times 10^{-10}$ erg cm^{-2} s^{-1}. This figure can now be used to make an estimate of the accretion disk luminosity L_{disk}:

$$L_{disk} = 4\pi \times 9 \times 10^{40} D_{100}^2 F \text{ erg s}^{-1} \tag{5.3}$$

where D_{100} is the distance to the star in 100 pc units. Using a value of D = 5, corresponding to a distance of d = 500 pc (as estimated by Krautter, Klaas & Radons 1987; see Section 5.6.2), the estimate of the disk luminosity is $L_{disk} \geq 1.85 \times 10^{34}$ erg s^{-1}. This is taken to be a lower limit because the observed flux is assumed to be some fraction of the total flux. The rate of mass accretion

through the disk $\dot{M}_{acc}$ can now be estimated using

$$L_{disk} = \frac{GM_{WD}\dot{M}_{acc}}{R_{WD}} \tag{5.4}$$

Taking reasonable estimates of the mass of the WD (M_{WD} = 0.8 $M_{\odot}$) and the radius of the WD (R_{WD} = 7 x 10^8 cm), a lower limit of the mass accretion rate of $\dot{M}_{acc} \geq 1.9 \text{ x } 10^{-9}\ M_{\odot} yr^{-1}$ is obtained. This lower limit is consistent with the range of mass accretion rates for nova-likes and dwarf novae in outburst of $3 \text{ x } 10^{-9} M_{\odot} yr^{-1} < \dot{M} < 1 \text{ x } 10^{-8} M_{\odot} yr^{-1}$, as discussed in Warner (1995). (This rough estimate of the range of mass accretion rates was obtained using estimates of the absolute visual magnitude.)

The estimate of the mass accretion rate can now be compared to the mass loss rate of the wind, calculated in Section 5.5. For an inclination angle of 15°, the product of the mass loss rate and the C^{3+} ion fraction is $\dot{M} q_{C^{3+}} = 0.3 \text{ x } 10^{-10} M_{\odot} yr^{-1}$. Using the estimate of the ion fraction of $q_{C^{3+}} = 3 \text{ x } 10^{-3}$, the mass loss rate from the wind is $\dot{M} = 1 \text{ x } 10^{-8} M_{\odot} yr^{-1}$. This makes the ratio of the wind mass loss rate to the mass accretion rate

$$\frac{\dot{M}_{wind}}{\dot{M}_{acc}} = 5.3 \tag{5.5}$$

Of course, to conserve energy, this ratio must be < 1. This likely implies that the mass accretion is indeed higher than the lower limit estimated above and also that the C^{3+} ion fraction is a lot higher than estimated (thereby reducing the estimate of the wind mass loss rate).

5.6.2 The origin of the bow-shock nebula

The bow-shock nebula associated with BZ Cam (see Figure 5.1) was discovered by Ellis, Grayson & Bond (1984) during a search for faint planetary nebulae on Palomar Sky Survey prints. The association of the nebula with the CV BZ Cam caused them to suggest that the nebulosity is a shell ejected in a nova eruption, rather than being a true planetary nebula.

Krautter, Klaas & Radons (1987) then obtained direct CCD images of BZ Cam, and carried out some long slit spectroscopy. Their observations were discussed in Section 5.1. They measured the mean radial velocities of the eastern and western limbs and put a limit on the expansion velocity of the nebula of $v_{exp} \leq 130 \text{ km s}^{-1}$. Measurements of the nitrogen to sulphur abundance ratio reveal it to be close to the solar value. The observed emission line ratios were then compared to those of photoionized objects (*e.g.* H II regions and planetary nebulae) and to those of shock excited objects

(*e.g.* supernova remnants) to ascertain which line excitation mechanism is operating. The observed emission line ratios imply that there is shock heating with partial photoionization. By assuming a canonical brightness of the system of $M_V = +4$ and $E(B-V) = 0.0$, the distance to BZ Cam is estimated to be $d \geq 500$ pc, which gives a linear diameter of the nebula of 0.25 pc.

The study by Hollis *et al.* (1992) used imaging and spectroscopy which is described in Section 5.1. The Hα, [N II] λ6584 and radio continuum images reveal the global morphology of the nebula while the [O III] λ5007 emission is confined to the apex regions, consistent with shock excitation. The emission line ratios are also consistent with shock excitation.

Two origins of the bow-shock nebula have been proposed. The nebula may be an evolutionary remnant, either from a nova eruption or as a planetary nebula, or it may be the result of the CV wind interacting with the interstellar medium. These ideas are discussed below.

An evolutionary remnant?

Ellis, Grayson & Bond (1984) were the first to suggest that the nebula associated with BZ Cam may be an old nova shell. Krautter, Klaas & Radons (1987) discount this idea for a number of reasons. The observed morphology, having a bow-shock structure, is unlike the shape of well known nova shells which are mostly ellipsoids. Assuming that the nebula *is* a nova remnant, its size implies that it is more than 250 years old, which is inconsistent with normal nova shell lifetimes of 10 – 100 years. It is also improbable that a nova eruption at this position in the sky, likely to have been at least second magnitude, could go unrecorded. A final argument against a nova eruption is the observed nitrogen to sulphur ratio. This is close to the solar value which implies that the nebula material is unprocessed.

Krautter, Klaas & Radons (1987) also consider a planetary nebula origin. The morphological structure of the nebula and the large offset of the CV from its centre would make this an unusual planetary nebula, although they point out the similarities between this object and the planetary nebula Abell 35. It is not clear that BZ Cam shares enough properties with the central star of Abell 35 to fit in with the planetary nebula scenario, and again one would expect the observed nitrogen to sulphur ratio to reflect the fact the nebular material will be processed.

A bow-shock caused by the current wind?

Hollis *et al.* (1992) explored the idea that the bow shock may be formed by a supersonically moving CV which emits a strong wind that interacts with the interstellar medium (ISM). They use a time-dependent bubble model (Weaver *et al.* 1977; Dyson & Williams 1980) in which the central star emits a high speed wind that ploughs into the ISM causing an outward bound shock in the interstellar gas. Kinetic energy is converted into thermal energy in a second shock inside the wind, setting up an inward facing shock front. The hot bubble of gas confined by the two shock fronts does work on the surrounding material and its expansion velocity drops. The region between the two shocks is then at uniform pressure and the bubble would continue to expand symmetrically into the ISM and eventually dissipate. The case of BZ Cam is complicated by the wind source which is moving supersonically with respect to the ISM. This produces a bow wave in the shape of a paraboloid of revolution.

Dynamic equilibrium is achieved when the momentum flux of the wind balances the ram pressure of the ISM. From this equality Hollis *et al.* calculate a distance from the CV to the inner shock front of 3.2 x 10^{16} cm, using a wind mass loss rate of $\dot{M}$ = 1.4 x $10^{-11} M_{\odot} yr^{-1}$. This mass loss rate was calculated by a comparison of UV *IUE* profiles to model profiles of Castor & Lamers (1979) in conjunction with a methodology developed by Krautter *et al.* (1981). However, before such a examination of the dynamical properties of the nebula can be carried out, it is very important to establish a good estimate of the wind mass loss rate. It is interesting to compare the distance to the shock front calculated by Hollis *et al.* to the value obtained when using the mass loss rate that was implied by the fits to the wind profiles carried out in Section 5.5. For an inclination angle of $i = 15°$, the product of the mass loss rate and the C^{3+} ion fraction is $\dot{M} q_{C^{3+}}$ = 0.3 x $10^{-10} M_{\odot} yr^{-1}$. Adopting a value for the C^{3+} ion fraction of $q_{C^{3+}}$ = 3 x 10^{-3} (see Section 5.5) gives an estimate of the wind mass loss rate of $\dot{M}$ = 1 x $10^{-8} M_{\odot} yr^{-1}$. This is considerably larger than the value adopted by Hollis *et al.* (1992) of $\dot{M}$ = 1.4 x $10^{-11} M_{\odot} yr^{-1}$. Using Equation 2 of Hollis *et al.* with the mass loss rate derived here gives a distance from the CV to the shock front of 2.3 x 10^{19} cm. This is also considerably larger than the value derived by Hollis *et al.* (3.2 x 10^{16} cm). As discussed above (Section 5.6.1), the value adopted in this study for the ion fraction is likely to be too low, and therefore the mass loss rate may be too high. This would make the derived figures more consistent with those of Hollis *et al.*. The differences between the calculated values clearly shows how necessary it is to establish a good estimate of the mass loss rate *before* attempting to constrain the dynamics of the bow-shock. Ultimately, uncertainties in the sizes of the wind cavity and the

thickness of the shocked wind region will affect models for the cooling mechanism of the shocked material.

5.7 Summary

BZ Cam is clearly an unusual object amongst CVs. It shows unambiguous evidence of a wind at optical wavelengths and it is also associated with a bow-shock nebula.

Unfortunately, it is not possible to compare directly the optical wind properties of BZ Cam with those of any other system. Both these and previous observations do not reveal an obvious correlation between the optical wind strength and the orbital phase. The strength of the UV wind-formed features does not appear to correlate with the orbital phase either, although the depth of the analysis is limited by the small archive data set available. The strength of the wind-formed C IV absorption feature is comparable to that of RW Sex, a system known to drive a strong outflow. Profile fitting allowed the product of the mass loss rate and the C^{3+} ion fraction to be estimated for BZ Cam. This value of $\dot{M}q_{C^{3+}}$ = 0.3 x $10^{-10} M_{\odot} yr^{-1}$, when combined with an estimate of the C^{3+} ion fraction of $q_{C^{3+}}$ = 3 x 10^{-3}, results in an estimate for the mass loss rate of $\dot{M}$ = 1 x $10^{-8} M_{\odot} yr^{-1}$. However, when comparing this value to an estimate of the lower limit of the mass accretion rate (1.9 x $10^{-9} M_{\odot} yr^{-1}$), it seems likely that the C^{3+} ion fraction is a lot higher.

The bow-shock nebula is unlikely to be an evolutionary remnant, as evidenced by the near-solar value of the observed nitrogen to sulphur ratio. Its origin is more likely to be connected to the interaction of the current CV wind with the ISM. Examination of the work carried out by Hollis *et al.* (1992) reveals the importance of the reliability of the wind mass loss rate. Before more detailed dynamical studies of the nebula properties are carried out, a good estimate of this value must be obtained.

Perhaps what makes BZ Cam unusual is its extremely low inclination angle. This system may be being viewed almost face-on. Potentially this is combined with a high mass transfer rate, resulting in strong optical wind signatures and a clear bow shock nebula.

Chapter 6

Conclusions

Presented in this thesis are multi-wavelength studies of three non-magnetic CVs. The major findings for each system are summarised in Sections 6.1.1, 6.1.2 and 6.1.3. Section 6.2 considers the future work suggested by the unresolved issues that these studies have raised.

6.1 Summary

6.1.1 V795 Herculis

This thesis has presented new high resolution optical spectroscopy of the nova-like variable V795 Her. Additional quasi-simultaneous *HST* observations have provided a unique multi-wavelength data set for this object. The optical spectroscopy reveals separate low and high velocity fluctuations in the emission features of the Balmer lines that are phased on the 2.6 hr orbital period. Also noted in the Balmer lines is an absorption component, redward of the line centre and stronger during the first half of the orbital cycle.

Previous studies (Casares *et al.* 1996; Haswell *et al.* 1994) invoked a magnetic scenario when interpreting the outer wing variations of the Balmer lines. These authors claim that this weak emission arises in the channeled accretion columns of a magnetic WD which is phase-locked with the accretion disk. This thesis has argued that this interpretation is fundamentally flawed. Examination of the requirements for establishing such a phase-locked geometry suggests that it is essentially impossible for the rotation of the WD to be locked to the binary motion in V795 Her. This argument

against an IP scenario is compounded by the current X-ray data (Rosen *et al.* 1995) which reveal only a weak X-ray signal and a lack of any clear X-ray modulation.

A disk-overflow scenario, based on the behaviour of SW Sex stars, has been presented in this thesis as a more realistic and compatible description of the (optical) line structure and behaviour of V795 Her. The outer wing *s*-waves are interpreted as a single broad component, cut into by a narrower absorption feature to create the double-humped profile. This broad emission arises from the point where the accreting gas stream has overflowed the outer rim and re-impacts in the inner disk regions (the re-impact site). Pure emission is observed in SW Sex stars, whereas the production of the double-humped profiles seen in V795 Her requires the broad component to be cut into by a narrow absorption feature. This is possible if the re-impact site produces a self-absorbed emission profile. A potential explanation for the difference, in this respect, between V795 Her and SW Sex stars is its lower inclination angle (the SW Sex stars are generally eclipsing systems). Further absorption is caused by the gas stream as it passes from the initial impact site to the re-impact site. It is unclear why this absorption is seen only during the first half of the orbital cycle, both in V795 Her and for the SW Sex stars in general.

The UV *HST* observations of V795 Her are broadly compatible with the disk-overflow scenario. A counterpart of the broad optical emission has been tentatively identified. The origin of the variable blueshifted absorption feature in the UV resonance lines is unclear. It may be a counterpart of the optical absorption produced as the gas stream travels from the initial impact site to the re-impact site. Why the UV counterpart is clear only when blueshifted in the second half of the orbital cycle and, indeed, why the optical absorption is obvious only when redshifted is as yet unresolved.

Analysis of the *HST* data set resulted in the first detection of the modulation of the UV resonance lines on the mooted orbital period of V795 Her. Additionally, the C IV line showed evidence of an outflow in V795 Her via an asymmetric, blueward absorption trough. Its constancy throughout the orbital cycle suggests that the observed profile variability is not connected with the wind formed features. This conjecture is supported by the strong correlation of the overall UV and optical line profile changes. The UV resonance lines show a common absorption component that is thought to arise in the disk photosphere and which makes a significant component to the overall line profile. It is clear that both disk emission and absorption make significant contributions to the UV line profiles. Such contributions are currently neglected in line synthesis models of CV winds.

6.1.2 SS Cygni

A new spectroscopic data set of the dwarf nova SS Cyg was presented in Chapter 4. Time-resolved optical data was recorded at the maximum of a long, asymmetric outburst. Archive UV *IUE* spectra from the same outburst were also examined. Analysis of the optical data confirms the presence of low velocity, stationary emission in the He II λ4686 and Hβ lines that was reported on recently by Steeghs *et al.* (1996). In contrast, their observations were made during a long, *symmetric* outburst.

Several possible sources of the low velocity, stationary emission were discussed. Gas stream emission was discounted as no part of the stream is at rest with respect to the centre of mass of the binary system. An explanation invoking inflowing magnetic accretion does not seem compatible with the low velocity of the stationary emission source. Emission as a result of an outflow also seems unlikely for this system. The most favoured scenario is that of slingshot prominences, as previously suggested by Steeghs *et al.* (1996). In this model, the region between the inner Lagrangian point and the WD is thought to be able to maintain a stable magnetic loop. The magnetic field confines a dense lump of gas at the summit of the loop. If this clump is then illuminated by the disk and the secondary star, an emission source will be observed that co-rotates with the secondary. This results in the low velocity, stationary emission reported here.

Some problems may exist with the slingshot prominence model. The low velocity, stationary emission has now been reported in SS Cyg on at least three occasions, always at similar velocities. Emission at comparable velocities has also been observed in another system, IP Peg. If the proposed prominences are caused by magnetic activity on the secondary star they can, in principle, appear anywhere on its surface. It seems strange that stationary components arising from such sites have not been observed at different velocities. There also seems to be no reason why these components shouldn't have been seen during quiescence: the magnetic activity of the secondary is not expected to depend on the outburst cycle and, as evidenced by observations of the illuminated inner face of the secondary, there is no reason why clumps shouldn't also be illuminated during quiescence.

6.1.3 BZ Camelopardalis

This thesis also presented new optical spectroscopy and archive UV *IUE* spectra of the peculiar nova-like variable BZ Cam. Analysis of the optical data set revealed P Cygni-type features in the

Balmer lines. This unambiguous evidence of a wind at optical wavelengths makes BZ Cam an unusual object amongst CVs. There is no convincing evidence for any orbital variability of the wind-formed features. The fitting of synthetic profiles to the Hβ line constrains the inclination angle of the system to $i < 15°$. This implies that BZ Cam is a nearly face-on system.

Also presented is an examination of archive UV *IUE* spectra. The strength of the wind-formed features does not appear to correlate with the orbital phase, although the depth of the analysis is limited by the small archive data set available. The UV data provide constraints on the product of the wind mass loss rate and the C^{3+} ion fraction. This value of $\dot{M}q_{C^{3+}} = 0.3 \times 10^{-10} M_{\odot} yr^{-1}$, when combined with an estimate (although crude) of the C^{3+} ion fraction of $q_{C^{3+}} = 3 \times 10^{-3}$, results in an estimate for the mass loss rate of $\dot{M} = 1 \times 10^{-8} M_{\odot} yr^{-1}$. A comparison to an estimate of the lower limit of the mass accretion rate ($1.9 \times 10^{-9} M_{\odot} yr^{-1}$) suggests that the value of the C^{3+} ion fraction is likely to be much higher.

BZ Cam is also unusual because it is associated with a bow-shock nebula. The nebula is unlikely to be an evolutionary remnant, as evidenced by the near-solar value of the observed nitrogen to sulphur ratio. A more likely origin is an interaction between the current CV wind and the ISM. Examination of work carried out by Hollis *et al.* (1992) reveals the importance of a reliable estimate of the wind mass loss rate before further dynamical studies of the nebula are carried out.

6.2 Future work

6.2.1 V795 Herculis

I feel that the most important issue to resolve in the study of V795 Her is the determination of the orbital period. An unambiguous determination has implications for the magnetic scenarios which invoke either an IP configuration or a system analogous, in outflow and inflow mechanisms, to T Tauri stars. In this second scenario the 2.6 hr period, which is normally assumed to be the orbital period, becomes the spin period of the WD.

Initial attempts to make a spectroscopic identification of the secondary at IR wavelengths via the TiO bands have not proved fruitful (Rosen *et al.* 1995). Should further work using this method reveal the secondary star, a more extensive data set could then be obtained and subsequently used to determine the orbital period from radial velocity variations. A further study which could be carried

out at IR wavelengths would be to make a photometric identification of the secondary star. It may be possible to detect the ellipsoidal variations caused by the distorted sphere of the secondary star as it moves in and out of the line of sight. From these variations the orbital period can be determined.

The detection of the secondary star at IR wavelengths, when combined with simultaneous optical spectroscopy, would help to establish the absolute phasing of the binary system. From models of disk-overflow systems, predictions about the phasing of absorption features due to the stream (as it passes from the initial impact site to the re-impact site) can be made. If the absolute phasing of the absorption features seen in V795 Her is known, these can be compared to the model predictions.

The importance of magnetic effects within this system may become clearer with the recording of a more robust X-ray data set. A definite lack of X-ray radiation would not favour the IP scenario for V795 Her. Of course, should a clear X-ray signal be detected, it should then be possible to find the period, if any, with which this signal modulates.

6.2.2 SS Cygni

The outstanding issue to be resolved in the study of SS Cyg is the origin of the low velocity, stationary emission. More extensive time-resolved data sets may reveal some pattern in the occurrence of the emission. The slingshot prominence model would be supported by observations of stationary components at different velocities that are due to the formation of magnetic loops at different regions on the secondary star. The model would also be supported by the observation of low velocity, stationary emission during quiescence. The clouds seen in single, rotating stars are formed and destroyed on timescales of a few days. Observations over the course of a full outburst cycle could establish the timescale of clump formation and destruction in the case of a CV.

A very long term project is the examination of emission occurrence over several decades. The proposed solar-type magnetic cycle length of the secondary star in SS Cyg is 7.3 yr. If the slingshot prominence model is correct, the occurrence of stationary emission may be modulated on this 7.3 yr period. The changes in magnetic activity on the secondary star may affect the production of the magnetic loops and hence the occurrence of the stationary emission.

6.2.3 BZ Camelopardalis

Further study of BZ Cam is clearly warranted. A better set of blue spectra would allow an investigation of the ionization mixture of the wind, including the He I, He II and Balmer lines. The transient wind events need to be examined using a more extensive, good signal-to-noise time series. For example, one week of INT time in which to trace the observed absorption may reveal if this behaviour is phased or repeatable. This could then shed light on the origin of the variability.

Better imaging of the bow-shock nebula would be useful in order to carry out a study of the dynamical nature of the probable interaction between the CV wind and the ISM. This work is likely to be valid only if a better estimate of the wind mass loss rate is obtained first. An improved estimate could be obtained from fitting model wind profiles to UV *HST* data. *HST* data could also be used to examine if there is any radial velocity motion of the emission component in the C IV profiles. This motion may trace non-wind emission sources.

The presence of a bow-shock nebula around a CV appears to be unusual, with the nebula surrounding BZ Cam being the only well documented case. It would be interesting to image other CVs which drive strong winds and explore if any of these systems is also surrounded by a nebula.

6.2.4 Other candidates for multi-wavelength spectroscopic studies

RW Sextantis

With a visual magnitude of 10.6 (Bolick *et al.* 1987), RW Sex is one of the brightest CVs known. It is already known to drive a fast wind from UV *IUE* observations (*e.g.* Prinja & Rosen 1995). Some time-resolved optical spectroscopy is reported by Beuermann, Stasiewski & Schwope (1992) in which they discover narrow Balmer emission line components from the secondary star. The resolution of the data is only 2.7 Å. No further spectroscopic studies were unearthed by my literature search. As a wind-driving system that has not been studied extensively at optical wavelengths, RW Sex seems a good candidate for a multi-wavelength spectroscopic study.

V3885 Sagittarri

The nova-like variable V3885 Sgr is of interest because optical studies (Cowley, Crampton & Hesser 1977; Haug & Drechsel 1985) reveal a spectrum characterised by complex, variable Balmer emission features superimposed on very broad, shallow absorption lines. UV spectroscopy (Guinan & Sion 1982; Haug & Drechsel 1985) shows evidence of an outflow. A study by Woods *et al.* (1992) found moderate variations in the UV resonance lines. These may be related to orbital variability. The combination of a wind outflow and complex optical emission suggest that a multi-wavelength study of this object would be worthwhile.

Appendix A

The method of Doppler imaging

A.1 A tutorial on the interpretation of Doppler maps

As described in Section 1.3, the technique of Doppler tomography produces an image of a CV in *velocity* coordinates. Figure A.1 shows the relation between these velocity coordinates and the spatial coordinates of the binary system.

Consider first the WD and the secondary star. In the binary frame of reference, the velocity of the WD is K_1 and the velocity of the secondary star is K_2. At the instant of time shown in the bottom frame of Figure A.1, the WD is moving towards the observer, and the secondary star is moving away. In Doppler coordinates, the centre of the secondary star is positioned a distance K_2 along the positive V_Y axis. The WD is positioned a distance K_1 along the negative V_Y axis. (The centre of mass of the binary lies at the origin of the Doppler map). The Roche lobe of the secondary star is mapped uniformly into a Roche lobe on the tomogram. Also plotted in both frames is the ballistic trajectory of the gas stream.

Emission from an accretion disk maps to a ring in the Doppler tomogram. Points 1 to 6 (on the position coordinates figure) lie on the outer edge of an accretion disk. In the Doppler tomogram, they have mapped to points 1 to 6 on the part of the mapped disk that lies closest to the WD. This is because the (spatially) outer edge of the disk has the lowest velocities and therefore lies closest to the WD on the Doppler map. The dotted lines on the position coordinates map also lie on the disk. The nearer they are to the WD, the higher the velocity of the disk material. Therefore on the Doppler map, they are transformed inside-out. When a ring of emission is observed on a Doppler map, it is

interpreted as arising from the accretion disk. The maximum velocity of the ring as measured on the map relates to the inner disk region and the minimum velocity to the outer portions.

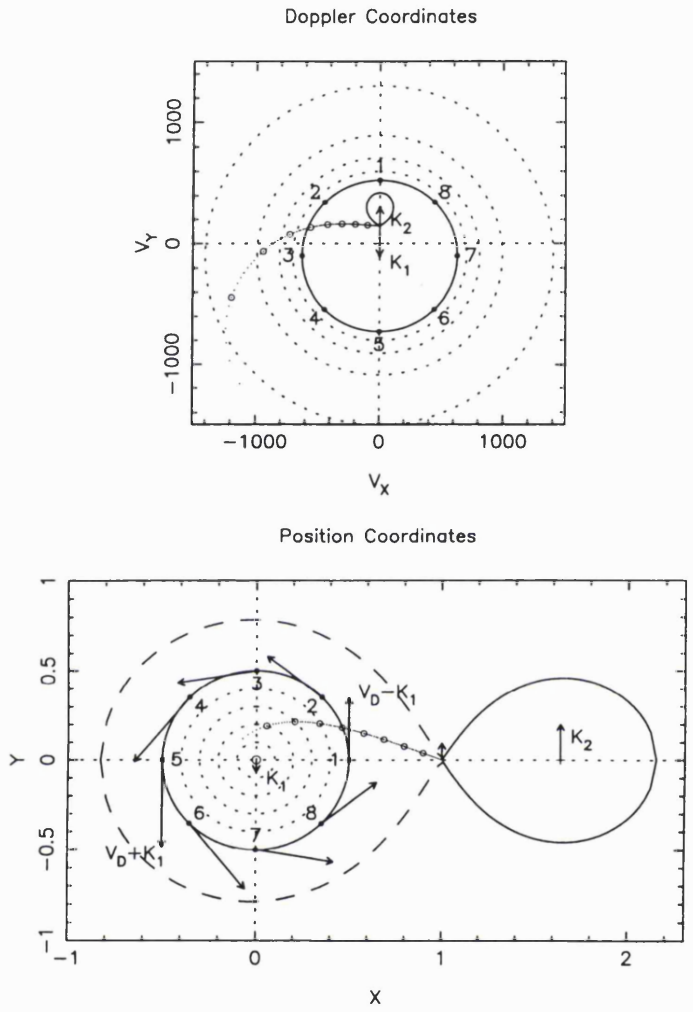

Figure A.1: The relation between the velocity coordinates in a Doppler map (top) and the spatial coordinates in the binary frame (bottom). The velocity of the WD is given by K_1 and the velocity of the secondary star is given by K_2. From Steeghs (1996).

Figure A.2 shows a simple schematic of a Doppler map. The main emission sites in a CV are marked. Emission from the disk will show up as a diffuse ring (with a position as is roughly marked by the dashed line). Emission from the secondary will lie inside the Roche lobe that is marked. A further source of emission may be the gas stream. As this figure clearly shows, the position of the stream and the secondary star overlap with the position of the accretion disk in velocity space. When interpreting Doppler maps, it should always be remembered that distinct emission sites may have the same velocity coordinates but entirely different spatial locations.

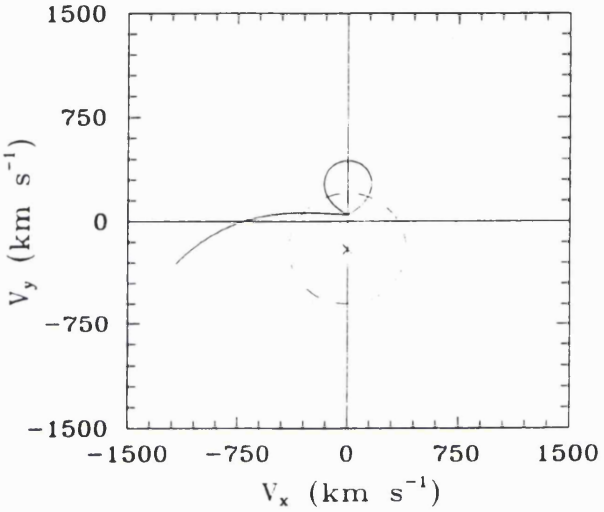

Figure A.2: Schematic of a Doppler map. From Kaitchuck *et al.* (1994).

Appendix B

Observing logs

Table B.1: Journal of optical spectroscopic observations of V795 Her, taken using the IDS

spectrum number	UT date	UT time	exposure time (s)
15	94-JUN-20	21:40:09	120.00
16	94-JUN-20	21:43:04	120.00
17	94-JUN-20	21:46:00	120.00
18	94-JUN-20	21:48:55	120.00
19	94-JUN-20	21:51:50	120.00
20	94-JUN-20	21:54:45	120.00
21	94-JUN-20	21:57:39	120.00
22	94-JUN-20	22:00:33	120.00
23	94-JUN-20	22:03:27	120.00
24	94-JUN-20	22:06:22	120.00
26	94-JUN-20	22:14:26	120.00
27	94-JUN-20	22:17:21	120.00
28	94-JUN-20	22:20:15	120.00
29	94-JUN-20	22:23:08	120.00
30	94-JUN-20	22:26:04	120.00

continued on next page

continued from previous page

spectrum number	UT date	UT time	exposure time (s)
31	94-JUN-20	22:28:58	120.00
32	94-JUN-20	22:31:52	120.00
33	94-JUN-20	22:34:46	120.00
34	94-JUN-20	22:37:40	120.00
35	94-JUN-20	22:40:34	120.00
43	94-JUN-20	23:27:47	120.00
44	94-JUN-20	23:30:42	120.00
45	94-JUN-20	23:33:38	120.00
46	94-JUN-20	23:36:34	120.00
47	94-JUN-20	23:39:28	120.00
48	94-JUN-20	23:42:22	120.00
49	94-JUN-20	23:45:17	120.00
50	94-JUN-20	23:48:11	120.00
51	94-JUN-20	23:51:06	120.00
52	94-JUN-20	23:54:00	120.00
55	94-JUN-21	00:10:05	120.00
56	94-JUN-21	00:13:00	120.00
57	94-JUN-21	00:15:56	120.00
58	94-JUN-21	00:18:53	120.00
59	94-JUN-21	00:21:47	120.00
60	94-JUN-21	00:24:43	120.00
61	94-JUN-21	00:27:37	120.00
62	94-JUN-21	00:30:32	120.00
63	94-JUN-21	00:33:26	120.00
64	94-JUN-21	00:36:20	120.00
69	94-JUN-21	01:14:57	120.00
70	94-JUN-21	01:17:54	120.00
71	94-JUN-21	01:20:49	120.00

continued on next page

continued from previous page

spectrum number	UT date	UT time	exposure time (s)
72	94-JUN-21	01:23:46	120.00
73	94-JUN-21	01:26:41	120.00
74	94-JUN-21	01:29:37	120.00
75	94-JUN-21	01:32:32	120.00
76	94-JUN-21	01:35:27	120.00
77	94-JUN-21	01:38:23	120.00
78	94-JUN-21	01:41:19	120.00
80	94-JUN-21	01:54:50	120.00
81	94-JUN-21	01:57:48	120.00
82	94-JUN-21	02:00:45	120.00
83	94-JUN-21	02:03:42	120.00
84	94-JUN-21	02:06:38	120.00
85	94-JUN-21	02:09:34	120.00
86	94-JUN-21	02:12:28	120.00
87	94-JUN-21	02:15:25	120.00
88	94-JUN-21	02:18:21	120.00
89	94-JUN-21	02:21:16	120.00
96	94-JUN-21	03:11:30	120.00
97	94-JUN-21	03:14:27	120.00
98	94-JUN-21	03:17:23	120.00
99	94-JUN-21	03:20:18	120.00
100	94-JUN-21	03:23:13	120.00
101	94-JUN-21	03:26:09	120.00
102	94-JUN-21	03:29:04	120.00
103	94-JUN-21	03:31:59	120.00
104	94-JUN-21	03:34:54	120.00
105	94-JUN-21	03:37:49	120.00
109	94-JUN-21	04:00:32	120.00

continued on next page

continued from previous page

spectrum number	UT date	UT time	exposure time (s)
110	94-JUN-21	04:03:28	120.00
111	94-JUN-21	04:06:25	120.00
112	94-JUN-21	04:09:20	120.00
113	94-JUN-21	04:12:17	120.00
114	94-JUN-21	04:15:13	120.00
115	94-JUN-21	04:18:08	120.00
116	94-JUN-21	04:21:04	120.00
117	94-JUN-21	04:23:59	120.00
118	94-JUN-21	04:26:55	120.00
122	94-JUN-21	04:59:53	180.00
123	94-JUN-21	05:04:02	180.00
124	94-JUN-21	05:08:11	180.00
125	94-JUN-21	05:12:16	180.00
126	94-JUN-21	05:17:07	180.00
153	94-JUN-21	21:09:19	300.00
154	94-JUN-21	21:15:28	300.00
155	94-JUN-21	21:22:00	300.00
156	94-JUN-21	21:27:56	300.00
157	94-JUN-21	21:33:50	300.00
158	94-JUN-21	21:39:45	300.00
159	94-JUN-21	21:45:40	300.00
161	94-JUN-21	21:56:55	300.00
162	94-JUN-21	22:02:50	300.00
163	94-JUN-21	22:08:45	300.00
164	94-JUN-21	22:14:40	300.00
165	94-JUN-21	22:20:34	300.00
167	94-JUN-21	22:32:32	300.00
168	94-JUN-21	22:38:27	300.00

continued on next page

continued from previous page

spectrum number	UT date	UT time	exposure time (s)
169	94-JUN-21	22:44:22	300.00
170	94-JUN-21	22:50:17	300.00
171	94-JUN-21	22:56:12	300.00
176	94-JUN-21	23:36:00	300.00
177	94-JUN-21	23:41:56	300.00
178	94-JUN-21	23:47:50	300.00
179	94-JUN-21	23:53:45	300.00
180	94-JUN-21	23:59:40	300.00
183	94-JUN-22	00:14:34	300.00
184	94-JUN-22	00:20:29	300.00
185	94-JUN-22	00:26:24	300.00
186	94-JUN-22	00:32:18	300.00
187	94-JUN-22	00:38:13	300.00
190	94-JUN-22	00:54:11	300.00
191	94-JUN-22	01:00:07	300.00
192	94-JUN-22	01:06:02	300.00
193	94-JUN-22	01:11:57	300.00
194	94-JUN-22	01:17:51	300.00
201	94-JUN-22	02:16:10	300.00
202	94-JUN-22	02:22:06	300.00
203	94-JUN-22	02:28:00	300.00
204	94-JUN-22	02:33:55	300.00
205	94-JUN-22	02:39:51	300.00
208	94-JUN-22	02:56:08	300.00
209	94-JUN-22	03:02:02	300.00
210	94-JUN-22	03:07:57	300.00
211	94-JUN-22	03:13:52	300.00
212	94-JUN-22	03:19:48	300.00

continued on next page

continued from previous page

spectrum number	UT date	UT time	exposure time (s)
218	94-JUN-22	04:09:23	300.00
219	94-JUN-22	04:15:19	300.00
220	94-JUN-22	04:21:15	300.00
221	94-JUN-22	04:27:12	300.00
222	94-JUN-22	04:33:07	300.00
224	94-JUN-22	04:44:10	300.00
225	94-JUN-22	04:50:05	300.00
226	94-JUN-22	04:56:01	300.00
227	94-JUN-22	05:01:56	300.00
228	94-JUN-22	05:07:51	300.00
254	94-JUN-22	21:06:26	300.00
255	94-JUN-22	21:13:44	300.00
256	94-JUN-22	21:19:39	300.00
257	94-JUN-22	21:25:34	300.00
258	94-JUN-22	21:31:29	300.00
259	94-JUN-22	21:37:35	300.00
261	94-JUN-22	21:48:08	300.00
262	94-JUN-22	21:54:03	300.00
263	94-JUN-22	21:59:58	300.00
264	94-JUN-22	22:05:52	300.00
265	94-JUN-22	22:11:47	300.00
267	94-JUN-22	22:22:52	300.00
268	94-JUN-22	22:28:47	300.00
269	94-JUN-22	22:34:42	300.00
270	94-JUN-22	22:40:37	300.00
271	94-JUN-22	22:46:32	300.00
290	94-JUN-23	00:57:33	300.00
291	94-JUN-23	01:03:28	300.00

continued on next page

continued from previous page

spectrum number	UT date	UT time	exposure time (s)
292	94-JUN-23	01:09:23	300.00
293	94-JUN-23	01:15:18	300.00
294	94-JUN-23	01:21:13	300.00
306	94-JUN-23	02:43:13	300.00
307	94-JUN-23	02:49:09	300.00
308	94-JUN-23	02:55:03	300.00
309	94-JUN-23	03:00:59	300.00
326	94-JUN-23	04:55:30	300.00
327	94-JUN-23	05:01:24	300.00
328	94-JUN-23	05:07:19	300.00
329	94-JUN-23	05:13:15	300.00
330	94-JUN-23	05:19:25	300.00
511	94-JUN-23	21:04:47	300.00
512	94-JUN-23	21:10:44	300.00
513	94-JUN-23	21:16:40	300.00
514	94-JUN-23	21:22:36	300.00
515	94-JUN-23	21:28:31	300.00
516	94-JUN-23	21:34:27	300.00
517	94-JUN-23	21:40:23	300.00
518	94-JUN-23	21:46:19	300.00
519	94-JUN-23	21:52:14	300.00
520	94-JUN-23	21:58:09	300.00
522	94-JUN-23	22:14:21	300.00
523	94-JUN-23	22:20:16	300.43
524	94-JUN-23	22:26:12	300.00
525	94-JUN-23	22:32:07	300.00
526	94-JUN-23	22:38:03	300.00
538	94-JUN-23	23:59:14	300.00

continued on next page

continued from previous page

spectrum number	UT date	UT time	exposure time (s)
539	94-JUN-24	00:05:10	300.00
540	94-JUN-24	00:11:06	300.00
541	94-JUN-24	00:17:03	300.02
542	94-JUN-24	00:22:58	300.00
554	94-JUN-24	01:38:03	300.00
555	94-JUN-24	01:43:59	300.00
556	94-JUN-24	01:49:57	300.00
558	94-JUN-24	02:01:49	300.00
768	94-JUN-25	21:31:28	300.00
769	94-JUN-25	21:37:27	300.00
770	94-JUN-25	21:43:24	300.00
771	94-JUN-25	21:49:19	300.00
772	94-JUN-25	21:55:15	300.00
773	94-JUN-25	22:01:11	300.00
774	94-JUN-25	22:07:09	300.00
776	94-JUN-25	22:19:26	300.00
777	94-JUN-25	22:25:21	300.05
789	94-JUN-25	23:35:03	300.00
790	94-JUN-25	23:40:58	300.00
792	94-JUN-25	23:50:32	300.00
793	94-JUN-25	23:56:28	300.00
794	94-JUN-26	00:02:24	300.00
795	94-JUN-26	00:08:20	300.00
796	94-JUN-26	00:14:16	300.00
797	94-JUN-26	00:20:12	300.00
798	94-JUN-26	00:26:09	300.00
800	94-JUN-26	00:36:07	300.00
801	94-JUN-26	00:42:03	300.00

continued on next page

continued from previous page

spectrum number	UT date	UT time	exposure time (s)
802	94-JUN-26	00:48:01	300.00
803	94-JUN-26	00:53:57	300.00
804	94-JUN-26	00:59:53	300.00
805	94-JUN-26	01:05:49	300.00
806	94-JUN-26	01:11:47	300.00
902	94-JUN-26	21:25:18	300.00
903	94-JUN-26	21:31:16	300.00
904	94-JUN-26	21:37:15	300.00
905	94-JUN-26	21:43:15	300.00
906	94-JUN-26	21:49:14	300.00
907	94-JUN-26	21:55:13	300.00
909	94-JUN-26	22:06:46	300.00
910	94-JUN-26	22:12:44	300.00
911	94-JUN-26	22:18:41	300.00
912	94-JUN-26	22:24:38	300.00
913	94-JUN-26	22:30:35	300.00
914	94-JUN-26	22:36:32	300.01
919	94-JUN-26	23:12:23	300.00
920	94-JUN-26	23:18:22	300.00
921	94-JUN-26	23:24:19	300.00
922	94-JUN-26	23:30:16	300.00
923	94-JUN-26	23:36:14	300.00
924	94-JUN-26	23:42:10	300.00
926	94-JUN-26	23:52:33	300.00
927	94-JUN-26	23:58:29	300.00
928	94-JUN-27	00:04:26	300.00
929	94-JUN-27	00:10:23	300.00
930	94-JUN-27	00:16:20	300.00

continued on next page

continued from previous page

spectrum number	UT date	UT time	exposure time (s)
931	94-JUN-27	00:22:18	300.00
933	94-JUN-27	00:41:37	300.00
934	94-JUN-27	00:54:08	300.00

Table B.2: Journal of optical spectroscopic observations of V795 Her, taken using the FOS

spectrum number	UT date	UT time	exposure time (s)
639	94-JUN-24	21:20:30	300.00
640	94-JUN-24	21:27:14	300.00
641	94-JUN-24	21:33:04	300.00
642	94-JUN-24	21:38:53	300.00
643	94-JUN-24	21:44:41	302.99
644	94-JUN-24	21:50:34	300.00
645	94-JUN-24	21:56:23	300.00
646	94-JUN-24	22:02:13	300.00
647	94-JUN-24	22:08:03	300.00
648	94-JUN-24	22:13:51	300.00
649	94-JUN-24	22:19:39	300.00
650	94-JUN-24	22:26:16	300.00
651	94-JUN-24	22:32:05	300.00
652	94-JUN-24	22:37:54	300.00
653	94-JUN-24	22:43:43	300.01
654	94-JUN-24	22:49:32	300.00
655	94-JUN-24	22:55:21	300.00
656	94-JUN-24	23:01:10	300.00
657	94-JUN-24	23:06:59	300.00
658	94-JUN-24	23:12:47	300.00
659	94-JUN-24	23:18:35	300.00
661	94-JUN-24	23:30:03	300.00
662	94-JUN-24	23:35:53	300.00
663	94-JUN-24	23:41:41	300.00
664	94-JUN-24	23:47:30	300.00
665	94-JUN-24	23:53:18	300.00

continued on next page

continued from previous page

spectrum number	UT date	UT time	exposure time (s)
666	94-JUN-24	23:59:08	300.00
667	94-JUN-25	00:04:57	300.00
668	94-JUN-25	00:17:38	300.00
669	94-JUN-25	00:23:27	300.00
670	94-JUN-25	00:29:15	300.00
671	94-JUN-25	00:36:38	300.00
672	94-JUN-25	00:42:28	307.33
673	94-JUN-25	00:48:27	300.00
674	94-JUN-25	00:54:15	300.00
675	94-JUN-25	01:00:04	300.00
676	94-JUN-25	01:05:55	300.01

Table B.3: Journal of UV *HST* observations of V795 Her (shortened)

spectrum number	HJD
1	2449523.6660094
2	2449523.6662409
3	2449523.6664608
...	...
484	2449524.0180873
485	2449524.0183072
486	2449524.0185272
487	2449525.2074433
488	2449525.2076747
489	2449525.2078946
...	...
970	2449525.5595670
971	2449525.5597869
972	2449525.5600068
973	2449527.0840079
974	2449527.0842393
975	2449527.0844592
...	...
1456	2449527.4361310
1457	2449527.4363509
1458	2449527.4365708

Table B.4: Journal of optical spectroscopic observations of SS Cyg

spectrum number	UT date	UT time	exposure time (s)
199	94-JUN-22	02:03:07	300.00
592	94-JUN-24	05:13:25	30.00
593	94-JUN-24	05:17:34	60.00
594	94-JUN-24	05:19:30	60.00
595	94-JUN-24	05:21:26	60.00
596	94-JUN-24	05:23:23	60.00
597	94-JUN-24	05:25:12	60.00
598	94-JUN-24	05:27:44	60.00
599	94-JUN-24	05:29:41	60.00
600	94-JUN-24	05:31:37	60.00
601	94-JUN-24	05:33:34	60.00
602	94-JUN-24	05:35:31	60.00
717	94-JUN-25	04:00:56	30.00
812	94-JUN-26	01:59:59	240.00
813	94-JUN-26	02:04:57	240.00
814	94-JUN-26	02:09:56	240.00
815	94-JUN-26	02:14:54	240.00
816	94-JUN-26	02:19:54	240.00
817	94-JUN-26	02:24:52	240.00
818	94-JUN-26	02:29:51	240.00
820	94-JUN-26	02:38:59	240.00
821	94-JUN-26	02:43:58	240.00
822	94-JUN-26	02:48:58	240.00
823	94-JUN-26	02:53:58	240.00
824	94-JUN-26	02:58:54	240.00
825	94-JUN-26	03:03:52	240.00
826	94-JUN-26	03:08:49	240.00

continued on next page

continued from previous page

spectrum number	UT date	UT time	exposure time (s)
828	94-JUN-26	03:18:28	240.00
829	94-JUN-26	03:23:26	240.00
830	94-JUN-26	03:28:23	240.00
831	94-JUN-26	03:33:21	240.00
832	94-JUN-26	03:38:19	240.00
833	94-JUN-26	03:43:18	240.00
834	94-JUN-26	03:48:14	240.00
836	94-JUN-26	03:58:24	240.00
837	94-JUN-26	04:03:21	240.00
838	94-JUN-26	04:08:18	240.00
839	94-JUN-26	04:13:16	240.00
840	94-JUN-26	04:18:14	240.00
841	94-JUN-26	04:23:09	240.00
842	94-JUN-26	04:28:06	240.00
847	94-JUN-26	05:01:45	240.00
848	94-JUN-26	05:06:42	240.00
849	94-JUN-26	05:11:40	240.00
850	94-JUN-26	05:16:39	240.00
851	94-JUN-26	05:21:38	240.00
852	94-JUN-26	05:26:53	240.00
853	94-JUN-26	05:32:38	240.00
938	94-JUN-27	01:19:44	300.00
939	94-JUN-27	01:25:44	300.00
940	94-JUN-27	01:31:42	300.00
942	94-JUN-27	01:41:39	300.00
943	94-JUN-27	01:47:38	300.00
944	94-JUN-27	01:53:45	300.00
945	94-JUN-27	01:59:43	300.00

continued on next page

continued from previous page

spectrum number	UT date	UT time	exposure time (s)
946	94-JUN-27	02:05:42	300.00
947	94-JUN-27	02:11:42	300.00
952	94-JUN-27	02:47:39	300.00
953	94-JUN-27	02:53:37	300.00
954	94-JUN-27	02:59:36	300.00
955	94-JUN-27	03:05:34	300.00
956	94-JUN-27	03:11:32	300.00
957	94-JUN-27	03:17:29	300.01
959	94-JUN-27	03:27:38	300.00
960	94-JUN-27	03:33:36	300.00
961	94-JUN-27	03:39:34	300.00
962	94-JUN-27	03:45:32	300.00
963	94-JUN-27	03:51:28	300.00
964	94-JUN-27	03:57:26	300.00
969	94-JUN-27	04:35:49	300.00
970	94-JUN-27	04:41:47	300.00
971	94-JUN-27	04:47:45	300.00
972	94-JUN-27	04:53:46	300.00
973	94-JUN-27	04:59:45	300.00
974	94-JUN-27	05:05:44	300.00
976	94-JUN-27	05:17:55	300.00
977	94-JUN-27	05:24:03	300.00

Table B.5: Journal of archive UV *IUE* observations of SS Cyg

image number	dispersion	aperture	observation date	exposure time (s)
SWP 51280	LOW	LARGE	94-JUL-01	40.000
SWP 51280	LOW	SMALL	94-JUL-01	105.000
SWP 51282	LOW	LARGE	94-JUL-01	40.000
SWP 51282	LOW	SMALL	94-JUL-01	105.000
SWP 51304	LOW	LARGE	94-JUL-03	40.000
SWP 51304	LOW	SMALL	94-JUL-03	105.000
SWP 51305	HIGH	LARGE	94-JUL-03	3600.000
SWP 51306	LOW	LARGE	94-JUL-03	44.000
SWP 51306	LOW	SMALL	94-JUL-03	115.000
SWP 51325	LOW	LARGE	94-JUL-05	50.000
SWP 51325	LOW	SMALL	94-JUL-05	130.000
SWP 51326	HIGH	LARGE	94-JUL-05	3960.000
SWP 51327	LOW	LARGE	94-JUL-05	50.000
SWP 51327	LOW	SMALL	94-JUL-05	130.000
SWP 51372	LOW	LARGE	94-JUL-08	140.000
SWP 51372	LOW	SMALL	94-JUL-08	360.000
SWP 51373	LOW	LARGE	94-JUL-08	112.000
SWP 51373	LOW	SMALL	94-JUL-08	288.000
SWP 51391	LOW	LARGE	94-JUL-10	130.000
SWP 51391	LOW	SMALL	94-JUL-10	480.000
SWP 51392	LOW	LARGE	94-JUL-10	160.000
SWP 51392	LOW	SMALL	94-JUL-10	480.000
SWP 51393	LOW	LARGE	94-JUL-10	230.000
SWP 51393	LOW	SMALL	94-JUL-10	600.000

Table B.6: Journal of optical spectroscopic observations of BZ Cam

spectrum number	UT date	UT time	exposure time (s)
624	97-FEB-05	06:07:39	300
625	97-FEB-05	06:12:49	300
626	97-FEB-05	06:17:59	300
627	97-FEB-05	06:23:09	300
629	97-FEB-05	06:33:28	300
630	97-FEB-05	06:47:27	600
631	97-FEB-05	06:57:58	600
632	97-FEB-05	07:21:50	600
633	97-FEB-05	07:33:39	600
635	97-FEB-05	07:45:41	600
636	97-FEB-05	07:55:51	600
637	97-FEB-05	08:06:01	600
639	97-FEB-05	08:18:54	300
640	97-FEB-05	08:24:04	300
641	97-FEB-05	08:29:14	300
642	97-FEB-05	08:34:24	300
644	97-FEB-05	08:44:45	300
646	97-FEB-05	08:52:26	300
648	97-FEB-05	09:02:47	300
649	97-FEB-05	09:07:57	300
650	97-FEB-05	09:13:08	300
651	97-FEB-05	09:18:18	300
653	97-FEB-05	09:26:53	300
654	97-FEB-05	09:32:03	300
655	97-FEB-05	09:37:12	300
656	97-FEB-05	09:42:22	300

continued on next page

continued from previous page

spectrum number	UT date	UT time	exposure time (s)
657	97-FEB-05	09:47:33	300
658	97-FEB-05	09:52:42	300
660	97-FEB-05	10:00:49	300
661	97-FEB-05	10:05:59	300
662	97-FEB-05	10:11:09	300
663	97-FEB-05	10:16:19	300
664	97-FEB-05	10:21:29	300
667	97-FEB-05	10:36:10	300
668	97-FEB-05	10:41:21	300
669	97-FEB-05	10:46:31	300
670	97-FEB-05	10:51:41	300
671	97-FEB-05	10:56:52	300
672	97-FEB-05	11:02:03	300
674	97-FEB-05	11:10:07	300
675	97-FEB-05	11:15:19	300
676	97-FEB-05	11:20:29	300
677	97-FEB-05	11:25:39	300
678	97-FEB-05	11:30:49	300
679	97-FEB-05	11:35:59	280
750	97-FEB-06	05:55:40	100
751	97-FEB-06	06:03:11	600
753	97-FEB-06	06:18:04	300
754	97-FEB-06	06:23:15	300
755	97-FEB-06	06:28:26	300
756	97-FEB-06	06:33:35	300
757	97-FEB-06	06:38:45	300
758	97-FEB-06	06:43:55	300
760	97-FEB-06	06:51:17	300

continued on next page

continued from previous page

spectrum number	UT date	UT time	exposure time (s)
761	97-FEB-06	06:56:27	300
762	97-FEB-06	07:01:37	300
780	97-FEB-06	08:34:50	300
781	97-FEB-06	08:40:00	300
782	97-FEB-06	08:45:10	300
783	97-FEB-06	08:50:20	300
784	97-FEB-06	08:55:30	300
785	97-FEB-06	09:00:40	300
787	97-FEB-06	09:07:39	300
788	97-FEB-06	09:12:48	300
789	97-FEB-06	09:17:59	300
790	97-FEB-06	09:23:08	300
791	97-FEB-06	09:28:18	300
792	97-FEB-06	09:33:29	300
794	97-FEB-06	09:40:40	300
795	97-FEB-06	09:45:50	300
796	97-FEB-06	09:51:00	300
797	97-FEB-06	09:56:10	300
798	97-FEB-06	10:01:20	300
799	97-FEB-06	10:06:30	300
801	97-FEB-06	10:13:23	300
802	97-FEB-06	10:18:33	300
803	97-FEB-06	10:23:44	300
804	97-FEB-06	10:28:54	300
805	97-FEB-06	10:34:04	300
806	97-FEB-06	10:39:14	300
808	97-FEB-06	10:46:47	300
809	97-FEB-06	10:51:57	300

continued on next page

continued from previous page

spectrum number	UT date	UT time	exposure time (s)
810	97-FEB-06	10:57:07	300
811	97-FEB-06	11:02:17	300
812	97-FEB-06	11:07:27	300
813	97-FEB-06	11:12:36	300
815	97-FEB-06	11:21:51	300
816	97-FEB-06	11:27:01	300
1009	97-FEB-09	07:37:20	300
1010	97-FEB-09	07:42:58	300
1011	97-FEB-09	07:55:10	300
1012	97-FEB-09	08:01:53	300
1013	97-FEB-09	08:07:21	300
1016	97-FEB-09	08:26:38	300
1017	97-FEB-09	08:31:48	300
1018	97-FEB-09	09:06:01	300
1019	97-FEB-09	09:12:06	300
1020	97-FEB-09	09:17:52	300
1021	97-FEB-09	09:24:09	300
1023	97-FEB-09	09:31:45	300
1024	97-FEB-09	09:37:35	300
1025	97-FEB-09	09:43:21	300
1026	97-FEB-09	09:52:33	300
1028	97-FEB-09	10:37:11	300
1029	97-FEB-09	10:42:48	300
1030	97-FEB-09	10:48:31	300
1031	97-FEB-09	10:54:19	300
1033	97-FEB-09	11:06:55	300
1034	97-FEB-09	11:13:16	300

Table B.7: Journal of archive UV *IUE* observations of BZ Cam

image number	dispersion	aperture	observation date	exposure time (s)
LWP 14485	LOW	LARGE	88-NOV-19	1499.832
LWP 14486	LOW	LARGE	88-NOV-19	1499.832
LWP 14487	LOW	LARGE	88-NOV-19	1499.832
LWP 14491	LOW	LARGE	88-NOV-20	1499.832
LWP 14492	LOW	LARGE	88-NOV-20	1379.819
LWP 14493	LOW	LARGE	88-NOV-20	1379.819
LWP 15335	LOW	LARGE	89-APR-10	1799.659
LWP 15336	LOW	LARGE	89-APR-10	1199.595
LWR 10029	LOW	LARGE	81-FEB-26	1200.000
LWR 16940	LOW	LARGE	83-OCT-07	1500.000
SWP 13372	LOW	LARGE	81-FEB-26	899.761
SWP 13372	LOW	SMALL	81-FEB-26	1799.652
SWP 21251	LOW	LARGE	83-OCT-07	1800.000
SWP 21948	LOW	LARGE	84-JAN-06	2099.480
SWP 22458	LOW	LARGE	84-MAR-10	2400.000
SWP 34774	LOW	LARGE	88-NOV-19	3599.844
SWP 34775	LOW	LARGE	88-NOV-19	1799.652
SWP 34776	LOW	LARGE	88-NOV-19	3599.844
SWP 34777	LOW	LARGE	88-NOV-19	1439.614
SWP 34784	LOW	LARGE	88-NOV-20	3599.844
SWP 34785	LOW	LARGE	88-NOV-20	3599.844
SWP 34786	LOW	LARGE	88-NOV-20	3599.844
SWP 34787	LOW	LARGE	88-NOV-20	2519.729
SWP 35975	LOW	LARGE	89-APR-10	3437.516
SWP 35976	LOW	LARGE	89-APR-10	1799.652
SWP 35977	LOW	SMALL	89-APR-10	4199.369

References

Arévalo, M. J., Solheim, J. E. & Lazaro, C. (1989), *Lect. Notes Phys.* **328**, 462.

Baluta, C., Nousek, J. & Mansperger, C. (1995), *B. A. A. S.* **186**, 2207.

Bartolini, C., Guarnieri, A., Lolli, M., Picciconi, A., Giovanelli, F., Gaudenzi, S. & Lombardi, R. (1985), *in* F. Giovanelli, ed., 'Multifrequency Behaviour of Galactic Accreting Sources', Inst. Astrofis. Spaziale., p. 50.

Bath, G. T. (1974), *Mon. Not. R. Astr. Soc.* **171**, 311.

Bath, G. T. & van Paradijs, J. (1983), *Nature* **305**, 33.

Beuermann, K., Stasiewski, U. & Schwope, A. D. (1992), *Astr. Astrophys.* **256**, 433.

Bianchimi, A. (1990), *in* A. Cassatella & R. Viotti, eds, 'Physics of Classical Novae', Berlin Springer-Verlag, p. 13.

Bianchini, A. (1987), *Mem. Soc. Astron. Ital.* **58**, 245.

Bolick, U., Beuermann, K., Bruch, A. & Lenzen, R. (1987), *Astrophys. Space. Sci.* **130**, 175.

Buckley, D. A. H., Sekiguchi, K., Motch, C., O'Donoghue, D., Chen, A. L., Schwarzenberg-Czerny, A., Pitsch, W. & Harrop-Allin, M. K. (1995), *Mon. Not. R. Astr. Soc.* **275**, 1028.

Camenzind, M. (1990), *in* 'Reviews in Modern Astronomy', Vol. 3, Springer, p. 234.

Cameron, A. C. & Robinson, R. D. (1989), *Mon. Not. R. Astr. Soc.* **236**, 57.

Cameron, A. C., Duncan, D. K., Ehrenfreund, P., Foing, B. H., Kuntz, K. D., Penston, M. V., Robinson, R. D. & Soderblom, D. R. (1990), *Mon. Not. R. Astr. Soc.* **247**, 415.

Casares, J., Martínez-Pais, I. G., Marsh, T. R., Charles, P. A. & Lazaro, C. (1996), *Mon. Not. R. Astr. Soc.* **278**, 219.

Castor, J. I. (1970), *Mon. Not. R. Astr. Soc.* **149**, 111.

Castor, J. I. & Lamers, H. J. G. L. M. (1979), *Astrophys. J. Suppl.* **39**, 481.

Castor, J. I., Abbott, D. C. & Klein, R. I. (1975), *Astrophys. J.* **195**, 157.

Cheng, F. H. & Lin, D. N. C. (1992), *Astrophys. J.* **389**, 714.

Clarke, J. T., Capel, D. & Bowyer, S. (1984), *Astrophys. J.* **287**, 845.

Cordova, F. & Mason, K. O. (1982), *Astrophys. J.* **260**, 716.

Cordova, F. A. & Howarth, I. D. (1986), *in* Y. Kondo. *et al.*, ed., 'Exploring the Universe with the *IUE* Satellite', Reidel, p. 395.

Cowley, A. P., Crampton, D. & Hesser, J. E. (1977), *Astrophys. J.* **214**, 471.

Dgani, R., Livio, M. & Soker, N. (1989), *Astrophys. J.* **336**, 350.

Drew, J. E. (1987), *Mon. Not. R. Astr. Soc.* **224**, 595.

Drew, J. E. (1990), Winds from disks, *in* 'Physics of Classical Novae', p. 228.

Drew, J. E. & Verbunt, F. (1985), *Mon. Not. R. Astr. Soc.* **213**, 191.

Drew, J. E. & Verbunt, F. (1988), *Mon. Not. R. Astr. Soc.* **234**, 341.

Dyson, J. E. & Williams, D. A. (1980), *Physics of the Interstellar Medium*, John Wiley and Sons.

Edwards, S., Strom, S. E., Hartigan, P., Strom, K. M., Hillenbrand, L. A., Herbst, W., Attridge, J., Merrill, K. M., Probst, R. & Gatley, I. (1993), *Astr. J.* **106**, 372.

Eggleton, P. P. (1976), *in* P. P. Eggleton, S. Mitton & J. A. J. Whelan, eds, 'Structure and Evolution of Close Binary Systems', Dordrecht Reidel, p. 209.

Ellis, G. L., Grayson, E. T. & Bond, H. E. (1984), *Publ. Astr. Soc. Pacif.* **96**, 283.

Frank, J., King, A. R. & Raine, D. J. (1985), *Accretion Power in Astrophysics*, Cambridge Astrophysics Series, Cambridge University Press.

Giovannelli, F. & Martínez-Pais, I. G. (1991), *Space Sci. Rev.* **56**, 373.

Griffith, D., Fabian, D. & Sion, E. M. (1995), *Publ. Astr. Soc. Pacif.* **107**, 856.

Guinan, E. F. & Sion, E. M. (1982), *Astrophys. J.* **258**, 217.

Hameury, J. M., King, A. R. & Lasota, J. P. (1986), *Mon. Not. R. Astr. Soc.* **218**, 695.

Haswell, C. A., Horne, K., Thomas, G., Patterson, J. & Thorstensen, J. R. (1994), Tomography of V795 her, *in* A. W. Shafter, ed., 'Interacting Binary Stars: a symposium held in conjunction with the 105th meeting of the Astronomical Society of the Pacific', Vol. 56, Astronomical Society of the Pacific Conference Series.

Haug, K. & Drechsel, H. (1985), *Astr. Astrophys.* **151**, 157.

Hellier, C. (1997), *Astrophys. J.* in press.

Hellier, C. & Robinson, E. L. (1994), *Astrophys. J. (Letters).* **431**, L107.

Hessman, F. V., Robinson, E. L., Nather, R. E. & Zhang, E. H. (1984), *Astrophys. J.* **286**, 747.

Hildebrand, R. H., Spillar, E. J. & Stiening, R. F. (1981), *Astrophys. J.* **243**, 223.

Hirose, M., Osaki, Y. & Mineshige, S. (1991), *Publ. Astr. Soc. Japan* **43**, 809.

Hoare, M. G. & Drew, J. E. (1993), *Mon. Not. R. Astr. Soc.* **260**, 647.

Hollis, J. M., Oliversen, R. J., Wagner, R. M. & Feibelman, W. A. (1992), *Astrophys. J.* **393**, 217.

Holm, A. V. & Gallagher, J. (1974), *Astrophys. J.* **192**, 425.

Honeycutt, R. K., Schlegel, E. M. & Kaitchuck, R. H. (1986), *Astrophys. J.* **302**, 388.

Horne, K. (1991), *in* A. W. Shafter, ed., 'Proceedings of the 12th North American Workshop on Cataclysmic Variables and X-ray Binaries'.

Horne, K. & Gomer, R. (1980), *Astrophys. J.* **237**, 845.

Horne, K. & Marsh, T. R. (1986), *Mon. Not. R. Astr. Soc.* **218**, 761.

Hoshi, R. (1979), *Progress Theor. Physics* **61**, 1307.

Howarth, I. D. (1978), *J. Brit. Astr. Assoc.* **88**, 458.

Howarth, I. D. & Prinja, R. K. (1989), *Astrophys. J. Suppl.* **69**, 527.

Howarth, I. D., Murray, J., Mills, D. & Berry, D. S. (1995), *in* 'SUN 50.17', Rutherford Appleton Laboratory.

Johns, C. M. & Basri, G. (1995), *Astrophys. J.* **449**, 341.

Kaitchuck, R. H., Schlegel, E. M., Honeycutt, R. K., Horne, K., Marsh, T. R., White II, J. C. & Mansperger, C. S. (1994), *Astrophys. J. Suppl.* **93**, 519.

Kallman, T. R. & Jensen, K. A. (1985), *Astrophys. J.* **299**, 277.

King, A. R., Frank, J. & Whitehurst, R. (1990), *Mon. Not. R. Astr. Soc.* **244**, 731.

Kley, W. (1991), *Astr. Astrophys.* **247**, 95.

Königl, A. (1991), *Astrophys. J.* **370**, L39.

Krautter, J., Klaas, U. & Radons, G. (1987), *Astr. Astrophys.* **181**, 373.

Krautter, J., Klare, G., Wolf, B., Duerbeck, H. W., Rahe, J., Vogt, N. & Wargau, W. (1981), *Astr. Astrophys.* **102**, 337.

Lanzafame, G., Belvedere, G. & Molteni, D. (1992), *Mon. Not. R. Astr. Soc.* **258**, 152.

Lanzafame, G., Belvedere, G. & Molteni, D. (1993), *Mon. Not. R. Astr. Soc.* **263**, 839.

Livio, M., Soker, N. & Dgani, R. (1986), *Astrophys. J.* **305**, 267.

Lombardi, R., Gaudenzi, S. & Giovanelli, F. (1987), *Astrophys. Space. Sci.* **130**, 275.

Lu, W. & Hutchings, J. B. (1985), *Publ. Astr. Soc. Pacif.* **97**, 990.

Mansperger, C. S., Kaitchuck, R. H., Garnavich, P. M., Dinshaw, N. & Zamkoff, E. (1994), *Publ. Astr. Soc. Pacif.* **106**, 858.

Marsh, T. R. & Horne, K. (1988), *Mon. Not. R. Astr. Soc.* **235**, 269.

Marsh, T. R. & Horne, K. (1990), *Astrophys. J.* **349**, 593.

Martínez-Pais, I. G., Giovanelli, F., Rossi, C. & Gaudenzi, S. (1994), *Astr. Astrophys.* **291**, 455.

Martínez-Pais, I. G., Giovanelli, F., Rossi, C. & Gaudenzi, S. (1996), *Astr. Astrophys.* **308**, 833.

Mauche, C. W. (1991), *Astrophys. J.* **373**, 624.

Mauche, C. W. & Raymond, J. C. (1987), *Astrophys. J.* **323**, 690.

Mauche, C. W. & Raymond, J. C. (1995), *in* J. R. Jokipii, C. P. Sonett & M. S. Giampapa, eds, 'Cosmic Winds and the Heliosphere', University of Arizona Press.

Meyer, F. & Meyer-Hofmeister, E. (1981), *Astr. Astrophys.* **104**, L10.

Meyerdierks, H. (1993), *in* 'SUN 86.9', Rutherford Appleton Laboratory.

Mineshige, S. (1988), *Astr. Astrophys.* **190**, 72.

Mineshige, S. & Wood, J. H. (1990), *Mon. Not. R. Astr. Soc.* **247**, 43.

Mironov, A. V., Moshkalev, A. G. & Sugarov, S. (1983), *Inf. Bull. Var. Stars.*

Nichols, J. S., Garhart, M. P., de la Pena, M. D. & Levay, K. L. (1993), *IUE New Spectral Image Processing System Information Manual: Low-Dispersion Data*, National Aeronautic and Space Administration.

Osaki, Y. (1974), *Publ. Astr. Soc. Japan* **26**, 429.

Osaki, Y. (1989), *Publ. Astr. Soc. Japan* **41**, 1005.

Osaki, Y. (1996), *Publ. Astr. Soc. Pacif.* **108**, 39.

Paczynski, B. & Sienkiewicz, R. (1981), *Astrophys. J. (Letters).* **28**, L27.

Papaloziou, J. & Bath, G. T. (1975), *Mon. Not. R. Astr. Soc.* **172**, 339.

Patterson, J. (1984), *Astrophys. J. Suppl.* **54**, 443.

Patterson, J. & Raymond, J. C. (1985), *Astrophys. J.* **292**, 550.

Patterson, J. & Skillman, D. R. (1994), *Publ. Astr. Soc. Pacif.* **106**, 1141.

Patterson, J., Patino, R., Thorstensen, J. R., Harvey, D., Skillman, D. & Ringwald, F. (1996), *Astr. J.* **111**, 2422.

Patterson, J., Robinson, E. L. & Kiplinger, A. L. (1978), *Astrophys. J.* **226**, L137.

Patterson, J., Thomas, G., Skillman, D. R. & Diaz, M. P. (1993), *Astrophys. J. Suppl.* **86**, 235.

Pavelin, P. E., Spencer, R. E. & Davis, R. J. (1994), *Mon. Not. R. Astr. Soc.* **269**, 779.

Piché, F. & Szkody, P. (1989), *Astr. J.* **98**, 2225.

Pneuman, G. W. & Kopp, R. A. (1971), *Sol. Phys.* **18**, 258.

Pringle, J. E. (1977), *Mon. Not. R. Astr. Soc.* **178**, 195.

Pringle, J. E., Verbunt, F. & Wade, R. A. (1986), *Mon. Not. R. Astr. Soc.* **221**, 169.

Prinja, R. K. & Rosen, S. R. (1993), *Mon. Not. R. Astr. Soc.* **262**, L37.

Prinja, R. K. & Rosen, S. R. (1995), *Mon. Not. R. Astr. Soc.* **273**, 461.

Prinja, R. K., Drew, J. E. & Rosen, S. R. (1992), *Mon. Not. R. Astr. Soc.* **256**, 219.

Prinja, R. K., Rosen, S. R. & Supelli, K. (1991), *Mon. Not. R. Astr. Soc.* **248**, 40.

Rappaport, S., Cash, W., Doxsey, R., McClintock, J. & Moore, G. (1974), *Astrophys. J.* **187**, L5.

Rappaport, S., Verbunt, F. & Joss, P. C. (1983), *Astrophys. J.* **275**, 713.

Ringwald, F. A. & Naylor, T. (1997), *in* D. T. Wickramasinghe, G. V. Bicknell & L. Ferrario, eds, 'Accretion Phenomena and Related Outflows', Vol. 121, ASP, p. 790.

Ritter, H. (1984), *Astr. Astrophys. Suppl.* **57**, 385.

Roberts, D. H., Lehár, J. & Dreher, J. W. (1987), *Astr. J.* **93**, 968.

Robinson, E. L. (1973), *Astrophys. J.* **186**, 347.

Robinson, E. L. (1976), *Ann. Rev. Astr. Astrophys.* **14**, 119.

Robinson, E. L., Barker, E. S., Cochran, A. L., Cochran, W. D. & Nather, R. E. (1981), *Astrophys. J.* **251**, 611.

Rosen, S. R., Branduardi-Raymont, G., Mason, K. O. & Murdin, P. G. (1989), *Mon. Not. R. Astr. Soc.* **237**, 1037.

Rosen, S. R., Prinja, R. K., Drew, J. E., Mason, K. O. & Howell, S. B. (1997), *Mon. Not. R. Astr. Soc.* in press.

Rosen, S. R., Watson, T. K., Robinson, E. L., Prinja, R. K., Misselt, K. & Shafter, A. W. (1995), *Astr. Astrophys.* **300**, 392.

Rozyczka, M. (1988), *Acta Astron.* **38**, 175.

Rozyczka, M. & Schwarzenberg-Czerny, A. (1987), *Acta Astron.* **37**, 141.

Russ, J. C. (1992), *The Image Processing Handbook*, CRC Press.

Schlegel, E. M., Barrett, P. E., de Jaeger, O. C., Chanmugam, G., Hunter, S. & Mattox, J. (1995), *Astrophys. J.* **439**, 322.

Shafter, A. W., Hessman, F. V. & Zhang, E. H. (1988), *Astrophys. J.* **327**, 248.

Shafter, A. W., Robinson, E. L., Crampton, D., Warner, B. & Prestage, R. M. (1990), *Astrophys. J.* **354**, 708.

Shlosman, I. & Vitello, P. (1993), *Astrophys. J.* **409**, 372.

Skillman, D. R. & Patterson, J. (1993), *Astrophys. J.* **417**, 298.

Smak, J. (1981), *Acta Astron.* **31**, 395.

Smak, J. (1984), *Acta Astron.* **34**, 161.

Spruit, H. C. & Ritter, H. (1983), *Astr. Astrophys.* **124**, 267.

Starrfield, S., Sparks, W. M. & Truran, J. W. (1974), *Astrophys. J.* **192**, 647.

Steeghs, D. (1996), *Doppler Tomography and Dynamics of Magnetic Structures in Cataclysmic Variables*, graduation thesis University of Utrecht.

Steeghs, D. T., Horne, K., Marsh, T. R. & Donati, J. F. (1996), *Mon. Not. R. Astr. Soc.* **281**, 626.

Stover, R. J., Robinson, E. L., Nather, R. E. & Montemayor, T. J. (1980), *Astrophys. J.* **240**, 597.

Szkody, P. & Mateo, M. (1986), *Astrophys. J.* **301**, 286.

Szkody, P. & Wade, R. (1981), *Astrophys. J.* **251**, 201.

Taam, R. E. & McDermott, P. N. (1989), *Astrophys. J. (Letters).* **319**, L83.

Thorstensen, J. R. (1986), *Astr. J.* **90**, 940.

Thorstensen, J. R., Ringwald, F. A., Wade, R. A., Schmidt, G. D. & Norsworthy, J. E. (1991), *Astr. J.* **102**, 272.

Thorstensen, J. R., Thomas, G. & Patterson, J. (1994), *in* A. W. Shafter, ed., 'Interacting Binary Stars: a symposium held in conjunction with the 105th meeting of the Astronomical Society of the Pacific', Vol. 56, Astronomical Society of the Pacific Conference Series.

van der Woerd, H., Heise, J., Paerels, F., Beuermann, K., van der Klis, M., Motch, C. & van Paradijs, J. (1987), *Astr. Astrophys.* **182**, 219.

van Teeseling, A. & Verbunt, F. (1994), *Astr. Astrophys.* **292**, 519.

van Teeseling, A., Beuermann, K. & Verbunt, F. (1996), *Astr. Astrophys.* **315**, 467.

Verbunt, F. (1982), *Space Sci. Rev.* **32**, 379.

Verbunt, F. (1997), *Mon. Not. R. Astr. Soc.* in press.

Vitello, P. & Shlosman, I. (1993), *Astrophys. J.* **327**, 680.

Warner, B. (1985), *in* P. P. Eggleton & J. E. Pringle, eds, 'Interacting Binaries', Dordrecht, Reidel, p. 367.

Warner, B. (1988), *Nature* **336**, 129.

Warner, B. (1995), *Cataclysmic Variable Stars*, Vol. 28 of *Cambridge Astrophysics Series*, Cambridge University Press.

Weaver, R., McCray, R., Castor, J., Shapiro, P. & Moore, R. (1977), *Astrophys. J.* **218**, 377.

Webbink, R. F. & Politano, M. (1993), On the origin of cataclysmic variables, *in* J. C. Leung & I. S. Nha, eds, 'New Frontiers in Binary Star Research', Vol. 38, ASP, p. 186.

Whitehurst, R. (1988), *Mon. Not. R. Astr. Soc.* **232**, 35.

Williams, G. A. (1983), *Astrophys. J. Suppl.* **53**, 523.

Williams, G. A. & Shipman, H. L. (1988), *Astrophys. J.* **326**, 738.

Wood, J. H., Marsh, T. R., Robinson, E. L., Stiening, R. F., Horne, K., Stover, R. J., Schoembs, R., Allen, S. L., Bond, H. E., Jones, D. H. P., Grauer, A. D. & Ciardullo, R. (1989), *Mon. Not. R. Astr. Soc.* **239**, 809.

Woods, J. A., Drew, J. E. & Verbunt, F. (1990), *Mon. Not. R. Astr. Soc.* **245**, 323.

Woods, J. A., Verbunt, F., Cameron, A. C., Drew, J. E. & Piters, A. (1992), *Mon. Not. R. Astr. Soc.* **255**, 237.

Zhang, E., Robinson, E. L., Ramseyer, T. F. & Shatrone, M. D. (1991), *Astrophys. J.* **381**, 534.